The Gas-Surface Interactions of Zirconium Based Metal-Organic Frameworks

By

Mason Chester Lawrence

A thesis submitted to the School of Graduate Studies in partial fulfillment of the requirements for the degree of

Doctor of Philosophy

Department of Chemistry

Memorial University of Newfoundland

July 2023

St. John's Newfoundland

Abstract

Metal-organic frameworks (MOFs) are a class of porous materials that are formed when inorganic metal cations or clusters (nodes) are combined with organic anions (ligands). With careful choice of both node and ligand a porous material that contains a large internal surface area can be formed. With a large internal surface area, the study of many real-world applications of MOFs have been investigated such as catalysis, gas separations, gas storage and drug delivery. This thesis explores how the modification of structural features (e.g., pore sizes, functional groups, defect concentration) in zirconium-based MOFs impacts the gas/vapour adsorption of two atmospherically abundant compounds.

Chapter 2 explores how water adsorption capabilities changes as the previously mention structural features are changed. The obtained results suggest that the water adsorbs by a water cluster growth mechanism that starts around the node. Estimation of the contact angle of water in the pore suggests that as the size of the ligand (i.e., pore size) is increased, the material becomes more hydrophobic. With the addition of pendant amine groups, the MOFs become more hydrophilic but the impact of the addition of the amine group decreases as the length of the ligand increases.

Chapter 3 focuses on how structural features impacts the carbon dioxide gas adsorption properties. Pore size, number of defects, cluster dehydration, and cluster functionalization were examined to determine which features had the biggest enhancements on the carbon dioxide gas adsorption. The experiments found that pore size

had the largest impact on the enthalpy of adsorption of carbon dioxide gas. MOFs that naturally had small pores, or were functionalized to reduce the pore size, had more confinement effects that lead to an increased enthalpy of adsorption. Furthermore, the experiments showed how important the cluster-containing μ_3-OH units were on carbon dioxide gas adsorption.

Finally, Chapter 4 outlines some projects that have been started, but due to the COVID-19 pandemic were unable to be completed. Some of these are direct extensions to the work in Chapter 2 and Chapter 3, while others are new projects that were thought of during my graduate program.

To my Family and to my wife, Melissa

Acknowledgements

As a young child and asked what I wanted to be when I "grew up" I would often reply "a doctor". Little did I know that I would become one, but not quite as I had envisioned. The journey to this point has not been an easy one, or one that I had even seen myself on. I was not able to get to this point alone; I had the help of many others along the way.

I would not be anywhere near this point without my supervisor Dr. Michael Katz. If it were not for Mike, I would have never had an opportunity to pursue research and find something I truly enjoy doing. Beyond the opportunity to do research, Mike has taught me countless in-lab skills, along with how to be a scientist. He encouraged me to ask questions, to think beyond the data, to look at the big picture, how to approach a problem, and how to solve it. He has always been encouraging when I began to doubt myself, and he constantly reassured me that I can do this. He always had a joke to help pick me up when I was having a rough day. Mike also provided advice on many matters outside of the lab, helping me navigate the challenges both in this degree and as life as a graduate student. I can never thank you enough Mike.

Without the help of the entire Katz group, I would not be where I am today. I joined the group in its early stages, so when I say the entire Katz group, I mean everyone. With this being said, there are a few people I need to give a special shout out to. Ellan, for a conversation every now and then to take our minds off the lab, but also to be someone to

bounce ideas off. Craig, for always knowing how to make a guy laugh, and Amanda for asking the questions that really made me think.

Thank you to my entire Family, for being a huge support system and always encouraging me to reach my goals. My parents Shirley, Chester, Mick and Laura, I would not be here without your constant love and support. Grandparents Luke and Eunice, thank you for believing in me from day one. I also can't forget to give a big shout out to my sister, brother-in-law, and brother. Holly, Patrick, and Andrew, thank you for everything you have done to help me along the way. To my friends, Taylor, Parsons, Josh, Luke, and Tim, thank you for your advice, banter, and support all these years.

I would also like to thank my committee members Dr. Francesca Kerton and Dr. Huck Grover for their support throughout this degree. I would also like to thank Dr. Celine Schneider for all her help with NMR experiments and analysis throughout this degree. Thank you to the School of Graduate Studies, Department of Chemistry, and Qalipu Fist Nations for your financial support.

Finally, I must thank my wife, Melissa. You have supported me along every single step of this journey and believed in me when I didn't even believe in myself. You celebrated the highs with me, and you helped me out of the lows. You may not realize how much encouragement you have given me these past five years, but you were a huge part of this accomplishment. A thank you will never show how grateful I am for your support.

COVID-19 Statement

During my PhD the COVID-19 pandemic began, and the ensuing shutdowns had a large impact on the capability to complete research.

Shortly before the initial lockdown of March 2020 the manuscript in preparation from the research in Chapter 2 was almost complete, with only three experiments left to perform before submission. Due to limited access to the lab for almost six months, the project was put on hold leading to submission to be postponed for almost a full year. If this delay had not been experienced this project would have been completed much sooner.

The initial results collected in Chapter 3 were done so in accordance with the back to lab plan that was put in place as restrictions from the initial lockdown. With limited access to the lab and instruments data collection took longer than if I would have had full access to the lab, this slowed the pace at which research could be completed. Without this hurdle data collection and interpretation would have been done much quicker.

Chapter 4 outlines some potential future projects along with some research that has already began. Without these delays the projects that were started would be near completion while some of the proposed project could have been started.

Table of Contents

List of Tables

List of Figures

List of Schemes

List of Abbreviations and Symbols

°	Degrees
1,1-F-BPDC	3,3'-Difluoro-[1,1'-biphenyl]-4,4'-dicarboxylic acid
^{1}H	Proton
2,2-F-BPDC	3,3',5,5'-tetrakis(fluro)biphenyl-p,p'-dicarboxylic acid
A	Surface Area of a Sample
Å	Ångstrom
AA	Acetic Acid
ATR-FTIR	Attenuated Total Reflection Fourier Transform Infrared Spectroscopy
ATZ	3-Amino-1,2,4-triazole
BDC	Benzene Dicarboxylate
BET	Brunauer, Emmet, and Teller
BPDC	Biphenyl-4,4'-dicarboxylate
C	BET Constant
c	Correction Factor
ca.	Approximately/Circa
CALF	Calgary Framework
cm^3	Centimeters cubed
CPM	Crystalline Porous Materials
d	Doublet
DABCO	Diazabicyclo[2.2.2]octane

DAC	Direct Air Capture
D_c	Critical Diameter
dd	Doublet of Doublets
deg	Degrees
DFT	Density Functional Theory
DMF	*N,N*-Dimethylformamamide
DMSO	Dimethylsulfoxide
DOBDC	2,5-Dioxido-1,4-benzenedicarboxylate
DUT	Durban University of Technology
Et- Me_4-TPDC	Diethyl-2',3',5',6'-tetramethyl-[1,1'1:4',1"-terphenyl]-4,4" dicarboxylate
Et-NH_2-TPDC	diehtyl-2'-amino-1,1′:4,1"-terphenyl-4,4"-dicarboxyate
g	Gram
G	Gibbs Energy
H	Enthalpy
HCl	Hydrochloric Acid
HKUST	Hong Kong University of Science and Technology
HVAC	Heating, Ventilation, and Air Conditioning
hz	Hertz
ICE	Initial, Change, Equilibrium
IRMOF	Isoreticular Metal-Organic Framework
ISE	Fraunhofer-Institute Solare Energiesysteme

J	Coupling Constant
K	Kelvin
K	Equilibrium Constant
kg	Kilogram
kJ	Kilojoule
KOH	Potassium Hydroxide
L	Liter
L	Cross Sectional Area of a Gas Molecule
M	Concentration in Moles per Leiter
m^2	Metres Squared
Me	Methyl
Me_4-H_2TPDC	2',3',5',6'-tetramethyl-[1,1'1:4',1"-terphenyl]-4,4"-dicarboxylic acid
MeOH	Methanol
mg	Milligram
MHz	Megahertz
MIL	Materials Institute Lavoiser
min	Minute
mmHg	Millimeters of mercury
mmol	Millimole
MOF	Metal-Organic Framework
mol	Mole
MW	Molecular weight

N_A	Avogadro's Constant
NH_2-H_2BPDC	2-Amino-biphenyl-4,4'-dicarboxylic acid
NH_2-H2TPDC	2'-Amino-1,1':4,1''-terphenyl-4,4''-dicarboxylic acid
nm	Nanometers
n_m	Monolayer Capacity
NMR	Nuclear Magnetic Resonance
NOAA	United States National Oceanic and Atmospheric Administration
NU	Northwestern University
ox	Oxalate
P	Pressure
PCN	Porous Coordination Network
ppm	Parts per million
PXRD	Powder X-ray Diffraction
q	Quartet
Qads	Quantity of Gas Adsorbed
Q_{Max}	Adsorption Capacity
R	Ideal Gas Constant
RH	Relative Humidity
rk	Pore Width
RPM	Rotations per Minuet
RT	Room Temperature
S	Entropy

s	Singlet
T	Temperature
t	Triplet
T_c	Bulk Critical Temperature of the Probe Molecule
TGA	Thermogravimetric Analysis
THF	Tetrahydrofuran
UiO	Universitetet i Oslo
V	Volume
Vm	Molar Volume of Liquid Water
ZIF	Zeolitic Imidazolate Framework
γ	Liquid/Vapour Surface Tension
δ	Chemical Shift
Δ	Change
θ	Contact Angle
σ	Size of Molecule Being Adsorbed

Chapter 1 : Introduction

Inorganic compounds where metal centres are bridged to form chains, sheets, and 3D structures have been around for a long time.[1–4] One of the oldest examples that comes to mind is Prussian Blue.[2] As shown Figure 1.1, Prussian Blue contains an octahedral iron(II) centre in the form of the $[Fe(CN)_6]^{4-}$ cyanometallate anion, where the cyanide anion is carbon bound to the iron(II) centre.[5] The nitrogen end of each of these cyanide units is further connected to an octahedral iron(III) centre. This connectivity continues in all three directions forming a 3D cubic framework.[2,5] To charge balance Prussian Blue, an additional potassium(I) cation is present inside the open space of the framework. Materials that contain metal centres bridged to one another by inorganic or organic ligands are part of the coordination polymer family.[6] Prussian blue has been shown to have many different practical applications such as dyes, an antidote for thallium poisoning, while analogues of Prussian blue has been introduced into batteries.[7–11] These analogues can contain different metals, potentially in different oxidation states, for the octahedral M(II), octahedral M(III), or the M(I) centre.[11]

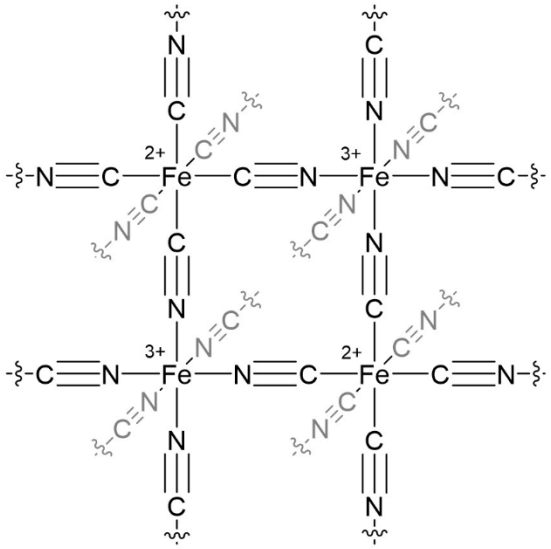

Figure 1.1: Prussian Blue.

While Prussian Blue is one example of a coordination polymer, there are many more examples that can be found throughout the literature.[12,13] Perhaps the simplest change from Prussian Blue is the use of cyanometallates that are not octahedral. Square planar cyanometallates such as $[Ni(CN)_4]^{2-}$ have been used to form the Hofmann Clathrates in which 2D sheets of $Ni[Ni(CN)_4]$ are formed with octahedral Ni(II) cations.[14] The octahedral Ni(II) contains two molecules (e.g., ammonia) in the two axial position of the sheet. Hofmann Clathrates have been used for separation of isomers of xylenes.[15] When the axial molecule on the Ni(II), is changed for a bridging ligand (e.g., pyrazine), then pillared Hofmann Clathrates are formed. By substituting the Ni(II) for other metals and by changing the length and type of pillared bridging ligand, a whole class of pillared Hofmann Clathrates can be formed.[16]

It is easy to see from this simple discussion that different cyanometallates, different metal cations, and different terminal (e.g., monodentate/chelating) or bridging ligands can

lead to different types of coordination polymers. With that in mind, other coordination polymers have been studied extensively and used for applications in dye remediation, electronics, and sensors to name a few examples.[17–21]

One natural extension of this work is to ask if coordination polymers with permanent porosity can be rationally designed from the approach outlined above (i.e., combining different metals and bridging ligands). One family of coordination polymers that have been well examined in the last ca. 25 years are metal-organic frameworks (MOFs).

1.1 Metal-Organic Frameworks

The first report of MOFs was in the late 1990's when Prof. Omar Yaghi and coworkers reported the combination of zinc(II) and benzene dicarboxylate (BDC) in solution under elevated temperatures to form MOF-5 (Figure 1.2), a porous material with high surface area that would develop a new field of chemistry.[22] The formula of MOF-5 was determined to be $Zn_4O(BDC)_3$ with a Zn_4O^{6+} cluster that formed in-situ and is connected to neighbouring Zn_4O^{6+} (Figure 1.2B) units through BDC^{2-} units (Figure 1.2A). The Zn_4O^{6+} and BDC^{2-} illustrate the two main components of any MOF, a node – the Zn_4O^{6+} in this example – and an anionic organic ligand – benzene dicarboxylate in this example. The node in MOF-5 is considered a six-connected node or an octahedral node. This means that each node connects with six BDC^{2-} ligands, hence six-connected. These six ligands arrange themselves around the node in an octahedral geometry. While in coordination chemistry, we would expect to find six metal-ligand bonds at approximately 90° to one another, in MOF chemistry, we refer to the number of ligands rather than the

number of metal-ligand bonds; depending on the ligand, these may be coincidently the same. In the case of MOF-5, the Zn_4O^{6+} node contains twelve Zn-O bonds from six different BDC^{2-} units. Organic ligands will be further discussed in Section 1.1.3, but briefly, the ligand needs to possess at least two Lewis-basic groups (e.g., two carboxylate groups in BDC) that preferentially bridge two nodes rather than chelate them. We can look at MOF-5 from a topology point of view where we simplify the node as a ball and the ligand, in the case of BDC, as a stick where the two ends of the stick connect to different nodes. As shown in Figure 1.2 this forms a 3D cubic network, and thus pore, topology. It should be noted that for clarity in Figure 1.2B the carboxylate group coming out of the page, which would be connected to the two black zinc centres, has been omitted. The topology of MOF-5 and Prussian Blue are the same, but there is considerably more internal surface area in MOF-5 than in Prussian Blue. There are also considerably more ways to increase the porosity of MOF-5 versus Prussian Blue.

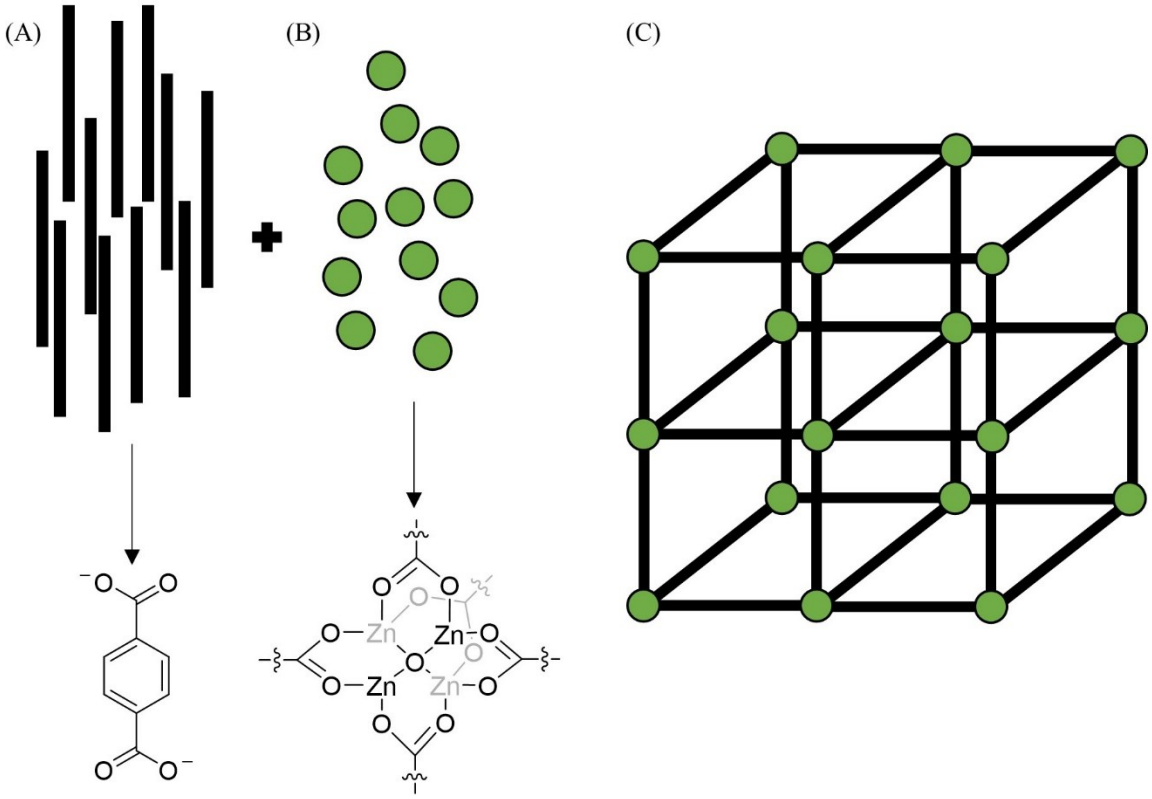

Figure 1.2: The combination of organic ligands (A) and inorganic nodes (B) to form a cubic three-dimensional topology which is porous (C). When benzene dicarboxylate is used as the organic ligand and a zinc node is used MOF-5 with a cubic structure is formed.

There are lots of possible topologies available by changing the connectivity of the node, the geometry of the connected node, the number of Lewis-basic groups on the node, and the relative orientation of the Lewis-basic groups around the node. Furthermore, the topology does not have to generate just one type of pore.

1.1.1 Metal-Organic Framework Nomenclature

MOF-5 being the first reported MOF is slightly counterintuitive, the 5 would suggest that it is the 5th MOF synthesized and published. Herein lies an issue with introducing MOFs to researchers from outside the field; there is often no obvious

association between the name of the MOF and the structural/topological features that would allow a researcher to determine what the MOF looks like and what it may be used for. Often, the nomenclature is simply two to three letters followed by some numbers. The letters can often indicate the institution at which the MOF was first discovered such as UiO, MIL, HKUST, DUT, CALF and NU to name a few examples (University of Oslo – Universitetet i Oslo in Norwegian, Materials Institute Lavoiser, Hong Kong University of Science and Technology, Dresden University of Technology, Calgary Framework, Northwestern University, respectively).[23–28] Some other names can include MOF, IRMOF, PCN, and ZIF (Metal-Organic Framework, Isoreticular MOF, Porous Coordination Network, Zeolitic Imidazolate Framework, respectively).[22,29–34] The latter set of names describe the material instead of the place it was synthesized. The numbers that follow often have no obvious significance, or no significance at all. This becomes cumbersome for someone just entering the MOF field, especially when different letter codes can contain similar nodes but either similar or different topologies. UiO, NU, and PCN can all refer to the same $Zr_6O_4(OH)^{12+}$ node.[23,28,35] The UiO family of MOFs, the focus of this thesis, have the same node and topology so the rational for the name is logical. MOFs such as the NU family of MOFs can have the same ligand/node combination in different topologies, the same node but different ligands in the same topology, or the same node but different ligands in different topologies. While undoubtedly each research team/teams have a consistent rationale for the names, in the absence of a "Rosetta stone" this can be challenging. Further confusion can occur when materials that have the same structure share a common name. For example, PCN-57 and UiO-68-Me_4 are the exact same MOF as are MOF-5 and

IRMOF-1.[36,37] For all the reasons listed above, while the MOF nomenclature may be frustrating/challenging, I will make every effort to introduce the important features of a MOF as they pertain to the discussions in the chapters ahead.

1.1.2 The Metal Node

As alluded to above, there are different types of metal nodes that are found throughout MOF literature and can exist in many different forms. One example is a cluster-based node that often forms during synthesis and can contain several of the same metal ions that are bridged by μ_x-oxo or μ_x-hydroxo ligands. This is observed in $Zr_6O_4(OH)_4^{12+}$ and Zn_4O^{6+} nodes mentioned in Section 1.1.1. $Zr_6O_4(OH)_4^{12+}$ (further discussed in Section 1.2) is found in the common UiO family of MOFs. This cluster contains six central zirconium atoms that are joined by four μ_3-oxo and four μ_3-hydroxo atoms.[23,38] Zn_4O^{6+} occurs in MOF-5 where the Zn(II) centres form a Zn_4O^{6+} node that contains four Zn(II) centres coordinated to a tetrahedral μ_4-oxo unit.[22,39]

There are no requirements for a metal node, other than it is a Lewis-acidic metal or group of metals. In the literature single metal sites such as manganese, chromium, iron, nickel, cadmium, and zinc and have been used as metal nodes in MOFs. Specifically, manganese and nickel can be found in MOF-74-Mn and MOF-74-Ni.[40–45] Iron and chromium can be seen in MIL-53-Fe and MIL-53-Cr, respectively.[24,46] In the ZIF and CdIF family of MOFs there are zinc and cadmium metals that are bridged to one another using the two nitrogen groups of an imidazolate core (ligands such as the imidazole in the ZIF and CdIF family of MOFs will be discussed in Section 1.1.3).[34,47] Synthesizing the same MOF topology but with a change in only the metal centres, as mentioned in MOF-74 and

MIL-53, is a common strategy when an ideal pore size or geometry is desired but a lower gravimetric surface area, increased stability, or decreased toxicity is also desired.

Focusing on MIL-53 (Figure 1.3), the metal ion M, is joined by four BDC ligands. The central metal is octahedral, bound to four oxygens from the dicarboxylate of the ligand, and two μ_2-oxygen atoms that connect neighbouring metals.[48] This bonding arrangement allows for the metals to form a chain rather than the discrete nodes of MOF-5 and UiOs.

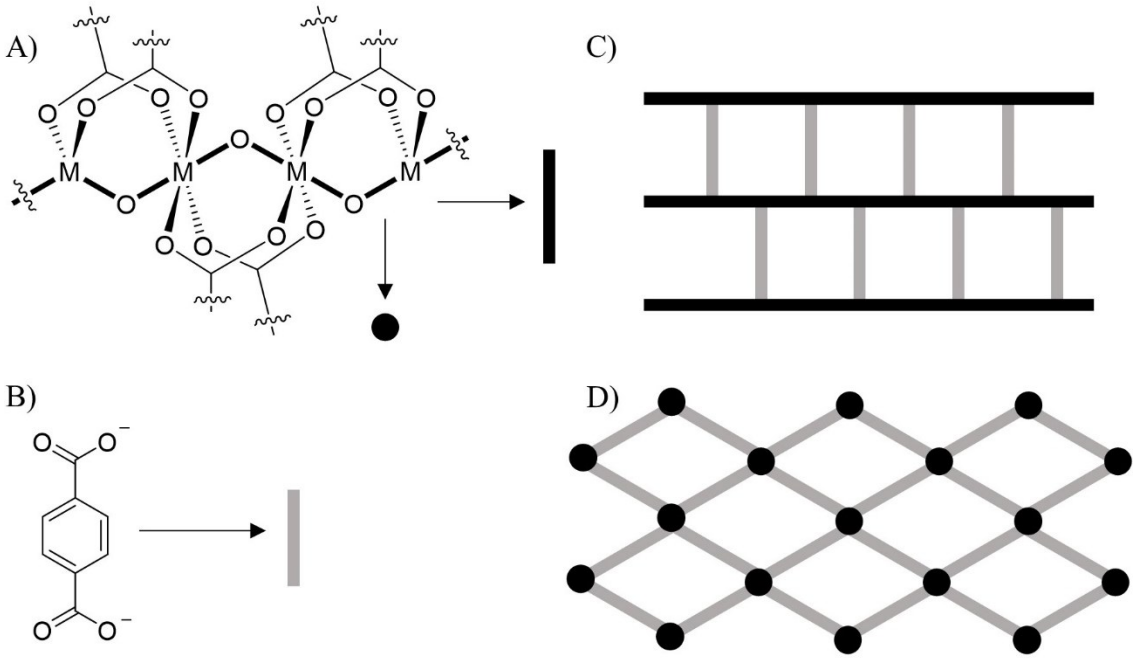

Figure 1.3: Structure of MIL-53 (A) metal-oxygen-metal backbone of the structure (B) benzene-1,4-dicarboxylate (C) and (D) showing the structure of the material looking down two different axis.

1.1.3 Organic Ligands

There is a lot of freedom with the type of ligand that is incorporated into MOFs. As long as the ligand is able to bridge two different metals rather than chelating a metal, then different properties, shapes, and functionalities can be utilized in the design of the MOF.[49]

These features can introduce new properties into the MOF, create different topologies, create new pore sizes/shapes, or change the size of the pore aperture.[50]

At the top of Figure 1.4, we see a schematic of an ideal ligand in MOF chemistry. The ideal ligand contains a rigid core that will help create a rigid framework. The core further contains at least two Lewis-basic groups that can bridge two metal centres. Perhaps the most common groups are carboxylates. These Lewis-base groups can be part of the core. For example, imidazole contains the two Lewis-basic nitrogen groups within the core structure. The last component of the ligand is optional. It is a functional group that can decorate the pore and introduce some form of functionality (e.g., gas binding, catalysis, etc.) to the porous structure.[51,52] Ideally, the presence of this group will not affect the overall topology of the MOF. This allows researchers to develop structure property relationship.

Perhaps the simplest bridging ligand that can be used with MOFs is the dianionic 1,4-benzene dicarboxylate ligand (Figure 1.4 bottom). As outlined above, the ligand contains a rigid core, two carboxylate groups that can each attach to a different node, and synthetic tunability to introduce functional groups into the pores of the MOF. There exist many examples in the literature of pendant groups installed on BDC.[53,54] Some of the most common groups are -OH, $-NH_2$, and $-NO_2$, but more complex systems have also been utilized.[54,55]

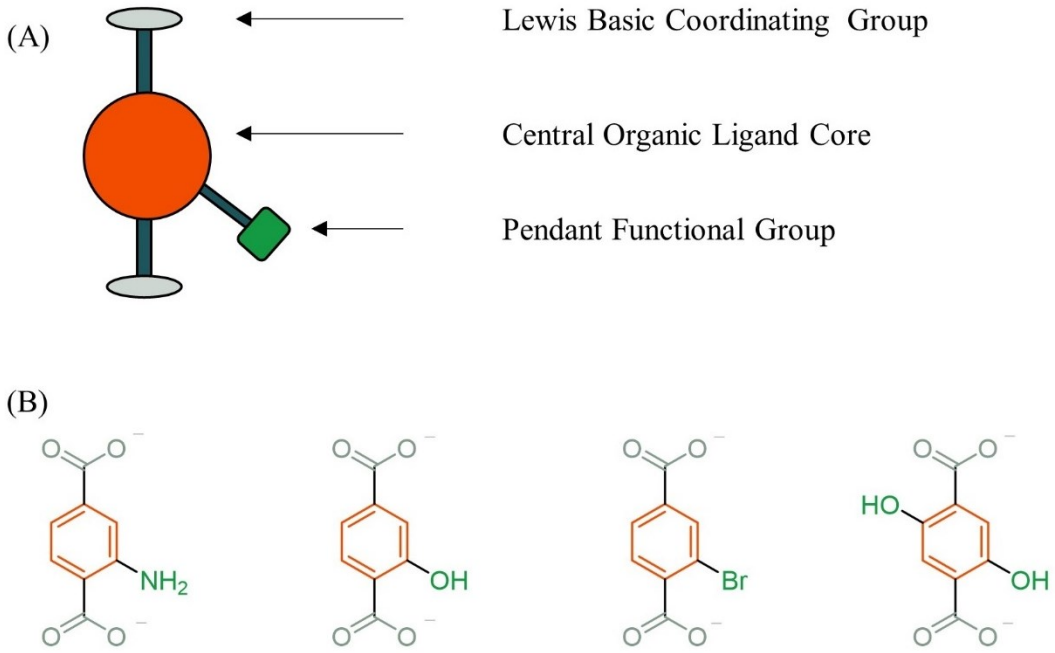

Figure 1.4: Outline of the features of an ideal MOF ligand (A). Some examples of functionalized benzene dicarboxylate ligands (B).

MOF-5 was synthesized with zinc and BDC to give a porous structure with defined pore shape and size.[22] For some applications, larger pores are necessary. This can be due to the total volume of gas that needs to be stored, the total accessible surface area that is needed to interact with a guest, or because the functional group that is introduced into the pore occupies too much space for the current MOF to accomodate.[30] To keep the same pore shape but increase the pore size and aperture, the length of the ligand can be extended from BDC to biphenyl-4,4′-dicarboxylate, [1,1′:4′,1″-terphenyl]-4,4″-dicarboxylate, or longer.[23,56] These ligands contain all the same capabilities of the parent BDC ligand but the MOF has larger pore properties.

The ligand can also be used to change the topology of the pore. Just as nodes can be six-connected or twelve-connected and generate one type of topology, changing the

number of connection points on the ligand can be used to generate different topologies with the same node. Starting from the ditopic BDC ligand, it can be easily seen how the tritopic trimesic acid (1,3,5-benzenetricarboxylic acid; H_3BTC) can be used to make MOFs with many of the same advantages as BDC.[57] For example, longer version of BTC can be made by introducing a spacer (e.g., phenylene) between the central ring and the carboxylate groups.[58] This approach to ligand design can be used to introduce additional Lewis-basic binding sites that can generate new topologies that can be tuned towards different applications (Figure 1.5).

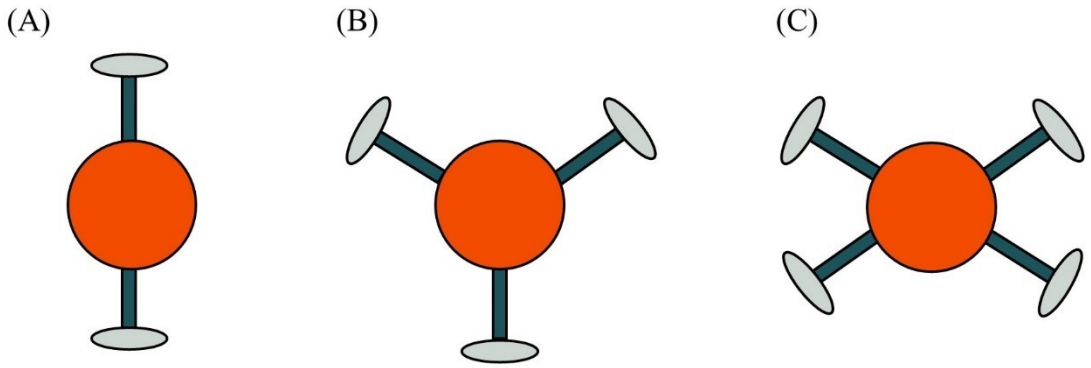

Figure 1.5: Examples of ditopic (A) tritropic (B) and tetratopic ligands (C). Red circles represent the centre of the ligand, the grey ellipses represent the Lewis-basic sites.

One example from the literature is the copper-based MOFs CuBDC (Figure 1.6) synthesized by Tan *et al*. and HKUST-1 (Figure 1.7). Both MOFs are copper node containing but have different organic ligands.[25,59] CuBDC contains BDC ligands and HKUST-1 contains BTC ligands. The CuBDC node is a copper paddlewheel dimer (Figure 1.6), where each copper is square planar and the node is four-connected. The node

is then joined to other nodes via BDC ligands. This coordination between the nodes forms 2D sheets, with small square openings.

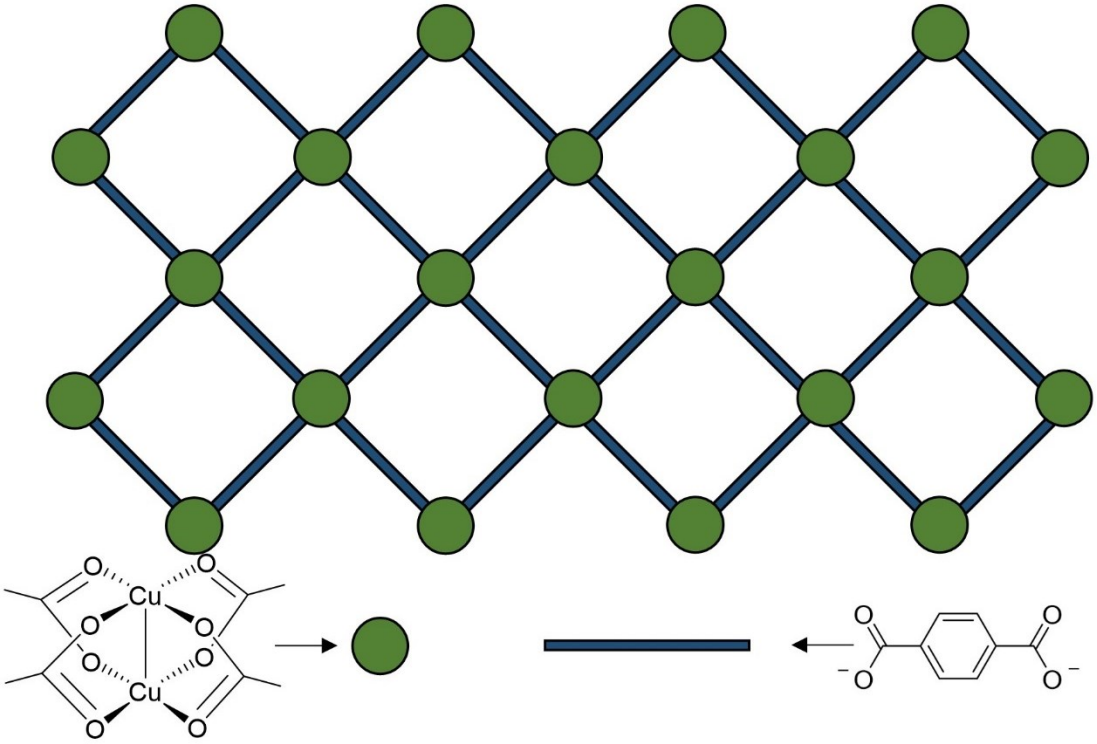

Figure 1.6: CuBDC structure showing sheets of Cu centres that are linked by terephthalic acids.

HKUST-1 is a MOF that also contains a paddlewheel-based copper node. One slight difference between the nodes is that in HKUST-1 there are two terminal water molecules in the remaining axial positions on the copper(II) centres. [25] This makes the node octahedral and four-connected, not square planar and four-connected.[59] However, when the sample is thermally treated, these two water molecules are displaced, resulting in the same node that was observed in CuBDC. Unlike the 2D structure of CuBDC, HKUST-1 contains two different types of pores. The pores in HKUST-1 can be described as a smaller, almost cubic, pore, and a larger hexagonal prism-based pore.

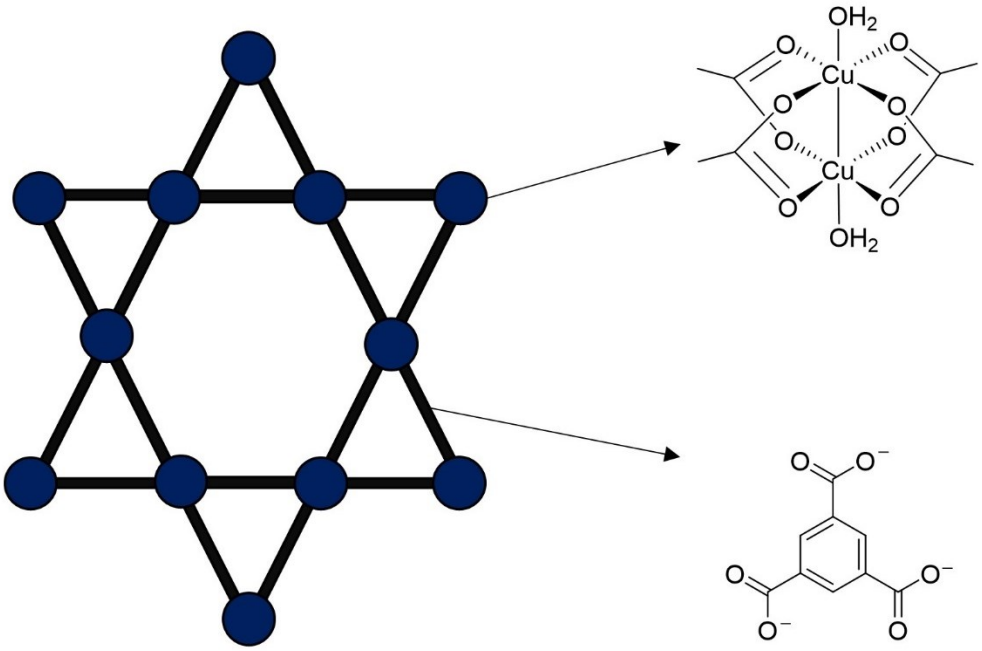

Figure 1.7: HKUST-1 with a central copper cluster and trimesic acid ligands.

While ditopic ligands tend to be the most popular in MOF synthesis, much larger ligands with up to eight carboxylate ligands present (Figure 1.8) have been utilized. Typically, benzene-based ligands are commonly used in MOF synthesis, however, there are many other bases for ligands, such as imidazoles, amino acids, and alkyl chains.[34,54,60,61]

Many of the MOF systems that have been discussed up to this point have only consisted of one type of ligand. However, there are examples in the literature that contain mixed ligands. There are many different types of mixed ligand MOFs. The mixed ligands could be a variable amount of the same core ligand with different functional groups on the ligand. For example, MOF-5 can be synthesized with 50% terephthalic acid and 50% 2-aminoterephthalic acid ligands.[62] We also see the addition of ligands with different cores/charges/connecting groups to create a new topology and pore structure.[56,63]

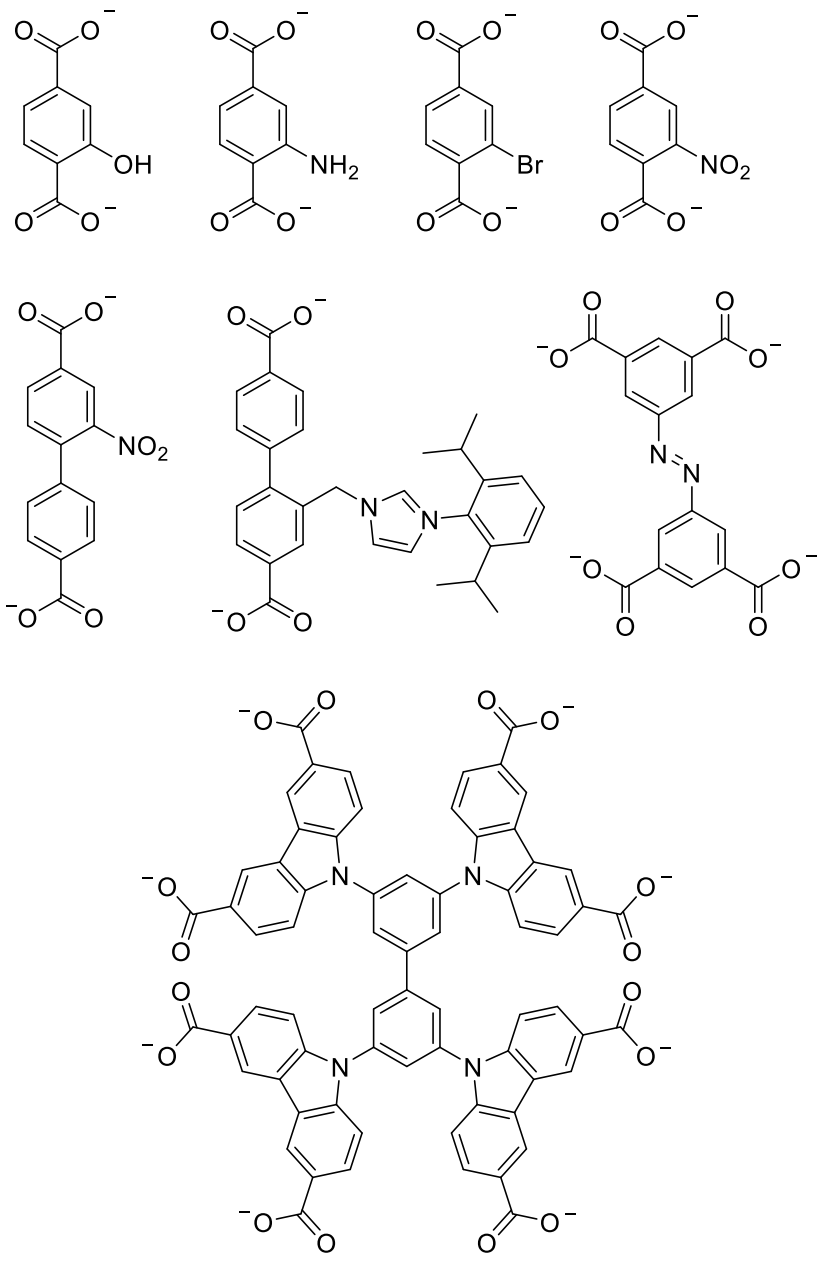

Figure 1.8: Examples of ligands incorporated into MOFs.[64–66]

One of the most common types of MOFs that included multiple ligands to form different pore structure is pillared paddlewheel MOFs. In many ways, these is like the pillared Hofmann clathrates discussed in the introduction. In the pillared paddlewheel MOFs, 2D sheets of $M_2(BDC)_2$ are extended into the third dimension using a neutral linear

nitrogen-based ligand such as 4,4'-bipyridine, diazabicyclo[2.2.2]octane (DABCO), and pyrazine (to name a few).[67–70] The MOF $Zn_2(BDC)_2(DABCO)$ is a common example of these types of MOFs in the literature.[67,71,72] As illustrated in Figure 1.9, the zinc coordinates to four BDC units to form the paddlewheel portion of the MOF. The DABCO molecules then form the pillar portion of the structure and link (i.e., pillar) the two sheets together forming a three-dimensional structure. The node is octahedral and six-connected.

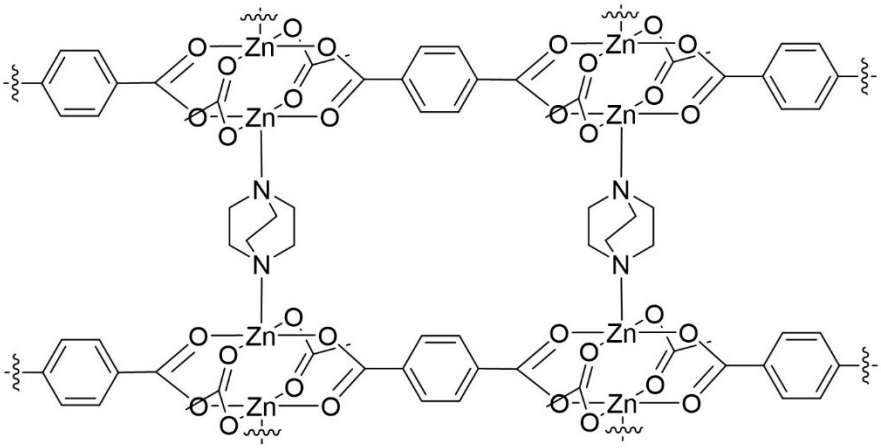

Figure 1.9: Structure of the pillared paddlewheel MOF $Zn_2(BDC)_2(DABCO)$.

1.1.4 Features of MOFs

One of the attractive features of MOFs is their large internal surface area, which can be used for a variety of applications.[73,74] The surface area of these MOFs is usually reported in metres squared per gram of material (m^2/g); this is referred to as the gravimetric surface area. Currently the surface areas of MOFs range from several hundreds, into the thousands. The largest recorded surface area to date is DUT-60 with an impressive 7800 m^2/g.[75,76] The gravimetric surface area is useful from an engineering standpoint; you can easily compare the surface area of one gram of each material. If the desire is for a material with a large internal surface and a low mass, replacing a heavy metal centre or

cluster for a lighter one can be an effective strategy in cluster containing MOFs to retain pore size and structure while decreasing the mass of material. If we consider UiO-66 with a surface area of 1580 m^2/g, and the formula $Zr_6O_4(OH)_4(BDC)_6$ it has a molar surface area of 2.62×10^6 m^2/mol.[56] If we were to replace the zirconium(IV) with the lighter titanium(IV), then there would be a decrease in the molar mass. The molar mass would fall from 1664.06 g/mol to 1403.92 g/mol. Since the topology of the material should remain the same, the molar surface area should also remain constant. With a molar surface area of 2.62×10^6 m^2/mol for Ti-UiO-66, the gravimetric surface area would be expected to be about 1875 m^2/g. This is an almost 20% increase in the gravimetric surface area by only replacing the metal present in the cluster-based node. Furthermore, MIL-53 synthesized with aluminum will have a lower molar mass compared to MIL-53 synthesized with iron. This would lead to more pores present in one gram of MIL-53-Al compared to MIL-53-Fe; this will lead to a higher gravimetric surface area.

From a chemistry view, the gravimetric surface area may not always be the ideal comparison. For MOFs that form the same topology but differ in the ligand being used or the metal in the node, a molar surface area is the ideal comparison. Between different MOF topologies a molar comparison can be more challenging given that different types of pores are present, and the formula weight may reflect a different percentage of the pore(s). Table 1.1 illustrates a few examples of the comparison of the gravimetric surface area and the molar surface area.

Table 1.1: Comparison of the gravimetric surface area and molar surface area of selected MOFs.

MOF	Chemical formula	Molar Mass (g/mol)	Gravimetric Surface Area (m^2/g)	Molar Surface Area (m^2/mol)
UiO-66	$Zr_6O_4(OH)_4(CO_2C_6H_4CO_2)_6$	1658.01	1580[56]	2.62×10^6
UiO-67	$Zr_6O_4(OH)_4(CO_2C_{12}H_8CO_2)_6$	2120.64	2500[56]	5.30×10^6
MIL-53-Al	$Al(OH)(CO_2C_6H_4CO_2)$	272.10	948[77]	2.58×10^5
MIL-53-Fe	$Fe(OH)(CO_2C_6H_4CO_2)$	300.96	23[46]	6.92×10^3
DUT-60	$[Zn_4O(CO_2C_{16}H_{12}CO_2)]_3(CO_2C_{42}H_{27}CO_2)_4$	4188.27	7839[75]	3.28×10^7
NU-1000	$Zr_6(\mu_3\text{-}OH)_4(\mu_3\text{-}O)_4(OH)_4(OH_2)_4(CO_2CO_2C_{40}H_{22}CO_2CO_2)_2$	2184.81	2050[63]	4.48×10^6

From the results in Table 1.1 it is clear that from a molar point of view we get very different surface areas. UiO-66 shows roughly 63% of the gravimetric surface area of UiO-67 but it shows less than 50% of the molar surface area. When comparing MIL-53-Fe and MIL-53-Al, there is a significant difference in the observed gravimetric surface area of one order of magnitude. However, on a per-mole basis, we see two orders of magnitude difference. Thus, it can be beneficial to compare molar surface areas to determine how changing a ligand or node effects the properties.

1.1.5 Chemical Formula of MOFs

The chemical formulas for most compounds are very intuitive and act as a quick identifier or shorthand notation for many chemicals. A few examples include methanol with a chemical formula of CH_3OH, benzene having a chemical formula of C_6H_6 and acetonitrile having a chemical formula of CH_3CN.

When thinking about MOFs, the chemical formulas may not be as intuitive as one would think, especially when defects must be considered. Defects are entropically favored and the picture of an infinite 3D structure of a MOF, or coordination polymer, is met with the reality that a crystal has a finite size and must terminate the infinite repeat unit.[78,79] This means that the perfect or ideal structure is unachievable. One of the most common defects observed is missing ligand defects, this is when a ligand is missing from where it is expected to be found.[80,81] These can be difficult to think about and include in the chemical formula for MOFs.

The best way to understand how MOF chemical formulas are generated is to think about it in two-dimensions as illustrated in Figure 1.10. In this figure we can see three different ways to consider the chemical formula of an infinite 2D sheet, and how to account for any missing ligand defects that may be present. All the representations are identical and lead to the same overall formula.

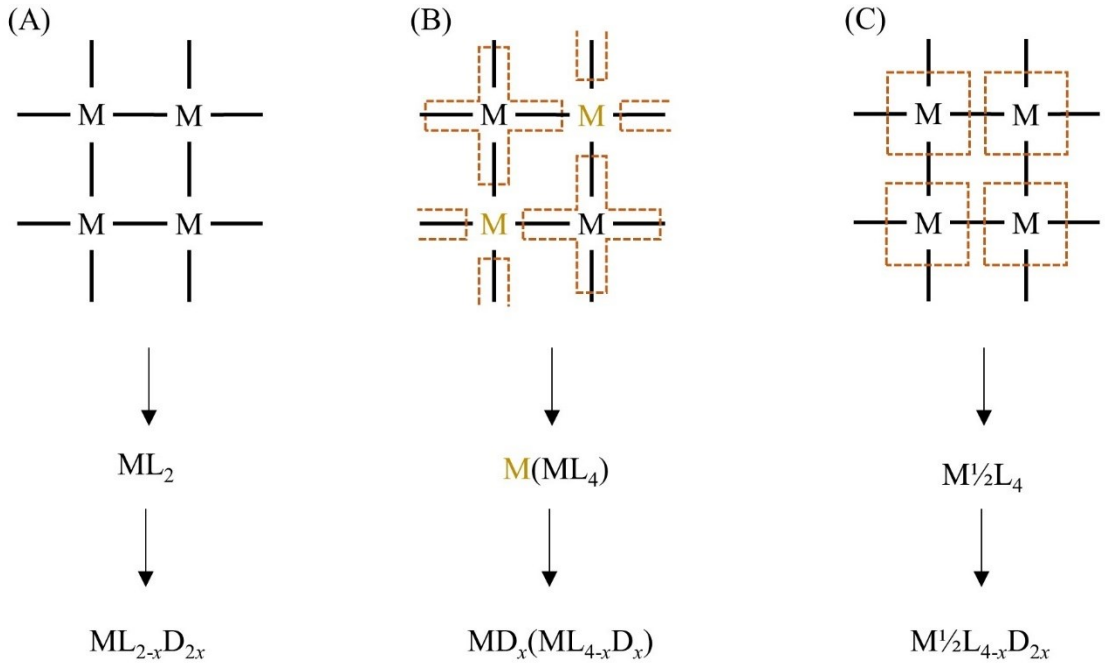

Figure 1.10: Three alternative ways to consider MOF chemical formulas and how each way accounts for missing ligand defects.

The formula of this 2D schematic MOF would be ML_2 (Figure 1.10A). Each metal is four-connected but each ligand is shared between two metals. However, there are a couple of different ways to come up with this formula. In Figure 1.10A each metal is connected to one ligand that is shared between two metals, which can be viewed as, $M½L_4$, that further simplifies to ML_2. When a defect is incorporated into this structure, we have the formula $ML_{2-x}D_{2x}$, where D is the defect in the material. The number of defects is twice that of the missing ligand due to the ditopic nature of the ligand coordinated to the metal. In other words, every time one ligand is removed, two defects are created (one on each metal the ligand was connected to).

Alternatively, we can view the 2D schematic MOF as a metal with four ligands $[ML_4]^{x-}$ attached to a metal with no ligands M^{x+} as illustrated in Figure 1.10B. $[ML_4]^{x-}$ are

inside the orange outline, while M^{x+} is represented by the yellow M. Each of the metal with no ligands is attached to three additional metals with four ligands. This pattern continues infinitely in both the *x*- and *y*-directions. In this representation, we can say $[ML_4]^{x-}$ is attached to M^{x+} to give {[M][ML_4]} which can be simplified to ML_2. When defects are considered, there would be a defect group present on the metal that was described as having "no ligands" and a defect group present on the $[ML_4]^{x-}$ ligand. This is due to the ditopic nature of the ligand; for each removed end we create one defect group. For example, a missing tritopic ligand would create three defects overall.

The third way we can think about the chemical formula of a MOF is shown in Figure 1.10C, in this case we view each metal connected to one half of the ligand, as illustrated by the orange squares this gives the chemical formula $M½L_4$. When we consider missing ligand defects, the new chemical formula would be $M½(L_{4-x}D_{2x})$.

We see that there are three different ways to think about and illustrate the chemical formula of MOFs. The first method outlined tends to be the one that is seen the most throughout the literature, and the way that the chemical formulas of MOFs will be referred to throughout this thesis.

1.2 UiO MOFs

This thesis will explore some of the properties of MOFs based on the UiO topology. With that in mind, it is worth spending some time focusing on the history and features of this family of MOFs. UiO-66 is perhaps the most famous of the UiO family of MOFs. UiO-66 was first reported by Professor Lillerude and coworkers in the Journal of the

American Chemical Society in 2008.[23] The manuscript briefly discussed the structure of the UiO family of MOFs. Lillerude suggested this family of MOFs had a lot of potential in the field due to the inherent stability of the zirconium cluster and the strength of the Zr-O bond. Lillerude was correct as there are over 4700 publications related to the UiO family of MOFs since the original publication.

The node for the UiO MOFs is a zirconium-based node with the formula $Zr_6O_4(OH)_4^{12+}$ as shown in Figure 1.11. The node is twelve-connected by linear, ditopic, carboxylate ligands.[23] Perhaps the most popular of the UiO MOFs is UiO-66 that utilizes the BDC^{2-} ligand.[23,56] In the defect-free UiO-66 structure, the formula is $Zr_6O_4(OH)_4(BDC)_6$. Each cluster is bridged to twelve other clusters via twelve BDC ligands. The topology of the UiO MOFs contain an octahedral pore and a smaller tetrahedral pore. The octahedral pore face shares with eight tetrahedral pores, and edge share with twelve tetrahedral pores. A portion of the overall topology illustrating one of each pore is shown in Figure 1.11.

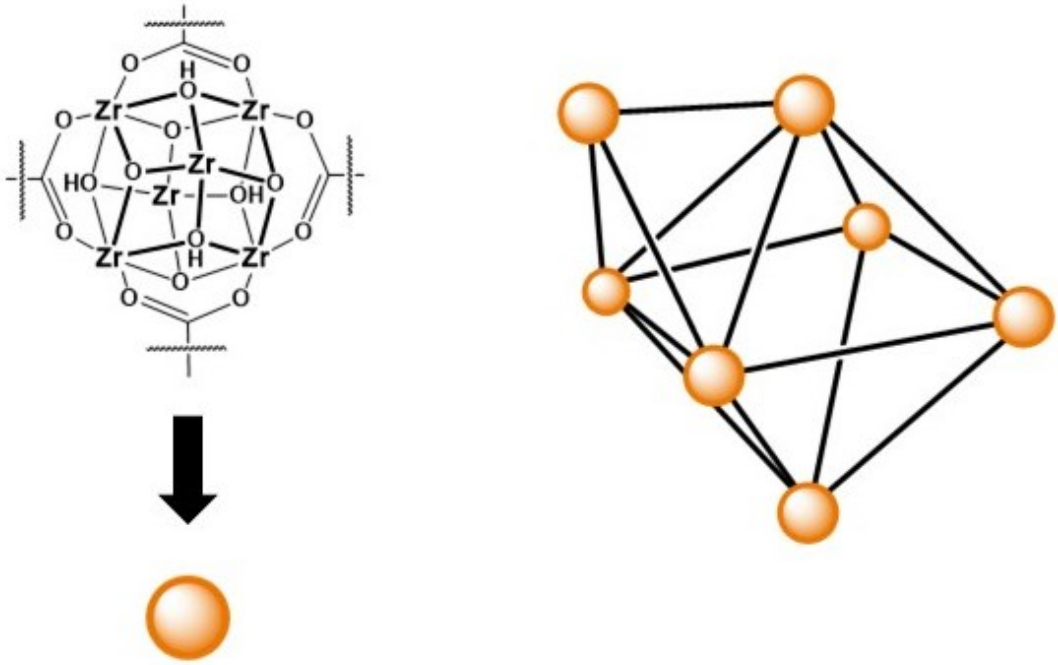

Figure 1.11: The $Zr_6O_4(OH)_4^{12+}$ node showing four of the twelve carboxylates (left), and a portion of the topology illustrating a face sharing octahedral and tetrahedral pore of UiO (right).

It should come as no surprise that by utilizing the same node and different linear ditopic carboxylate-containing ligands, that an isoreticular MOF with different pore sizes can be formed. For example, when H_2BDC is replaced by H_2BPDC (biphenyl-4,4'-dicarboxylic acid) in the synthesis of the MOF, then the large pore UiO-67 is formed.[23,56] By further increasing the ligand by one phenylene group, UiO-68 is formed. Structurally, as the ligand length increases, we see an increase in the pore size. The tetrahedral pore increases from 0.38 nm to 0.55 nm and finally to 0.99 nm as we move from UiO-66 to UiO-68.[82] Similarly, the octahedral pore increases from 0.80 nm to 1.31 nm to 1.72 nm.[82] Depending on the synthesis used to make these MOFs, the gravimetric surface

area increases from 1580 m^2/g for UiO-66, to 2500 m^2/g for UiO-67, and finally to 3300 m^2/g for UiO-68-Me_4.[35,56]

1.2.1 Defects in UiO MOFs

As mentioned in Section 1.1.5 defects exist in all materials and are unavoidable. The UiO family of MOFs are no exception. This means that the perfect structure of $Zr_6O_4(OH)_4(ligand)_6$ is unachievable.[83] One type of defect observed in the UiO family of MOFs are missing ligand defects, and if we are to include these defects into the chemical formula, then the chemical formula would be $Zr_6O_4(OH)_4(ligand)_{6-x}(defect)_{2x}$.[36,38] The amount of defect present is directly related to the amount of missing ligand. This ensures that the material does not contain any coordinately unsaturated metal centres and that the missing dianionic ligand is charge compensated by two anionic ligands. One of the defects that has been proposed is the presence of two OH^- and two H_2O molecules, as illustrated in Figure 1.12. While OH^- and H_2O are common defect caps for UiO MOFs, they are not the only ones reported in the literature.[83–85] Work by De Vos and colleagues has shown that the addition of trifluoracetic acid during the synthesis of UiO-66 caused the trifluoracetic acid to become a part of the structure of the material as a defect cap in the form of the trifluoroacetate anion.[80] Furthermore, work by Ameloot has illustrated that soaking UiO-66 in methanol over several days causes defects to become capped with CH_3O^-/CH_3OH.[86]

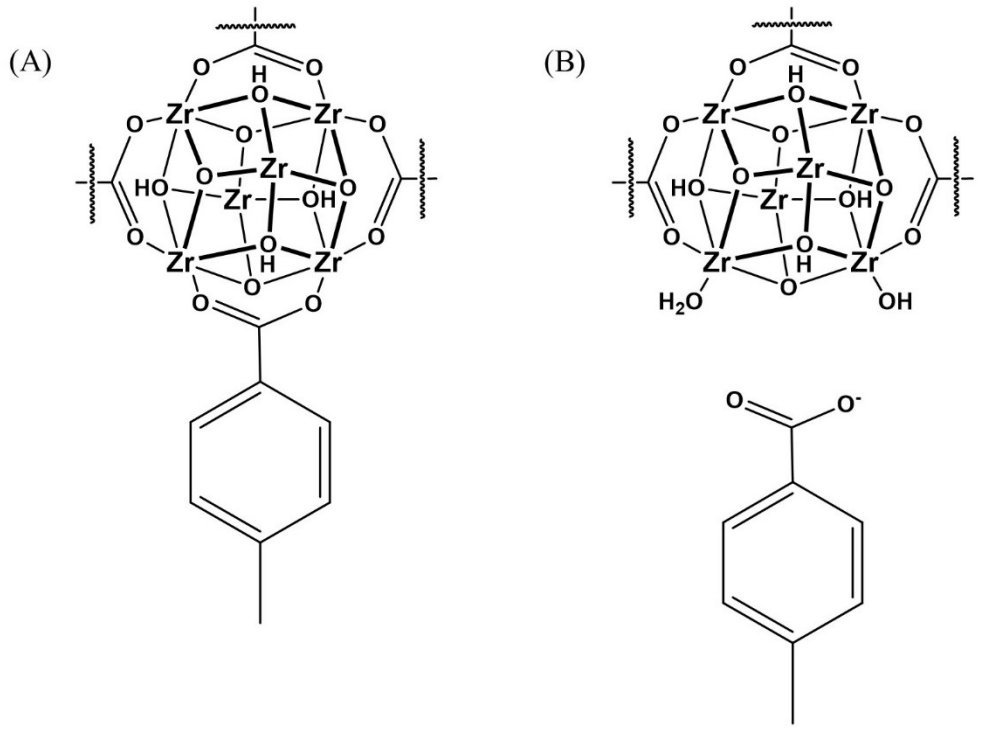

Figure 1.12: Zirconium cluster showing one BDC ligand attached via a carboxylate (A), and a Zirconium cluster that has a missing ligand defect that is capped with a OH^-/H_2O pair (B).

Using UiO-66 as an example, each carboxylate on a ligand is coordinated to two zirconium atoms via a bridging bidentate mode (Figure 1.13). Thus, both OH^- and H_2O are required to completely replace the ligand. This ensures that the zirconium is fully coordinated and charge balanced. Given that each ligand in UiO-66 is bridging two nodes, how these defects charge balance the formula can be confusing at times. In UiO-66 the zirconium cluster has twelve 1,4-benzendicarboxylate ligands attached as indicated in Figure 1.13. Which gives a chemical formula of $Zr_6O_4(OH)_4(BDC)_6$ (See Section 1.1.5 for chemical formulas of MOFs). However, we can also consider the chemical formula to be $Zr_6O_4(OH)_4½(BDC)_{12}$. The second way gives more clarity that twelve benzene dicarboxylate ligands are connected to one cluster.

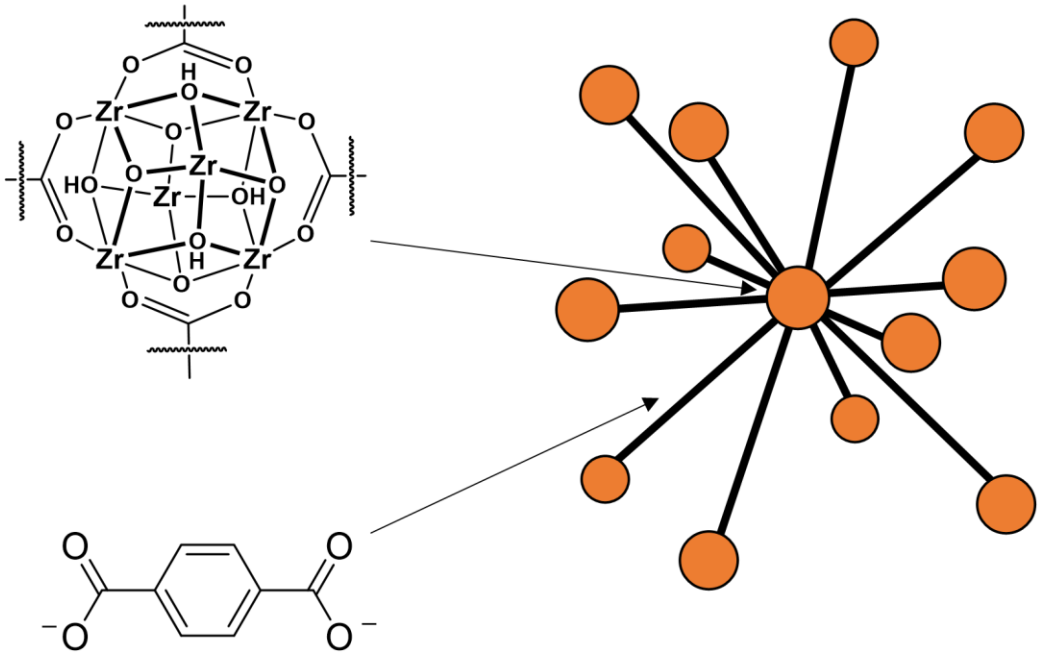

Figure 1.13: The zirconium cluster of UiO-66, and all UiO-based MOFs, and how it is connected to other zirconium clusters through BDC in the ideal structure. Each node is a twelve-connected node.

The formula for UiO-66 has been previously shown to be $Zr_6O_4(OH)_4(BDC)_6$.[23] If we think about the formula the second way outlined in Section 1.1.5 we still arrive at the chemical formula that is used in the literature.[23] We view UiO-66 as being comprised of a zirconium node with no ligands attached to a node with twelve ligands attached to it. The cluster with no ligands attached has a chemical formula of $[Zr_6O_4(OH)_4]^{12+}$. While the cluster that has the twelve ligands attached has the chemical formula of $[Zr_6O_4(OH)_4(BDC)_{12}]^{12-}$. When the two are connected we get the chemical formula $[Zr_6O_4(OH)_4][Zr_6O_4(OH)_4(BDC)_{12}]$, which simplifies to $Zr_6O_4(OH)_4(BDC)_6$, the general formula for UiO-66.

If a single ligand is removed from the MOF as illustrated in Figure 1.14, and replaced by OH^-/H_2O defect caps as previously discussed, the bonding between clusters and chemical formula is altered.

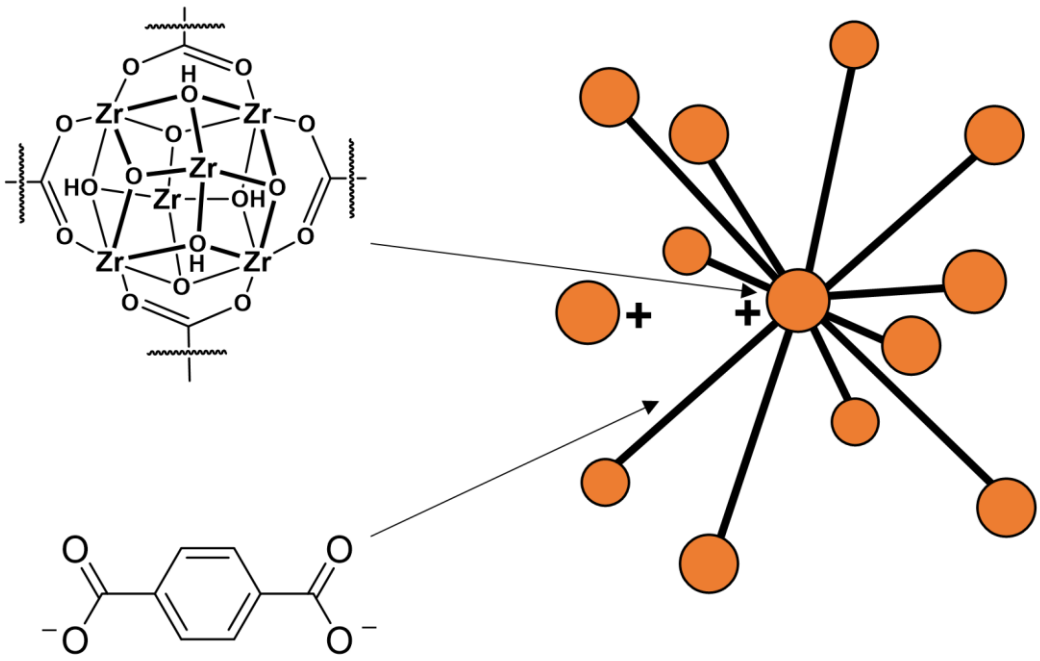

Figure 1.14: The zirconium cluster of UiO-66, and all UiO-based MOFs, and how it is connected to other zirconium clusters through BDC with one missing 1,4-benzenedicarboxylate introducing defects.

In Figure 1.14 the orange sphere on the far left can represent the cluster with no ligands being coordinated to the cluster containing eleven ligands, in this case the orange cluster in the centre. Once the OH^- and H_2O defect caps are incorporated, the cluster without the ligands would now have the chemical formula $Zr_6O_4(OH)_4(OH)(H_2O)^{11+}$, as the OH^- and H_2O has filled the two open coordination sites on the zirconium cluster. Using the nomenclature in Figure 1.10B, the cluster with ligands would have the chemical formula $Zr_6O_4(OH)_4(BDC)_{11}(OH)(H_2O)^{-11}$, where OH^- and H_2O replaces the ligand that was removed. From these two chemical formulas it is evident that the removal of one ligand

causes the incorporation of two OH^-/H_2O pairs, one on each cluster. Thinking about these two clusters in relation to each other, we now have a bonding of $[Zr_6O_4(OH)_4(OH)(H_2O)][Zr_6O_4(OH)_4(BDC)_{11}(OH)(H_2O)]$, which can be simplified to $Zr_6O_4(OH)_4(BDC)_{5.5}(OH)(H_2O)$. This illustrates how one missing ligand causes two OH^-/H_2O pair to be incorporated into the chemical structure. This provides us with the general formula for UiO based MOFs with missing ligand defects and a OH^-/H_2O occupying the ligand-vacant metal sites to be $Zr_6O_4(OH)_4(Ligand)_{6-x}(OH)_{2x}(H_2O)_{2x}$.

Missing ligand defects cause new cluster capping molecules to become incorporated and thus also causes a change in the molar mass. Defect free UiO-66 would have a molar mass of 1664.06 g/mol, while the material containing one missing ligand would have a molar mass of 1617.03 g/mol, a 3% decrease. The change in molar mass is dependent on the new incoming cluster capping molecules, and the number of ligands that are missing.

Knowing the number of defects in MOFs becomes very important when comparing surface areas. As previously mentioned, the molar mass of a MOF plays a large role in the gravimetric surface area. Decreasing the molar mass will lead to more material in one gram, which will increase the surface area. However, once we begin to remove ligands, we also remove surface that gas can bind to, which will decrease the surface area. To really understand the impact on surface area from the missing ligands it is very important to quantify the number of defects present and compare the molar surface areas. Common literature methods for determining missing ligands include quantitative NMR or thermogravimetric analysis (TGA).[38,87]

1.2.2 UiO Stability

Lillerud had originally alluded to the stability of UiOs making them ideal for real world and lab scale applications.[23] Since its initial discovery there have been many investigations into the stability of these MOFs.[54,88–90] The thermal stability of UiO-66 is well established and it is stable to a relatively high temperature of 620 K. The original 2008 paper indicated that the zirconium node would begin to decompose at 803 K.[23] Additional studies by Lillerud and others have been performed on the thermal stability of the UiO family of MOFs. Functionalized versions of UiO-66 have shown to also exhibit robust thermal stability.[54,91,92] UiO-66-NH_2 and UiO-66-NO_2 both retained crystallinity when heated to 573 K in air, while UiO-66-Br showed much higher stability and does not begin to decompose until 723 K.[54]

UiO-66 has also been cited to retain shape and crystallinity when exposed to different solvents. Lillerud had shown the stability of UiO-66 and its derivatives in ethanol, water and hydrochloric acid down to a pH of 1 (equivalent to 0.1 M hydrochloric acid).[54] Walton and co-workers also explored the stability of both UiO-66 and UiO-67 to organic solvents such as isopropanol, methanol, chloroform, pyridine, and acetone.[93] They monitored the change in crystallinity via powder X-ray diffraction (PXRD) and ATR-FTIR. UiO-66 and UiO-67 showed little change to the crystallinity and overall structure when soaked in the organic solvents, indicating that these MOFs are stable in these solvents.[93] UiO-66 has also been show to be stable in low pH conditions as well, with it being well documented that it is stable at a pH of 0-1 for prolonged amounts of time.[23,93–95] Waltons work also illustrated a point that became a topic of great debate in the MOF

community. When UiO-66 was submerged in water, removed, and activated (heating under vacuum to remove any residual solvent), then UiO-66 retained its crystallinity. When the same experiment was performed for UiO-67, there was almost a complete loss of crystallinity.[93] They attributed this to the torsional strain (i.e., the angle of rotation between the two aromatic rings) that could be relieved via the hydrolysis of the node-ligand bond and thus the collapse of the MOF.

To further explore the stability of UiO-67 in water, Hupp and coworkers investigated the impact of solvent exchange after soaking UiO-67 in water for an extended period of time, but before activation of the material. They had hypothesized that instability in water was due to the thermal activation from water in the pores (i.e., capillary forces) and not the material sitting in the water.[88] To test this hypothesis, they allowed UiO-67 to sit in water for 24 hours followed by solvent exchange with acetone prior to thermal activation. The nitrogen gas adsorption isotherms and PXRDs were measured before and after water soaking. Without solvent exchange, the material showed dramatic broadening in the PXRD pattern along with loss of nearly all porosity, as indicated by almost no nitrogen gas adsorption. The acetone-exchanged material retained all the peaks in the PXRD pattern, and the nitrogen gas adsorption remained unchanged relative to the parent material. This indicated that the instability of UiO-67 comes from the activation from water and not actually by being submerged into water.

1.2.3 Functionalized UiOs

Tailoring the ligand in MOFs to contain the desired functionality is a popular strategy used to impart properties to the pore.[96–98] Kaskel and coworkers have synthesized proline-functionalized biphenyl and triphenyl dicarboxylate ligands and incorporated them into UiO-67 and UiO-68, respectively (Figure 1.15).[99]

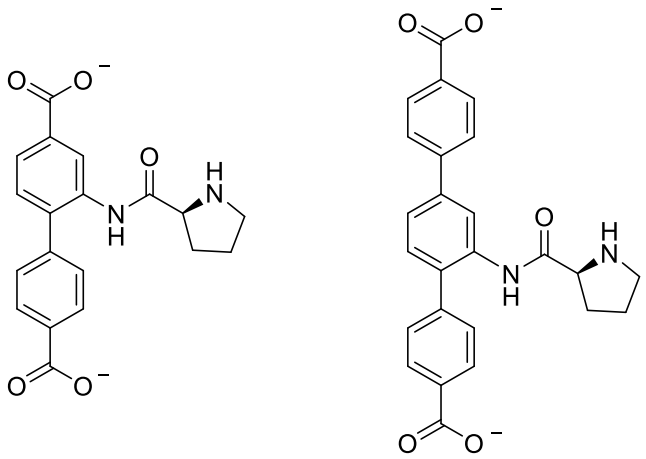

Figure 1.15: Proline functionalized biphenyl dicarboxylic acid and terphenyl dicarboxylic acid.

These MOFs were then used to catalyze the reaction between 4-nitrobenzaldehyde and cyclohexanone. Without the MOF and only the proline functionalized ligand present in solution, a yields of 60% with slight favor of the *anti* product was observed. When the proline functionalized UiO-67 was used, the yield was drastically reduced to 11% with almost no preference for the *sin* or *anti* product. In comparison, proline functionalized UiO-68 showed vast improvement and had a reaction yield of 97% and almost a 9:1 preference to the *syn* product. Kaskel and coworkers had attributed the change in reaction yield to the increased pore size in UiO-68 compared to UiO-67. With the larger pore size

present, diffusion of both starting materials (4-nirobenzaldehyde and cyclohexanone) along with the final product is much easier, attributing to the increased yield.

As previously mentioned in Section 1.2.1 De Vos added trifluoracetic acid to UiO-66 during the synthesis to create defects capped with trifluoroacetate anions.[100] These MOFs were subsequently used to catalyze the reaction of citronellal to isopulegol. The addition of trifluoroacetic acid drastically enhanced the conversion of the cyclization reaction. Without the trifluoroacetic acid modulator present, there was a conversion of approximately 20% after 10 hours. When 20 equivalents of trifluoracetic acid were included in the synthesis, then the conversion increased to 75% after 10 hours. To ensure that the increase in catalyst was not due to the trifluoracetate present in the MOF but rather due to the defect sites created because of the addition of the modulator, UiO-66 was heated to 593 K. Once heated to this temperature, trifluoracetic acid groups dissociated leaving open metal sites. ^{19}F NMR confirmed there were no trifluoro groups present in the sample and the catalysis was due to the open metal sites.

UiO based MOFs have also been used in water purification applications, Davies and coworkers have used functionalized UiO-66 to remove heavy metals including Cd^{2+}, Cr^{3+}, Hg^{2+} and Pb^{2+}.[101] UiO-66-NH_2, in which the ligand is the aminoterephthalic acid, was post-synthetically modified to replace the pendant amine group with other nitrogen-containing functional groups such as thiocyanate, methylthiourea (NHC(S)NHMe) and isocyanate, as shown in Figure 1.16.

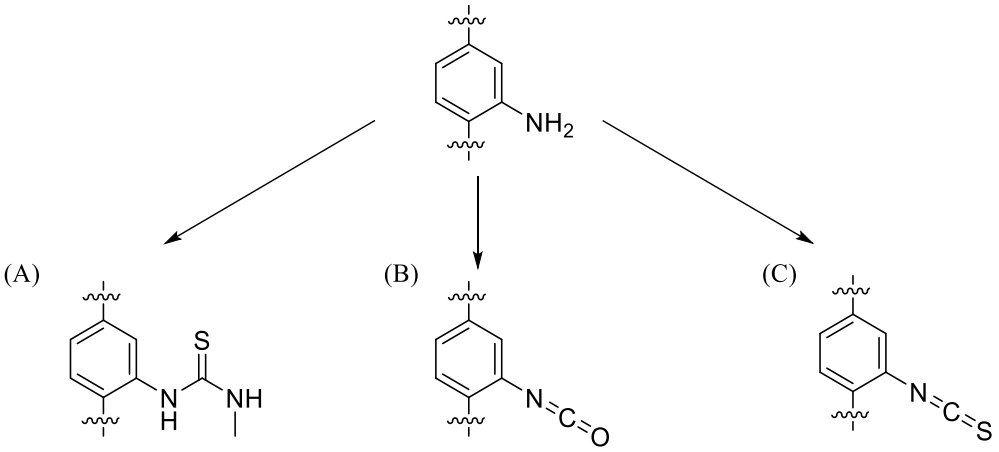

Figure 1.16: Functionalization of UiO-66-NH_2 to other nitrogen containing compounds for the removal of heavy metals from water. (A) UiO-66-NHC(S)NHMe (B) UiO-66-NCO (C) UiO-66-NCS.

By incorporating these functional groups, the removal of the previously mentioned heavy metals were removed in varying levels, as illustrated in Table 1.2.

Table 1.2: Efficiencies of functionalized UiO-66 for the removal of heavy metals from water.

	UiO-66-NH_2	**UiO-66-NCO**	**UiO-66-NCS**	**UiO-66-NHC(S)NHMe**
Cd^{2+}	18%	18%	35%	50%
Cr^{3+}	27%	22%	70%	65%
Hg^{2+}	8%	11%	91%	97%
Pb^{2+}	33%	26%	99%	73%

Davis has shown that when the functional group contains a sulfur atom, the adsorption is greatly increased. The authors report 95% and 99% removal of Pb^{2+} and Hg^{2+} from water with these MOFs respectively. The authors had also illustrated how the incorporation of the sulfur containing compounds was a great enhancement over the amine functionalized UiO-66.[101]

1.3 Applications of MOFs

This thesis will explore the adsorption of water vapour and carbon dioxide gas in zirconium-based UiO family of MOFs. Before we can dive into the results obtained, it is important to familiarize ourselves with the work that has been done in the literature. This section will provide a brief review of some of the strategies used to enhance the carbon dioxide and water vapour adsorption in many different MOFs along with results that researchers have obtained.

1.3.1 Gas Adsorption

With the large internal surface area as mentioned in Section 1.1, gas adsorption onto the surface of the MOFs has been greatly explored, and will be an active aspect of this thesis. Before exploring the different applications of MOFs for gas adsorption it is first important to understand how gases bind to a surface.

There are two main ways that a gas can adsorb onto a surface, the first is chemisorption. Chemisorption is when the incoming gas molecules undergo a chemical reaction with the surface of the material. This changes both the gas and the surface of the material.[102] This adsorption process leads to a very strong interaction between the gas and the surface as new bonds are formed. It can be quite difficult, or sometimes impossible, to break these bonds and reverse the reaction. Chemisorption can be advantageous in MOFs and has been taken advantage of for the removal of hydrogen sulfide gas from the environment. Zou and co-workers studied the interactions between hydrogen sulfide gas and different MOFs. UiO-66-NH_2 has provided some results of interest.[103] The pendant

amino group was able to react with the incoming hydrogen sulfide gas to form a pendant NH_3SH (Figure 1.17). To recover the original material and hydrogen sulfide gas, the MOF was heated to 573 K. This high temperature suggests that the hydrogen sulfide underwent a chemical reaction with the MOF, making it very hard to thermally reverse. PXRD analysis and nitrogen gas adsorption surface areas also indicate that a chemical reaction had occurred and the NH_3SH had formed. Furthermore, not all the hydrogen sulfide was able to be recovered through desorption, indicating that a chemical reaction had occurred. This indicates that part of this process is through chemisorption.

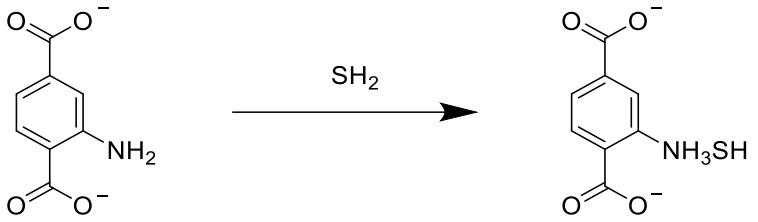

Figure 1.17: Reaction of 2-aminoterepthalicarboxylate (the ligand in UiO-66-NH_2) with hydrogen sulfide gas.

The second adsorption method is physisorption. This is the most common interaction that we see in gas adsorption in MOFs. This is where intermolecular forces such as dipole interactions or quadrupolar interactions occur between the gas molecules and the surface of the MOF.[104] These interactions are much weaker than chemisorption, and of these interactions the dipole-dipole interactions would be the strongest followed by the quadrupolar interactions. When a gas molecule is physisorbed onto the surface of a material, there is no chemical change unlike chemisorption. Since there is no chemical change, both the gas and the surface remain mostly unchanged making it possible for

desorption to occur easier due to only intermolecular forces needing to be overcome instead of the breaking of chemical bonds.

Physisorption occurs for many different molecules in MOFs. One of the most common examples of physisorption in MOFs is nitrogen gas adsorption. Nitrogen gas is often used to determine the surface area of MOFs and will be further discussed in Section 1.4.4.1. Nitrogen gas however does not contain a permanent dipole, but it does contain partial charges (Figure 1.18). The centre of a nitrogen molecule, the triple bond, contains a localized positive charge. While the outsides edges, where a lone pair is present, contain a localized negative charge. With these electropositive and electronegative regions, there are quadrupolar interactions between the nitrogen molecules and the surface of the MOF where the gas becomes physiosorbed (Figure 1.18 bottom).

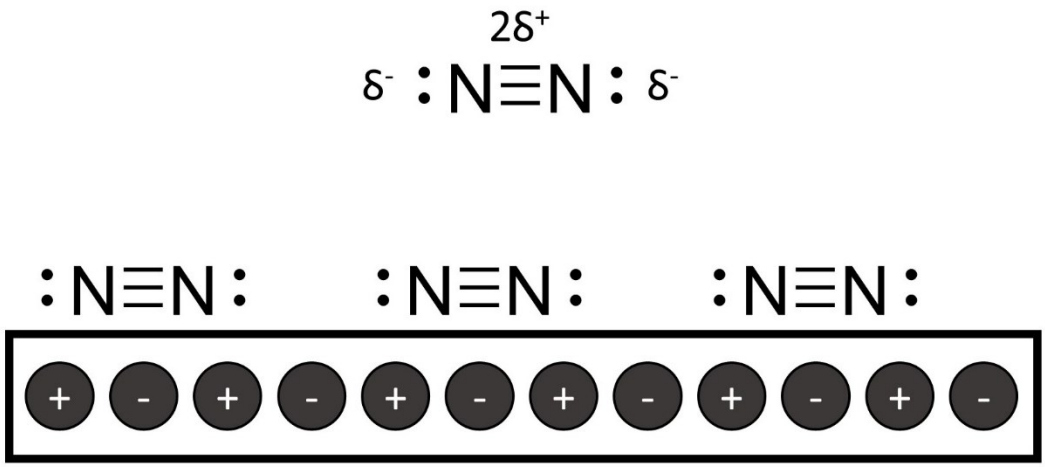

Figure 1.18: Localized electronegative and electropositive charges in nitrogen (top). Nitrogen gas being physiosorbed onto a surface the contain both positive and negative regions (bottom).

1.3.2 Carbon Dioxide Adsorption

Global warming has been linked to the increase of greenhouse gases in the atmosphere. This has led to increased average temperatures, melting of polar ice caps, and a change in the pH of the ocean, to outline a few examples.[105–109] These changes have led to loss of animal habitats, which in turn has caused decreased animal populations leading to the extinction of certain species while threatening extinction to many others.[110–112] It has also led to the change of life in rural and indigenous communities, change of costal landscapes, and changes in the day to day lives of people all over the world.[113–115] One of the primary anthropogenic greenhouse gases responsible for these effects is carbon dioxide.[116,117] According to NOAA (United States National Oceanic and Atmospheric Administration), atmospheric carbon dioxide partial pressures in 2021 was recorded to be almost 415 ppm, compared to 359 ppm in 1994.[118] While this is only a small change in a short amount of time, carbon dioxide levels were consistently around 280 ppm before the industrial revolution.[109] Since the industrial revolution there has been a dramatic increase in the burning of fossil fuels for industrial applications, massive deforestation, increase in transatlantic shipping and international travel, and a population boom. All these processes lead to the increase of carbon dioxide.[119,120]

Due to the continuous rising of atmospheric carbon dioxide levels, researchers have been interested in removal of carbon dioxide gas.[121,122] Ideally, the elimination of these emissions should be done where carbon dioxide is produced and the partial pressure is the highest, and easiest to interact with.[123] This is not to say that removal of carbon dioxide from the air (direct-air-capture; DAC) is not important. However, strategies like direct air

capture for environmental sequestration of carbon dioxide are much more difficult due to the low partial pressure of carbon dioxide in the environment. Thus, while focus from emission sources and DAC is critical as we aim to reach net-zero by 2050, focus on emission sources is likely to be easier and more fruitful. MOFs are an attractive material for the sequestration of carbon dioxide. This is largely due to their larger internal surface areas and easy functionalization that can be utilized to improve the adsorption capacity and selectivity of carbon dioxide over other gases.[51,67,124] Functionalization of MOFs has been carried out in several ways. Some researchers have focused on installing organic functional groups (e.g., $-NH_2$) onto the ligand/node that will interact or bond with carbon dioxide.[51,125] Other works have relied on creating open metal sites.[126] These open metal sites are often due to metals that are in lower coordination numbers than they would prefer to be in and in geometries that would allow gases to readily coordinate with the metal. For example, a metal that would prefer to be in an octahedral geometry but was found in a 5-coordinate square-based pyramidal geometry would likely coordinate to a Lewis-basic gas-phase ligand like carbon dioxide to form an octahedral geometry. While these are two methods that have been used to enhance the adsorption of carbon dioxide gas, in principle, they can be combined to form materials that feature both of these approaches.

1.3.2.1 Pendant Functional Groups

When deciding which functional group to incorporate into a MOF, it is important to consider the chemical properties of carbon dioxide. Carbon dioxide is non-polar. However, it does contain a quadrupole, the local positive area is located on the central carbon while the negative ends are located on the terminal oxygen molecules. The two

quadrupoles in this molecule allow for intermolecular interactions leading to physisorption. Functional groups can be employed in MOFs that are capable of interacting with the quadrupoles causing physisorption. However, pendant groups that are capable of a chemical reaction or chemisorption, have also been seen in the literature. Yaghi and coworkers had explored the carbon dioxide adsorption in IRMOF-74-III-$(CH_2NH_2)_2$ (Figure 1.19).[127,128] This magnesium-based MOF with a 2′,5′-bis(aminomethyl)-3,3″-dioxido-[1,1′:4′,1″-terphenyl]-4,4″-dicarboxylate ligand showed great affinity for carbon dioxide gas, compared to the unfunctionalized IRMOF-74-III and IRMOF-74-III-CH_2NH_2. What is interesting about this work is that relative to the unfunctionalized MOF, the functionalized MOF showed 2.33 times more uptake at pressures below 100 Torr. To determine if the carbon dioxide was chemisorbed or physiosorbed onto the material, a second carbon dioxide gas adsorption isotherm was run right after the first isotherm. If the two isotherms looked the same, then it would indicate that physisorption is occurring. However, they had noticed a 17% drop in carbon dioxide uptake at 800 Torr, and an 83% drop at 0.8 Torr. This indicated that both chemisorption and physisorption were occurring. At low pressures of carbon dioxide, the pendant methylamine is a very reactive site and the authors hypothesized that there was covalent bonding between the carbon dioxide and the methylamine. Through solid-state NMR experiments, the authors were able to determine that the carbon dioxide had chemisorbed onto the ligand and created a carbamate (Figure 1.19).

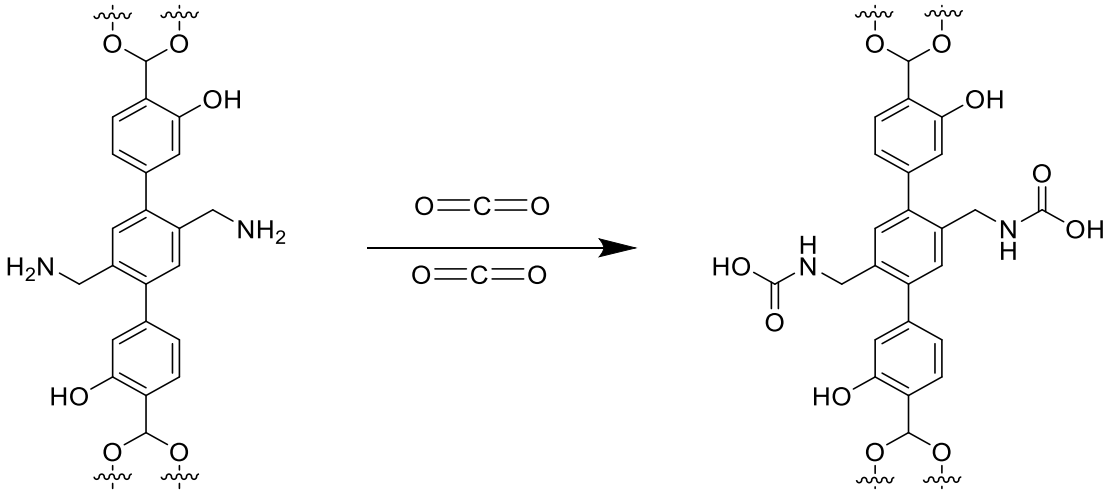

Figure 1.19: Reaction of the IRMOF-74-III-$(CH_2NH)_2$ ligand with carbon dioxide to from a carbamic acid.

Al-MIL-53 is a MOF that is traditionally made with aluminum nitrate and terephthalic acid. It has been shown that replacement of the terephthalic acid with 2-aminotherepthalic acid will form the same MOF topology, but the pores will now be decorated with an uncoordinated amino group and the MOF Al-MIL-53-NH_2 will be formed. In 2009, Deyaner and coworkers examined the gas adsorption capacity properties of both Al-MIL-53 and Al-MIL-53-NH_2.[129] They had hypothesized that the addition of the pendent anime would act as a Lewis basic binding site for the Lewis-acidic carbon atom of carbon dioxide. From their variable temperature carbon dioxide adsorption experiments they were able to extract the enthalpies of adsorption of carbon dioxide onto the MOF. The enthalpies of adsorption for Al-MIL-53 were found to be –20.1 kJ/mol, only slightly higher than the enthalpy of vaporization of carbon dioxide (–15 kJ/mol).[130] In other words, this is not a strong interaction. However, Al-MIL-53-NH_2 was found to have an enthalpy of adsorption almost two times larger (–38.4 kJ/mol). This clearly demonstrates how pendent groups can be used to enhance gas adsorption properties.

MIL-125, comprised of a central $Ti_8O_8(OH)_4$ node and terephthalic acid ligand is another example of a MOF where a simple substitution of terephthalic acid for 2-aminoterepthallic acid leads to an increase in the adsorption capacity and enthalpy of adsoption for carbon dioxide.[131] In 2011, Ahn and coworkers compared the carbon dioxide adsorption in MIL-125 and MIL-125-NH_2.[131] At 298 K they reported a difference of 10 mg/g in the carbon dioxide adsorption capacity, MIL-125 had a capacity of 15 mg/g, while MIL-125-NH_2 had a capacity of 25 mg/g. Throughout their study they had determined that MIL-125-NH_2 showed significant improvement in the heats of adsorption (–31 kJ/mol) when compared to the parent material (–21 kJ/mol). This further shows that the replacement of terephthalic acid with 2-aminoterepthalic acid leads to an enhancement of carbon dioxide adsorption.

The above examples are ones in which the ligand was functionalized, thereby enhancing the MOF properties. This is not the only way to introduce functional groups in a MOF. Through post synthetic modification, a process in which the structure of the MOF is modified after it has been formed, pendant groups can be installed onto open metal sites. It is worth noting that open metal site doesn't necessarily refer to a coordinately unsaturated metal centre but rather a metal centre that has a non-framework ligand that can be substituted. These groups can be terminal or bridging water, hydroxy, or halogen groups (to name a few). Cabello *et al.* took advantage of the open chromium site present in Cr-MIL-100, and installed either ethylenediamine or *N,N'*-dimethylethylenediamine to enhance the carbon dioxide adsorption (Figure 1.20).[132] By grafting these groups onto the MOF, they observed a large improvement in the amount of carbon dioxide that was

adsorbed and an increase in the enthalpy of adsorption. Relative to the unfunctionalized Cr-MIL-100, when ethylenediamine was grafted onto the MOF node, the carbon dioxide adsorption capacity of the MOF increased by 50% at 308 K. When *N,N'*-dimethylethylenediamine was grafted, a mere 6% increase was observed. Examining the enthalpy of adsorption, the unfunctionalized Cr-MIL-100 was determined to have an enthalpy of adsorption of –63 kJ/mol at zero coverage. For both tethered MOFs (ethylenediamine and *N,N'*-dimethylethylenediamine), an enthalpy of adsorption of −80 kJ/mol was observed at zero coverage. This is nearly 20 kJ/mol more exothermic. This increase is attributed to the addition of the amine groups.

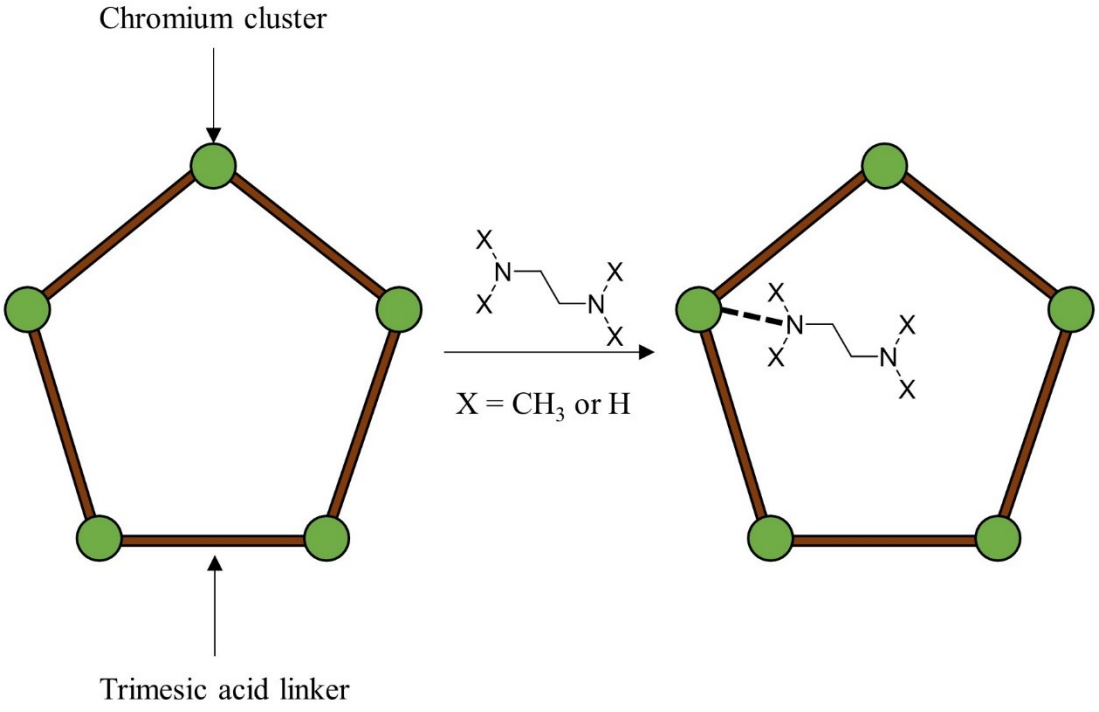

Figure 1.20: Cr-MIL-100 (left) grafted with diamines (right) to enhance carbon dioxide adsorption.

1.3.2.2 Open Metal Sites

As previously mentioned in Section 1.1.5 and Section 1.3.2.1 missing ligand defects are common, and as a result, metal sites that are not occupied by the Lewis-basic group of the ligands are not part of the MOF framework. Instead, the metal centres become coordinated to charge-compensating anions or solvent molecules such as OH^- or H_2O. The neutral pendent groups can be removed via vacuum and heating resulting in an unsaturated metal site. However, instead of adding a molecule that will graft into the pore once the solvent molecules have been removed, the metal site can remain uncoordinated and an incoming gas or vapour molecules can fill the vacant site, becoming saturated once again. Researchers have investigated if MOFs containing open metal sites are beneficial for the adsorption of carbon dioxide gas.[133,134]

Caskey and coworkers explored how different metal centres inside of a MOF containing the same ligand and topology could alter the affinity for carbon dioxide.[135] They investigated the uptake of Zn/DOBDC, Co/DOBDC, Ni/DOBDC, and Mg/DOBDC where DOBDC is the tetra anionic 2,5-dioxido-1,4-benzenedicarboxylate. The metal/DOBDC MOF is also known as MOF-74 and a schematic of it can be seen in Figure 1.21. This MOF has a geometry consisting of hexagonal pore channels (i.e., a honeycomb structure) that are formed when the ligand coordinates to an octahedral metal centre, but only using five of the six octahedral coordination sites. The remaining site contains a thermally removable solvent molecule. Returning to the structure briefly, the 2,5-dioxido-1,4-benzenedicarboxylate form the sides of the hexagonal pore while

connecting to the metal centre either via a carboxylate or a phenoxide. The metal centre is located at the corner of the hexagonal pore.

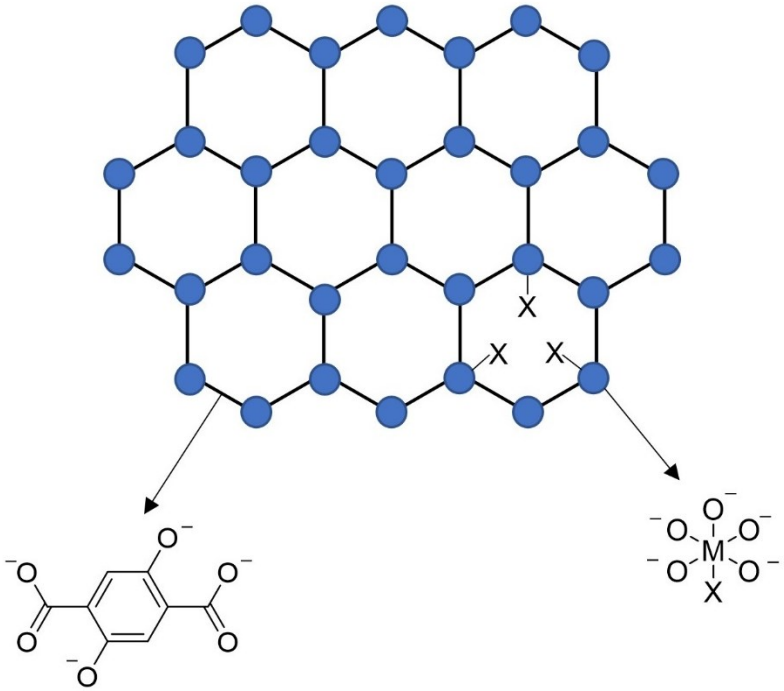

Figure 1.21: Structure of MOF-74 illustrating the series of hexagonal pores, along with the 2,5-dioxido-1,4-benzenedicarboxylate and the metal centres (M) that can coordinated to solvent molecules (X).

During the synthesis of these MOFs, the metals become fully coordinated by solvent molecules such as water, DMF, or other organic solvents that are present. These molecules decorate the inside of the hexagonal pores. Activation via vacuum and heat is often enough to remove these coordinated solvent molecules and form a coordinately unsaturated five-coordinate metal centre. The metal centre now has an open metal site facing the inside of the hexagonal pore, providing a site for carbon dioxide, or potentially other gases, to coordinate onto. When examining the data on a per metal centre basis, the magnesium containing MOF had an uptake of 12 carbon dioxide molecules per metal

centre; not all the carbon dioxide guests were coordinated to the metal of course. The cobalt and nickel derivatives of MOF-74 had an uptake of 7 molecules per centre, and when zinc was utilized, only 4 molecules per centre was observed. Interestingly, the zero loading heats of adsorption of these materials followed the same pattern. Mg/DOBDC had an enthalpy of adsorption value of −47 kJ/mol while the nickel and cobalt containing MOFs were less exothermic (−41 and −37 kJ/mol respectively). Oddly, the enthalpies of adsorption for Zn/DOBDC were not reported. Caskey attributes the enhanced enthalpy and adsorption capacity of Mg/DOBDC to the ionic like bond that can be formed between the magnesium of the MOF and the oxygen of the carbon dioxide. The observed magnesium carbon dioxide bond is hypothesized to be very ionic, which can provide favorable binding locations for additional carbon dioxide to adsorb.

One of the most attractive properties about MOFs, is that you can incorporate almost any ligand that has been designed for a specific application into a porous material. Zhou and coworkers thought about introducing open metal sites in a very interesting and unique way.[136] They had designed a metal-organic complex (sadly, not a MOF) that was designed to have the optimal distance between the two metal centres to fit a carbon dioxide molecule. They set out to design a molecule that had a distance of approximately 0.74 nm between the two metal centres; this would allow for a carbon dioxide molecule to sit inside while having interactions with the metal centres, but not form a chemical bond. Having strong interactions without forming bonds is ideal as it allows for the gas to be adsorb reversibly from the pore without the input of a lot of energy. The ligand of choice was a

di-substituted naphthalene, 3,3'-(naphthalene-2,7-diyl)dibenzoic acid. When these ligands were reacted with metal salts, then they formed a cage-like structure as seen in Figure 1.22.

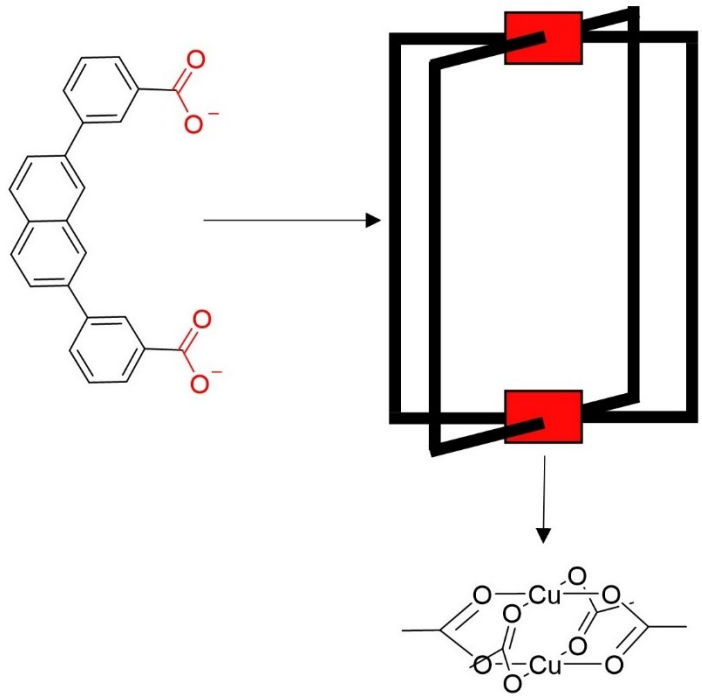

Figure 1.22: Formation of cage that was utilized to capture carbon dioxide.

While the cage that has been formed provides the ideal size for the adsorption of carbon dioxide gas, it lacks the infinite 3D network that we are use to seeing in MOFs. Zhou and coworkers were well aware of this and also designed a ligand that would form this same cage but have additional carboxylic acids to bridge cages and form a MOF. The ligand 5,5'-(naphthalene-2,7-diyl)isophthalic acid (Figure 1.23) was synthesized and with this modification and a copper centre, the MOF PCN-88 was formed.

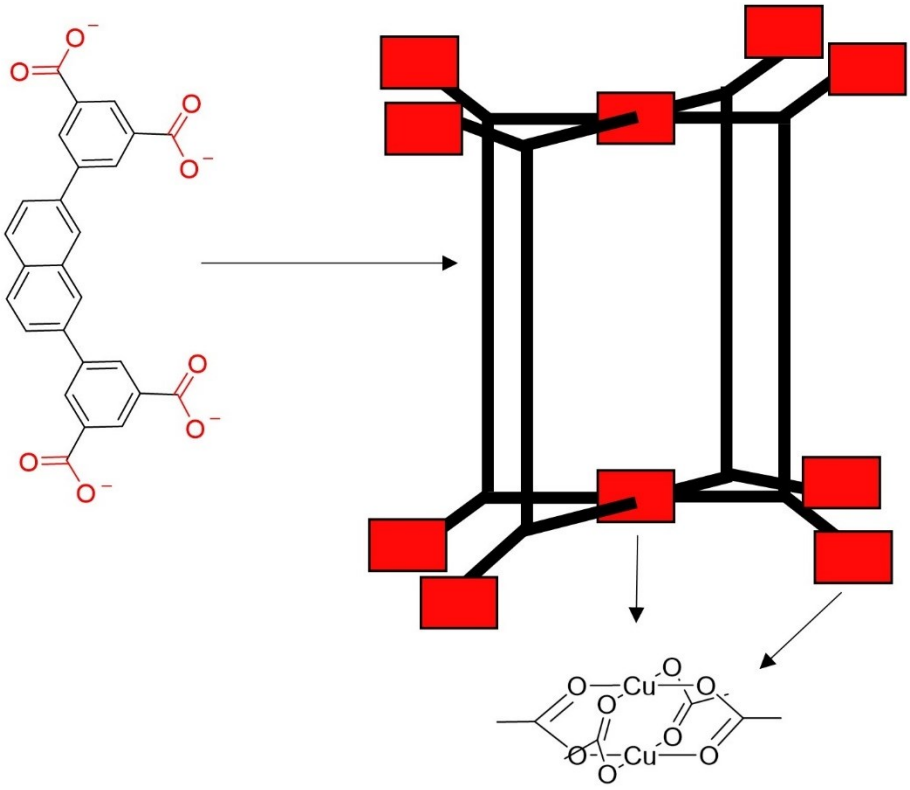

Figure 1.23: PCN-88 formed from a copper centre and a disubstituted naphthalene ligand.

Previously mentioned, the metal centres often become substituted by water or other solvent molecules. This is no different for PCN-88, The copper centre has solvent molecules attached that are removed under vacuum with slight heating. PCN-88 not only displayed a large carbon dioxide uptake at 1 atmosphere and temperatures of 273 and 296 K (7.14 and 4.20 mmol/g, respectively), but it showed great selectivity for carbon dioxide over nitrogen and methane. The zero-coverage enthalpy of adsorption was found to be −27 kJ/mol. While this is not the highest value that we have discussed at this point, it illustrates the strategy of pore confinement to increase carbon dioxide adsorption. Furthermore, one advantage of these lower heats of adsorption is that low energy input is

required to regenerate PCN-88 and desorb the carbon dioxide; if the balance between adsorption enthalpy and regeneration can be optimized, then this class of MOFs would be ideal for real world applications.

With the goal of carbon dioxide storage in mind Hupp and co-workers set out to design a material that contained a large pore that would be beneficial for this application.[28] In order to obtain such a large pore size, an expanded version of trimesic acid was chosen to make NU-100. NU-100 is a copper containing paddlewheel MOF that has copper centres connected by a 1,3,5-tris[1,3-carboxylic acid-5-(4-(ethynyl)phenyl))ethynyl] benzene ligand (Figure 1.24). During the activation process for this MOF, the copper centre becomes uncoordinated, which leads to a higher carbon dioxide adsorption at low pressure than computational predictions. The carbon dioxide strongly interacts with the open metal coordination site thereby enhancing the uptake abilities of this MOF.

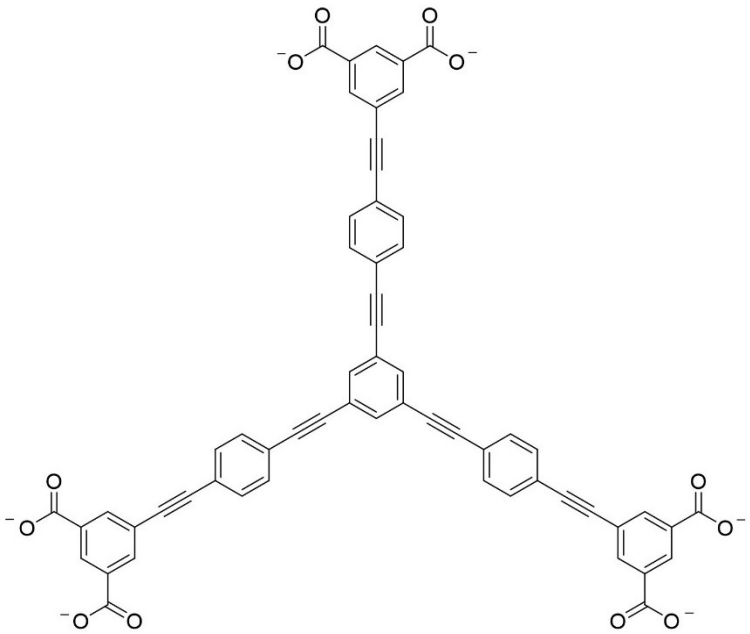

Figure 1.24: 1,3,5-tris[1,3-carboxylic acid 5-(4-(ethynyl)phenyl))ethynyl] benzene ligand found in NU-100.

1.3.2.3 Pore Size

Carbon dioxide is a relatively small gas molecule with a kinetic diameter of 0.33 nm.[45] Due to such a small size, the use of micropores has proven to be advantageous in the adsorption and selective uptake of carbon dioxide. This has been taken advantage by many different research groups,[45,137,138] and one of the most famous examples of this comes from the Shimizu lab where the MOF CALF-20 has been employed industrially and has removed literal tons of carbon dioxide from the atmosphere to date.[27]

CALF-20 is comprised of a zinc centre that is connected by 1,2,4-triazolate and oxalate ligands (Figure 1.25). The MOF possess three different pore sizes, the smallest being 0.273 × 0.291 nm, the middle pore is 0.194 × 0.311 nm and the largest pore being 0.274 × 0.304 nm.

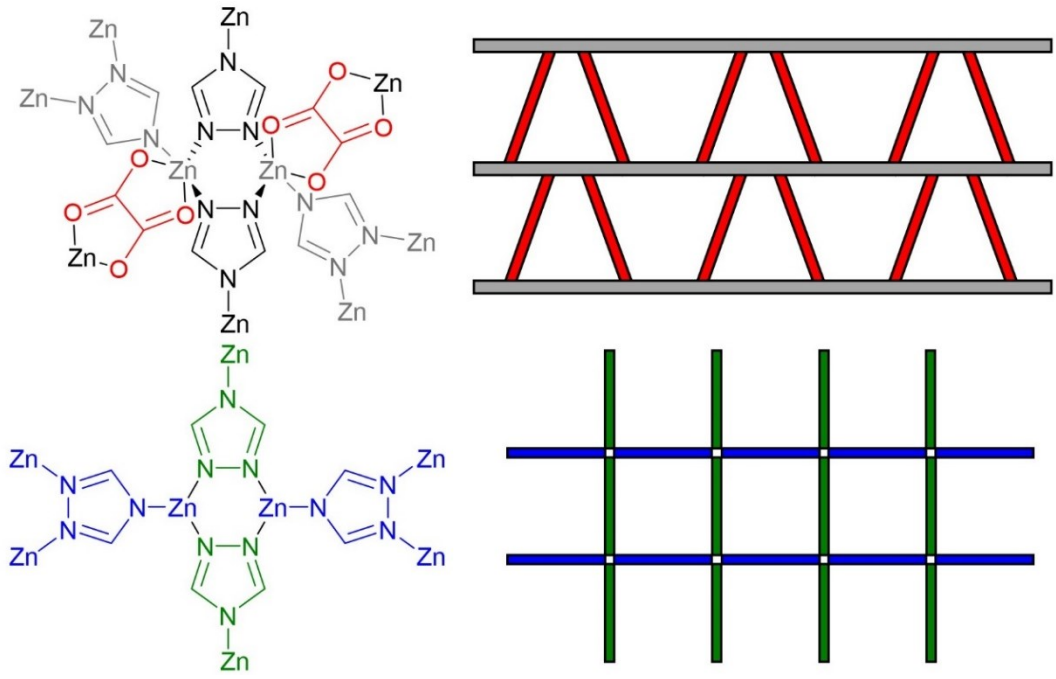

Figure 1.25: CALF-20 shown from two different views. Top shows the pillared paddlewheel view and illustrates two different pore sizes and a view showing the more square pore (bottom).

CALF-20 can adsorb 4.07 mmol of carbon dioxide per gram of MOF at 1.2 bar. The enthalpy of adsorption is −39 kJ/mol at zero coverage. The enhanced adsorption in this MOF is attributed to the presence of the smaller pores. While CALF-20 has an impressive enthalpy of adsorption at zero coverage, it is not the reason why this MOF has been employed into industrial applications. CALF-20 has a large adsorption selectivity of carbon dioxide over relevant other gases. In laboratory experiments CALF-20 has shown selectivity to carbon dioxide over both nitrogen gas and water vapour. This is attributed to the ideal pore sizes that favor carbon dioxide gas over water vapour. This illustrates how optimizing pore size can lead to industrially used MOFs.

MIL-88 (Figure 1.26) contains metal sites that are often capped with hydroxides or other solvent molecules that are easily removed under heat and vacuum as previously mentioned in Section 1.3.2.2. However, the generation of these metal sites are not used for the coordination of carbon dioxide in this case. Feng and co-workers explored how the open metal sites can be used as binding locations for a tritopic ligand capable of binding (bridging) to three of the metal sites at once, which leads to the creation of a new series of smaller pores.[139] The authors hypothesized that the confinement of these pores would lead to higher enthalpies of adsorption for carbon dioxide.

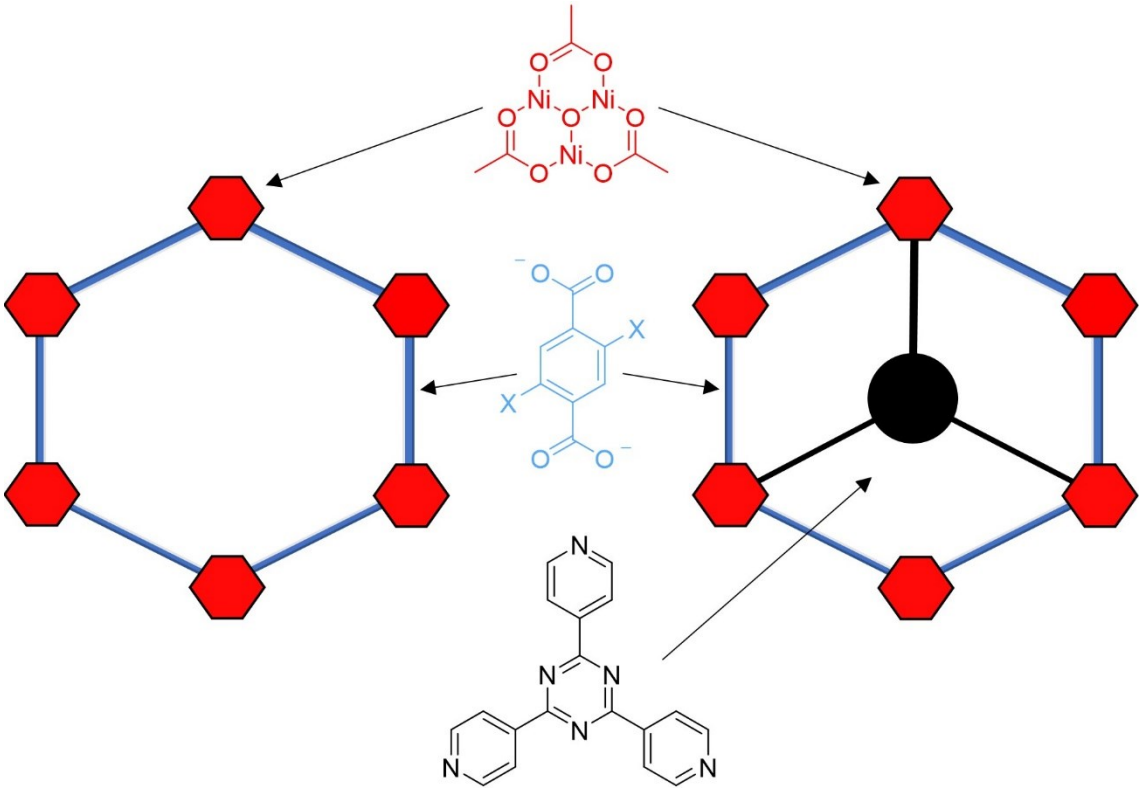

Figure 1.26: MIL-88 (left) that has been functionalized with a tritopic neutral ligand to reduce the pore size and enhance carbon dioxide adsorption. X on the middle blue benzene dicarboxylic acid can either be H for the unfunctionalized version or OH for the hydroxy version.

Feng and coworkers synthesized and monitored a series of MIL-88 MOFs containing a nickel-based node with varying organic ligands and a tritopic ligand to functionalize the pore. The organic ligands that were examined were benzene-1,4-dicarboxylate and 2,5-dihydroxybenzene-1,4-dicarboxylate. The pore segmenting ligands introduced into the material was 2,4,6-tri(4-pyridnyl)-1,3,5-triazine (Figure 1.26). These MOFs were named CPM-33a and CPM-33b (CPM = crystalline porous materials) respectively.

The implementation of these segmenting ligands led to the decrease of the typical 1.04 nm wide pore to three smaller 0.45 nm segments. These new pores lead to confinement effects that provide pores with the optimal size for carbon dioxide adsorption. CPM-33a displayed an impressive carbon dioxide adsorption capacity of 137.2 cm^3/g at 273 K and 1 bar. The addition of the hydroxy functionality (CPM-33b) led to a significant increase in the uptake with a measured adsorption capacity of 173.9 cm^3/g. At the time of this report, these values were among the highest reported for carbon dioxide adsorption in a MOF without open metal sites. The enthalpy of adsorption of CPM-33a and CPM-33b were reported to be −22.5 kJ/mol and −25.0 kJ/mol at zero coverage respectively.

1.3.3 Water Adsorption

The idea of using MOFs for water adsorption is not new, but great developments have been made in recent years.[140] There are several things that must be taken into consideration when developing a MOF for water adsorption. In almost any application for water adsorption (e.g., industrially, environmentally, etc.), the first consideration is competitive binding. In other words, a MOF needs to preferentially bind water over other guests. Another point to consider is stability of the material under operating conditions. Lastly, it is important to consider the recyclability and reusability of the MOF.[140–142]

MOFs have been investigated by Janiak and coworkers for their potential as solid-state adsorbents for heating and cooling applications.[143] In 2009 they reported ISE-1, a nickel containing MOF that has benzene-1,3,5-tricarboxylate (BTC) and

1,2-bis(1,2,4-triazol-4yl)ethane as its organic ligands. In lab testing, ISE-1 performed well throughout 10 cycles, capable of collecting 280 g of water per kilogram of MOF.

In 2013 Janiak published a follow-up paper using a series of Cr MIL-101 (Figure 1.27) MOFs for heat transformation processes.[144] MIL-101 contains BDC as its organic ligand, which can easily be functionalized to contain $-NO_2$ and $-NH_2$ functionalities. These two functionalized MOFs demonstrated great reusability over 40 cycles. Janiak also determined the enthalpies of adsorption. MIL-101 showed an enthalpy of adsorption of −45 kJ/mol while the amine and nitro functionalized materials had enthalpies of −43 and −48 kJ/mol respectively. The water uptake capacities of these MOFs were also reported to be 1.06 g of water per g of MOF and 0.60 g of water per g of MOF for the amine and nitro versions of Cr-MIL-101, respectively. This work illustrated how the addition of hydrophilic functional groups (i.e., amines) increased the loading potential of Cr-MIL-101 without having a detrimental impact on the other adsorption properties of the MOF.

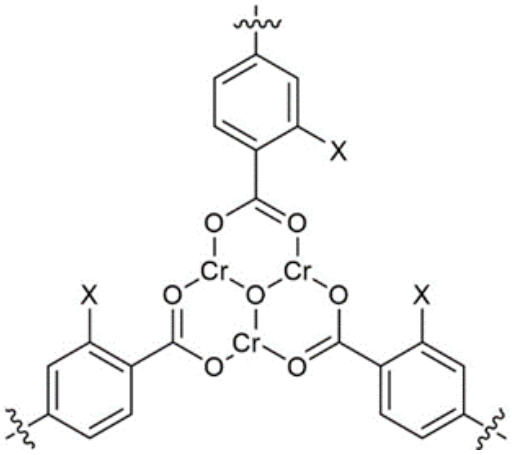

Figure 1.27: The local structure around the node of Cr-MIL-101. X indicates the location of substitution where functional groups such as $-NO_2$ or $-NH_2$ were installed for water adsorption/desorption applications.

Over the past several decades, we have been approaching a water shortage and considerable research has gone into obtaining potable water that does not require high energy inputs and can be used in remote areas. Yaghi and coworkers have put a tremendous amount of work into developing a system that is capable of adsorbing water vapour from the air at very low relative humidity while also being able to desorb the water without a large amount of energy input.[142] MOF-801 (Figure 1.28) was determined to be the ideal candidate for this application. MOF-801 is comprised of the same central zirconium node as the UiO family and uses a fumarate ligand as the bridging ligand.[145] The fumarate ligand is smaller than the BDC ligand used in UiO-66. This provides a smaller pore size that leads to adsorption of water at a lower relative humidity.

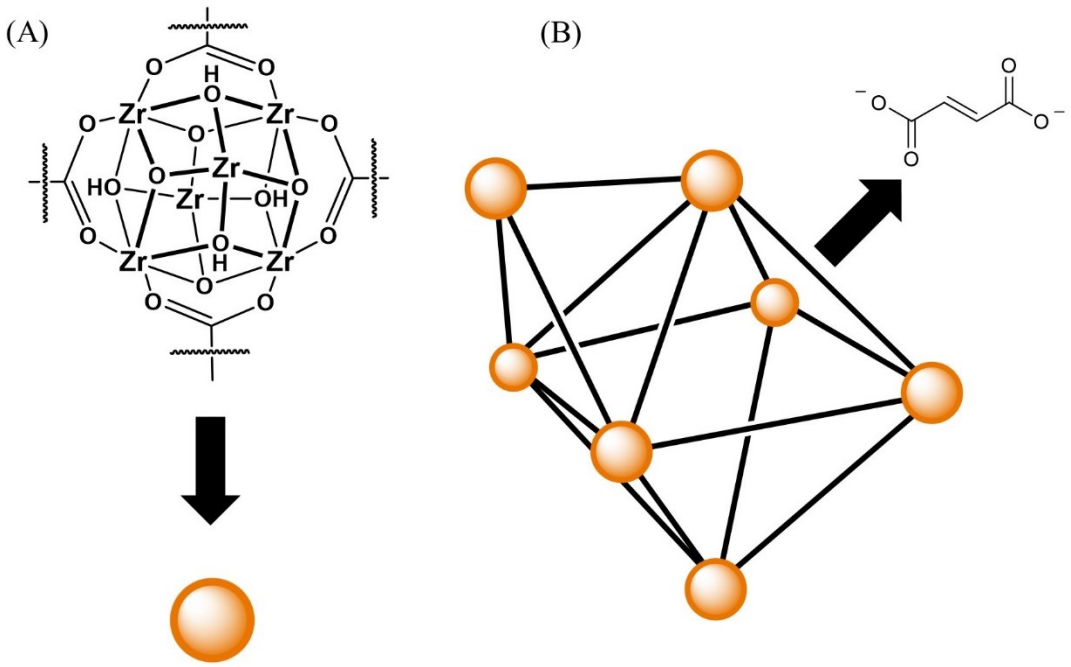

Figure 1.28: MOF-801. (A) the zirconium cluster. (B) an octahedral and tetrahedral pore that form the overall 3D topology where the orange spheres represent the node, and the black lines represent the fumarate ligand.

MOF-801 was demonstrated to adsorb water as a relative humidity just above 0% with a very steep uptake once a relative humidity of 10% was achieved. Its maximum uptake was reported to be 450 cm^3/g at a relative humidity of 90%.[142] This uptake is equivalent to 36 w/w %. Yaghi had attributed the high uptake of water to be due to the small pore sizes of MOF-801, which was reported to be 0.74, 0.56 and 0.48 nm.[142] These pore sizes are ideal for water-water interactions leading to condensation inside the pores. These materials also showed great reusability and stability of the MOF in humid conditions. In many ways, this MOF is the ideal material to easily adsorb and desorb through pressure swing adsorption (i.e., changes in humidity).

To show the potential of MOF-801 for water adsorption, Yaghi and coworkers built a proof-of-concept system that used MOF-801 to adsorb and desorb water from the air.[146] They deployed the apparatus outside of Temple, Arizona where the natural pressure and temperature swings between a high of 40% relative humidity during the night, to a low of about 10% relative humidity during the day.[146] Due to the large difference in the amount of water vapour in the air during the day and night the device was built to adsorb water vapour during the night and desorb the water vapour during the day. The device was equipped with a heater that would be powered by solar energy during the day to provide heat to the MOF and thermal desorption of the water would occur. During their field tests with the device deployed they were met with promising results. Using 3 g of MOF-801 in their system, and the weather patterns over the five tested cycles, they estimated, based on in-lab adsorption studies, that the device should be able to harvest 0.75 g of water. However actual measurements were not possible due to the small setup that was deployed. While

this value may seem low, it illustrated the potential of MOFs for water harvesting applications. Using the collected data, Yaghi and coworkers estimate that 1 kg of MOF-801 would be able to harvest 0.12 L of water per day. While 0.12 L is not a lot of water per kg of MOF, it does illustrate the concept and potential that MOFs have as water harvesting materials.

Yaghi and coworkers have continued to work on MOFs for atmospheric water adsorption. In 2019 they reported their results for MOF-303 (Figure 1.29).[147] MOF-303 consist of an aluminum based central back bone (Figure 1.29C), which are connected to each other via 1-H-pyrazole-3,5-dicarboxylate. This forms a 3D topology that has a one-dimensional rhombic shaped pore with a diameter of approximately 0.6 nm. MOF-303 starts to adsorb water well below 5% relative humidity and saturates by 20% relative humidity. The total water adsorption uptake is 500 cm^3/g. Based on the hydrophilic 1-H-pyrazole-3,5-dicarboxylate ligand, the desorption is not energy intensive and the isotherms show very little hysteresis. This indicates that this is an easily reversible process. In a lab setting the device could produce 1.3 L kg_{MOF}^{-1} day^{-1}. This is an order of magnitude higher than the previous generation of MOFs that were used.

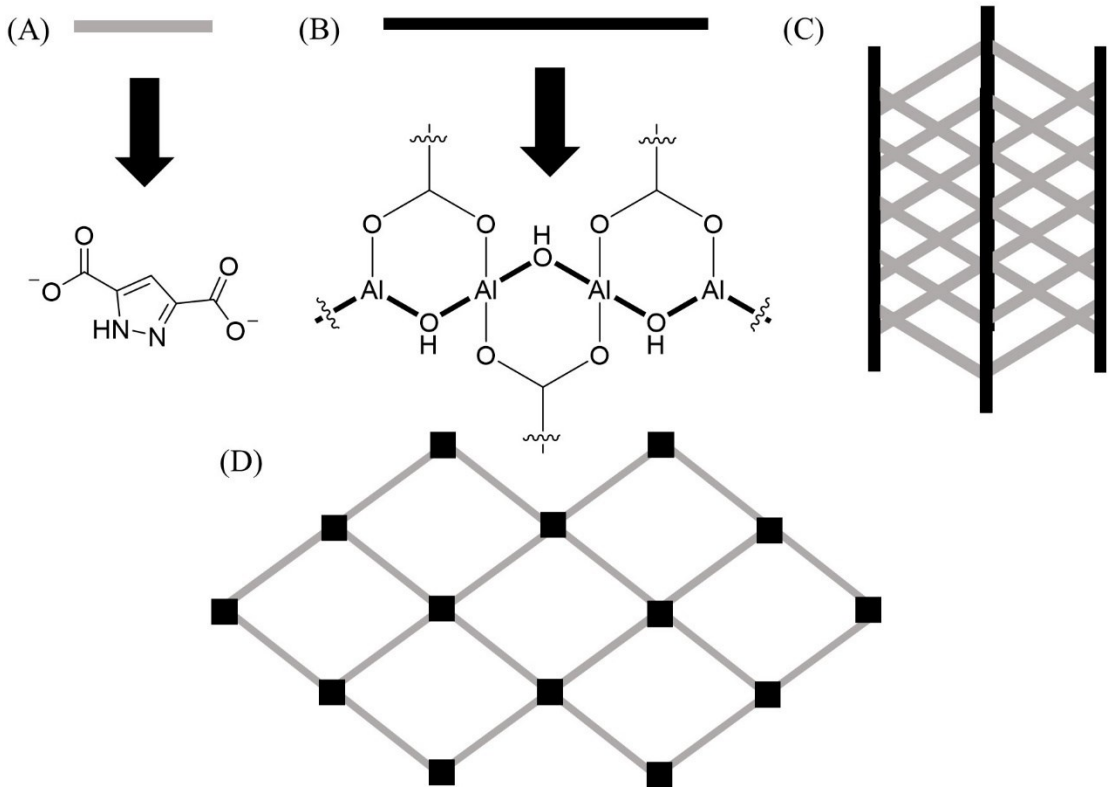

Figure 1.29: Grey rods represent the 1H-pyrazole-3,5-dicarboxylic acid ligand (A), while the black rods represent the aluminum chain (B), when combined they form long channels and a rhombic pore (C and D).

MOF-303 also has faster adsorption kinetics than MOF-801. When MOF-303 was deployed for water capture, it was observed that after an hour of air flowing through the system, the relative humidity upstream and downstream were the same. This suggests that the sample is at equilibrium. For comparison, MOF-801 took almost one hundred minutes to reach saturation in real world conditions.[145] Once equilibrium had been reached, the MOF-303 system was heated to promote the desorption of water. Using the quick adsorption and desorption cycles became very advantageous and lead to multiple adsorption/desorption cycles in a single day.

To demonstrate the real-world applications of MOF-303 as a water harvesting device, it was deployed in the Mojave Desert. On average 0.7 L kg_{MOF}^{-1} day^{-1} was isolated in a region averaging temperatures of 300 K and a relative humidity of only 10%, during the day. This was an improvement of almost ten times over MOF-801, but only about half of what they expected to have based on the lab trials.[147]

These select examples illustrate the need and potential for MOFs to be used as water harvesters, with very promising results from real world deployment of devices incorporating MOFs.

1.4 Gas Uptake Isotherms

As outlined previously, MOFs take advantage of a lot of gas phase chemistry. To study the gas adsorption properties of MOFs, the standard methodology requires us to determine how much gas adsorption is possible as a function of pressure at constant temperature (i.e., the gas adsorption isotherm). An isotherm can be measured at almost any temperature for any gas. However, if the measurement temperature is too high, then there will not be any adsorption of the gas onto the surface.

This thesis heavily relies on the analysis of gas adsorption isotherms. With that in mind, this section will provide a brief introduction to the instrumentation used to make these measurements, and a few theories of gas adsorption.

1.4.1 Measuring the Gas Uptake of a Material

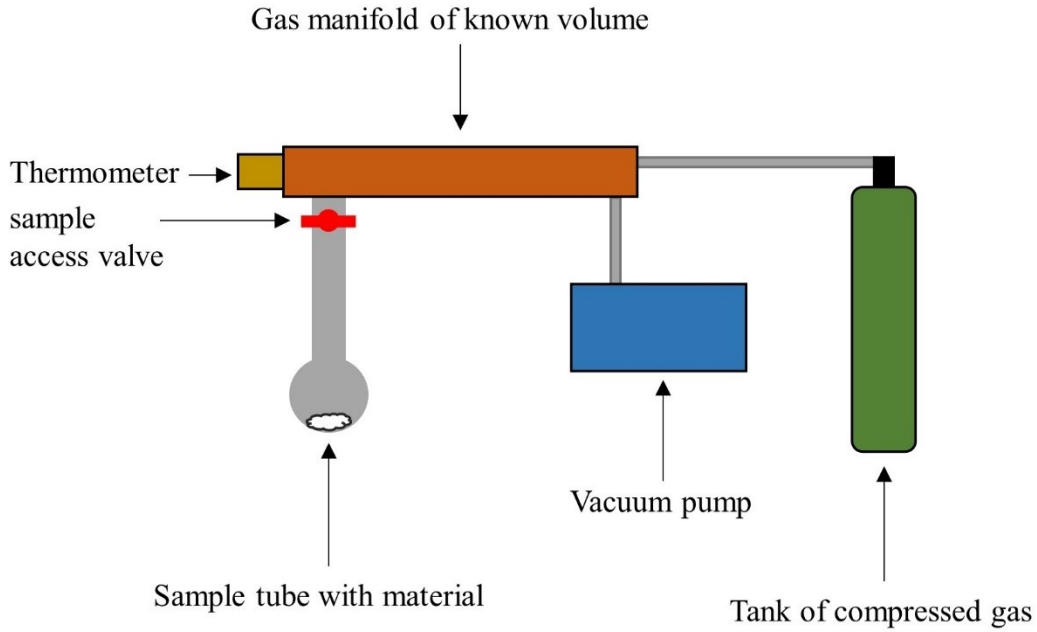

Figure 1.30: Basic schematic of a gas adsorption instrument.

Figure 1.30 illustrates the basic schematic of a gas adsorption instrument. The instrument uses either a tank of compressed gas or a sample holder that contains a volatile liquid and its vapour as the source for the adsorbate. The instrument is also equipped with a thermometer and a vacuum pump. The thermometer is used to measure the temperature of the manifold. Some instruments contain a heater around the manifold to ensure that the manifold is kept at a constant temperature. The vacuum pump is used to evacuate the material prior to starting the experiment and, in combination with the gas source, it helps to ensure that the target pressures can always be reached.

The manifold of the instrument has a precisely calibrated volume (V_1). For a measurement, the instrument first introduces a gas into the manifold at some pressure (P_1).

Following the ideal gas law, this can be used to determine the moles of gas that are in the manifold before any adsorption occurs. At this point, the sample control valve is opened. This exposes the gas to the porous material. Given the sample holder has a non-zero volume, the new volume of the new total volume is ($V_2 = V_1 + V_{sample\ tube}$). Once equilibrium is reached between the sample and the gas, the pressure of the system is measured (P_2). From here, there are a few different possibilities that can result.

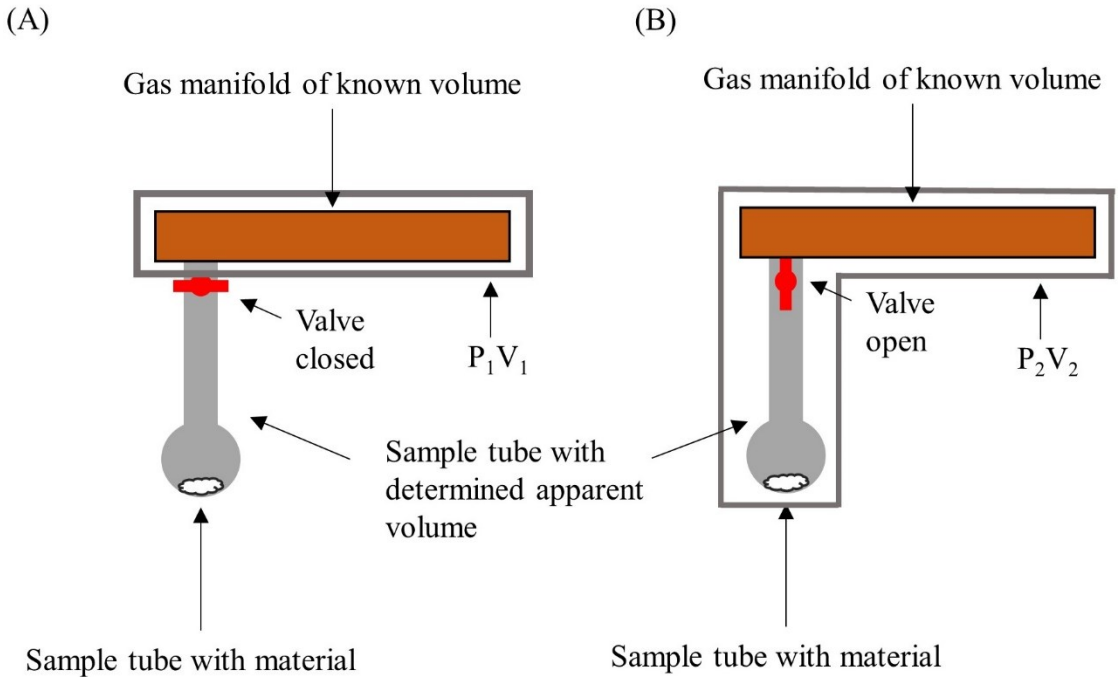

Figure 1.31: Schematic of the instrument with the sample access valve closed (A) and open (B).

$$P_1V_1 = P_2V_2 \qquad 1.1$$

The simplest scenario is when the moles of gas are identical before and after the sample is exposed to gas (i.e., $n_1 = n_2$ or equation 1.1). In this case, there has been no gas adsorbed onto the material. This can occur for several reasons. The sample could be

non-porous, the sample could have a pore aperture too small for the gas to enter, or the sample could be already saturated with gas from a previous data collection.

The second scenario is when P_1V_1 is greater than P_2V_2. The instrument is ideally a sealed system, meaning that if the number of moles of gas is no longer the same before and after sample exposure, then the gas must have been adsorbed (Equation 1.2) onto the material of interest *(Qads)*. Measuring *Qads* at different pressures (P_2) produces the gas adsorption isotherm.

$$P_1V_1 = P_2V_2 + Q_{ads} \qquad 1.2$$

This *Qads* leads to the production of an isotherm, a plot showing the amount of gas adsorbed as a change in pressure.

1.4.2 Extraction of Thermodynamic Properties

For gas adsorption isotherms, it is possible to extract thermodynamic properties such as the equilibrium constant, the enthalpy of adsorption, the entropy of adsorption, and the Gibbs free energy of the adsorption process.[148,149] Most often, the enthalpy of adsorption is the thermodynamic property of interest. To extract this information, we need to fit the isotherm to a model. There are many different models that have been developed for adsorption.[150–153] Depending on the isotherm model and the assumptions it makes, the model may contain an equilibrium constant or a variable that is proportional to the equilibrium constant. In this case, the determination of the rest of the thermodynamic parameters is relatively straight forward. As illustrated in Equation 1.3, the equilibrium

constant is related to the Gibbs energy and thus the entropy and enthalpy of the adsorption process.

$$K = e^{\frac{-\Delta G}{RT}} = e^{\frac{-(\Delta H - T\Delta S)}{RT}} = e^{\frac{\Delta S}{R} - \frac{\Delta H}{RT}} \qquad 1.3$$

From Equation 1.3, it is evident that we cannot find the enthalpy of adsorption with a single isotherm. There are an infinite number of *ΔS* and *ΔH* values that will satisfy a single *ΔG*, and thus *K*. However, if we measure the gas adsorption isotherms at different temperatures, then we obtain a different equilibrium constant at each measured temperature, which can be related back to different equilibrium constants and thus *ΔS* and *ΔH* can be determined.[154] Further rearrangement of Equation 1.3 results in the linear form of the Van't Hoff relation (Equation 1.4). Thus, having multiple equilibrium constants determined from variable temperature gas adsorption isotherms results in a straight line (Figure 1.32) when the *ln(K)* is plotted versus T^{-1}. The slope of this line is proportional to *ΔH* and intercept is related to *ΔS* (Equation 1.4).

$$\ln(K) = \frac{\Delta S}{R} - \frac{\Delta H}{RT} = \frac{\Delta S}{R} - \frac{\Delta H}{R} \cdot \frac{1}{T} \qquad 1.4$$

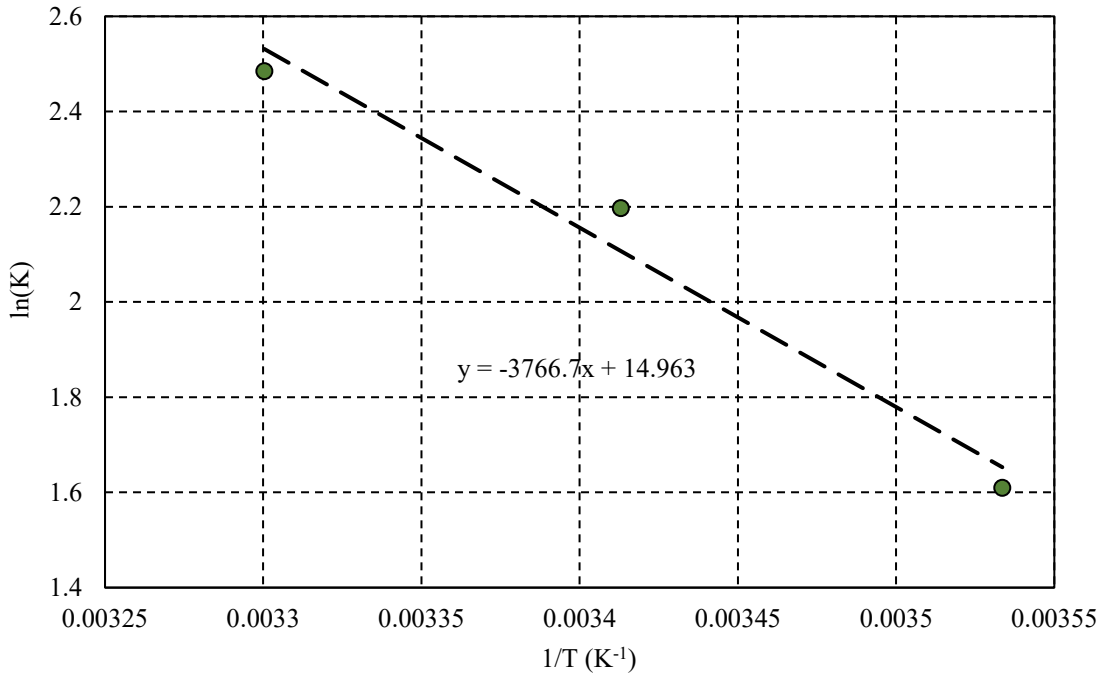

Figure 1.32: Van't Hoff Plot and line of best fit.

1.4.3 Models of Gas Adsorption

To extract the thermodynamic parameters as explained above, we need isotherm models that relate the isotherm shape to the equilibrium constant. Many different models have been developed for fitting gas adsorption data, and they all make varying assumptions or are empirically derived. This section will provide a brief overview of a few different models that can be found in the literature. One of the simplest models, and yet most effective model, for gas adsorption is the Langmuir adsorption model. Since the Langmuir model is used in depth in Chapter 3, an in-depth discussion is provided here.

1.4.3.1 Langmuir Model

The Langmuir model assumes that the entire surface that a gas is adsorbing onto is homogeneous. This means that only one type of binding site is present. This gives a straightforward equilibrium of surface (A) plus gas (B) results in gas on surface (C).

$$A + B \rightleftharpoons C$$

From here, it is straightforward to determine the equilibrium constant. The equilibrium constant can be found from the following formula.

$$K = \frac{[C]}{[A][B]} \qquad 1.5$$

Using an Initial, Change, Equilibrium (ICE) tale, we can expand on K. For simplicity, if we write [A] in terms of surface coverage, then we can state that the maximum adsorption capacity is 1 and thus the max (i.e., initial) value of [A] is 1. Since we are exposing our MOFs to some initial pressure, we can call this $P_{initial}$. For simplicity, at the initial point, [C] is equal to 0 (i.e., no adsorption has occurred). The change that is experienced for the surface, is a loss of some amount of adsorption sites (x). This results in a loss of [A] by x, a decrease in the pressure by P_{loss}, and the formation of x adsorbed sites. The resulting equilibrium value for the surface becomes 1-x. The final pressure is P_{final} (i.e., P_2 in Equation 1.2). The equilibrium value for the amount of gas on the surface is x.

Table 1.3: ICE table for the determination of the equilibrium constant in the Langmuir equation.

	A	**B**	**C**
Initial	*1*	$P_{initial}$	*0*
Change	*-x*	$-P_{loss}$	$+x$
Equilibrium	*1-x*	$P_{final} = P_2$	$+x$

From the equilibrium values found in Table 1.3, Equation 1.5 can be rewritten as Equation 1.6. A rearrangement to Equation 1.7 results in the Langmuir equation with K being the Langmuir constant.

$$K = \frac{x}{(1-x)(P_f)} \qquad 1.6$$

$$x = \frac{KP}{(1+KP)} \qquad 1.7$$

For a Langmuir isotherm to be valid, only one adsorption site must be present at any given pressure. This means that only one gas adsorption layer (monolayer) can form, or rather additional adsorption layers can't occur until the previous layer is filled. More accurately, at every measured pressure (P_2 in Equation 1.2) the adsorption process must represent the same monolayer adsorption.[155] This is illustrated in Figure 1.33. The Langmuir theory makes several assumptions, the first is that the entire surface is homogeneous, and the binding of gas to a surface is the same across the entire material. Secondly, it assumes that there are no interactions between neighboring gasses, and the only interaction is between the gas and the surface.[156]

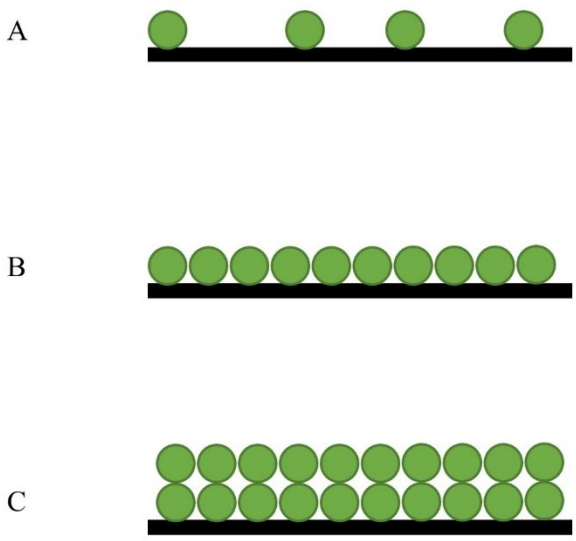

Figure 1.33: Adsorption of gas onto a surface, where the black line represents a surface, and the green spheres represent gas molecules. A illustrates the beginning of adsorption onto the surface, B represents the monolayer forming, and C represents the completion of the next adsorption layer. A Langmuir model fits the data until B.

Equation 1.7 exists with the quantity adsorbed having a maximum value of 1. This is because we solved the equation based on the relative amount of the surface coverage, *x*. For any material, the maximum adsorption will be different and thus we define *x* as the ratio of the quantity adsorbed (Q_{ads}) to the maximum quantity that can be adsorbed (Q_{max}). This results in Equation 1.8.

$$Q_{ads} = Q_{max} \frac{KP}{(1 + KP)} \qquad 1.8$$

In the Langmuir equation, it is assumed that the entire surface is homogeneous. For many materials, this is not necessarily the case. Materials can have multiple sites for gases to adhere. One method to account for this difference is to use the sum of two Langmuir equations to describe the gas adsorption process. Each equation represents its own

adsorption site with its own Q_{max} and its own equilibrium constants (K_1 and K_2), and therefore their own adsorption entropy and enthalpy. This is the dual-site Langmuir isotherm model (Equation 1.9).[157]

$$Q_{ads} = Q_{max1}\,\frac{K_1 P}{(1 + (K_1 P))} + Q_{max2}\,\frac{K_2 P}{(1 + (K_2 P))} \qquad 1.9$$

1.4.3.2 Toth Model

The Toth model is another model that is popular for fitting isotherms. The model looks similar to a single-site Langmuir model. However, the Toth model includes a homogeneity factor (t), to account for the fact that the surface acts as a single binding site, but it is not necessarily homogeneous.[155]

$$Q_{ads} = Q_{max}\frac{KP}{(1 + (KP)^t)^{1/t}} \qquad 1.10$$

It is obvious that when the homogeneity factor is equal to 1, then the Toth equation reduces down to a single-site Langmuir equation; this also defines the upper-most limit to the homogeneity factor. The lower that the homogeneity factor deviates from unity, the less homogeneous the sample is assumed; the lower limit for the factor is 0.

1.4.3.3 Brunauer-Emmet-Teller Model

The Langmuir and Toth models both make assumptions about how gases adsorb onto a surface. In both models, it is assumed that monolayers grow one at a time and have to be complete before the next monolayer can start.[155] However, for some gases and some materials, this is not necessarily how gases bind to surfaces. It is possible that before the

first monolayer has completed, the formation of partial multilayers occurs. Brunauer, Emmet, and Teller (BET) have developed a theory capable of modeling such data.[158] Figure 1.34 illustrates the difference between how the layers form in the Langmuir theory and BET theory.

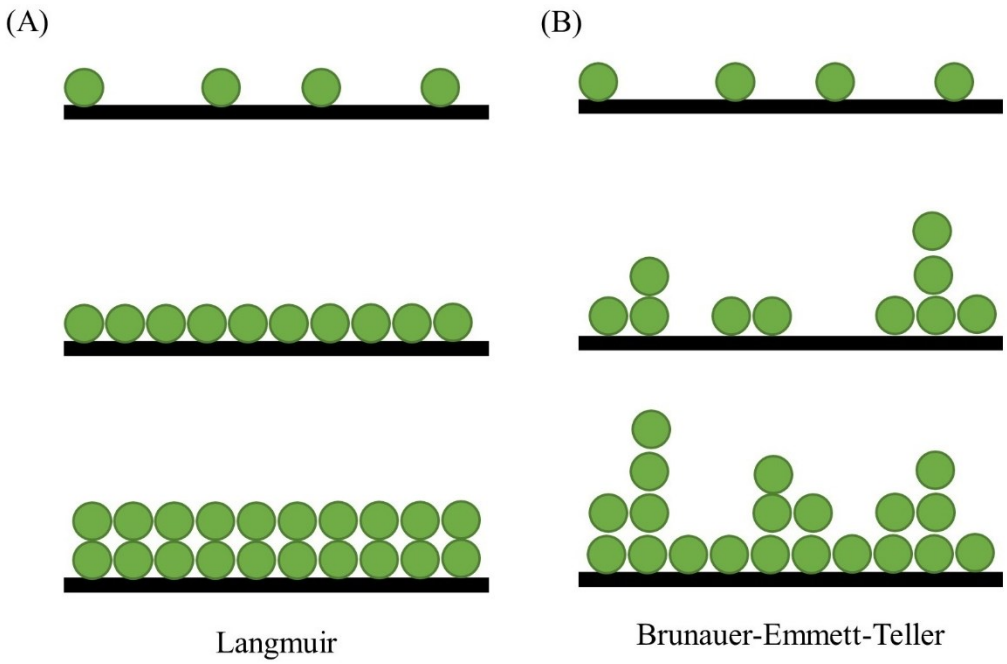

Figure 1.34: Comparison of Langmuir (A) and BET (B) adsorption models.

$$\frac{{}^{p}/_{p^\circ}}{n(1-{}^{p}/_{p^\circ})} = \frac{1}{n_m C} + \frac{C-1}{n_m C}\left(\frac{p}{p^\circ}\right) \qquad 1.11$$

The BET equation can be expressed as shown in Equation 1.11. In Equation 1.11, *n* represents the amount of adsorbed gas at a given relative pressure, similar to *Qads* in the Langmuir model.[159] The relative pressure is represented by P/P°, where P represents the pressure and P° represents the saturation pressure of the adsorbate. n_m represents the monolayer capacity of the material. The constant C is a factor that relates to the energy

difference between the first layer and the remaining layers; this constant is commonly referred to as the BET constant.[159]

While many other theories of gas adsorption are present in the literature, these were focused on as they are referenced throughout this thesis.

1.4.4 Information Obtained from Isotherms

1.4.4.1 Surface Area

One of the most common measurements taken from gas adsorption data is often the surface area of the material of interest. This can be determined from the monolayer coverage of the gas on the surface. At this point our complete surface is covered by a known number of gas molecules. Knowing the physical size of the gas molecule of interest, it is a simple calculation to determine the surface area. Figure 1.35 illustrates this concept. If we consider the probe gas molecules (i.e., blue cylinders in Figure 1.35) to be adsorbed nitrogen gas molecules, then it can be observed that 65 molecules are adsorbed onto the surface of the material. The cross-sectional area of a molecule of nitrogen gas is 0.162 nm^2, and with 65 molecules of nitrogen on the surface the surface has an area of 10.5 nm^2. If we also know the mass of this surface, then we can determine the gravimetric surface area.

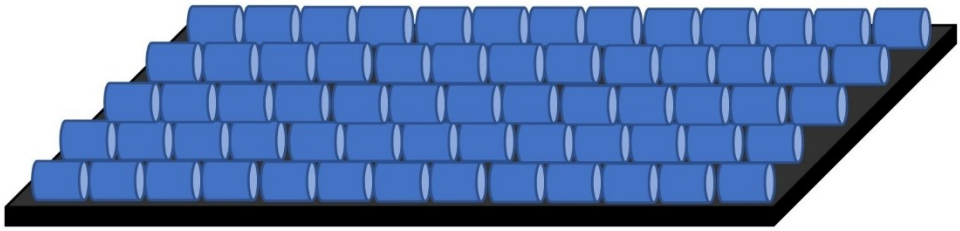

Figure 1.35: Gas molecules adhered to a surface in a monolayer for the determination of the surface area.

For a Langmuir adsorption isotherm, the surface area can be determined from Q_{max}. Assuming Q_{max} is measured in mols/g, we can easily determine how many molecules are in Q_{max} and thus determine the surface area by using the cross-sectional area of the probe molecule. If Q_{max} is reported in cm^3/g, then we can use the molar volume of the probe gas to determine how many gas molecules are present and then use the cross-sectional area to determine the surface area.[159] This is often referred to as the Langmuir surface area or the probe gas accessible Langmuir surface area.

For BET theory, it is more challenging to determine the surface area. However, BET derived surface areas have been determined to be more accurate. Langmuir surface areas are an overestimate.[160] This is because multilayer formation occurs before the first monolayer is complete. To calculate the BET surface area of a material it is unfortunately not as straight forward as the Langmuir model. Equation 1.11 is in the form of a straight line if we plot of $(P/P^o)/[n_m(1- P/P^o)]$ versus (P/P^o). The slope (S) of this straight line would represent $(C-1)/n_mC$ and an intercept (I) represents $1/n_mC$. Using the slope and the intercept, we can calculate both n_m and C.[159]

$$S = \frac{(C-1)}{n_m C} \quad 1.12$$

$$I = \frac{1}{n_m C} \quad 1.13$$

$$C = \frac{S}{I} + 1 \quad 1.14$$

$$n_m = \frac{1}{S+I} \quad 1.15$$

As with the Langmuir model, once the monolayer capacity is determined, solving for the surface area becomes quite simple. We simply convert the monolayer capacity to number of gas molecules and multiply it by the cross-sectional area of the probe molecule. This is done using the following equation.[159]

$$A = \frac{n_m N_A L}{MW} \quad 1.16$$

In this equation A represents the BET-derived surface area of the sample, n_m is the monolayer capacity, N_A is Avogadro's constant, L is the cross-sectional area of the probe gas molecule, and MW is the molecular weight of the gas molecule. To obtain the gravimetric or molar surface area of the sample, one would need to divide the surface area of the sample by the mass of the sample, or number of moles of the sample, respectively.

The challenge with an isotherm is that the BET equation does not fit the whole isotherm. This is primarily because the BET equation doesn't have an adsorption limit. In other words, the BET equation does not have a Q_{max} and thus must deviate at some point from the collected gas adsorption isotherm. With that in mind, it is important to determine

what pressure region will yield the correct probe gas accessible BET surface area. Four criteria have been developed to help determine the pressure region to be used.[158,159]

The first criteria is that the BET constant *C*, must be positive. The *C* constant in the BET equation is a relationship between the energy of adsorption of the first monolayer, and all other layers that would form after. This value must be positive to indicate the favorable adsorption of the first monolayer.

The second criteria is a plot of $n(1- P/P^o)$ vs. P/P^o inside the selected pressure range must always be increasing for a BET equation; this plot is often called a Rouquerol plot and is an alternative way to view BET theory. Data points where the data is decreasing cannot be used as they deviate from the theory. The quantity of gas adsorbed is represented by *n*. As gas begins to adsorb, the value of $n(1- P/P^o)$ will increase, however, once *n* approaches the amount of gas required for complete saturation of the material, the value of *n* will remain constant. $n(1- P/P^o)$ will begin to decrease as (P/P^o) increases. This criterion forces the equation to only consider the gas adsorbed before saturation.

The third criterion is that the pressure, (P/P^o), at which n_m is calculated, must be inside the pressure range selected in the second criteria. This is somewhat of a self-check for the BET theory, if a value of n_m is going to be calculated from a region of data, then it makes sense that the data must contain within it the calculated value of n_m.

The final criteria that must be met is that the calculated pressure at which n_m should occur is within 10% of the actual pressure of n_m. The equation that is used to calculate the

pressure at which n_m occurs is outlined in Equation 1.17. This criterion is another self-check for the BET theory. If a pressure is calculated at which n_m is said to occur, then it should be relatively close to the actual pressure at which n_m occurs inside the selected data set.

$$\left(\frac{p}{p^\circ}\right)_{n_m} = \frac{1}{\sqrt{C}+1} \qquad 1.17$$

As an example of how the BET region is selected and each criterion is accounted for, a nitrogen isotherm of UiO-66 will be used as an example (Figure 1.36D).

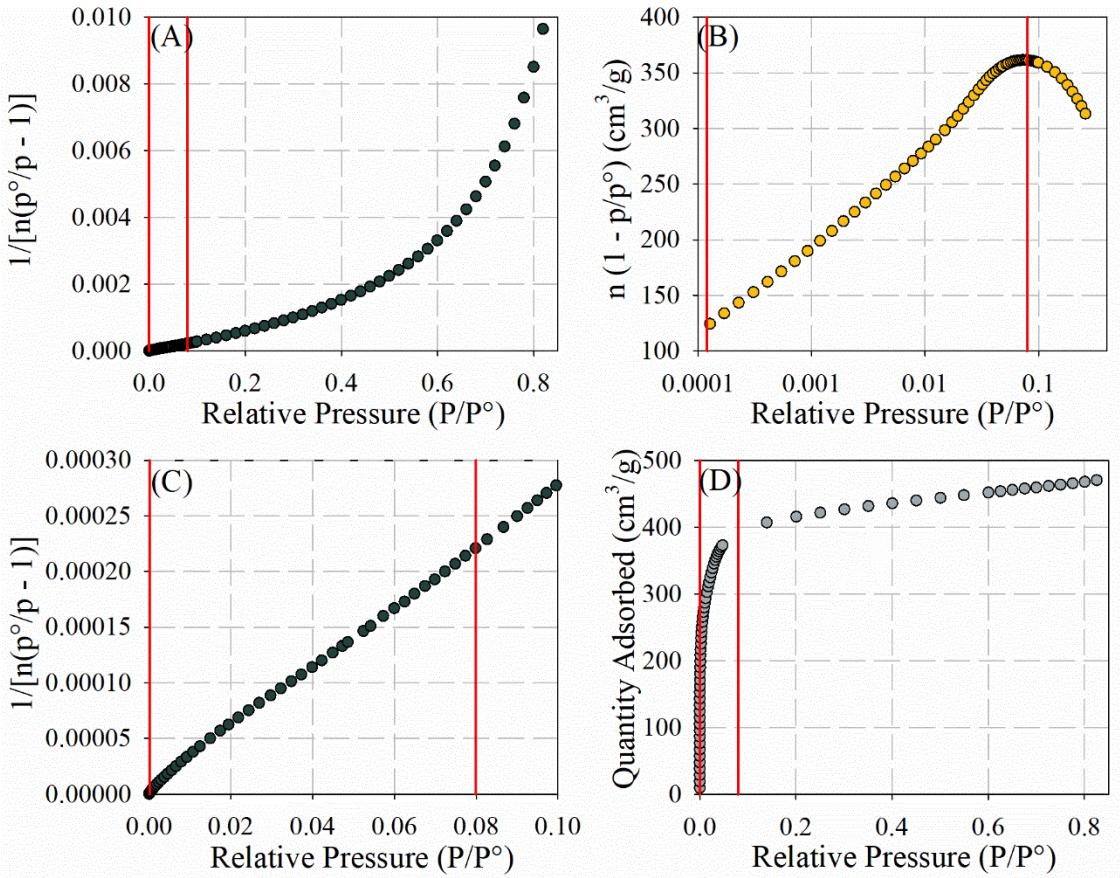

Figure 1.36: Nitrogen Isotherm of UiO-66 and applying BET theory to obtain the surface area. (A) plot of *n(P/P°-1)* versus *(P/P°)* (B) plot of *n(1- P/P°)* versus *(P/P°)* (C) Zoomed in plot of *n(P/P°-1)* versus *(P/P°)* to see the linear region (D) *n* versus *(P/P°)*.

The selected region of the curve to be fit to BET theory is bracketed by two red lines in Figure 1.36. Figure 1.36A is the linear form of the BET Equation 1.11. Figure 1.36C is a zoomed in segment of Figure 1.36A to show the linear region that has been selected. As can be seen from the figure, the data is not linear over the whole region. Calculating the value of *C* from this region provides us with a value of 528. This value is positive and thus criterion one is met. Figure 1.36B, is the Rouquerol plot and within the two red lines, the value of $n(1- P/P^o)$ is increasing with respect to (P/P^o); This meets the second criterion. In this example the value for n_m is calculated to be 368 cm^3/g. The third criteria states that the monolayer adsorption quantity must occur inside of the selected region. Using Figure 1.36D, we can see that 368 cm^3/g occurs at a relative pressure of 0.043 (P/P^o), which is inside the selected region of 0.00012 to 0.08 (P/P^o). The final criteria states that using Equation 1.17, the calculated value of (P/P^o) for monolayer adsorption should be within 10% of the actual value of 0.043 (P/P^o). In this example the relative pressure is calculated to be 0.042 P/P^o, which satisfies the final criteria. Thus, all four of the criteria are met and a nitrogen gas accessible BET surface area of 1600 m^2/g is determined for this sample of UiO-66.

In the field of MOF chemistry, determining the surface area of the materials is a quick diagnostic test to confirm that a new porous material, or the desired porous material has been made. During different experiments where MOFs are employed, surface area is often measured before and after the experiment is complete to provide insight into the stability and recyclability of the material.

1.4.4.2 Pore Size Distributions

Gas adsorption isotherms can also provide insight into the pore sizes of the materials. Based on the material of interest it may contain micropores, mesopores or macropores. Micropores are defined as pores with an internal diameter less than 2 nm, where a macropore has an internal diameter greater than 50 nm. The pores that fall into the range between 2 and 50 nm are classified as mesopores.[159] The most common way the pore size of these materials is calculated is through density functional theory (DFT) calculations.[161] The experimentally obtained isotherms are fit to models. Each model has a collection of isotherms that have been computationally generated based on their pore size and how the pore interacts with the gas.[162] In other words, each model knows the shape of an isotherm based on a specific pore size. These models are called Kernels. Pore size distributions are determined by deconvoluting the shape of the isotherm into a linear combination of the different pore sizes in the kernel. As an analogy, this is like a pocket full of change where you know the mass and the total value, and you use the knowledge of the mass of each coin and their dollar value to determine how many of each coin is present.

These pore size distributions are useful in the identification of materials, and identifying materials that are best suited for applications based on the need for a specific pore size. From these pore size distributions, you can determine if a gas will be able to be stored inside the material or if the material can be used for separations of gases of different sizes.

When fitting measured data to different pore size models the first thing that needs to be considered is the shape of the pore. This is limited to either a cylindrical shaped pore or a slit shaped pore.[159,163] In the case of MOFs, we tend to use the cylindrical based model. This is because when you look at the structure of the material, the pores look more like channels (cylinders) than sheets (slits). Slit shaped pores are more fitting to a structure of two-dimensional sheets such as graphite where gases may absorb into between these sheets. Once we have determined the shape of the pore, we need to determine the most appropriate model to use. The models contain information on how a pore of a particular size and functionality will adsorb a specific gas. Each model that is used is for a particular gas at a given temperature, if the temperature of analysis is different than the temperature of the model, then the data will not provide an accurate model of the pore sizes and distributions; the software will also not let you use a kernel that doesn't match the gas and temperature used in the data collection.

The models for pore size distribution also assume the nature of the adsorbent-adsorbate interactions. In the cases for the models that we have access to in the gas adsorption software package, the software assumes that the entire surface of the adsorbent, in this case the MOF, is completely homogeneous. MOFs contain two main components, the inorganic centre and the organic ligand as previously mentioned. With two distinct regions, that adsorb gases differently, the material deviates from the expected homogeneous surface. Furthermore, if there are large ligands that are functionalized differently, then the surface again would deviate from how a Kernel would predict.

MOFs containing pores of many different shapes and sizes, along with having surfaces that depend on the node and ligand in a way that ca not easily be predicted by one Kernel. This means that it is very challenging (if not impossible) to make Kernels that would work with all MOFs. To calculate the pore size of MOFs we use the models that we have available to us. Using the model that makes the most chemical sense, along with giving a pore size that agrees with other published literature data or computational data, we can then determine if the calculated pore sizes are accurate.

1.5 Motivation of this Thesis

With many people living in water scarce regions, and climate change happening before our eyes, lots of research has been done to find ways to obtain potable water, along with reduce the amount of greenhouse gases in the environment. From the previous sections it is evident that MOFs can be a key contributor when it comes to removing moisture from the air as a source of potable water, and as materials to remove carbon dioxide from the atmosphere.

The goals of this thesis that will be discussed in Chapter 2 and Chapter 3 were never to create the material that would be the best water harvester, or the best at removing carbon dioxide. The goal was to understand the processes at play, and what features of MOFs are important for water and carbon dioxide adsorption. In other words, my goal was not to build a better mouse trap, but to understand what makes a good mouse trap. As previously outlined in the literature, the most popular strategy for target gas adsorption tends to be to install a functional group and determine if the adsorption of the target gas has been

improved. While this is an important, and effective strategy, other features of the MOF (e.g., pore size, number of defects, etc.) that may have impacts on gas adsorption are overlooked. This thesis takes the family of UiO MOFs and monitors the adsorption of target gases by modifications in pore size, number of defects and types of defects present. Chapter 2 investigates the mechanism of how water vapour binds in a series of UiO MOFs that have different pore sizes, and number of defects. Chapter 3 examines what features, such as defects, pore size and cluster functionalization have an important role in the adsorption of carbon dioxide gas.

Going into this work, it was my hope that these investigations would provide a deeper understanding of how gases bind and what features enhance the gas binding capabilities in the UiO series of MOFs. This knowledge can then lead to the development of new materials, or the enhancement of already existing MOFs to improve water and carbon dioxide adsorption.

Chapter 2: The Mechanism of Water Adsorption in UiO Metal-Organic Frameworks

Statement of Co-authorship

This chapter has been published under the title "Analysis of the Water Adsorption Isotherms in UiO-Based Metal-Organic Frameworks" in *J. Phys. Chem. C* 2022, 126, (2), 1107–1114.

Authors: Mason C. Lawrence and Prof. Michael J. Katz

This work was done in the Katz research group where Mason C. Lawrence was the first author who performed the synthetic work, data collection, data analysis, and was responsible for the preparation of the manuscript. Michael J. Katz was the principal investigator for this project, who was responsible for preparation of the manuscript, and contributed to the analysis and interpretation of collected data.

The manuscript has been reproduced in this chapter with modifications to provide an extended discussion of the obtained results.

2.1 Introduction

As outlined in Section 1.3, MOFs have been used for many applications. One emerging application is the use of MOFs for humidity regulation and water harvesting (Section 1.3.3). As a short refresher, the porosity of MOFs makes them ideal for many applications in gas adsorption. This does not just include gases such as carbon dioxide, hydrogen, and methane, but it includes vapours such as water and ammonia.[145,164–169] The ability to adsorb water vapour has important implications in harvesting water from the air in both indoor and outdoor environments. Outdoors, harvesting water from the environment can enable economic growth by providing potable water for agricultural-related products. This is especially important in areas with poor water supplies. Additionally, providing potable water has direct implications on human health. Indoors, maintaining the relative humidity (RH) of a building between 30 – 60% is ideal to reduce mold, while also maintaining comfort. Heating, ventilation, and air conditioning systems (HVAC) are energy intensive, requiring up to 50% of the industrial and 31% of the residential building energy consumption.[170,171] If a passive system that is capable of maintaining the humidity levels can be found, then HVAC costs could be greatly reduced.

In addition to water harvesting applications, water adsorption in MOFs can be used in heat transformation applications. This relies on the thermodynamics of adsorption/desorption. Heat is required to break adsorbent-adsorbate interactions. If the associated enthalpy can be provided by the temperature associated with a hot room, then the air is cooled by heat transfer to the desorption process. The reverse process can also be performed. Given that the formation of the adsorbent-adsorbate interaction is exothermic,

the heat emitted by the adsorption process can be transferred to a cold air stream. Thus, the air is heated by the adsorption process. Given the high density of adsorption sites in a MOF, there is considerable potential for MOFs to be employed in heat transformation processes.[172,173]

In addition to the direct applications of water adsorption, there are several indirect roles associated with water adsorption. For example, water has the potential to act as a competitive inhibitor when other gases (e.g., carbon dioxide, methane)[174] are being adsorbed. This decreases the efficacy of the MOF in real-world applications. Alternatively, water can act as a promotor, assisting in adsorption/desorption processes via hydrogen bonding.[175] Thus, it is crucial to understand how water behaves inside MOFs.

Water adsorption in MOFs tends to be overlooked quite frequently. This is because the role of water on the stability of MOFs is often the focus rather than gaining a deeper understanding regarding how water interacts with MOFs. As mentioned in Section 1.2, certain UiO MOFs are quite sensitive when it comes to interaction with water and care must be taken when activating the material from both liquid water and adsorbed water or the material may degrade. However, if we ignore how water is adsorbed into these materials, with regards to stability, co-adsorption, and the adsorption mechanism, then we limit and prevent advancements from being made in the field.

With regards to water vapour adsorption in MOFs, there are three different water-adsorption mechanisms (Figure 2.1A).[141,164,176] Capillary condensation, occurs when a monolayer of water is deposited evenly onto the walls of the MOF. Subsequently,

additional water layers grow until two layers of water coalesce (i.e., capillary condensation). Once condensation occurs, no further water vapour can be absorbed because the pores are full. This method is recognized by a water adsorption/desorption isotherm that contains considerable hysteresis in the adsorption versus desorption step (Figure 2.2B) but does completely adsorb back to the original position. For capillary condensation to occur, the surface of the material must be homogeneous with regards to the water adsorption process. Around room temperature, capillary condensation occurs in pores that are greater than 2 nm in width.[141] This is outlined by Equation 2.1.

$$D_c = \frac{4\sigma T_c}{(T_c - T)} \qquad 2.1$$

In Equation 2.1, D_c represents the critical diameter; this is the point at which the pore filling is continuous and reversible. Any pore size larger than the critical diameter can show capillary condensation, and conversely, any pore size that is smaller than the critical diameter cannot show capillary condensation behaviour. σ represents the size of the molecule that is being adsorbed, for water this value is approximately equal to 0.28 nm. T represents the temperature of analysis. T_c is the bulk critical temperature of the probe molecule, this is the temperature at which the gas cannot be converted into a liquid, regardless of pressure applied. For water this is approximately 647 K. If capillary condensation is not a viable mechanism due to the pore size being smaller than the calculated size at the adsorption temperature, then one of the alternative mechanisms must be in operation.

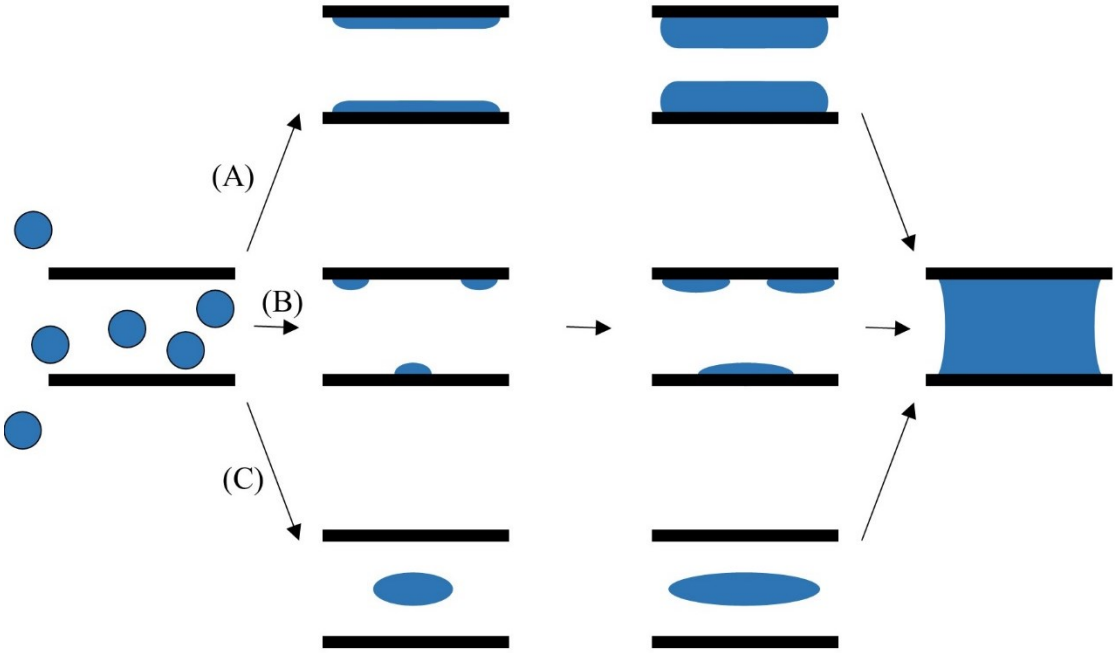

Figure 2.1: Mechanisms by which water vapour adsorption and condensation (potentially) occur inside the pores of MOFs.

The second mechanism of water adsorption is adsorption and growth of water clusters from a nucleation site. In this mechanism, the surface of the MOF is not homogeneous and water vapour prefers to nucleate and grow from a favourable hydrophilic site. This is very likely the operating mechanism for gas adsorption in MOFs since nodes and ligands are not likely to appear homogeneous to a water molecule. Furthermore, as 2 nm pores in MOFs are, often, at the large side of pore apertures, the critical diameter for capillary condensation has not been met. With this in mind, the nucleation site on MOFs can either be the node of the MOF (e.g., open metal site, hydrophilic oxo/hydroxy/aqua-containing nodes), or another hydrophilic portion of the MOF such as $-NH_2$ or -OH functional groups that decorate the pore of the MOF (Figure 2.1B). While a small amount of the gas can be chemically bound to the cluster or the node of the MOF, the adsorption mechanism for the bulk of the incoming gas is physisorption. This mechanism has been

explored in smaller MOFs such as MOF-801, where all pores are smaller than the 2 nm outlined above.[142] For MOFs that grow via the cluster-growth mechanism, once the water cluster has nucleated, the water clusters grow as a function of increasing water vapour content (partial pressure/relative humidity) until they cannot grow any further. The water clusters either coalesce to form a continuous water phase in the MOF (Figure 2.1 right hand side) similar to what occurs in capillary condensation, or the water cluster stops growing because the MOF becomes too hydrophobic for the next layer of water molecules to grow off of the cluster.

Systems that have water adsorption mechanisms based on the cluster-growth mechanism illustrated here are often recognized by isotherms that display hysteresis in the nucleation portion of the isotherm. Given the nucleation step can be chemisorption (potentially reversible), not all of the adsorbed water vapour becomes desorbed at the same pressure that it took to adsorb the vapour. This is due to the interactions between the water molecules and the nucleation sites inside the pore, or the walls of the material. This leads to more water adsorbed inside the material compared to the initial adsorption phase (Figure 2.2C). To completely remove the adsorbed water in this situation, either a lower pressure is required, or the sample needs to be heated to remove the nucleation site. In a worst-case scenario, solvent exchange (potentially at elevated temperatures) prior to thermal activation may be required.

The final water adsorption pathway occurs for very hydrophobic materials where a water cluster forms in the pore without contact with the surface and grows until the pore is filled or the hydrophobic surface prevents further cluster growth.[177] This mechanism is not

commonly observed in MOFs. However, if it were to occur, then it would require a hydrophobic MOF in which the node has no open coordination sites, the node is not hydrophilic, there are no defects that could be hydrophilic, and the ligands are also sufficiently hydrophobic to prevent water vapour adsorption. Hydrophilic defects are often caused by missing nodes/ligands where the remaining carboxylic acid/carboxylate (missing node) or terminal water molecules (compensating for a missing ligand) is hydrophilic. As such, these defects often provide sites (OH^-, H_2O, etc.) that are favorable for molecules such as water vapour to bind. The adsorption third mechanism can be recognized in a water isotherm where the desorption curve closely follows the adsorption curve (Figure 2.2A) even at low relative pressures. The desorption often follows the adsorption curve very closely because the water molecules are not strongly interacting with the pores and a small decrease in reduced pressure allows the system to re-establish equilibrium by releasing water vapour from the water cluster (i.e., desorption).

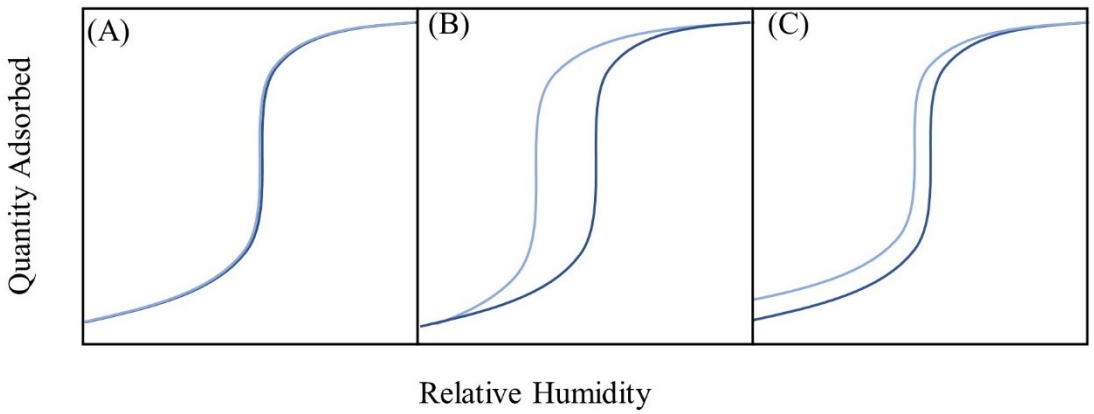

Figure 2.2: Examples of water isotherms exhibiting a desorption curve that closely follows the adsorption curve (A) one showing hysteresis, but still completely desorbs (B) and isotherm showing hysteresis but not all water is desorbed (C).

In the present work, I focused my attention to six MOFs that differ in the ligand length, ligand functionality, and defect density while maintaining the topology of the material. The MOFs investigated herein are the UiO-family (Figure 2.3) that contain $Zr_6O_4(OH)_4^{12+}$ nodes linked via six, assuming no defects, linear ditopic dicarboxylate-based ligands. These ligands form a large octahedral pore, and a smaller tetrahedral pore; for more information on the UiO family of MOFs see Section 1.2. I selected three unfunctionalized MOFs (UiO-66, UiO-67, and UiO-68-Me_4/PCN-57) and three functionalized MOFs (UiO-66-NH_2, UiO-67-NH_2, and UiO-68-NH_2). The amino-functionalized UiOs were specifically chosen due to the multitude of applications where the amino-functionality enhances the properties of the MOF or is otherwise utilized to introduce new functional groups into the pore of the MOF.[53,178,179] By keeping the topology the same, the role of ligand length and functionality can lead to a general trend that can be applied to other MOF systems. It is worth briefly mentioning that UiO-68 was not explored herein due to the low solubility of the parent ligand. As such, PCN-57 was utilized. PCN-57 uses a functionalized version of the PCN-57 ligand, the 2',3',5',6'-tetramethyl-[1,1'1:4',1''-terphenyl]-4,4''-dicarboxylic acid ligand; this is a terphenyl ligand with four methyl groups on the central aromatic ring. As PCN-57 was not synthesized by the research group that synthesized UiO-66 and UiO-67, they opted to use their own Porous Coordination Network (PCN) nomenclature. For the purpose of this thesis, I have opted to call the MOF UiO-68-Me_4 and leave out the PCN-57 nomenclature. I believe this is important for clarity.

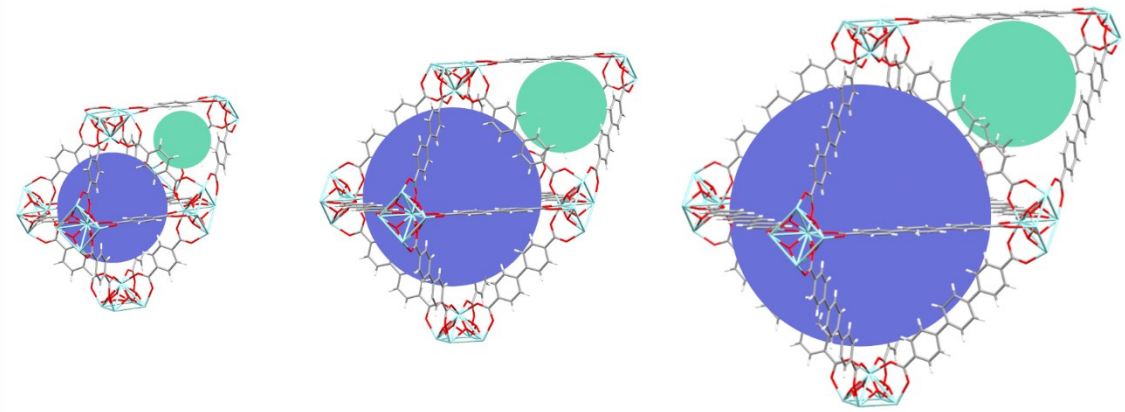

Figure 2.3: UiO-66 (left), UiO-67 (middle) and UiO-68 (right). The octahedral pores are illustrated by the large purple circles, while the tetrahedral pores are illustrated by the smaller green circles.

2.2 Results and Discussion

UiO-66, UiO-66-NH_2, UiO-67, and UiO-67-NH_2 were synthesized using the well-established "hydrochloric acid" procedure. This procedure involves combining zirconium tetrachloride along with the organic ligand (terephthalic acid, aminoterepthalic acid, 4,4-biphenyldicarboxylic acid, or 2-amino-4,4-biphenyldicarboxylic acid respectively) in 15 mL of DMF with either 1 mL (UiO-66, UiO-66-NH_2) or 0.5 mL (UiO-67, and UiO-67-NH_2) of hydrochloric acid. Unlike the acetic acid procedure (see Chapter 3) for the synthesis of UiO-66, the hydrochloric acid procedure is high yielding, and has been well documented to work with many derivatives of both terephthalic acid and 4,4-biphenyldicarboxylic acid. One key difference between the hydrochloric acid procedure and the acetic acid procedure is that the hydrochloric acid procedure produces highly defective UiOs. More specifically it has been shown to create missing ligand defects (See Section 1.2.1 for further discussion).

The unfunctionalized UiO-68-Me_4 and the amino functionalized UiO-68-NH_2 were more difficult to synthesize; the hydrochloric acid procedure has not resulted in the formation of UiO-68s. While there are multiple procedures in the literature for the synthesis of UiO-68s, in our hands many of these did not work. After several attempts, UiO-68-Me_4 was synthesized using zirconium chloride as the source for the node, and using trifluoracetic acid as a modulator, as outlined by Cui and coworkers.[180] On the other hand, UiO-68-NH_2 was synthesized using a modified procedure outlined by Blight, Fogan, and coworkers.[96] In my hands, and other members of the group, the synthetic reproducibility of these MOFs was not great. During this project it was found that these initial procedures produced these UiO-68s prior to the COVID shutdown. Strangely, after lab work resumed, these procedures no longer produced the MOFs with reasonable gas adsorption isotherms and X-ray diffractograms, and I had to shift to a different method to synthesize these MOFs. For UiO-68-Me_4, the post-COVID procedure involved using zirconyl chloride and benzoic acid as the modulator as outlined by Goswami *et al*.[35] The post-covid procedure for UiO-68-NH_2 required zirconium chloride and benzoic acid as published by Schaate *et al*.[181] Although determining a synthetically versatile and reproducible synthesis of these MOFs is critical, this was outside of the scope and available timeframe of this thesis. For consistency, the pre-shutdown (COVID-19) MOFs are the primary data in this chapter (data collected prior to March 2020). Where necessary, the post-shutdown (August 2020) MOFs are utilized. Some differences in the isotherms are discussed in Appendix A. While there are small differences noticed in the isotherms, the observed conclusions remain true regardless of the synthetic procedure followed.

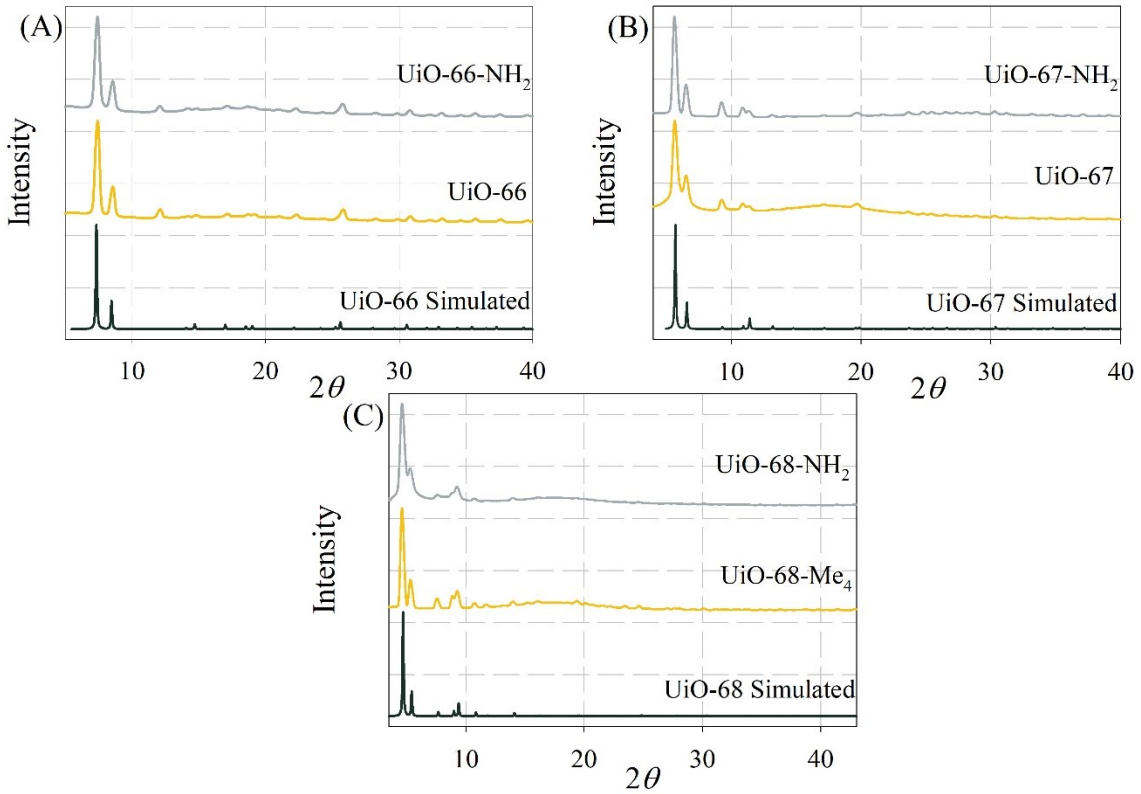

Figure 2.4: Powder X-ray diffractograms of the six MOFs examined in this chapter and their respective simulated diffractograms. UiO-66 (A), UiO-67 (B), and UiO-68 (C). The simulated spectrum for the MOFs is shown as the green trace (lowest stack), the unfunctionalized MOF is the yellow trace (middle stack), and the amino-functionalized MOF is the grey trace (top stack).

2.2.1 Powder X-Ray Diffraction

With the three unfunctionalized MOFs and three amino-functionalized MOFs synthesized, our first method of characterization was via powder X-ray diffraction. In all six MOFs the measured X-ray diffractograms match the simulated structures quite well. This is the first indication that we have synthesized the desired material (Figure 2.4).

The measured diffractograms of our six materials show narrow and well-defined peaks, which indicate a crystalline material. In my experience, when the synthetic procedure is not successful the peaks are considerably broader with the first two peaks

often appearing as a single peak. Gas adsorption properties of samples that contain these broad diffractograms are always considerably lower than expected. In the measured patterns for the unfunctionalized and the amino-functionalized UiO-66 we notice that the (*2 2 0*) reflection at 12º in *2θ* is present in the observed but not in the simulated diffractograms. This peak is always observed in UiO-66. If an atom/molecule is placed in the pore of the simulated structure of UiO-66, then a non-zero intensity for the (*2 2 0*) is observed. This suggests that residual solvent or gas molecules are present in the pore and contribute to the diffractogram. This same observation can be made for the UiO-67s (9º in *2θ*). UiO-68s on the other hand do show a peak in the simulated diffractogram that corresponds to this plane (7º in *2θ*). With the powder X-ray diffractograms matching the simulated ones, we were able to continue to move forward in characterizing our MOFs. While powder X-ray diffraction is a necessary characterization tool, it does not provide complete information on the crystallinity of the MOF. If the MOF is a mixture of crystalline and amorphous material the crystalline portion would dominate the diffractogram and provide little indication that there was amorphous material present. Other techniques are required to completely characterize the MOFs in this study.

2.2.2 Thermogravimetric Analysis

Section 2.2.3 will illustrate that all six MOFs have nitrogen gas adsorption isotherms and nitrogen gas accessible BET surface areas that are consistent with the literature values. Given the need to discuss the similarities and differences in the adsorption properties for both nitrogen gas and water vapour, it was first important to quantify the number of missing ligands (see Section 1.2.2) in each MOF. This was done by using TGA

as outlined by Lillerude *et al*.[83] One other literature method for the determination of the degree of missing ligands is the use of quantitative NMR. While this can be an effective method, it was not successful for these MOFs.[38] In our hands the reproducibility was a major issue. From the same batch of MOF we would obtain very different results ranging from three missing ligands to more than six ligands present. Dissolution of the MOF also became an issue. Once the MOF was dissolved, there would often be some small insoluble impurities that we suspect was zirconium oxide, but we could not be certain that it did not contain any ligand. The TGA method was far more successful. An outline of the procedure used, using UiO-66 as an example, is outlined below.

To determine the number of missing ligands, a small amount of MOF was placed on a platinum pan (7-10 mg), placed in the TGA, and its weight monitored as the sample was heated in the presence of oxygen up to 876 K. At these temperatures, the organic components of the MOF oxidized and decomposed leaving only zirconium oxide behind. This can be illustrated by the following balanced equation.

$$Zr_6O_4(OH)_4(BDC)_6 + 45\,O_2 \xrightarrow{\Delta} 6\,ZrO_2 + 48\,CO_2 + 14\,H_2O$$

While the above equation is accurate for UiO-66, it is worth noting that at temperatures above 623 K, the node is known to dehydrate and evolve two equivalences of water, leaving two new O^{2-} units on the node; this is formed by the proton transfer from one cluster-bound hydroxide to another. With that in mind, the final decomposition step is better described by the new chemical equation shown below.

$$Zr_6O_6(BDC)_6 + 43\,O_2 \xrightarrow{\Delta} 6\,ZrO_2 + 48\,CO_2 + 12\,H_2O$$

From the amount of zirconium oxide that remains after complete decomposition of the MOF, we can determine the amount of zirconium that was present in the MOF. To simplify the process of determining the number of missing ligands, the first step is to normalize the mass of ZrO_2 to 100%; this is equivalent to stating that the final mass of ZrO_2 is 100 mg. For the purpose of this work, this is known as the end plateau in the TGA (see Figure 2.5). We next have to determine what normalized mass we would have if we had a defect-free MOF. This ideal plateau can be calculated by taking the 100% of ZrO_2, converting it to moles, using the relationship that it takes six zirconium centres to make one node, and then converting this to percent (or similarly mass) of MOF assuming no defects (i.e., six ligands). The ideal plateau is calculated by the following equation.

$$Ideal\ Plateau = \left(\frac{Molar\ Mass\ of\ Dehydrated\ MOF}{Number\ of\ Zirconiums\ per\ Node * Molar\ Mass\ ZrO_2}\right) 100\%$$

For a defect-free MOF, the ideal plateau is calculated to be 220%. The relationship between the ideal plateau and the end plateau (i.e., 100% as defined above) represents the number of ligands that have decomposed. The difference can be used to calculate the weight percent of each of the six ligands using the following equation:

$$Ligand\ Weight\ Percentage = \frac{(Ideal\ Plateau - End\ Plateau)}{Number\ of\ Ligands\ in\ Ideal\ MOF}$$

For UiO-66 the number of ligands in the ideal structure is known to be six, which means the ligand weight percentage is equal to 20%. Thus, we know that for every 20% loss between the observed plateau and the end plateau we have one ligand. Thus, we can then

use the difference between the experimental plateau and the end plateau to calculate how many ligands we have (x). This can be done using the following formula:

$$x = \frac{Experimental\ Plateau - End\ Plateau}{Ligand\ Weight\ Percentage}$$

The experimental plateau is the normalized percent mass of the MOF at the point after the node is dehydrated; this includes the defect sites and the μ_3-hydroxides on the node. Using UiO-66 as the example (Figure 2.5A). we have an experimental plateau of 196%, end plateau of 100% and a ligand weight percentage of 20% therefore, x is calculated to be 4.8. The number of defects present would be the ideal number of ligands subtract the number of ligands calculated, for UiO-66 it is determined to have 1.2 missing ligands. Once we have determined the number of ligands (and defects) present we were able to determine the chemical formula for each MOF as discussed in Section 1.2.1.

The resulting TGA plots for all six MOFs studied and their observed, theoretical, and end plateaus are shown in Figure 2.5, while Table 2.1 shows all the results from the calculations. Determining the experimental plateau involves making an estimate of where the MOF is truly dehydrated. Due to the slope in the TGA trace between 473 K and 673 K it can be difficult to determine the exact point of dehydration and therefore the experimental dehydrated mass. To estimate the number of missing ligands and molar mass, we picked a few places along the dehydration curve where we would consider the trace to represent post dehydration and pre decomposition. We then re-calculated the number of missing ligands, and molar masses in these extreme cases to determine the error associated with our calculations.

Table 2.1: Number of ligands per formula unit and the resulting molecular weight for each MOF synthesized in this study.

MOF	**Ligands per Formula Unit Observed**	**Molecular Weight (g/mol) $Zr_6O_4(OH)_4L_{6-x}(d)_{2x}$**
UiO-66	4.8 ± 0.2	1550 ± 30
UiO-66-NH_2	3.8 ± 0.2	1510 ± 40
UiO-67	5.1 ± 0.2	1970 ± 50
UiO-67-NH_2	3.9 ± 0.2	1820 ± 50
UiO-68-Me_4	5.4 ± 0.1	2730 ± 40
UiO-68-NH_2	5.4 ± 0.1	2510 ± 30

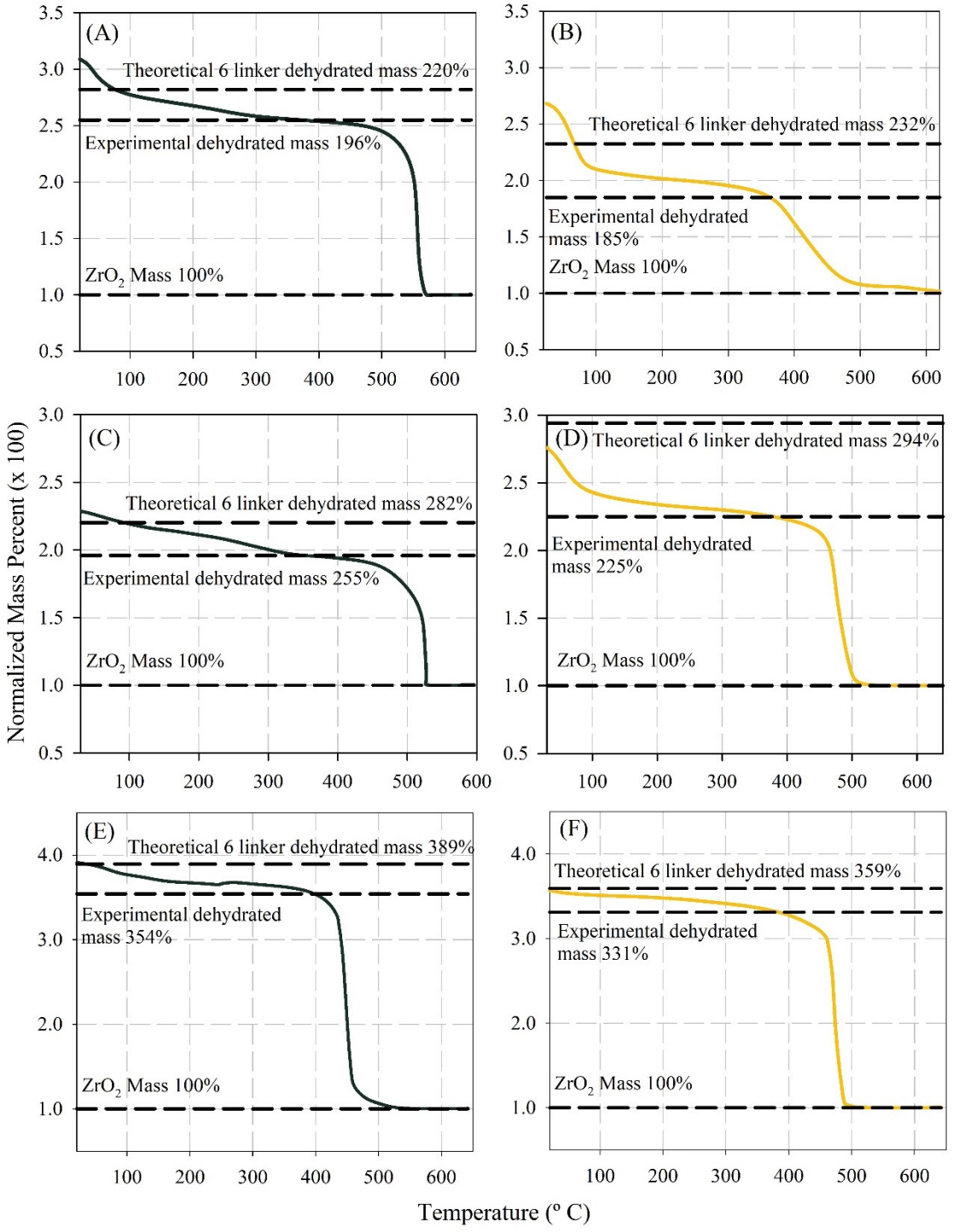

Figure 2.5: TGA of the MOFs studied outlining the normalized theoretical 6 ligand dehydrated mass, the normalized experimental dehydrated mass and the normalized ZrO_2 mass. (A) UiO-66, (B) UiO-66-NH_2, (C) UiO-67, (D) UiO-67-NH_2, (E) UiO-68-Me_4, (F) UiO-68-NH_2.

2.2.3 Nitrogen Gas Adsorption Isotherms

To further characterize our MOFs and confirm they have been successfully synthesized, the nitrogen gas adsorption isotherms were measured at 77 K. From these measurements we were able to determine their nitrogen gas accessible BET surface area and pore size distributions. While the powder X-ray diffractograms do indicate the desired material has been formed, the gas adsorption properties are a better measure of the bulk properties. This is because crystalline materials have sharper peaks and amorphous materials have considerably broader peaks. Thus, in powder X-ray diffractograms a small amount of crystalline material can easily dominate a diffractogram.

2.2.3.1 BET Surface Area

Table 2.2: MOF Characterization data from nitrogen gas adsorption isotherms.

	Nitrogen gas accessible BET Surface Areas (m^2/g)	
MOF	**Observed**	**Literature**
UiO-66	1480	1580
UiO-66-NH_2	1100	1200
UiO-67	2500	2500
UiO-67-NH_2	2000	2080
UiO-68-Me_4	3475	3300
UiO-68-NH_2	3350	3750

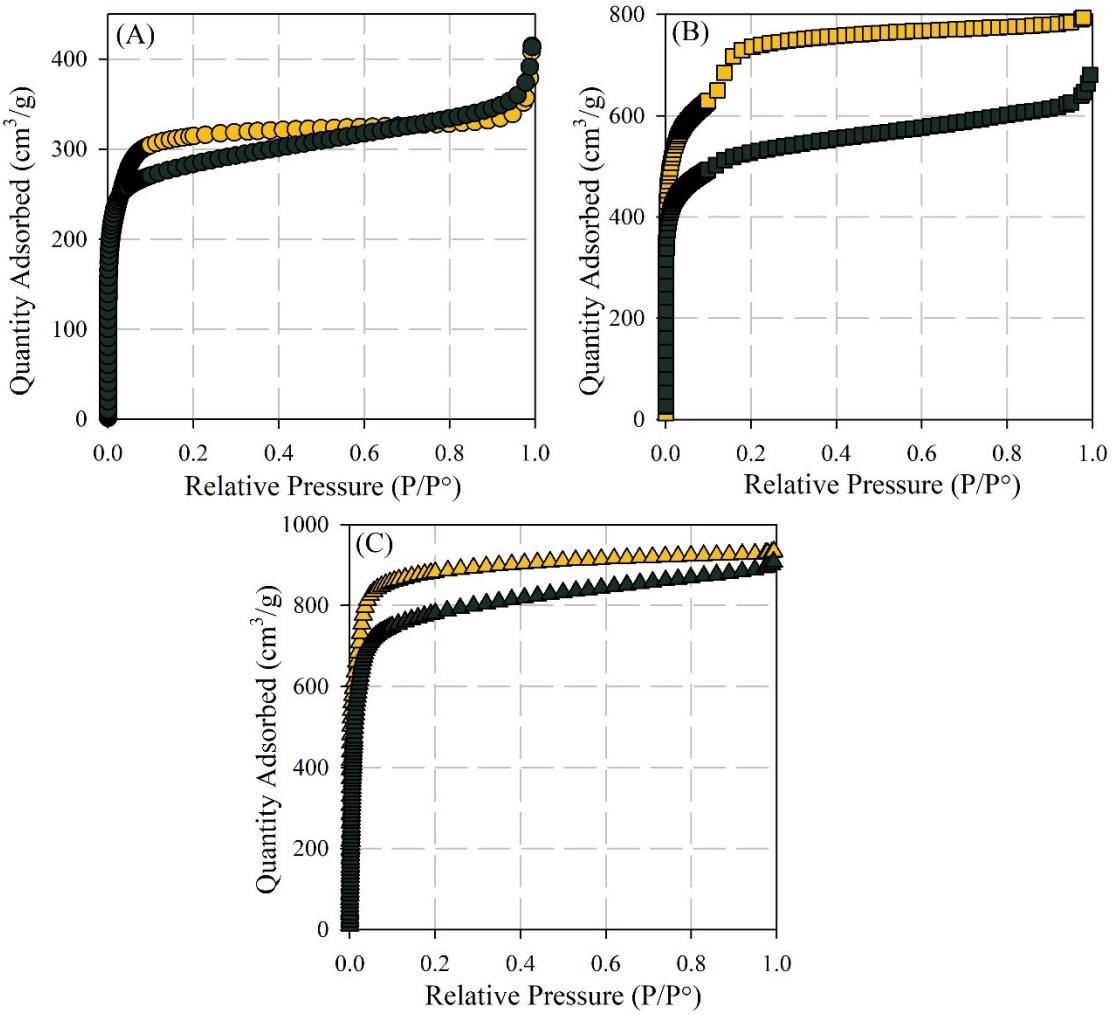

Figure 2.6: Nitrogen gas adsorption isotherms, measured at 77 K of the unfunctionalized UiOs (yellow trace) and amino-functionalized (green trace). (A) UiO-66 and UiO-66-NH_2. (B) UiO-67 and UiO-67-NH_2. (C) UiO-68-Me_4 and UiO-68-NH_2.

From the nitrogen gas adsorption isotherms (Figure 2.6) the nitrogen gas accessible BET surface area was determined for each of the six MOFs. The results are shown in Table 2.2. The obtained BET surface areas match the literature values quite well. This confirms that we have successfully synthesized each MOF. It should be noted that there is a difference of approximately 10% between the observed and literature values. This is quite common in the field of MOF chemistry. This difference is often due to batch-to-batch

difference in the synthesized MOFs, along with each person's interpretation of the BET region of the isotherm (see Section 1.4.3.3) and the available number of data points in this region.

It was observed that as the ligand length increases, so does the nitrogen gas accessible surface area. UiO-66 showed a surface area of 1480 m^2/g while UiO-67, which contains a longer ligand had a surface area of 2500 m^2/g. From the TGA results displayed in Table 2.1, both UiO-66 and UiO-67 both contain roughly the same number of defects. This result indicates the effect of the added surface for the nitrogen gas to adsorb outweighs the added molecular mass of the ligand.

The effect of the amino functionality is more difficult to assess. Assuming a MOF with the same number of ligands (or alternatively defects), the added pendant group provides increased molecular weight, which will lower the gravimetric surface area (as outlined in Section 1.1 and Table 1.1), while providing larger surface for the gas molecules to adsorb onto, which will increase the surface area. These features will have opposing, but not necessarily equal, effects. We have calculated the surface area of UiO-66 to be 1480 m^2/g, and UiO-66-NH_2 to be 1100 m^2/g. Upon first inspection we could believe that the addition of the pendant amino caused a large enough change to the molar mass to outweigh the increase in accessible surface area to decrease the surface area by 380 m^3/g. However, when we consider the difference in the number of ligands in UiO-66-NH_2 versus UiO-66 (approximately one more ligand in UiO-66 than UiO-66-NH_2; Table 2.1), and the similar molecular weight between the two ligands (1550 versus 1510 g/mol for UiO-66 and UiO-66-NH_2), then a molecular weight argument would not be likely here. Therefore, the

difference in these MOFs would be due to the number of missing ligands. The decrease in surface area is thus due to the fewer ligands in UiO-66-NH_2 and thus less surface for gas to adsorb onto. The surface area effect is larger than the molecular weight effect. This is similarly observed for UiO-67 and UiO-67-NH_2 (1970 versus 1820 m^2/g with one and two missing ligands respectively) in which the increased number of defects lowers the observed surface area more than the molecular weight changes.

For UiO-68-Me_4 and UiO-68-NH_2 we see very little difference in the observed nitrogen gas accessible BET surface areas. Both MOFs contain approximately half a missing ligand per formula unit. UiO-68-NH_2 has a surface area of 3350 m^2/g with a molecular weight of 2510 g/mol. UiO-68-Me_4 has a surface area of 3475 m^2/g while having a molecular weight of 2730 g/mol. Based on the previous trends with UiO-68-Me_4 containing a larger molar mass, we would expect it to have a lower surface area compared to UiO-68-NH_2. However, we observe the opposite. UiO-68-Me_4 has a slightly larger surface area, this indicates that while the four additional methyl groups per ligand add roughly 200 g/mol in additional weight, they also provide enough surface area to offset the additional mass increase.

2.2.3.2 Pore Size Distribution

Further characterization of the six MOFs in this study involved calculating the pore size distribution from the available isotherm data in Figure 2.6. Examining the pore size provides insight of the structure of the pores, indicating how missing ligand defects would cause a change in the pore size distribution compared to defect free material. As mentioned

in Section 1.4.4.2 there are currently no models (i.e., Kernels) available that have been designed to take into consideration all the structural features of MOFs. As such, we are limited by the available models in the software package provided by Micromeritics. With that in mind, for any MOF the ideal approach is to compare all the available models and compare the quality of the fits between the model and the observed isotherms. In this work we assume that the model that provides the lowest error would be the model that represents the pore size the best. Using cylindrical shaped pores, which is consistent with what is expected for a MOF, there are three available models to fit nitrogen gas adsorption data at 77 K. These models are cylindrical pores on an oxide surface, Tarazona, and Pillared clay.

2.2.3.2.1 Data Fitting to Calculate Pore Size Distribution

Figure 2.7 and Table 2.3 illustrate the fits of the three pore size models for UiO-66 and UiO-66-NH_2. All three fit the experimental data quite well, as observed in Figure 2.7 and all these fits could be used to calculate the pore sizes of the materials. Table 2.3 illustrates the standard deviation of the models from the experimental data and the lowest standard deviations represent the best fit. The best fits for UiO-66 and UiO-66-NH_2 come from the pillared clay model. Additionally, the cylindrical pores on an oxide surface model also fits quite well. For these two models, a very low standard deviations of 1.04 cm^3/g and 0.44 cm^3/g is observed.

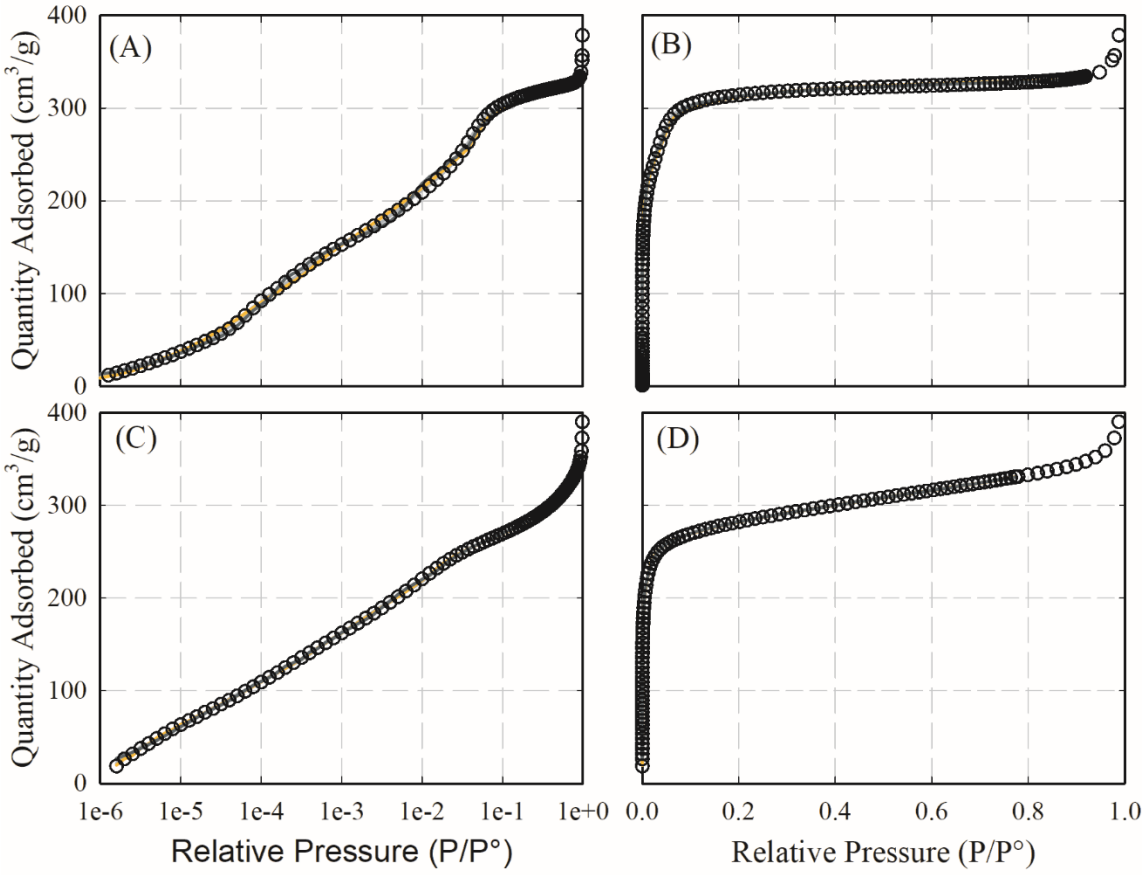

Figure 2.7: Pore size distribution model fits for UiO-66 (A, B) and UiO-66-NH_2 (C, D). Green trace represents the Tarazona model, yellow trace is cylindrical pores on an oxide surface model, grey trace represents the pillared clay model. These traces may be difficult to see showing how well the model fits the experimental data.

Table 2.3: Standard deviation for pore size distribution fits of UiO-66 and UiO-66-NH_2.

	UiO-66	**UiO-66-NH_2**
Tarazona	2.99 cm^3/g	1.29 cm^3/g
Cylindrical Pores on an Oxide Surface	2.63 cm^3/g	0.44 cm^3/g
Pillared Clay	1.04 cm^3/g	0.98 cm^3/g

All the fits for UiO-66 and UiO-66-NH_2 look quite well relative to one another. With longer ligands used in UiO-67, UiO-67-NH_2, UiO-68-Me_4, and UiO-68-NH_2, the pore

sizes increase, and the models begin to deviate from the experimental data leading to notably poorer fits.

Figure 2.8 illustrates the fit of the three models for UiO-67 and UiO-67-NH_2. Examining the fits for UiO-67 it is quite clear that cylindrical pores on an oxide surface is not a great fit (Figure 2.8A, yellow trace).

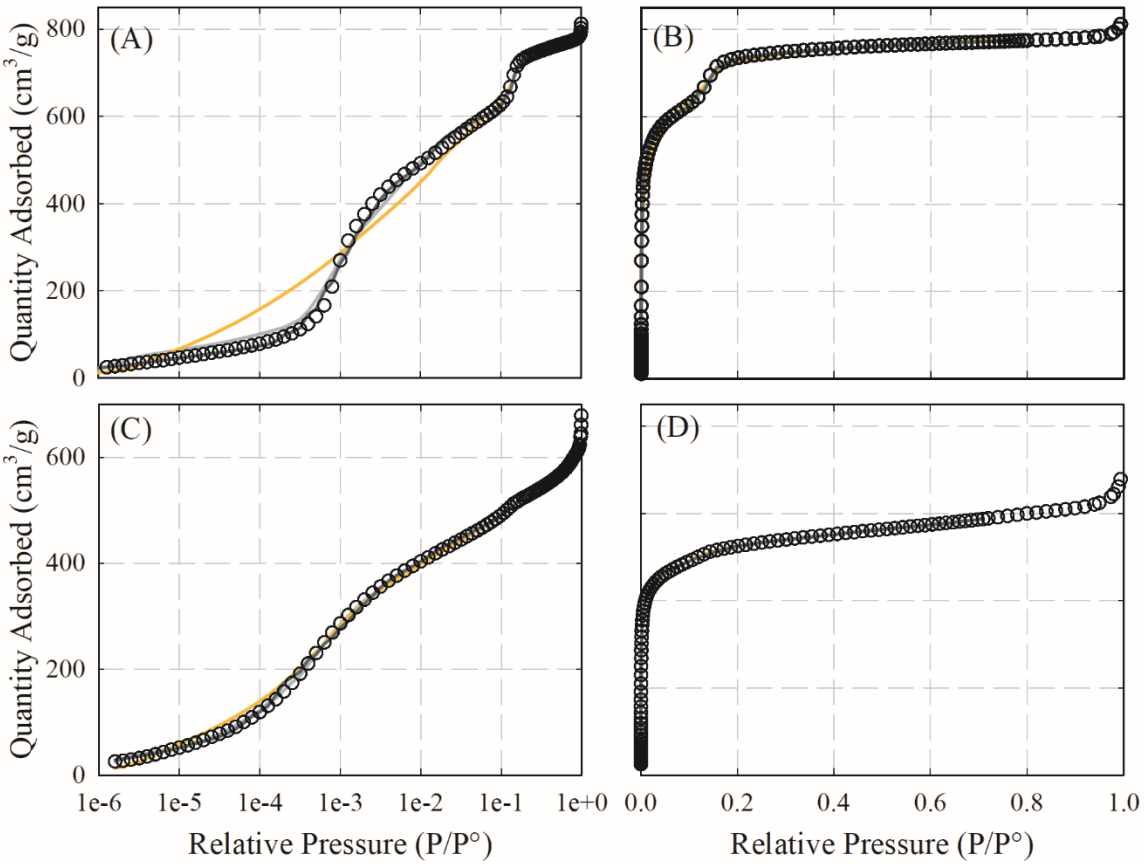

Figure 2.8: Pore size distribution model fits for UiO-67 (A, B) and UiO-67-NH_2 (C, D). Green trace represents the Tarazona model, yellow trace is cylindrical pores on an oxide surface model, grey trace represents the pillared clay model. These traces may be difficult to see showing how well the model fits the experimental data.

While the Tarazona and pillared clay models show worse fits than what is observed for UiO-66 (Table 2.3 versus Table 2.4), there is considerably more agreement between the data and the model for these fits versus the oxide surface model.

The nitrogen gas adsorption isotherm for UiO-67 (Figure 2.8 and Figure 2.6) shows a step in the isotherm at approximately 0.15 P/P^o. This is an indication that there are at least two different pore sizes and that they are different in size. While it is well known that UiOs have two different pore sizes (one tetrahedral pore and one larger octahedral pore), the lack of any step in any of the other MOFs likely suggests that these pores are more likely defect based than the expected pore sizes for these MOFs; we will see in Chapter 3 that changing the synthesis of UiO-67 produces different shaped isotherms. With this in mind, it is critical to accurately fit the shape of the isotherm for meaningful pore size distributions.

Turning our attention to the fits to the amino-functionalized UiO-67, all three models appear fit the data much better than the fits for UiO-67. In the nitrogen gas adsorption isotherm, we don't see the step that is observed for UiO-67. This indicates that the pores present in UiO-67-NH_2 are similar in size. Given that UiO-67-NH_2 has more missing ligands than UiO-67, it would be reasonable to expect to see a larger number of defect-based pores rather than the expected pore sizes for this MOFs.

Examining the standard deviations of these fits displayed in Table 2.4, these models do not fit UiO-67 as well as they fit UiO-66. The standard deviation jumps from 1.04 cm^3/g to 7.37 cm^3/g for the best fitting models. UiO-67-NH_2 also deviated from the models, but

not as severely as UiO-67. The best fitting model for UiO-67-NH_2 illustrated a standard deviation of 2.17 cm^3/g, just slightly above the values observed for UiO-66.

Table 2.4: Standard deviation for pore size distribution fits of UiO-67 and UiO-67-NH_2.

	UiO-67	**UiO-67-NH_2**
Tarazona	7.37 cm^3/g	3.83 cm^3/g
Cylindrical Pores on an Oxide Surface	35.6 cm^3/g	7.47 cm^3/g
Pillared Clay	13.2 cm^3/g	2.17 cm^3/g

Turning our attention to UiO-68-Me_4 and UiO-68-NH_2, it is quite evident that at this ligand length none of the three models fit the data very well (Figure 2.9). While UiO-68-NH_2 shows acceptable agreement with the Tarazona model, over-interpreting the data for these larger MOFs should not be done.

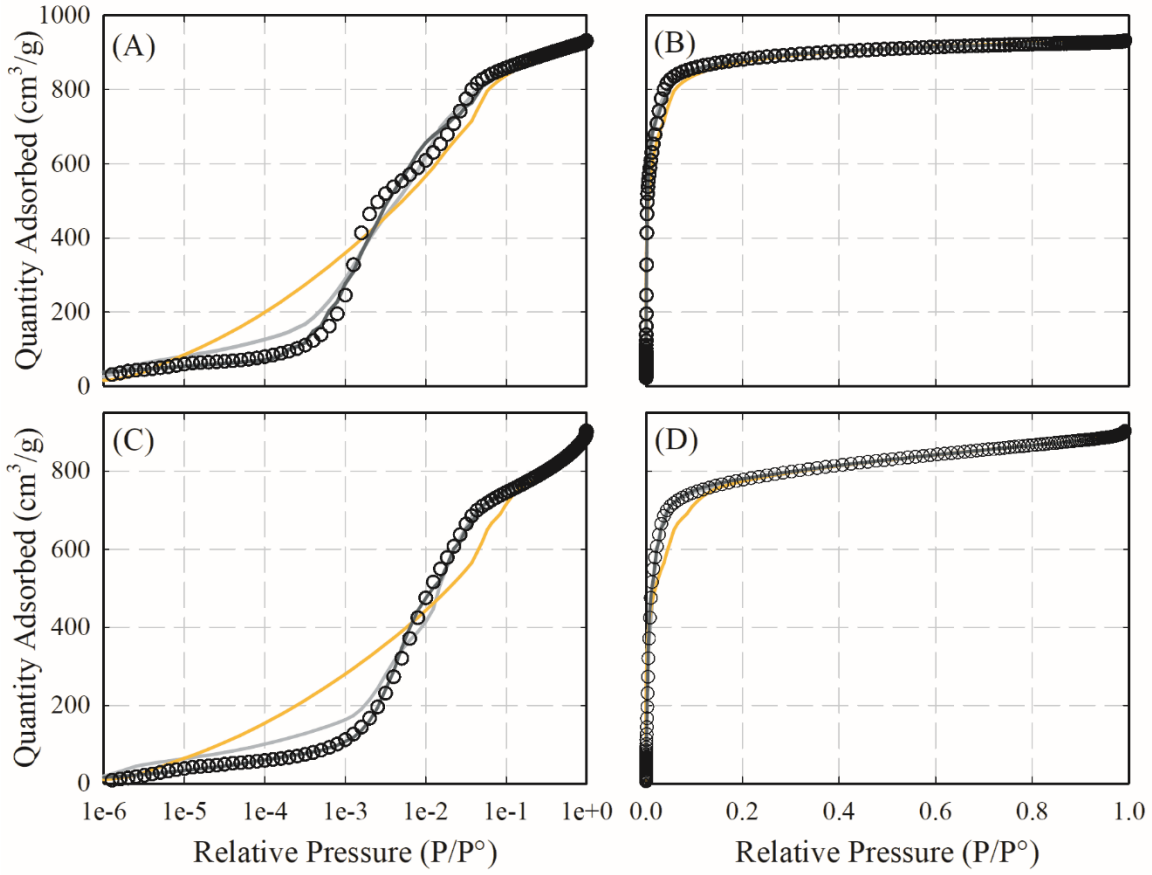

Figure 2.9 Pore size distribution model fits for UiO-68-Me_4 (A, B) and UiO-68-NH_2 (C, D). Green trace represents the Tarazona model, yellow trace is cylindrical pores on an oxide surface model, grey trace represents the pillared clay model. These traces may be difficult to see showing how well the model fits the experimental data.

The standard deviations of the fits (Table 2.5) for UiO-68-Me_4 are very poor, with the best model (Tarazona) having a standard deviation of 13.1 cm^3/g. This standard deviation is on the high end of which I am comfortable reporting a pore size for. However, due to the lack of models for MOFs, it is the best representation that we have available. UiO-68-NH_2 had one model (Tarazona) that showed reasonable agreement with a standard deviation of 6.1 cm^3/g, very similar deviation that was observed in UiO-67.

Table 2.5: Standard deviation for pore size distribution fits of UiO-68-Me_4 and UiO-68-NH_2.

	UiO-68-Me_4	**UiO-68-NH_2**
Tarazona	13.1 cm^3/g	6.1 cm^3/g
Cylindrical Pores on an Oxide Surface	45.3 cm^3/g	69.0 cm^3/g
Pillared Clay	19.8 cm^3/g	20.1 cm^3/g

The models that we have fit all six of these MOFs to are designed for more homogeneous surfaces (e.g., oxide surface or a clay material). As the length of the ligand is increased, the ratio of inorganic to organic component of the MOF decreases. With this decrease the material tends to deviate away from a homogeneous material. UiO-67-NH_2 has an interesting result. With the pores being closer in size, and less of the organic ligand present due to the missing ligand defects, the material may appear more homogeneous, which leads to better fits between the isotherm and the models used to calculate the pore size distribution. The UiO-68s may deviate from the models for similar reason. Longer ligands are introduced deviating the material further from homogeneity. In this case we have two different binding sites. The first site comes from the inorganic component of the MOF, while the second site comes from the organic component. Each of these sites would have different binding forces. The models that we are using only assume that the surface change as a factor of pore size is predictable (i.e., homogeneous). The ligands that were used in this study also have functional groups (methyl, or amino) that further cause a deviation from homogeneity, hence the hesitation to overinterpreted the results.

2.2.3.2.2 Pore Sizes from Nitrogen Isotherms

With the experimental data properly fit for the calculation of the pore sizes present in each MOF we can now turn our attention to the interpretation of the data. The geometry of the UiO family of MOFs produce an octahedral and tetrahedral pore in the ratio of 1:2.[182] Assuming a defect-free material, it can be expected to see two main pore sizes consistent with a larger octahedral pore and a smaller tetrahedral pore. From computational data on the defect-free MOFs, the tetrahedral pore width increases from 3.8 Å to 5.5 Å to 9.7 Å as the ligand increases in length in UiO-66, UiO-67 and UiO-68-Me_4. Similarly, the larger octahedral pore increases in width from 8.0 Å to 13.1 Å to 17.2 Å, respectively.[82]

In UiO-66 and UiO-66-NH_2 (Figure 2.6A), there appear to be two pores. The observed pore widths of UiO-66 are centred around 11 Å and 17 Å with UiO-66-NH_2 appearing at slightly lower widths (10 Å and 15 Å) and with a broader distribution. We attribute the broadness of these peaks to the additional missing ligands in UiO-66-NH_2.[183] As more ligands are removed, the peaks in the pore size distribution will begin to broaden and overlap. The smaller pore observed in the nitrogen gas adsorption isotherm of the UiO-66s is consistent with the experimental and computational octahedral pore width of UiO-66.[56,82,184] The larger observed pore in the UiO-66s is due to the merging of pores caused by missing ligand defects.[56,184–186] Although it is not uncommon to observe a pore width consistent with the tetrahedral pore in pristine UiO-66,[184] the presence of defects has been demonstrated to reduce the incremental surface area of the tetrahedral pore while increasing the incremental surface area for defect-based pores. In the synthesis outlined in

Section 2.4.2 the procedure required concentrated hydrochloric acid to be added (12 M). The 1 mL of acid in 15 mL of DMF produces a concentration of 0.75 M. Our data for UiO-66 is consistent with the pore size distribution trend observed by Liang *et al*. where they had a slightly higher acid concentration of 0.92 M.[184]

The pore size distributions of UiO-67s (Figure 2.10C and D) also agreed with literature values. The peak observed at approximately 12 Å can be attributed to the octahedral pore, while the larger pore observed at 25 Å in UiO-67 comes from missing ligand defects causing multiple pores to merge into a singular larger defect based pore; this is what was expected based on the shape of the isotherm for UiO-67. This is the same observation made for the UiO-66s and should not be surprising given these MOFs are made via the same synthetic procedure.[56]

The pore size distributions for UiO-68-Me_4 and UiO-68-NH_2 are shown in Figure 2.10F. Unlike the other four MOFs discussed in this chapter, the errors associated with the pore size distribution fits for the nitrogen gas adsorption isotherms are notably worse for UiO-68-Me_4 and UiO-68-NH_2 (Figure 2.9 and Table 2.5). We are thus hesitant to overly interpret these pore size distributions. The pore size distributions of UiO-68-Me_4 exhibits two pores form the nitrogen gas adsorption isotherms. (11 Å and 17.5 Å in width). The amino-functionalized UiO-68-NH_2 illustrates only one dominant pore centred around 15 Å wide. This pore is consistent with the octahedral pore. Unlike UiO-66 and UiO-67, which have pore widths larger than their amino-functionalized counterparts, UiO-68-Me_4 has an octahedral pore width smaller than UiO-68-NH_2.

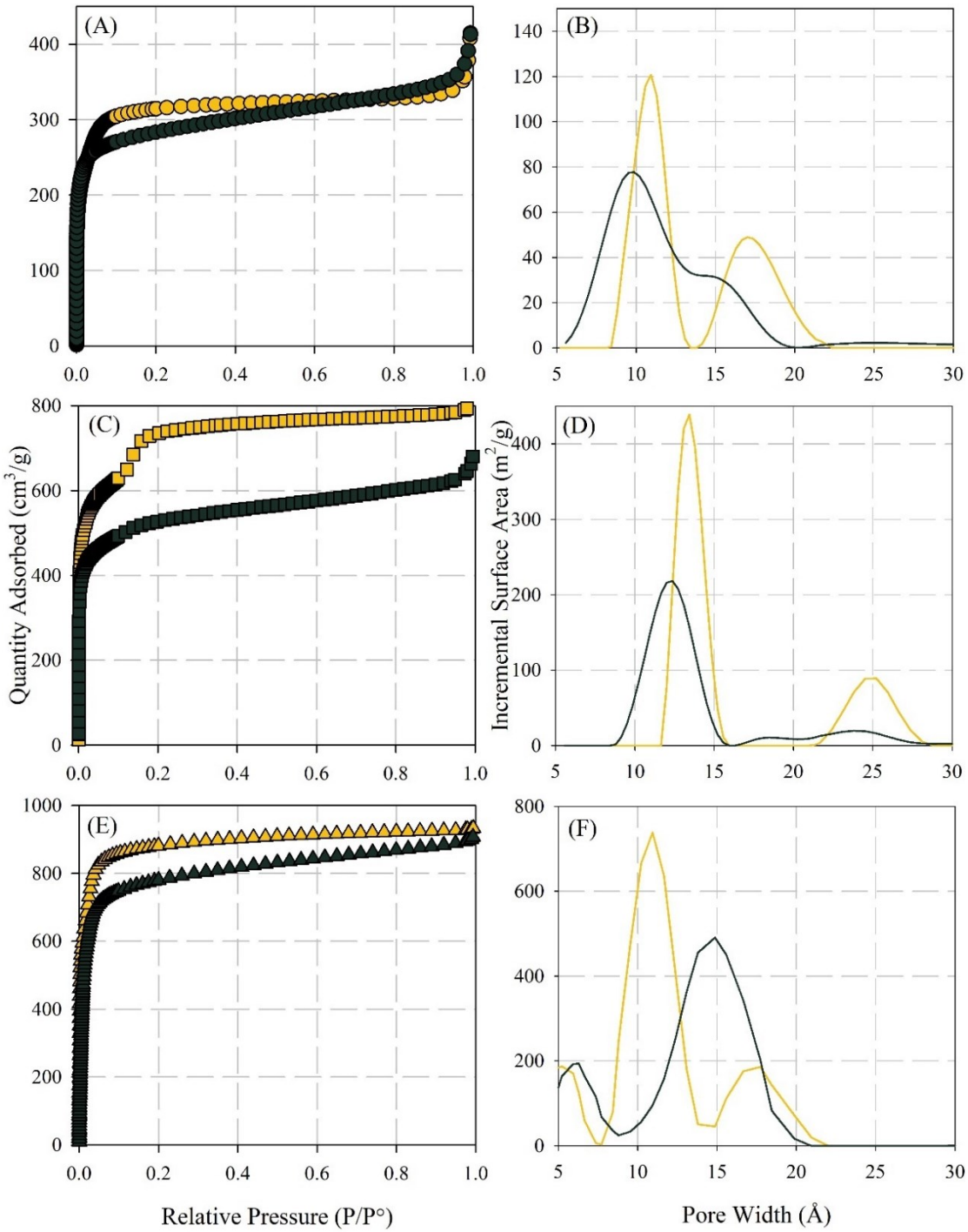

Figure 2.10: Nitrogen isotherms (left) and Pore size distributions (right) of UiO-66 (A) UiO-66-NH_2 (B) UiO-67 (C) UiO-67-NH_2 (D) UiO-68-Me_4 (E) and UiO-68-NH_2 (F). The yellow trace represents the unfunctionalized MOFs while the green trace represents the amine functionalized MOFs.

This is attributed to the larger steric profile of the four methyl groups in UiO-68-Me_4. These four methyl groups are facing the insides of the pores thereby reducing the amount of free volume inside of these pores. These values are within the range of the previously mentioned computational values.[82]

2.2.3.2.3 Argon Isotherms for Pore Size Distribution

For all the MOFs, we further probed the argon gas adsorption isotherms, measured at 77 K (Figure 2.11). Using a smaller probe gas could potentially allow for exploration into the micropore region. Using argon compared to nitrogen also eliminates any potential binding from the quadrupole in nitrogen gas. The analysis of argon gas adsorption is recommended to be done at 87 K. However, this is very difficult without access to liquid argon or a cryo-chiller. Since this is a common obstacle in the MOF community models for argon adsorption at 77 K have been developed. With these models, I had hoped to confirm the presence of a tetrahedral pore in the UiO-66's and UiO-67's.

Figure 2.11 illustrates both the argon adsorption curves and the pore size distribution for all six MOFs analyzed in this study. We can first observe that the isotherms are different from those obtained from the nitrogen isotherms at 77 K; this is especially true for UiO-66-NH_2 and UiO-67-NH_2. Furthermore, assessing the argon accessible BET surface areas (Table 2.6) we notice large discrepancies between these values and those calculated from the nitrogen isotherms. The differences in the calculated surface area can be attributed to the analysis temperature of 77 K being below the triple point of argon leading to complications in pore filling. With this potential complication in mind, I did not

want to over interpret these results.

Table 2.6: Nitrogen and argon gas accessible surface areas for UiO MOFs.

	Gas accessible BET Surface Areas (m^2/g)	
MOF	**Nitrogen**	**Argon**
UiO-66	1480	1400
UiO-66-NH_2	1100	690
UiO-67	2500	1734
UiO-67-NH_2	2000	1120
UiO-68-Me_4	3475	2770
UiO-68-NH_2	3350	5400

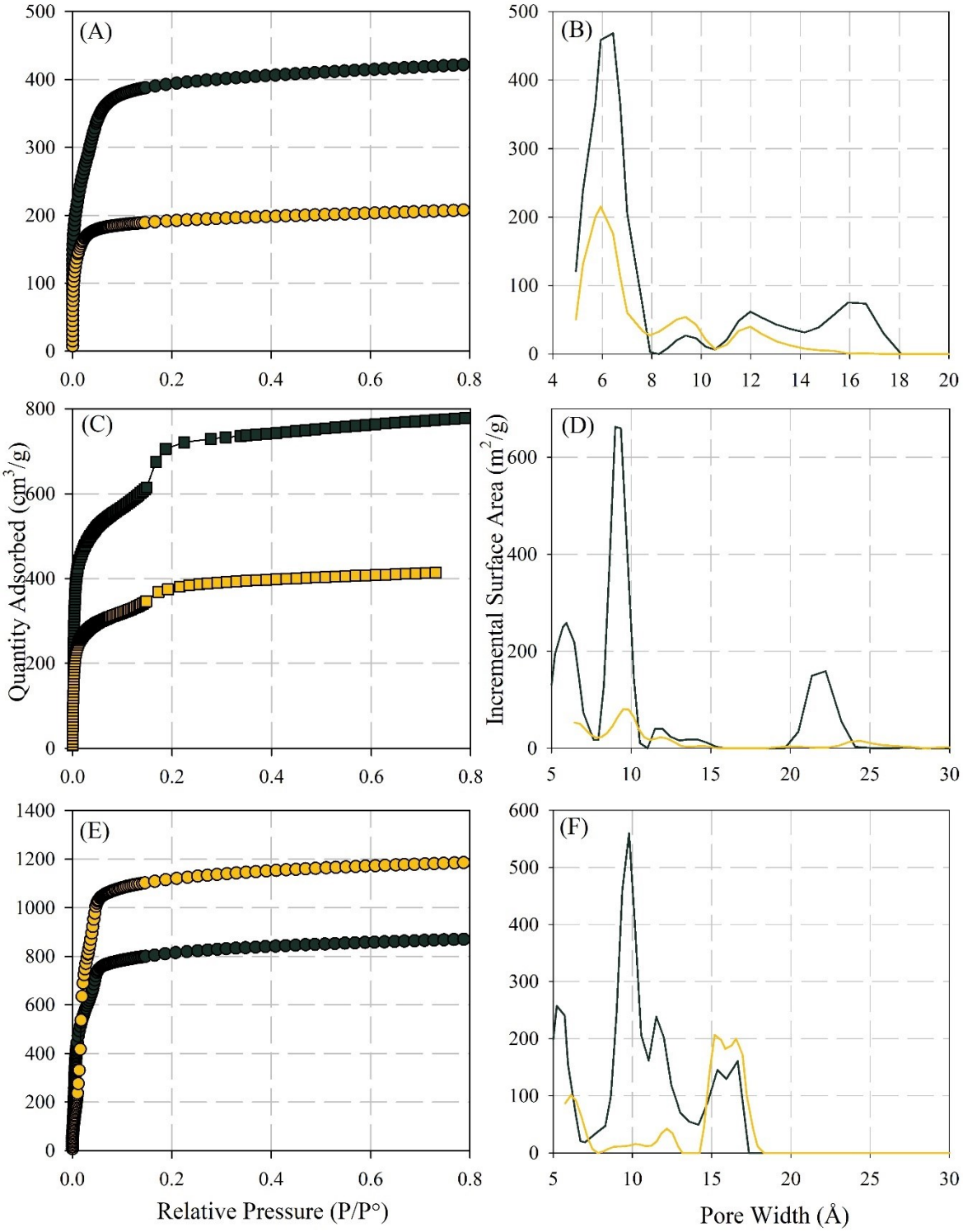

Figure 2.11: Argon isotherms (left) and pore size distributions (right) of UiO-66 (A) UiO-66-NH_2 (B) UiO-67 (C) UiO-67-NH_2 (D) UiO-68-Me_4 (E) and UiO-68-NH_2 (F).

Examining the pore size distributions of these MOFs (Figure 2.11,B,D,E) they appear to be much different to those calculated from the nitrogen gas adsorption. This discrepancy can be attributed to the analysis temperature of 77 K compared to the recommended 87 K for argon isotherms. The pore size distribution models that we have access to for argon gas at 77 K are not great representations of gas adsorbing to the surface of a MOF, leading to hesitation to say if the tetrahedral pore would be present or not.

While I had hoped that using argon gas adsorption would provide meaningful insight into the tetrahedral pores of UiO-66s and UiO-67s, this was not the case. Without access to liquid argon, or a cryo-chiller capable of maintaining 87 K there were no pore size models available to give meaningful results.

2.2.4 Water Adsorption Isotherms

With the pore characteristics determined, we turned our attention to water adsorption isotherms carried out at 295 K. Figure 2.12A illustrates the water adsorption isotherms for the unfunctionalized MOFs (UiO-66, UiO-67, and UiO-68-Me_4) while Figure 2.12B illustrates the water adsorption isotherms for the amino-functionalized MOFs (UiO-66-NH_2, UiO-67-NH_2, and UiO-68-NH_2); the data are summarized in Table 2.7 with the isotherms displayed in Figure 2.12. Figure 2.19 displays the water isotherm with the desorption curve present.

To further understand the interactions between the water vapour and the MOF we first need to determine the mechanism at which the water vapour is adsorbing. The three main mechanisms were outlined in Section 2.1. The first is capillary condensation.

Examining the desorption isotherms (Figure 2.12 clear points), none of the isotherms show a hysteresis loop consistent with capillary condensation.[141] The third method was the water cluster/droplet forming in the pore without contact to the pore walls due to the presence of extremely hydrophobic ligands. In the six MOFs that were examined, the ligands used are not extremely hydrophobic. An example of an extremely hydrophobic ligand would be the use of 2,2',3,3',5,5',6,6'-octafluoro[1,1'-biphenyl]-4,4'-dicarboxylate ligand on UiO-67. Since these MOFs do not fall into these two water adsorption mechanisms, they must fall into the water cluster growth mechanism. We hypothesize that the cluster growth occurs from the hydrophilic $Zr_6O_4(OH)_4^{12+}$ node.

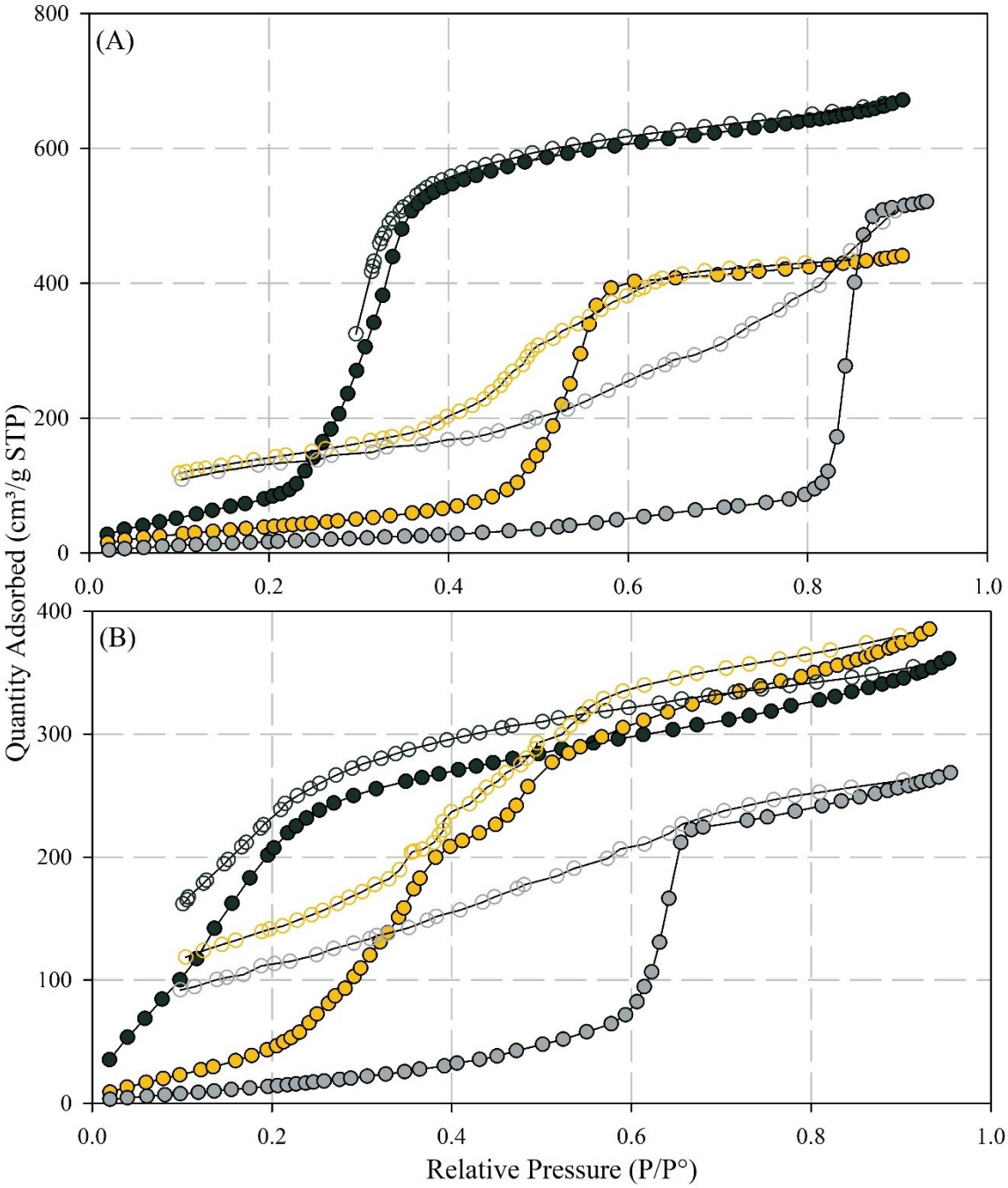

Figure 2.12: Water isotherms of (A) UiO-66 (green) UiO-67 (yellow) and UiO-68-Me_4 (grey) and (B) UiO-66-NH_2 (green) UiO-67-NH2 (yellow) and UiO-68-NH_2 (grey).

There are three main features associated with these isotherms: the pre pore-filling stage, pore-filling, and the post pore-filling adsorption capacity. The results obtained for

UiO-66 (Figure 2.12 top, green trace) are consistent with previously published results.[184,187–189] It should be noted that, in this work, UiO-66 shows greater water vapour uptake than previous literature values. This is due to the higher surface area than reported in other works. Previously published UiO-66 water adsorption shows a total uptake of 2.2 mol H_2O/m^2 surface area,[188] normalizing our uptake capacity we obtain 2.1 mol H_2O/m^2 surface area indicating that our uptakes are in agreement with previously published results.

Table 2.7: Water adsorption data of UiO MOFs.

MOF	Adsorption onset (RH)	P_{cond}/P_{sat} (RH)	Adsorption Step Width (RH)
UiO-66	22%	30.95 ± 0.08	18.4± 0.03
UiO-66-NH_2	0%[a]	11.94 ± 0.13	38.3 ± 0.04
UiO-67	47%	52.89 ± 0.08	14.4 ±0.03
UiO-67-NH_2	20%	32.4 ± 0.03 49.9 ± 0.05	24.8 ±0.07 14.0 ± 0.13
UiO-68-Me_4	75%	79.00 ± 0.03	7.63 ± 0.10
UiO-68-NH_2	36%	32.4 ± 0.03 49.9 ± 0.05	16.8 ± 0.07 23.1 ± 1.4

[a] No water cluster formation region is observed.

2.2.4.1 Pre Pore-Filling

It has been suggested that the pre pore-filling in MOFs is due to node-centred water cluster growth.[189] As illustrated in Figure 2.13, the pre pore-filling stage seems to stop at roughly the same uptake for all six MOFs. Normalizing the water adsorption isotherms for the water:zirconium ratio (Figure 2.13), we notice that all the MOFs adsorb approximately one water molecule per zirconium molecule just as pore filling starts. Where the MOFs defer is at the relative humidity that this ratio occurs. The smaller the pore, the lower the relative humidity. This suggests that the water cluster formation stage is dependent on the pore sizes and pore functionality of the MOFs. From an application point of view, these results indicate that as long as the relative humidity remains below the pore filling step, water can safely co-exist within the MOF and with other analytes in the pore. Extrapolating to larger MOFs, the relative humidity under which advantageous cooperative behaviour/adsorption can occur is expected to increase without risk.

Examining the amino-functionalized MOFs, the trend of the pre pore-filling occurring when the water/zirconium ratio is 1:1 is still observed. However, the point at which this ratio occurs is shifted to much lower relative humidity. UiO-66-NH_2 reaches this ratio as soon as water adsorption starts, where the unfunctionalized UiO-66 does not have this ratio until almost 20% relative humidity. UiO-67-NH_2 and UiO-68-NH_2 both obtain this ratio lower than the unfunctionalized parent material, 27% and 39% lower respectively. The pore sizes for the amino functionalized MOFs are comparable to the unfunctionalized versions, meaning the reason for the stark change in the pre pore-filling portion of the isotherms must come from the addition of the amino functionality.

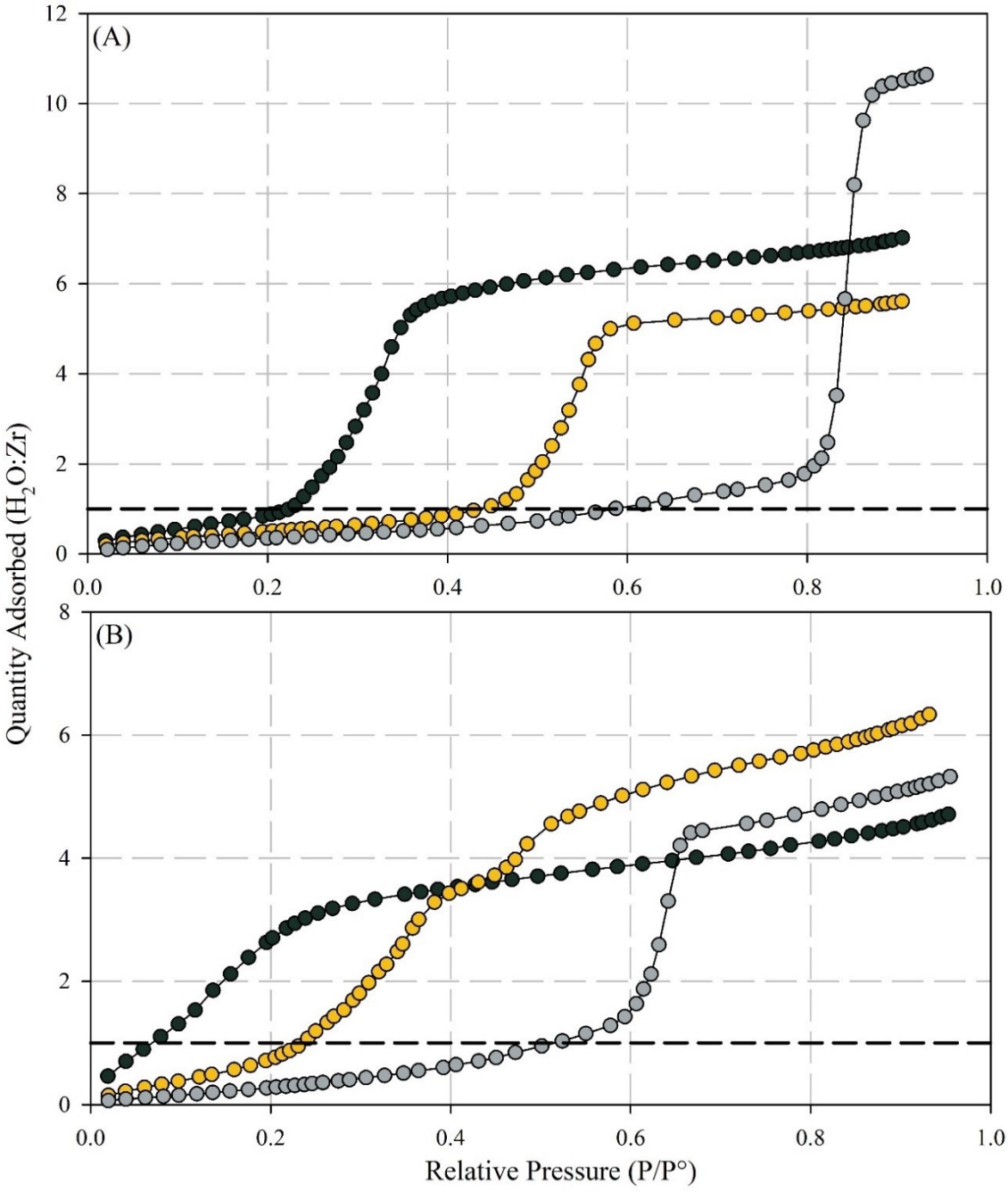

Figure 2.13: Water molecules adsorbed per zirconium molecule for (A) UiO-66 (green) UiO-67 (yellow) and UiO-68-Me_4 (grey) and (B) UiO-66-NH_2 (green) UiO-67 NH_2 (yellow) and UiO-68- NH_2 (grey) (bottom).

2.2.4.2 Pore Filling

With the pre pore-filling adsorption examined, we turned our attention to pore-filling of water in the pores. For the three unfunctionalized MOFs (UiO-66, UiO-67, and UiO-68-Me_4) and UiO-66-NH_2, the condensation stage occurs in one step. For UiO-67-NH_2, and UiO-68-NH_2, the condensation occurs in two steps. For UiO-67-NH_2, the second step is due to a small impurity of biphenyl-4,4'-dicarboxylate (BPDC) in the 2-aminobiphenyl-4,4'-dicarboxylate (NH_2-BPDC) ligand; this produces some amount of UiO-67 with UiO-67-NH_2. For UiO-68-NH_2 the relative contribution of the first step depends on the synthetic procedure (Appendix A).

To further ascertain how the pores are changing, we calculated the apparent contact angle of the water inside the pore via the Kelvin equation (Equation 2.2).

$$\ln\left(\frac{P_{cond}}{P_{sat}}\right) = \frac{2\mathrm{V}_m\gamma\cos\theta}{\mathrm{r}_k\mathrm{RT}} \qquad 2.2$$

The Kelvin equation relates the partial pressure (P_{cond}/P_{sat}) at which the centre of the adsorption step occurs (Table 2.6, column 3) to the adsorbate properties (the molar volume of liquid water, Vm; and the liquid/vapour surface tension, γ), the adsorbent properties (pore width, r_k), and the interactions between the adsorbent and the adsorbate (contact angle, θ; in this work we refer to this as the apparent contact angle). While the Kelvin equation is likely an oversimplification of the physical properties inside the MOF, the apparent contact angle facilitates a comparison between different MOFs.

The Kelvin equation is typically used for capillary condensation that is occurring inside the pore of a material, and while this may not be the mechanism at which the water droplet forms inside of the MOF it still can be used to calculate the droplet size. The contact angle will still hold true for the droplet of water as it does not matter how the droplet had formed. Due to the roughness of the surface of the material we were not able to directly measure the contact angle that has formed between the droplet and the surface of the MOF. Even if we were able to perform this measurement, it may not reflect the interaction of the water vapour and the inside of the pore.

Qualitatively, as the pore size of the MOF increases, the relative pressure associated with pore filling shifts to higher relative humidity. This is consistent with the Kelvin equation, which illustrates that the position of the condensation step (P_{cond}/P_{sat}) shifts to higher relative pressure as the pore width (r_k) increases. Comparing the amino-unfunctionalized MOFs with those of their respective amino-functionalized counterparts, a shift in P_{cond}/P_{sat} to lower relative humidity is observed. Given that the pairs of MOFs (e.g., UiO-66 vs. UiO-66-NH_2) have similar pore size distributions (r_k), the stark difference in water adsorption must be due to a change in the adsorbent adsorbate properties within the pore (θ); unsurprisingly, the amino-functionalized MOFs appear more hydrophilic (smaller apparent contact angle, θ) than their unfunctionalized counterparts.

Table 2.8: Calculated apparent contact angle and pore width of UiO MOFs.

MOF	Apparent Contact angle (°)	Cylindrical Pore Width ($2*r_k$) (Å)
UiO-66	54.0	10.8
UiO-66-NH_2	13.0	9.89
UiO-67	66.5	13.5
UiO-67-NH_2	49.5	12.4
UiO-68-Me_4	83.1	10.8
UiO-68-NH_2	71.0	14.7

Using the pore size distributions form nitrogen gas adsorption isotherms as a measure for the pore width in the Kelvin equation (Equation 2.2, $2*r_k$), and P_{cond}/P_{sat} from the water adsorption isotherms, a quantitative measure of the apparent contact angle (θ) can be calculated (Table 2.8). Assuming the surface of the framework was perfectly wettable ($\theta = 0°$), the pore width for UiO-66 would be 18.4 Å. This is considerably larger than the expected pore width from the nitrogen gas adsorption isotherm. This implies that the surface of UiO-66, and the larger MOFs, is not perfectly wettable. Adjusting the apparent contact angle (θ) until the calculated pore width ($2*r_k$ in Equation 2.2) matches the observed pore size distribution (Figure 2.6), the apparent contact angle for UiO-66 is estimated to be 54.0°. The more hydrophilic UiO-66-NH_2 has an apparent contact angle that is 41° lower (13.0°). As the ligand length increases, so does the apparent contact angle (Table 2.8). However, the effect of the amino substituent on the apparent contact angle decreases considerably with increasing pore width (17° decrease for UiO-67-NH_2 and a

12.1° decrease for UiO-68-NH_2). This suggests a cooperative effect when the amino substituents are in proximity of the node. This further suggests that the ligands are hydrophobic in the absence of any hydrogen bonding groups.

The position of the amino group in UiO-66-NH_2 is different than the position in UiO-67-NH_2 and UiO-68-NH_2. Figure 2.14 illustrates the difference in position of the amino-functionality in UiO-66-NH_2 and UiO-67-NH_2. While we know that the pore shape for these MOFs is octahedral and tetrahedral, the square 2D illustration is much simpler and the discussion remains the same.

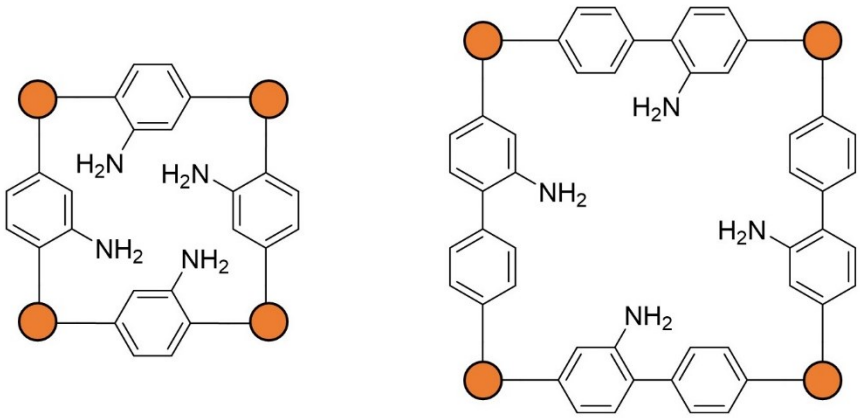

Figure 2.14: Position of -NH_2 functional group in UiO-66-NH_2 (left) and UiO-67-NH_2 (right).

UiO-66-NH_2 has the amino functional group pointing towards a cluster, where UiO-67-NH_2 and UiO-68-NH_2 always have the amino functional group pointing approximately into the centre of the pore and not near the cluster. We had originally hypothesized that the water cluster formation begins from the hydrophilic zirconium centre. Having the amino functional group that is capable of hydrogen bonding with water

molecules near the zirconium node creates a synergistic relationship that makes these materials more hydrophilic.

The apparent contact angle calculated for these MOFs are consistent with hydrophilic materials. With the exception of UiO-66-NH_2, which borders on a perfectly wettable ($\theta = 0°$ would yield a dominant pore with of 10.1 Å), the remaining MOFs have apparent contact angles comparable to common organic polymers (e.g., poly(vinyl acetate) = 80°, polymethyl methacrylate = 68°, polycarbonate = 88°).[190–192]

Given the relationship between pore aperture/functionality and the water adsorption isotherms, it is reasonable to conclude that the pore-filling step should mirror the pore size distribution. (Figure 2.15). It is no surprise that the pore is centred at the same size, as the pore size from the nitrogen isotherm was used in the Kelvin equation. The interesting result however is the breadth of the peak distribution determined from both nitrogen gas and water vapour adsorption are similar. Only large discrepancies are noticed in UiO-68-NH_2 and to a lesser extent UiO-68-Me_4; both of these MOFs had pore size distributions that had higher errors than would be ideal for determining the breadth and distribution of pore sizes. This illustrates that the breadth of the water adsorption step is related to the breadth of the pore size distribution within the MOF.

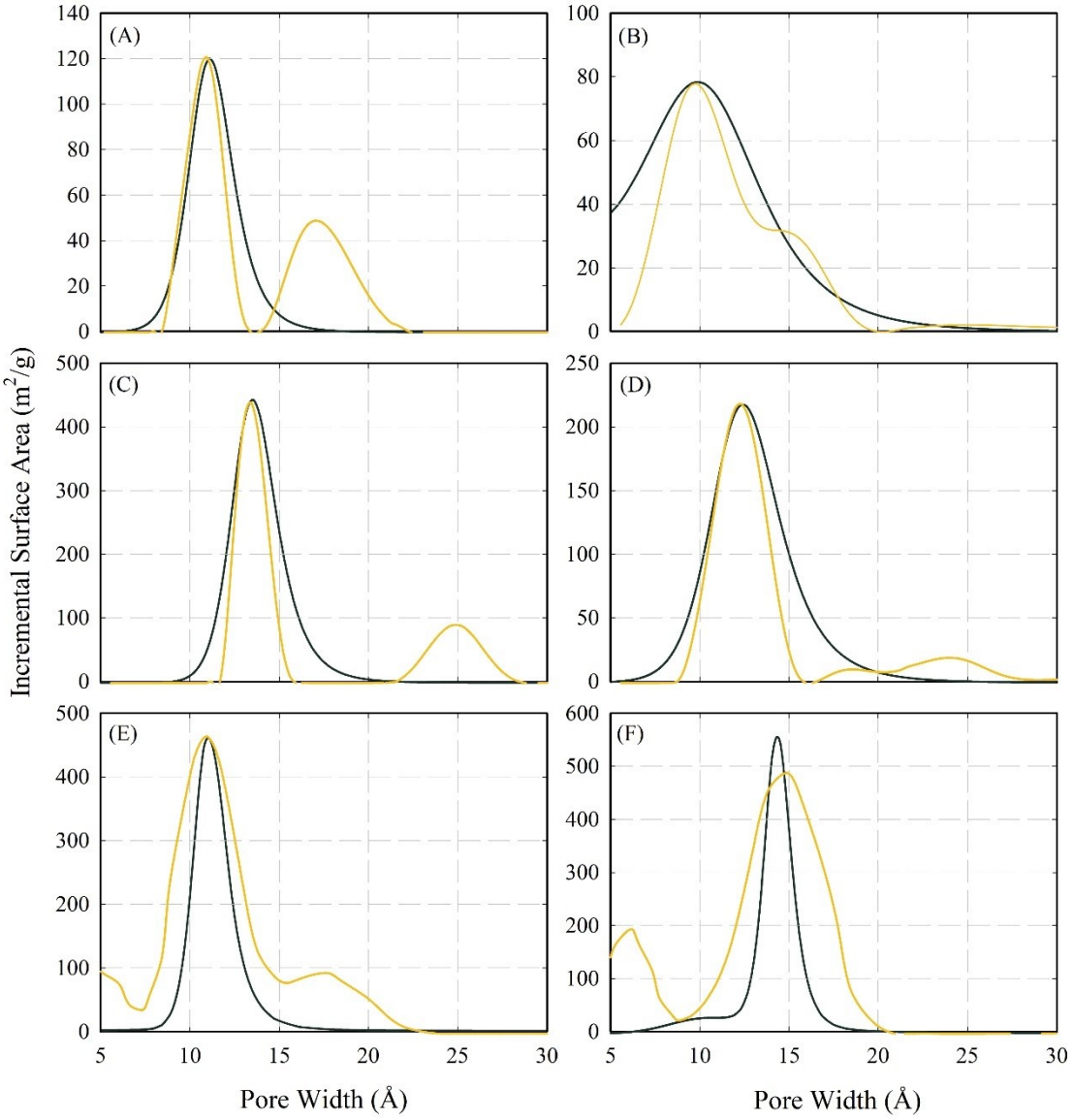

Figure 2.15: Comparison of the pore size distribution from nitrogen adsorption isotherms (yellow trace) and the determined pore size from the Kelvin equation simulated water vapour adsorption isotherms (green trace). (A) UiO-66, (B) UiO-66-NH_2, (C) UiO-67, (D) UiO-67-NH_2, (E) UiO-68, (F) UiO-68-NH_2.

To further look at the adsorption process, we extracted the isosteric enthalpies of adsorption for UiO-66 using variable temperature water vapour adsorption data. Water

isotherms were measured at 295, 305 and 315 K (Figure 2.16) in order to extract the enthalpies of adsorption.

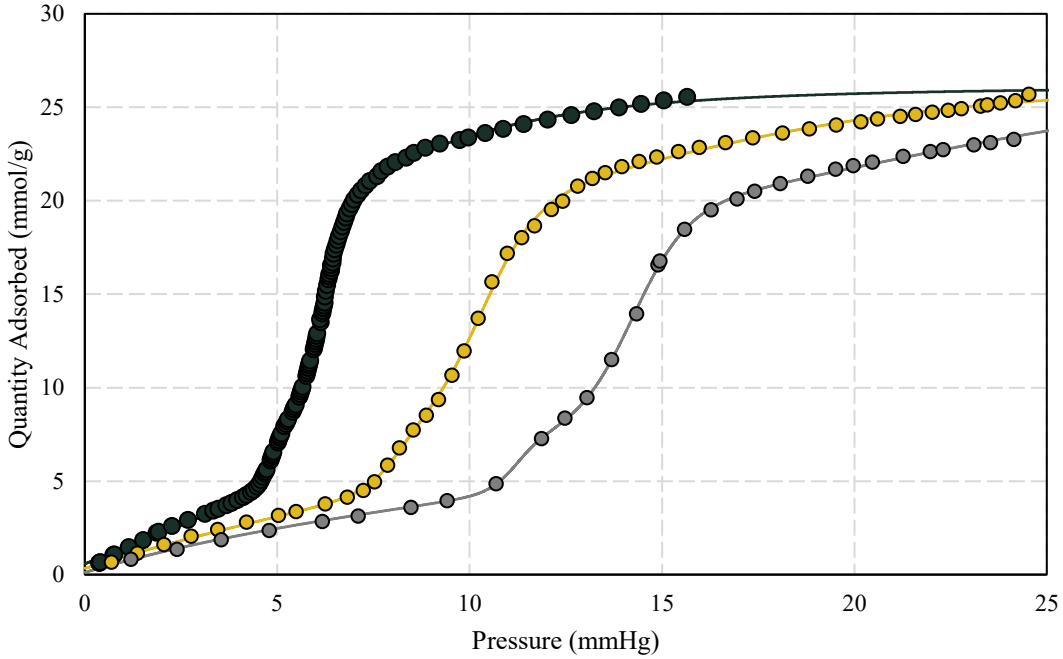

Figure 2.16: Water isotherms of UiO-66 measured at 295 K (green trace) 305 K (yellow trace) and 315 K (grey trace). Lines represent the fit of the isotherm using equation 2.3.

$$Q_{Adsorbed} = a(1 - e^{-b*P}) + Q_{max1}\frac{1}{1 + e^{\frac{-(P-P_{cond1})}{\beta 1}}} + Q_{max2}\frac{1}{1 + e^{\frac{-(P-P_{cond2})}{\beta 2}}} + Q_{max3}\frac{1}{1 + e^{\frac{-(P-P_{cond3})}{\beta 3}}} \quad 2.3$$

For isosteric heats of adsorption, a chemically meaningful equation is often the best choice (see Chapter 3), however, any equation that fits the data well and interpolates between the data points is sufficient to determine the isosteric heats of adsorption. Thus, for isosteric heats of adsorption, the three water isotherms were fit using the equation

above. The data was fit in the data plotting software SigmaPlot 13, using a global fit having Q_{max1}, Q_{max2}, and Q_{max3} being locked into being the same value for all three isotherms and fit to Equation 2.3. The above equation is not chemically meaningful, but it is a good model of the experimental data. In the equation $Q_{adsorbed}$ represents the quantity of gas adsorbed. The first term in the equation is used to fit the pre step portion of the isotherm. The remaining three terms represent three different adsorption sties (steps) in the isotherm. In each one of these steps, Q_{max} represents the maximum quantity adsorbed for the site. P is the pressure. P_{cond} represent the pressure of condensation at one of three different sites. β relates to the width of the step associated with the pore size at each site. The parameters a, Q_{max1}, Q_{max2}, and Q_{max3} were forced to being identical for all 3 temperatures; this is a chemically reasonable restraint that states the number of absorption sites at each site stay constant across the temperature range explored. Furthermore, this enabled us to better fit the low-pressure data necessary to determine the isosteric heats at low loadings. The isosteric heats at constant loading were numerically determined. This was done through the Clausius-Clapeyron equation, with the error for the isosteric heats of adsorption being determined from the error of the slope in the Clausius-Clapeyron equation.

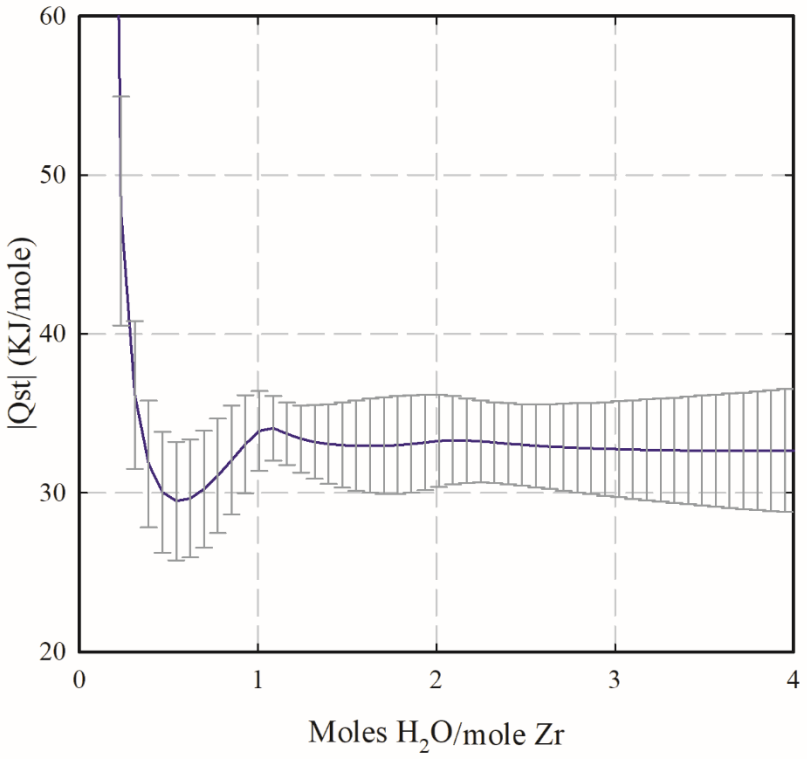

Figure 2.17: Isosteric heats of adsorption of water adsorbed onto UiO-66. The error bars are derived from the error associated with the slope of the fit to the Clausius Clapeyron equation.

As shown in Figure 2.17 for water adsorption leading up to 1 water:zirconium, the enthalpies are quite high owing to the formation of the first node-water interaction. Subsequently, the enthalpies reflect the enthalpy of vaporization for water (−44 kJ/mol). Having a high enthalpy of adsorption for the first interaction of node-water interaction supports our hypothesis that before any water cluster growth can occur the ratio of water to zirconium must be 1:1.

2.2.4.3 Water Adsorption capacity

In comparison to the nitrogen gas adsorption isotherms, the water adsorption capacity for all the MOFs appears more similar than different. Normalizing the water

adsorption isotherms to water per zirconium (Figure 2.13), an interesting observation emerges. The water adsorption isotherms seem to only adsorb 5 (UiO-66-NH_2 and UiO-67, UiO-68-NH_2), 8 (UiO-66, UiO-67-NH_2), or 10 (UiO-68-Me_4) water molecules per zirconium. UiO-66 and UiO-66-NH_2 have the smallest pore sizes, as determined by the nitrogen adsorption isotherms, and they adsorb 8 and 5 molecules of water per zirconium respectively. As the ligand size is expanded, it would be expected that the number of water molecules per zirconium centre should increase. However, UiO-67-NH_2 only adsorbed 8 molecules of water per zirconium, the same as UiO-66 which has much smaller pores. Similarly, UiO-67 adsorbed 5 molecules of water per zirconium, the same as UiO-66-NH_2 which again, has much smaller pores. We hypothesized that UiO-67-NH_2 could adsorb more water per zirconium centre that unfunctionalized UiO-67 due to the presence of more defects (one missing ligand versus two, Table 2.1), along with the addition of the amino functional group. With more missing ligands, there are more open zirconium sites for the water vapour to adsorb. Moving into UiO-68-Me_4 and UiO-68-NH_2 it is observed that UiO-68-Me_4 has the largest water vapour adsorption per zirconium molecule at ten, where the amino version only showed five. While UiO-68-Me_4 adsorbed the most, it was only two water molecules more than UiO-66, which had a pore size of almost half of those in UiO-68-Me_4.

These observations lead us to believe that if the ligand is extended beyond one phenylene group (UiO-66/UiO-66-NH_2), then the water molecules cluster around the node with neighbouring clusters not able to connect with each other (Figure 2.18). It is unclear from this work if water clusters around each node, like a shell, or around each zirconium

(Figure 2.18). We hypothesize that this is around each zirconium rather than each node, but computational work is necessary to confirm this. Of particular note is that there is considerable space remaining in the larger MOFs for other gases to fill the unused volume and interact with the node/water cluster.

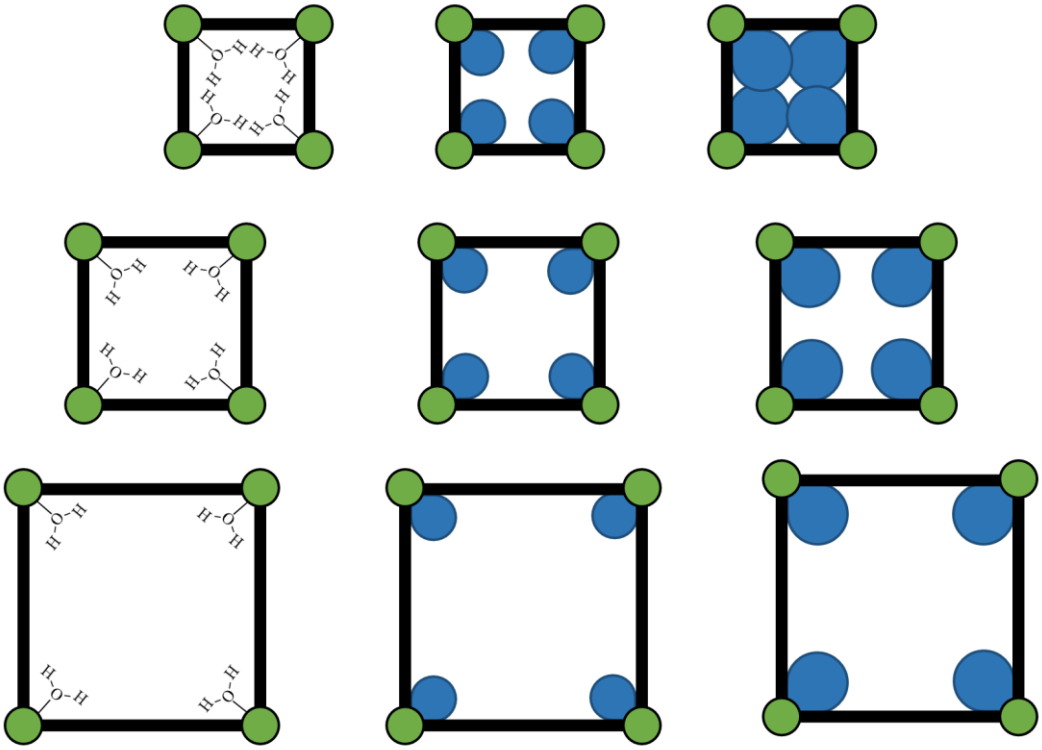

Figure 2.18: Water cluster growth from the cluster of UiO-66 (top) UiO-67 (middle) and UiO-68-Me_4 as the relative humidity increases (left to right).

The presence of this excess space makes these materials ideal for separation of water from different gas mixtures such as carbon dioxide or methane that may contain traces of water vapour. It also provides an avenue of exploration for mixed gas adsorption experiments. If water vapour is present in the MOF, does it make it more favorable or more difficult to adsorb other gases such as carbon dioxide or nitrogen.

2.2.5 Water Swing Experiments

The recyclability of these materials was also investigated by performing water isotherms that consisted of an adsorption to a given point followed by a desorption curve back down to a lower humidity. Analyzing how closely the adsorption curve follows the desorption curve will give us insight on how well water vapour desorbs from the material. If there are any detrimental effects from the desorption of water, then they would also become apparent in these cycling studies. Of the desorption isotherms, it appears that UiO-66 displays a small amount of hysteresis, which indicates that the desorption of the water vapour is relatively easy. This is consistent with the water cluster growth mechanism discussed in Section 2.1. The hysteresis observed for UiO-66 is not the typical hysteresis that MOF chemists are used to seeing. In typical hysteresis, there is a difference in the desorption and adsorption isotherms, with the desorption isotherm found further to the left of the adsorption isotherm (Figure 2.2B). In the case of the water isotherms for UiO-66 the hysteresis is observed in the vertical direction, where the desorption curve appears higher than the adsorption curve Figure 2.2C.

The UiO-67s and UiO-68s do not show the same desorption trace, in these isotherms the hysteresis is more difficult to interpret (Figure 2.19). This can be interpreted in a few different ways. The first being that there the initial binding of water is very strong, and the desorption requires more energy to remove thereby causing the hysteresis. The second interpretation is that there is a structural change in the MOF. For example, the MOF could have decomposed after being exposed to water vapour and the water vapour becomes chemically bonded to the resulting decomposition material. While the desorption trace on

the isotherm can provide insight that one of these scenarios occurred, it cannot tell which one occurred. To determine this, we performed pressure swing experiments. If the adsorption and desorption curves are reproducible, then it would indicate that the hysteresis is due to the water vapour not being completely desorbed under reduced pressure. If the desorption and adsorption curves are not reproducible, and the desorption curves end at drastically different points after being exposed to higher relative humidity, then it could indicate a structural change in the material.

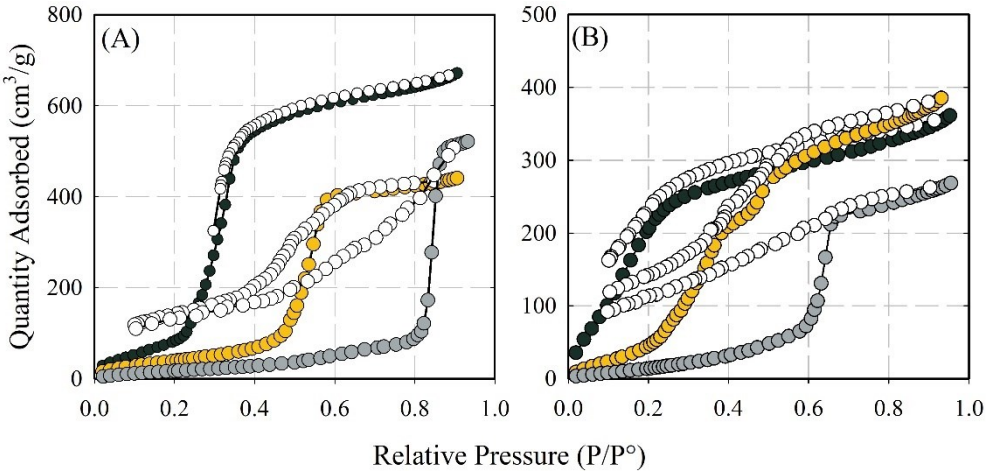

Figure 2.19: Water adsorption (color trace)/desorption (white trace) isotherms of (A) UiO-66 (green), UiO-67 (yellow), UiO-68-Me_4 (grey), (B) UiO-66-NH_2 (green), UiO-67-NH_2 (yellow), UiO-68-NH_2 (grey).

The first MOF that was investigated was UiO-66, the sample was first exposed to approximately 20% relative humidity, followed by a desorption back to approximately 15% relative humidity, followed by an adsorption to approximately 30% relative humidity, and then desorption back to 15% relative humidity. This was repeated until the sample reached approximately 90% relative humidity. The collected isotherms are shown in Figure 2.20. Figure 2.20A displays the low-pressure water vapour adsorption. In these experiments, it is observed that the desorption trace follows the adsorption trace quite well,

desorbing to roughly the same point. Desorbing from approximately 28% relative humidity (white trace with blue outline Figure 2.20A) shows a very small amount of hysteresis. This is very little compared to the amount present in the UiO-67s and UiO-68s (see below). This indicates that the process is reversible, and that the hysteresis is due to the water vapour having a strong interaction with the MOF and not being able to completely desorb at the same pressure the adsorption occurred at; lower pressure and potentially heat would be required to remove any residual water. This data also indicates that the material remains intact. When these experiments are extended to higher relative humidity (Figure 2.20B), including relative humidity values above the pore-filling step, the same trend is observed. For UiO-66 only a very small amount of hysteresis observed after each additional run, confirming that the material has remained intact when the water is desorbed under vacuum.

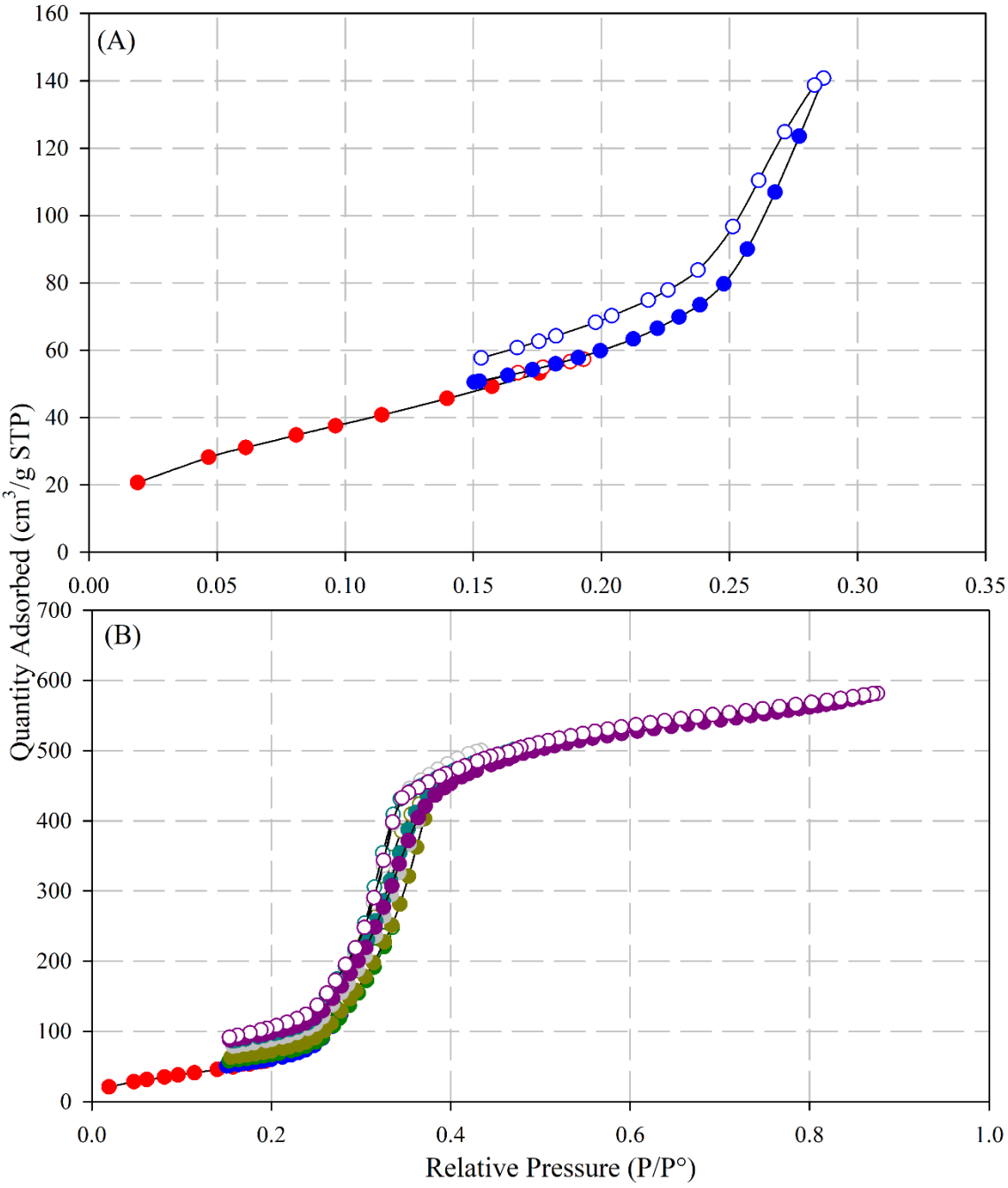

Figure 2.20: Water swing isotherms of UiO-66 at low pressure (A) and full relative humidity range (B). The solid makers indicate the adsorption curves while the unfilled markers represent the desorption curves. Each colour represents a new adsorption/desorption swing.

Preforming the same series of experiments on UiO-67 can provide insight into the stability and water adsorption and desorption process. In our hands and in the literature, it has been observed that UiO-67 is more sensitive in the presence of water compared to UiO-66.[89,93,193] With this sensitivity in mind, I hypothesized that several cycles would be very detrimental to the MOF.

Examining the low-pressure water isotherms shown in Figure 2.21A it is evident that the adsorption and desorption processes are reversable, especially in the low-pressure region. Hysteresis is not present until the MOF is exposed to 55% relative humidity and then desorbed. 55% relative humidity is about half of the way up the large adsorption step that is present in the water isotherm. The desorption trace (white with green outline; Figure 2.21B) ended just below 100 cm^3/g. This is the same value that is observed from the desorption trace in Figure 2.19A. This suggests that the hysteresis observed may be due to strong MOF-water interactions that would require even lower pressures, or potentially heat, to fully remove the adsorbed water. The observed hysteresis was not necessarily a change in the structure of the material. To determine if there was a structural change further cycling experiments would be required.

Once the MOF is brought to saturation (Figure 2.21B, green trace) there were some very different results. The desorption curve (Figure 2.21B, white trace with green outline) did not follow the adsorption closely and displayed some hysteresis indicating some water remains adsorbed. Furthermore, each time UiO-67 was dosed to a higher relative humidity (Figure 2.21B, maroon, grey, and blue trace) the original curvature and saturation that was observed in a single run (Figure 2.19A) is no longer observed. This indicates that there was

a structural change in the material after exposure to water vapour at these relative humidities.

In our hands after a single water isotherm of UiO-67 from 0% relative humidity to 90% relative humidity desorption down to 10% displayed a complete loss of surface area indicating that decomposition of the material occurs. This agrees with literature observations as mentioned in Section 1.2.2. The activation from water via heat and vacuum can be problematic. Hupp, Farah and coworkers have reported that placing UiO-67 in liquid water for 24 hours does not alter the powder X-ray diffractogram.[88] However, once the sample has been exposed to liquid water and activated under heat and vacuum a loss in crystallinity and porosity is observed. The authors attribute this to the capillary forces associated with the removal of water. It has also been demonstrated that washing the water-soaked MOF with organic solvents (acetone) to remove any water from the pores and heating the MOF under vacuum retains both the surface area and crystallinity. The data presented here do not completely agree with the results of Hupp, Farah and coworkers. In the experiments that were performed UiO-67 was exposed to a slightly different environment. I hypothesize that the decomposition of UiO-67 must occur under vapour-based conditions. Our data indicates that UiO-67 decomposes when exposed to humidity conditions above the large uptake of water vapour (54% and 75% relative humidity) regardless of the activation procedure.

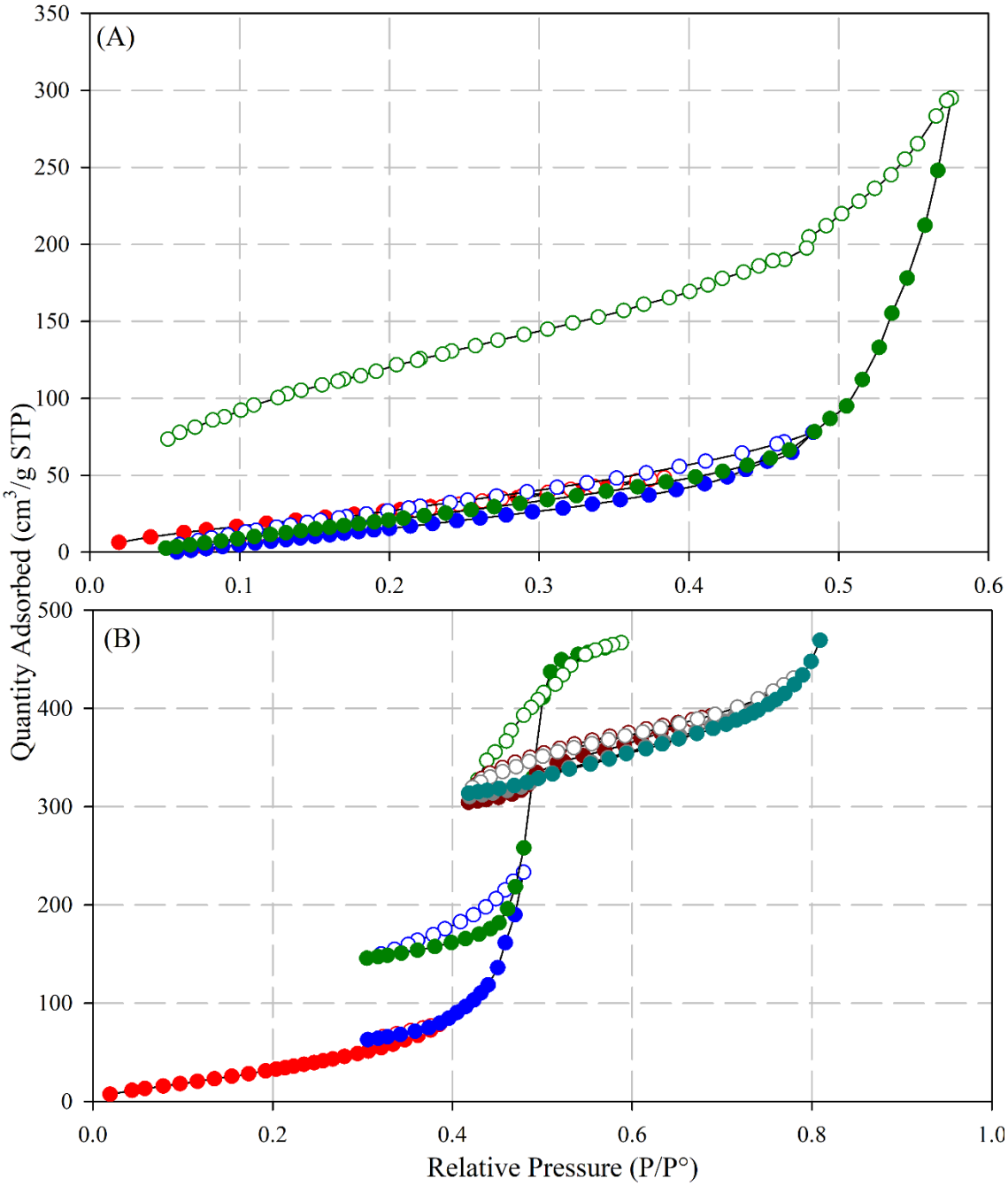

Figure 2.21: Water swing isotherms for UiO-67. (A) showing the low-pressure adsorption. (B) showing adsoprion and desorption acorss the full relative humidity range. Each colour represents a new adsorption/desorption swing.

These same experiments were performed for UiO-68-Me_4 (Figure 2.22), and similar results were observed for that of UiO-66 and UiO-67. Below the step in the isotherm, the

adsorption and desorption curves are very reversible. Cycling below the large upswing in relative humidity, there is very little difference between the adsorption and desorption curves; there is no notable hysteresis. Once the MOF is exposed to relative humidity above the large upswing in the water isotherm (ca. 75% RH), then hysteresis is observed. As the MOF is cycled from saturation back down to 20% relative humidity, the ending point of the desorption curve is always around the same point, roughly 100-150 cm^3/g (2 water molecules per zirconium), and the hysteresis curves appear to be similar when exposed to higher relative humidity. It is of particular note that the higher the relative humidity that the sample is exposed to leads to a desorption curve that ends at a higher quantity adsorbed. This could be due to strong interactions between the initially adsorbed water molecules and incoming water molecules that only occur at higher relative humidity. This provides insight that the hysteresis is due to the removal of the water vapour and the hysteresis loop may completely close with lower pressure. With the hysteresis curves being so consistent, it is a strong indicator that the material is not as sensitive to decomposition as observed with UiO-67.

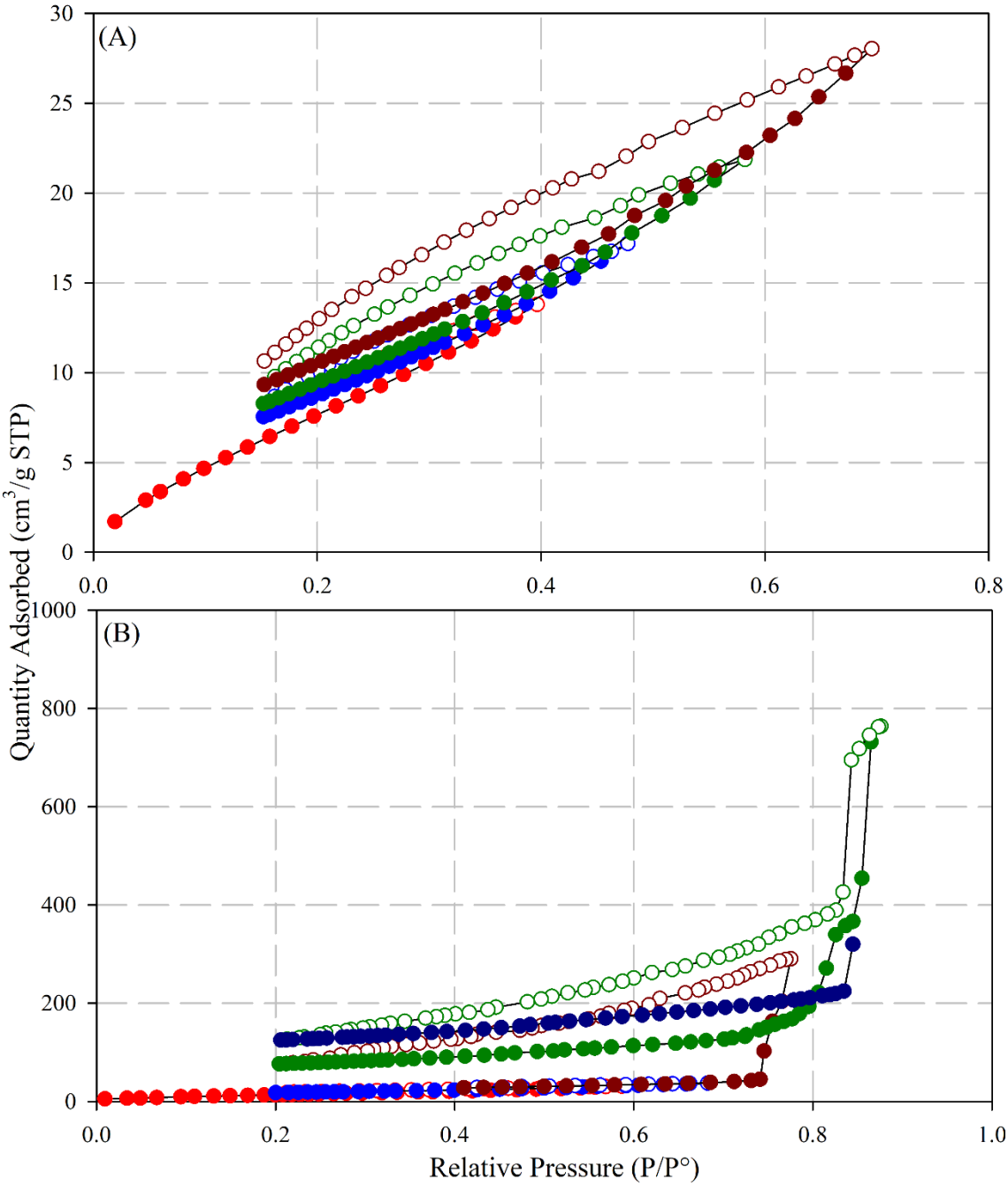

Figure 2.22: Water swing isotherms for UiO-68. (A) showing the low-pressure adsorption. (B) showing adsorption and desorption across the full relative humidity range. Each colour represents a new adsorption/desorption swing.

I hypothesize that the increased stability of UiO-68-Me_4 comes from the presence of the four methyl groups on the ligand. The addition of these methyl groups restricts the

movement of the aromatic rings, making it behave similar to UiO-66. UiO-67 on the other hand has free rotation between the two aromatic rings. If a water molecule was to cleave the zirconium-oxygen bond, then the biphenyl ligand may rotate to a lower energy confirmation and the free carboxylate may not be close enough to the cluster to re-attach. UiO-66 only has one aromatic ring, and UiO-68-Me_4 loses a lot of that dihedral rotation due to the sterics of the methyl groups. If a ligand was to detach from these MOFs it has a better chance to reattach to the cluster.

2.2.6 Long Term Water Vapour Studies

The obtained data illustrates that water vapour clusters around the node. To ascertain how this affects the MOF, we examined the nitrogen-accessible BET surface area of the unfunctionalized MOFs after expose to water vapour at relative humidity below the pore filling step. Humidity chambers of 25%, 54%, and 75% were made using potassium acetate, magnesium nitrate, and sodium chloride saturated solutions in water. As has been previously demonstrated, and verified herein, when UiO-66 is exposed to 75% humidity (above the relative humidity required for saturation) for 100 days, the nitrogen-accessible BET surface area remained unchanged.[194]

UiO-67 on the other hand did not show the same long-term stability that we observed in UiO-66. After as little as one day at 75% relative humidity there is almost a complete loss of nitrogen-accessible surface area (Figure 2.23 green trace). 75% relative humidity is above the threshold for saturation of UiO-67 making it no surprise that the MOF had decomposed.[88–90,93]

When exposed to 54% relative humidity, an environment where there is still adsorption of water (greater than one water per zirconium) but not saturation of water, there was still complete loss of nitrogen accessible surface area after as little as four days (Figure 2.23 yellow trace). This result gave an interesting insight into why the MOF may be decomposing. If activation from water was the only issue, then we should not see a larger loss in surface area as time progressed. With the result observed for the 54% relative humidity exposure it indicates that the presence of water vapour, will cause the decomposition of the MOF, not necessarily the activation from water alone. The decomposition happens faster at a relative humidity closer to that required for saturation, which is why the decomposition happened faster when exposed to 75% relative humidity. At 25% relative humidity exposure, an environment much lower than the uptake of one water molecule per zirconium molecule there was no significant change in the nitrogen accessible surface area even after 100 days, indicating there was not enough water vapour present to cause the decomposition of the MOF.

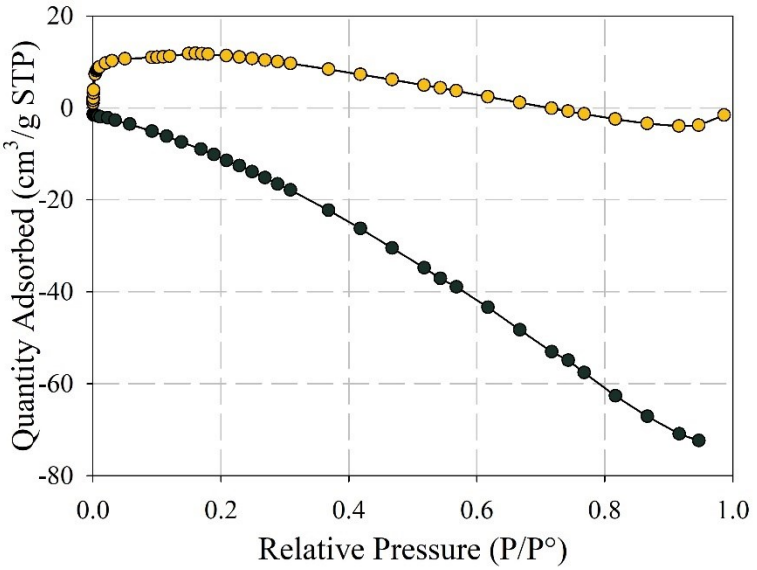

Figure 2.23: Nitrogen Isotherms of UiO-67 measured after 1 day at 75% relative humidity (green trace) and four days at 54% relative humidity (yellow trace).

With regards to UiO-68-Me_4, at over 100 days at 54% RH there was no significant loss in the surface area. Agreeing with the observations made for UiO-67 suggesting that exposure to humidity below the large upswing in water adsorption had no detrimental effect to the MOF.

Furthermore, the powder X-ray diffractograms were measured of all six MOFs after a water isotherm just below the large upswing in water adsorption was measured. The diffractograms are shown in Figure 2.24 A and for each of the UiO-66s there is no evidence of deviation from the sample prior to humidity exposure; all peaks remain consistent with the fresh MOF and the simulated diffraction pattern.

Since UiO-67 lost all porosity when exposed to 75% and 54% relative humidity there was no new information to be learned measuring the diffractograms of these samples. It was more insightful to expose them to humidity below the large upswing in adsorption

to determine if the crystallinity is retained. An adsorption and desorption isotherm were preformed up to 40% relative humidity. From Figure 2.24B it is clear that the diffractograms of UiO-67 and UiO-67-NH_2 remain unchanged indicating the material remains crystalline after exposure to humidity below that of the large upswing in adsorption. UiO-67-NH_2 (Figure 2.24 B) did show some peak broadening at 3-5° 2θ and a loss of most peaks above 10° 2θ. 40% relative humidity is part way up the adsorption curve for UiO-67-NH_2, this broadening and loss of peaks may be due to slight decomposition of the MOF.

Examining the diffractograms from the UiO-68s we see that the materials remain crystalline after being exposed to a relative humidity of approximately 70%. There is no observed peak broadening or missing peaks. Just like UiO-67, exposing the material to below the pore filling step there is no observed loss in crystallinity, this once again illustrates that at partial pressures below the pore-filling stage, these MOFs are stable for prolonged periods of time.

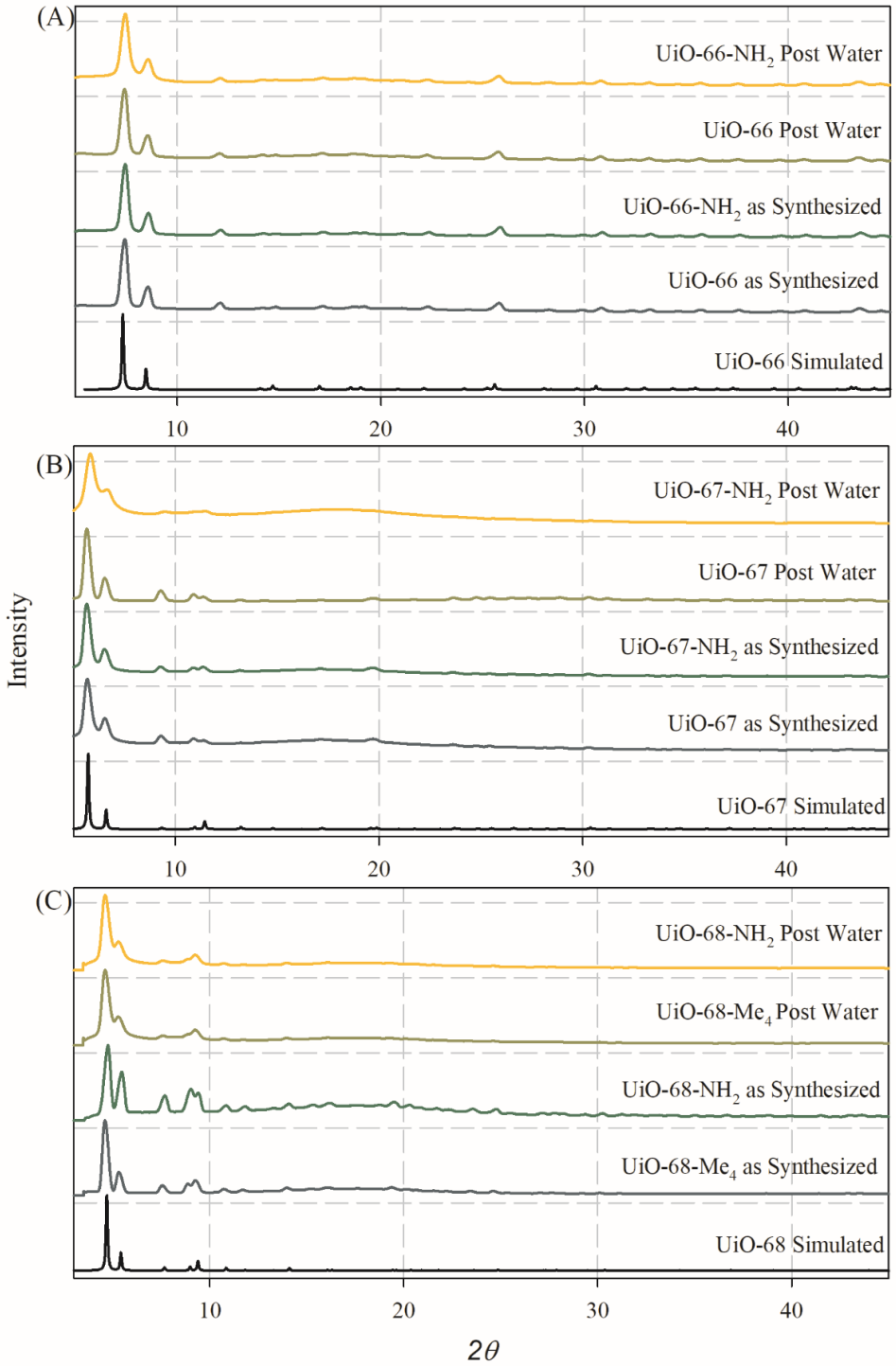

Figure 2.24: Powder X-ray diffractograms for UiO-66 (A) UiO-67 (B) UiO-68 (C). i) simulated spectrum, ii) unfunctionalized pre-water exposure, iii) unfunctionalized post-water exposure, iv) amino functionalized pre-water exposure and v) amino functionalized post water exposure.

2.3 Conclusions

Water adsorption onto porous materials shows great promise for removal of water vapour from the air. Simultaneously, for other applications, water vapour adsorption may inhibit or enhance chemistry inside a porous material. The work presented herein presents an in-depth look at zirconium-based MOFs by analyzing the water adsorption isotherms using nitrogen adsorption isotherms as a point of comparison.

Extending our results toward the applications of zirconium-based MOFs, there are three conclusions that can be drawn from our work. Firstly, at relative pressures below the occurrence of pore-filling, water reversibly adsorbs approximately one water molecule per zirconium centre. This indicates that the porous structure is still capable of adsorbing other gases and may even offer advantageous hydrogen bonding to assist in adsorption, catalysis, and/or chemical reactivity. Furthermore, at these partial pressures, we observed no detrimental effect on these MOFs. Secondly, the hydrophobicity of the pore increases as the pore width increases. These results indicate that zirconium-based MOFs as large or larger than UiO-68 are safe from interference or structural changes at most humidity levels. This is ideal for MOF applications in high humidity environments where we expect water to safely co-exist with the MOF. Lastly, with consideration to HVAC systems, UiO-66 is an ideal candidate for passive HVAC systems. The onset of water adsorption is centred around the ideal indoor air conditions.

2.4 Experimental

2.4.1 General Methods

All reagents were purchased from chemical suppliers and used without further purification. ^{1}H-NMR was collected on a Bruker 300 or 500 Avance spectrometer, with the instrument used specified in the description for each synthesis procedure.

2.4.2 Synthesis

2′-amino-1,1′:4,1′′-terphenyl-4,4′′-dicarboxylic acid (NH_2-H_2TPDC)

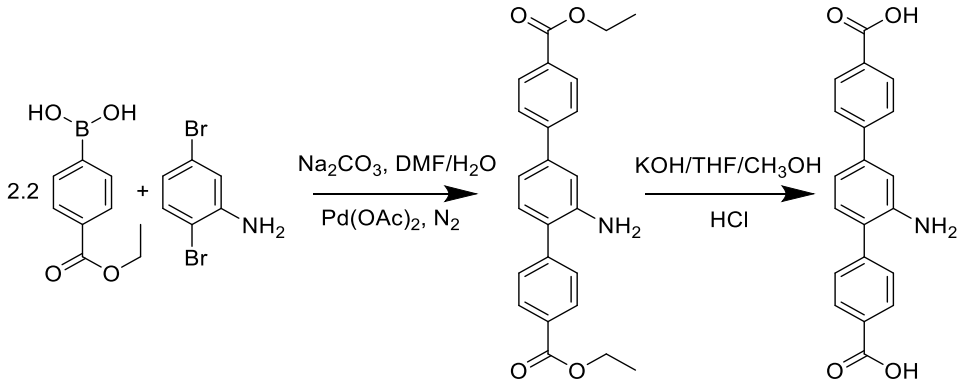

Scheme 2.1: Synthesis of 2'-amino-1,1:4,1"-terphenyl-4,4"-dicarboxylic acid.

The first step in the synthesis of NH_2-H_2TPDC was a Suzuki coupling to form the terphenyl ligand with an ethyl protected carboxylic acid, diethyl-2'-amino-1,1:4,1"-terphenyl-4,4"-dicarboxylate (Et-NH_2-TPDC) Similar to literature methods,[195] 94 mL of *N,N*-dimethylformamide (DMF) and 80 mL of deionized water were combined in a 3-neck 500 mL round bottom flask and sparged with nitrogen gas while stirring. After thirty minutes 3.7116 g (14.913 mmol) of 2,5-dibromoanaline, 8.1487 g (45.255 mmol) of 4-(ethoxycarbonyl)phenylboronic acid, 5.600 g (82.341 mmol)

of sodium bicarbonate, and 0.1200 g (0.5118 mmol, 3.4 mol%) of palladium acetate was added to the flask. The contents were heated at 363 K for sixteen hours under a flow of nitrogen gas. Subsequently, the reaction was cooled to room temperature and the grey precipitate was isolated by suction filtration. The precipitate was dissolved in ethyl acetate and washed with water to remove any salts from the organic fraction. The layers were separated, and the organic layer was dried over magnesium sulfate. The solvent was removed under heat and reduced pressure to yield a brown solid of Et-NH_2-TPDC with a 52% yield (3.0179 g, 7.755 mmol). The ^{1}H-NMR spectrum was collected on a Bruker 500 MHz Avance spectrometer. The data were consistent with literature values.[195] ^{1}H-NMR (500 MHz, Chloroform-*d*): δ 8.10 (d, *J* = 8.2, 2H), 8.07 (d, *J* = 8.2, 2H), 7.63 (d, *J* = 8.2 Hz, 2H), 7.55 (d, *J* = 8.2 Hz, 2H), 7.19 (d, *J* = 7.8 Hz, 1H), 7.06 (dd, *J* = 7.8, 1.8 Hz, 1H), 6.98 (d, *J* = 1.8 Hz, 1H), 4.37 (q, *J* = 7.2 Hz, 2H), 4.36 (q, *J* = 7.2 Hz, 2H), 1.38 (t, *J* = 7.2 Hz, 3H), 1.37 (t, *J* = 7.2 Hz, 3H).

Synthesis of 2′-amino-1,1′:4,1″-terphenyl-4,4″-dicarboxylic acid (NH_2-H_2TPDC)

To deprotect Et-NH_2-H_2TPDC, the brown solid was added to a 250 mL round bottom flask containing 65 mL of tetrahydrofuran (THF). The flask was heated at 338 K. Once the temperature was reached, 32 mL of 5.5 mol/L potassium hydroxide (KOH) in methanol was added and allowed to reflux overnight. The reaction was then removed from heat and cooled to room temperature. The precipitate was isolated by suction filtration, and subsequently suspended in 65 mL of THF. 3.3 mL of trifluoracetic acid was added to the suspension and the suspension was stirred for two hours. The yellow product was isolated by suction filtration and washed with deionized water (3 × 100 mL) followed by methanol

(3 × 20 mL). The ^{1}H-NMR spectrum was collected on a Bruker 300 MHz Avance III spectrometer. The spectrum for NH_2-H_2TPDC was consistent with the literature.[196] This reaction was quantitative. ^{1}H-NMR (300 MHz, DMSO-d_6): δ 8.02 (d, J = 8.2 Hz, 4H), 7.74 (d, J = 8.2 Hz, 2H), 7.61 (d, J = 8.2 Hz, 2H), 7.17 (d, J = 7.9 Hz, 1H), 7.16 (d, J = 1.8 Hz, 1H), 7.02 (dd, J = 7.9, 1.8 Hz, 1H).[195]

2',3',5',6'-Tetramethyl-[1,1'1:4',1''-terphenyl]-4,4''-dicarboxylic acid (Me$_4$-H$_2$TPDC)

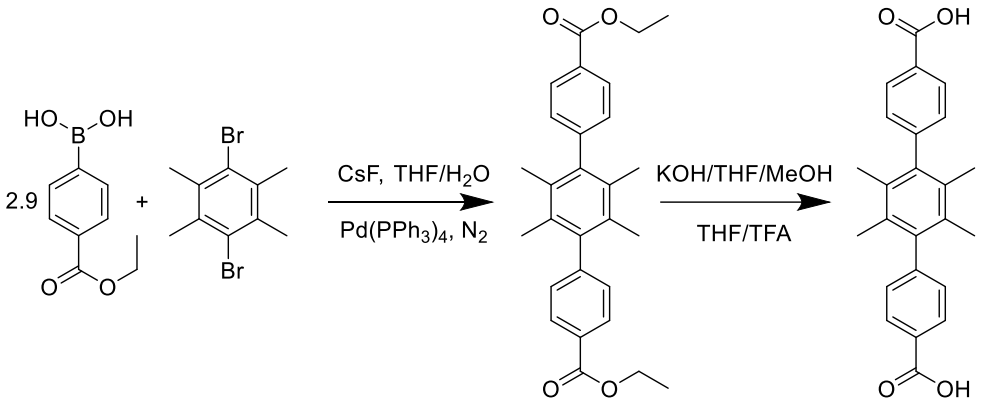

Scheme 2.2: Synthesis of 2',3',5',6' tetramethyl [1,1'1:4',1'' terphenyl] 4,4'' dicarboxylic acid.

Similar to NH_2-H_2TPDC the first step in the synthesis of Me$_4$-H_2TPDC was a Suzuki coupling that would yield the terphenyl ligand with an ethyl protected carboxylic acid, diethyl-2',3',5',6' tetramethyl [1,1'1:4',1'' terphenyl] 4,4'' dicarboxylate (Et-Me$_4$-TPDC). In a slightly modified method from the literature,[197] 5 mL of DMF and 5 mL of deionized water were combined in a 20 mL Biotage microwave vial and sparged with nitrogen gas for thirty minutes. After sparging, 0.1050 g (0.3596 mmol) of 3,6-dibromdurene, 0.2050 g (5.154 mmol) of 4-(ethoxycarbonyl)phenylboronic acid, 1.1500 g (7.570 mmol) of cesium fluoride and 0.0200 g (0.01731 mmol, 1.6 mol %) of

tetrakis(triphenylphosphine)palladium(0) was added to the vial and sparged with nitrogen gas for five minutes. The vial was placed in a Biotage Initiator microwave reactor for thirty-five minutes at a temperature of 413 K. The reaction was subsequently cooled to room temperature and the precipitate was isolated by suction filtration. The filtrate was washed with deionized water (2 × 25 mL) followed by washing with acetone (3 × 15 mL) resulting in a grey precipitate of Et-Me_4-H_2TPDC in a 75% yield (0.1133 g, 0.2634 mmol). The ^{1}H-NMR spectrum was collected on a Bruker 500 MHz Avance spectrometer. The data was consistent with literature values.[197] ^{1}H-NMR (500 MHz, Chloroform-*d*): δ 8.12 (d, *J* = 8.6 Hz, 4H), 7.26 (d, *J* = 8.6 Hz, 4H), 4.41 (q, *J* = 7.1 Hz, 4H), 1.91 (s, 12H), 1.42 (t, *J* = 7.1 Hz, 6H). Note: $CDCl_3$ overlaps with the doublet at 7.26 ppm, the integration of half the doublet was utilized to determine the relative integration.

Synthesis of 2',3',5',6'-tetramethyl-[1,1':4',1''-terphenyl]-4,4''-dicarboxylic acid (Me_4-H_2TPDC)

The product of the Suzuki-coupling from the previous step, Et-Me_4-TPDC, was dissolved in 40 mL of THF/methanol mixture (50:50) and 20 mL of 1 mol/L KOH in water was added and allowed to reflux overnight. The mixture was then removed from heat and allowed to cool to room temperature. The organic solvents were removed under reduced pressure and heat. The remaining solution was acidified with 1 mol/L hydrochloric acid until a pH of 1 was reached. At this point, a white powder was observed. The precipitate was isolated by suction filtration and washed with deionized water (3 × 25 mL) and methanol (3 × 10 mL). The ^{1}H-NMR spectrum was collected on a Bruker 300 MHz Avance III spectrometer. The data was consistent with literature values.[197] This reaction was

quantitative. ^{1}H-NMR (300 MHz, DMSO-d_6): δ 8.04 (d, J = 8.3 Hz, 4H), 7.29 (d, J = 8.3 Hz, 4H), 1.87 (s, 12H).

2-Nitrobiphenyl-4,4'-dicarboxylate (NH_2-H_2BPDC)

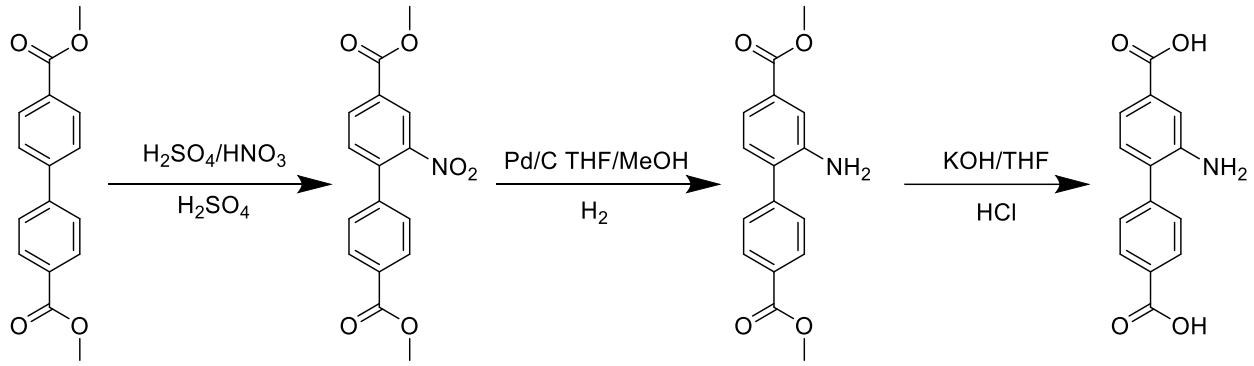

Scheme 2.3: Nitration overview of H_2BPDC.

Nitration Overview

The first step in the production of NH_2-H_2BPDC, is the nitration of dimethyl biphenyl-4,4'-dicarboxylate. Traditionally, the literature preparations for this step are done on relatively large scales (ca. 20 g).[198] In our hands, scaling down the reaction without further modifications lead to a mixture of the mono-, di-, and un-substituted complexes. The main modification for this reaction is to use a more dilute HNO_3/H_2SO_4 solution, to prevent localized high concentrations of HNO_3, and to pre-cool the HNO_3 solution. We believe that scaling down this reaction results in every drop of HNO_3/H_2SO_4 solution overreacting before it can evenly mix into solution. The more dilute solution slows down the kinetics thereby preventing the formation of the di-nitrated compound.

Synthesis of 2-nitro-dimethyl-biphenyl-4,4'-dicarboxylate

In a 25 mL round bottom flask, 0.5000 g (1.850 mmol) of dimethyl biphenyl-4,4'-dicarboxylate was dissolved in 5 mL concentrated H_2SO_4. 12 mL of a concentrated solution of H_2SO_4 with 0.125 mL of HNO_3 was chilled in an ice bath for fifteen minutes. The diluted HNO_3/H_2SO_4 solution was added dropwise to the 25 mL round bottom flask with stirring. The temperature was maintained below 278 K. The solution was stirred for thirty minutes and subsequently poured into a 600 mL beaker full of ice producing a white precipitate. The solution was stirred for forty-five minutes before the precipitate was isolated by suction filtration, washed with 500 mL of deionized water, and allowed to dry overnight to give a 92% yield (0.5366g, 1.703 mmol). The ^{1}H-NMR spectrum was collected on a Bruker 300 MHz Avance III spectrometer. ^{1}H-NMR (300 MHz, Chloroform-*d*): δ 8.56 (d, *J* = 1.7 Hz, 1H), 8.30 (dd, *J* = 8.0, 1.7 Hz, 1H), 8.12 (d, *J* = 8.6 Hz, 2H), 7.54 (d, *J* = 8.0 Hz, 1H), 7.41 (d, *J* = 8.6 Hz, 2H), 4.00 (s, 3H), 3.95 (s, 3H).

Synthesis of 2-amino-dimethyl-biphenyl-4,4'-dicarboxylate

In a 250 mL round bottom flask 0.6600 g (2.093 mmol) of 2-nitro-dimethyl-biphenyl-4,4'-dicarboxylate was dissolved in a 50:50 mixture of THF and methanol. 0.0700 mg (0.06578 mmol) of 10% palladium on carbon was added. The flask was capped with a rubber septum and a balloon of hydrogen (aprox. 4 L) was used to sparge the solution. An additional balloon of hydrogen (aprox. 4 L) was used to maintain a positive pressure of hydrogen over the reaction. The reaction was stirred overnight (ca. twenty

hours) at room temperature. The next morning, the solution was filtered through celite and washed with 20 mL of THF and 20 mL of methanol. The solvent was removed under reduced pressure resulting in a brown solid. No further purification was performed. This reaction was quantitative. The ^{1}H-NMR spectrum was collected on a Bruker 300 MHz Avance III spectrometer. ^{1}H-NMR (300 MHz, Chloroform-d): δ 8.13 (d, J = 8.3 Hz, 2H), 7.55 (d, J = 8.3 Hz, 2H), 7.49 (dd, J = 7.9 Hz, 1.6 Hz, 1H), 7.45 (d, J = 1.6 Hz, 1H), 7.18 (d, J = 7.9 Hz, 1H), 3.95 (s, 3H), 3.92 (s, 3H).

Synthesis of 2-amino-biphenyl-4,4'-dicarboxylic acid (NH_2-H_2BPDC)

In a 250 mL round bottom flask 0.5000 g (1.753 mmol) of 2-amino-dimethyl-biphenyl-4,4'-dicarboxylate was dissolved in 50 mL of THF and 50 mL of 1 mol/L aqueous KOH solution. The resulting solution was heated to 313 K and stirred overnight. Subsequently, the organic solution was removed under heat and reduced pressure. The aqueous solution was acidified with 1 mol/L hydrochloric acid until a pH of 1 was reached. The resultant off white precipitate was isolated by suction filtration and washed with 150 mL of deionized water (3 × 50 mL). This reaction was quantitative. The ^{1}H-NMR spectrum was collected on a Bruker 300 MHz Avance III spectrometer. ^{1}H-NMR (300 MHz, DMSO-d_6): δ 8.00 (d, J = 8.3 Hz, 2H), 7.57 (d, J = 8.3 Hz, 2H), 7.42 (d, 1.7 Hz, 1H), 7.22 (dd, J = 7.8 Hz, 1.7 Hz, 1H), 7.12 (d, J = 7.8 Hz, 1H).[199]

Synthesis of UiO-66

UiO-66 was synthesized according to previously published literature procedures as follows.[56] 0. 1255 g (0.5385 mmol) of zirconium tetrachloride and 0.1247 g (0.7506 mmol)

of terephthalic acid were added to a 25 mL Duran vial. To the vial 15 mL of DMF and 1 mL of concentrated hydrochloric acid was added, and the vial capped. The solution was sonicated until all solids were dissolved resulting in a clear colourless solution, this took approximately five minutes. Once all solids were dissolved the vials were placed in a 353 K oven overnight. The jar was removed from the oven cooled to room temperature and the resulting solid and solution was transferred to a 50 mL centrifuge tube and centrifuged at 7800 RPM for three minutes, the solution was decanted and 15 mL of fresh DMF was added, and the process was repeated three times. After three washes with DMF the same process was repeated with methanol three times. After the final washing the centrifuge tube with the white powder was placed in an oven at 353 K overnight to remove any residual methanol.

Synthesis of UiO-66-NH_2

UiO-66-NH_2 was synthesized following previously published literature procedures as follows.[56] 0.1340 g (0.7481 mmol) of 2-aminoterepthalic acid was added to a 25 mL Duran vial followed by 0.1250 g (0.5364 mmol) of zirconium tetrachloride. 15 mL of DMF was then added followed by 1 mL of concentrated hydrochloric acid. This solution was then sonicated until a clear yellow solution remained. The reaction mixture was then placed in a 353 K oven overnight. Upon removal from the oven the mother liquor was exchanged for 25 mL of methanol, both solution and resulting precipitated were transferred to a 100 mL round bottom flask, the Duran vial was then rinsed with an additional 25 mL of methanol, and this was added to the round bottom flask and refluxed overnight. The reaction was then removed from heat and transferred to a 50 mL centrifuge tube. The

resulting precipitate and solution were centrifuged at 7800 RPM for three minutes. The methanol was then decanted, and 20 mL of fresh methanol was added, and the tube was shaken to redistribute the solid and it was then placed back into the centrifuge and the process was repeated a total of three times. Once this was complete the methanol was decanted and the solid was placed in a 353 K oven overnight to dry.

Synthesis of UiO-67

UiO-67 was synthesized by using previously published procedures as follows.[56] 0.0673 g (0.2888 mmol) of zirconium tetrachloride and 0.0922 g (0.3806 mmol) of 4,4-biphenyldicarboxylic acid were added to a 25 mL Duran vial. To the vial 15 mL of DMF and 0.5 mL of concentrated hydrochloric acid was added and the vial capped. The solution was sonicated for approximately ten minutes, not all the solids dissolved. Once sonication was complete, the vials were placed in a 353 K oven overnight. The jar was removed from the oven, cooled to room temperature and the resulting solid and solution was transferred to a 50 mL centrifuge tube and centrifuged at 7800 RPM for three min. The solution was decanted and 15 mL of fresh DMF was added and the process was repeated three times. After three washes with DMF, the same process was repeated with methanol three times. After the final washing the centrifuge tube with the white powder was placed in an oven at 353 K overnight to remove any residual methanol.

Synthesis of UiO-67-NH_2

UiO-67-NH_2 was synthesized by using previously published procedures as follows.[56] 0.0670 g (0.288 mmol) of zirconium tetrachloride and 0.0920 g (0.395 mmol) of

2-amino-biphenyl-4,4'-dicarboxylic acid was added to a 25 mL Duran vial. To the vial 15 mL of DMF and 0.5 mL of concentrated hydrochloric acid was added, and the vial capped. The solution was sonicated for approximately ten minutes, not all the solids dissolved. Once sonication was complete, the vials were placed in a 353 K oven overnight. The jar was removed from the oven, cooled to room temperature, and the resulting solid and solution was transferred to a 50 mL centrifuge tube and centrifuged at 7800 RPM for three minutes. The solution was decanted and 15 mL of fresh DMF was added. This process was repeated three times. After three washes with DMF the same process was repeated with methanol three times. After the final washing the precipitate was transferred to a vial to be used in a Tousimis Samdri-PVT-3D supercritical drier with fresh anhydrous ethanol. The ethanol was exchanged twice a day for fresh anhydrous ethanol for three days. On the third day, the MOF was supercritical dried in order to activate the material.

Synthesis of UiO-68-Me_4

Method A (Post-COVID shutdown procedure): Following the synthesis by Goswami *et al*.[35] In a 50 mL Pyrex jar, 0.1200 g (0.3724 mmol) of zirconyl chloride octahydrate, 0.1000 g (0.2685 mmol) of Me_4-H_2TPDC, 20 mL of DMF, and 1.000 g of benzoic acid (8.189 mmol) were combined and sonicated for three minutes. The resulting solution was placed in the oven at 373 K overnight. Once removed from the oven and cooled to room temperature, the mixture was transferred to a 50 mL centrifuge tube and centrifuged for five minutes at 7800 RPM. The solution was decanted, and (25 mL) fresh DMF was added, shaken, centrifuged, and the solution was decanted. This process was

repeated a total of three times. This process was then repeated three times with 25 mL methanol. The resulting precipitate was placed in a vacuum oven at 353 K overnight.

Method B (Pre-COVID shut down procedure): This MOF was prepared from a slightly modified procedure outlined by Cui *et al*.[180] In a 50 mL Pyrex Jar, 0.0460 g (0.197 mmol) of zirconium chloride, 0.0640 g (0.171 mmol) of Me_4-H_2TPDC, 40 mL of DMF, and 1 mL of trifluoroacetic acid were combined and sonicated for three minutes. The resulting solution was placed in the oven at 393 K for four days. Once removed from the oven and cooled to room temperature the mixture was transferred to a 50 mL centrifuge tube and centrifuged for five minutes at 7800 RPM. The solution was decanted, and (25 mL) fresh DMF was added, shaken, centrifuged, and the solution was decanted. This process was repeated a total of three times. This process was then repeated three times with 25 mL methanol. The resulting precipitate was placed in a vacuum oven at 353 K overnight.

Synthesis of UiO-68-NH_2

Method A (Post COVID shutdown): In a slightly modified procedure outlined by Schaate *et al*.[181] 0.1200 mg (0.5150 mmol) of zirconium tetrachloride, 1.8800 g of benzoic acid (15.394 mmol) and 20 mL of DMF were combined in a 50 mL Pyrex jar and sonicated for three minutes. After sonication a clear colorless solution resulted, 0.1700 g (0.5100 mmol) of NH_2-H_2TPDC and 0.028 mL of deionized water were added and sonicate again for three minutes to form a cloudy yellow solution. This was placed in a 393 K oven overnight. Once removed from the oven and cooled to room temperature, the sample and solvent were transferred to a 50 mL centrifuge tube and centrifuged for five minutes at

7800 RPM. The solution was decanted, and (25 mL) fresh DMF was added, shaken, centrifuged, and the solution was decanted. This process was repeated a total of three times. This process was then repeated three times with 25 mL methanol. The resulting precipitate was placed in a vacuum oven at 80 °C overnight.

Method B (Pre-COVID shutdown): Following a slightly modified literature procedure,[96] In a 50 mL Pyrex jar 0.1300 mg of L-proline (1.129 mmol), 0.0540 mg of zirconium tetrachloride (0.2317 mmol), 0.0730 mg of NH_2-H_2TPDC (0.2190 mmol) and 10 mL of DMF were combined and sonicated for five minutes and a cloudy yellow solution formed. 20 μL of concentrated hydrochloric acid was added and sonicated again for two minutes. This was then placed in a 393 K oven overnight. Once removed from the oven and cooled to room temperature, the sample and solvent were transferred to a 50 mL centrifuge tube and centrifuged for five minutes at 7800 RPM. The solution was decanted and (25 mL) fresh DMF was added, shaken, centrifuged, and the solution was decanted. This process was repeated a total of three times. This process was then repeated three times with 25 mL acetone. The resulting precipitate was placed in a vacuum oven at 353 K overnight.

2.4.3 Gas Adsorption

Excluding UiO-67-NH_2, prior to gas adsorption measurements, samples were activated on a Micrometrics Smart Vac-Prep by heating at a rate of 5 K/min to 363 K and holding at this temperature for thirty minutes under vacuum. Subsequently, the sample was heated to 423 K at 5 K/min and held for six hundred minutes under vacuum. UiO-67-NH_2

was activated by first exchanging the synthesis solvent with ethanol over several days and subsequently activated by supercritical drying using a Tousimis Samdri-PVT-3D supercritical drier.[56,200]

Nitrogen Isotherms were collected on a Micrometrics 3Flex instrument at 77 K. Water isotherms were measured at 295 K on a Micrometrics 3Flex instrument. In order to expose the sample to water vapour, a 3Flex sample holder containing 5 mL of distilled, deionized water was installed on one of the three sample ports and subsequently used as a dosing port. Prior to analysis, the water was subjected to three freeze-pump-thaw cycles to remove any dissolved gases.

2.4.4 Thermogravimetric Analysis

Thermogravimetric analysis was run on 6-10 mg of sample using a TA instruments Q500. The samples were heated under air with a flow rate of 50 mL/min starting at room temperature and ending at 923 K at a rate of 10 K/min.

2.4.5 Powder X-Ray Diffraction

Powder X-ray diffraction patterns were collected on Rigaku XtalLAB Synergy-S X-ray diffractometer with a copper radiation source with the divergent slits set to 86%. Patterns were measured from 3º to 50º in 2θ.

Chapter 3: Structure Property Relationship Between UiO Based Metal-Organic Frameworks and Carbon Dioxide Adsorption

Statement of Co-authorship

This chapter has not yet been published; however, a manuscript is in preparation. We believe that computational data will greatly enhance the discussion, along with support our experimental data. We are currently in collaboration with Prof. Tom Woo at the University of Ottawa and awaiting those results before the submission of the manuscript.

Authors: Mason C. Lawrence and Prof. Michael J. Katz

This work was done in the Katz research group where Mason C. Lawrence was the first author who performed the synthetic work, data collection data analysis and was responsible for the preparation of the manuscript. Michael J. Katz was the principal investigator for this project, who was responsible for preparation of the manuscript, and contributed to the analysis and interpretation of collected data.

The draft of the manuscript has been reproduced in this chapter with modifications to provide an extended discussion of the obtained results.

3.1 Introduction

Carbon dioxide levels in the atmosphere have been increasing over the past several decades. This has led to increased global temperatures, melting of ice caps, and rising ocean levels, as previously mentioned in Section 1.3.2. One of the primary sources for this change is the burning of fossil fuels and various industrial processes. With this in mind, a great deal of research using MOFs to remove carbon dioxide from the environment has been undertaken, as discussed in detail in Section 1.3.2. The work examines how pore structure and function relate to the adsorption of carbon dioxide (i.e., structure property-relationships). With the multitude of node/ligand combinations and the resultant 3D porous structures, there are many structure property relationships that yield insights regarding what makes a MOF excel at carbon dioxide adsorption. Many strategies and examples of MOFs being used for carbon dioxide adsorption can be found in Section 1.3.2. Additional examples include the work of Long and co-workers who have shown that cooperative behaviour of terminal amino groups in Mg_2(dobpdc) (dobpdc = 4,4'-dioxidobiphenyl-3,3'-dicarboxylate), installed via post synthetic modification onto the open metal sites in Mg_2(dobpdc), can lead to the formation of a carbamate.[125] They have also shown that while the addition of the terminal amine is important, the length of the functional group is also important. With a functional group of a certain length hydrogen bonding between the amine of the functional group on the neighboring cluster is present, allowing for the carbamate to be held in place (Figure 3.1).[124]

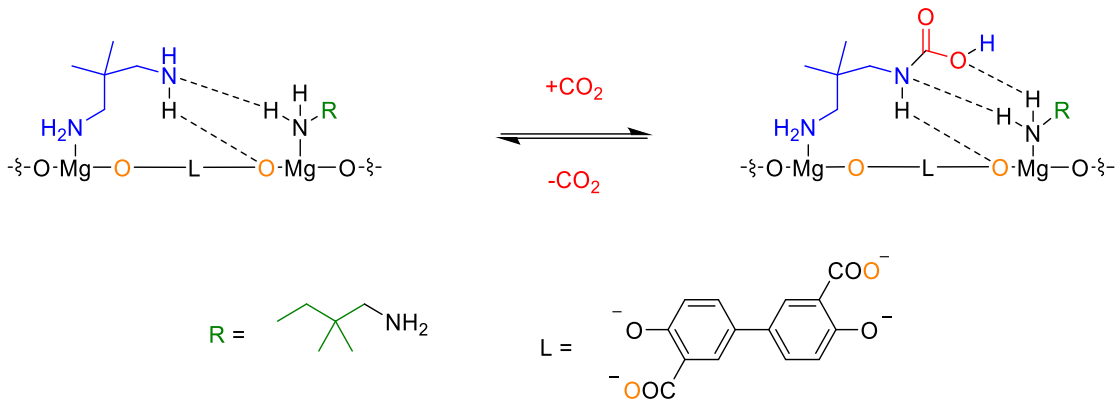

Figure 3.1: Formation of a carbamate from inside Mg_2(dobpdc). The carbamate is stabilized by hydrogen bonds from nearby metal clusters.

In the work of Shimizu and co-workers, modification of the pore size and aperture of $Zn_2(Atz)_2ox$ (Atz, 3-amino-1,2,4-triazole and ox, oxalate) has shown a larger uptake in carbon dioxide adsorption compared to reported MOFs.[51,201] The authors attribute the orientation of the Atz and ox in the pores of the MOF for this enhanced adsorption. Two different locations for the carbon dioxide to bind have been identified, the first being near the free amine group of the Atz ligand and the second being near the ox ligand. In the first position near the free amine group, Shimizu and coworkers have shown X-ray crystallographic data that suggest that the hydrogen molecules of the free amine group have hydrogen bonding interactions with the ox groups that are in backbone of the MOF. This indicates that the carbon dioxide is coordinated through the interaction of the lone pair on the nitrogen atom and the carbon atom of carbon dioxide. The second interaction is between the oxygen of carbon dioxide and the carbon of the ox ligand in the backbone of the MOF. They had also observed an interaction between the oxygen of the carbon dioxide in the first position and the carbon atom of the carbon dioxide in the second position.

In UiO-66, Morris and co-workers have shown, through IR and computational studies, that there are three different places that the carbon dioxide molecules are able to bind in the MOF.[202] The first binding location is through hydrogen bonding between the μ_3-OH found inside the zirconium cluster and an oxygen atom of the carbon dioxide. The second location is identified as carbon dioxide being located inside the smaller tetrahedral the pore and dispersion forces with the π-electrons present in the benzene dicarboxylate ligand. The final binding site they discuss for UiO-66 is the binding between the incoming carbon dioxide gas and a zirconium molecule from the cluster that has an open coordination site due to missing ligand defects.

With our ongoing interest in gas phase chemistry in MOFs, and especially those gases that are present in the atmosphere, we were interested in further exploring the structure property relationship of carbon dioxide adsorption in UiO-66 and UiO-67.

Traditionally, researchers would modify the functional groups decorating the pore to study the structure property relationships. One of the simplest modifications we can imagine from the UiO family of MOFs would be the addition of a pendant amine group to compare the uptake capabilities of UiO-66 and UiO-66-NH_2. In 2014 Janiak and coworkers published a paper that explored how the addition of an amine functional group to Cr-MIL-101 would change the carbon dioxide adsorption of the MOF.[203] They quickly realized the importance of the additional amino group as the carbon dioxide adsorption at 1 bar and 293 K increased from 15.5 weight percent in the unfunctionalized MOF to 22.2 weight percent in the amino functionalized MOF. Its also common to explore an increase in the pore sizes of the materials, an example from the UiO family of MOFs would

be the increase in pore size moving from UiO-66 to the larger pore UiO-67. In the literature Rosi *et al*. synthesized a zinc MOF with biphenyl dicarboxylate ligands that is anionic.[204] The MOF is charge balanced by a cationic species, normally dimethylammonium. By changing the cationic species to larger molecules such as tetramethylammonium, tetraethylammonium or tetrabutylammonium the volume of the pore would change. They observed a decrease in pore volume from 0.75 cm^3/g in the parent material containing dimethylammonium cation, to 0.65 cm^3/g when the tetramethylammonium cation is used, to 0.55 cm^3/g when tetraethylammonium cation is used, and 0.37 cm^3/g when the tetrabutylammonium cation is used. With this decrease in pore volume there is an increase in the carbon dioxide enthalpy of adsorption, The smallest pore volume MOF was found to have an enthalpy of adsorption of –31.2 kJ/mol while the unfunctionalized MOF had an enthalpy of adsorption of –21.9 kJ/mol. While this is an important methodology for structure property relationships, there are other comparisons that have not been explored. We were interested in examining the role of defects and how they can alter carbon dioxide adsorption.

Defects are inherent to all materials. They are entropically favoured and enthalpically disfavoured resulting in an optimal number of defects based on the synthesis and inherent properties of a material. What has made defect studies in MOFs so challenging is that often it is difficult to control the number and types of defects. As illustrated in Chapter 2, missing ligand defects are very common in UiO MOFs when made via the very commonly used hydrochloric acid procedure. It has been shown that approximately one to two missing ligand defects are formed in UiO-66, UiO-67, and their derivatives.[36,38]

Thankfully, for the UiO family of MOFs, controlling defects has been well examined. Zhou and co-workers have investigated the role of adding small amounts of acetic acid (final concentrations of 0.3 to 1.2 M) and had discovered that increasing the amount of acetic acid lead to a higher number of defects present.[205] They had also noted that increasing the reaction time from 24 to 48 hours results in the formation of larger pore volumes, indicating missing ligand defects. In these systems, the shape of the isotherm deviates from what is traditionally observed. This suggest that mesopores are beginning to form. Furthermore, Behrens and co-workers have investigated the role of benzoic acid as a modulator in UiO-66 and UiO-67.[181] They have reported that adding up to 30 equivalents of benzoic acid during the synthesis of these MOFs leads to the incorporation of more ligands, decreasing the number of missing ligand defects.

The UiO family of MOFs were discussed in detail in Section 1.2. In brief, these MOFs contain a central zirconium cluster with the formula $Zr_6O_4(OH)_4^{+12}$. These clusters are connected by linear ditopic organic ligands (benzene dicarboxylate for UiO-66, and biphenyl dicarboxylate for UiO-67).[23,56] Once the ligands and clusters are combined, porous material containing a large octahedral pore and smaller tetrahedral pore is formed. By varying the synthetic procedure, the missing ligands are either replaced by capping carboxylate groups or terminal water/hydroxide groups on the node.[183,205] Post synthetically, the node of the MOF can be dehydrated. The dehydration removes any hydrogen-bond donor groups from the node while also creating an open site on the cluster where previously a μ_3-OH group can be found.[38] The new node has the formula $Zr_6O_6^{12+}$ and can be seen in Figure 3.2.

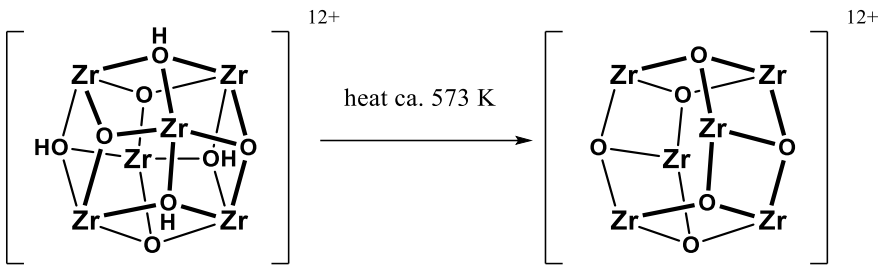

Figure 3.2: Dehydration of the $Zr_6O_4(OH)_4^{12+}$ cluster to $Zr_6O_6^{12+}$.

Lastly, Ameloot and co-workers have shown that partial solvolysis of some ligands, or the replacement of terminal water groups and terephthalate ligands with methanol/methoxy groups, is possible by soaking the MOF in methanol for up to three days.[86]

The strategy illustrated above of adding a functional group and observing the change in the MOF behaviour is common in the literature, and quite effective. However, in this project we take a step back and want to examine the structure of the MOF and how the inherent pore features contributes to the adsorption properties of the materials. For example, we have the ability to examine how the defect free structure of UiO-66 adsorbs carbon dioxide in the presence of the μ_3-OH and in the absence of it. Similarly, we can repeat these experiments with defect-containing UiO-66 in the presence and absence of the μ_3-OH groups. In addition to this, steric bulk can be added to the defect sites by replacing the water/hydroxide defects with methanol/methoxy defects. This would not only remove the hydrogen-bonding water/hydroxide defects but also potentially change the pore size of the MOF. By repeating all of the work on UiO-66 with UiO-67, we can separate the role of the pore from that of the surface.

Based on the aforementioned synthesis/post synthetic modifications, we explore six variations of UiO-66 and six variations of UiO-67 for their carbon dioxide adsorption properties. These variants have enabled us to determine what features of zirconium-based MOFs favour carbon dioxide adsorption and what features are benign.

3.2 Results and Discussion

3.2.1 Pristine and Defective UiO-66 and UiO-67

We started exploring the gas adsorption properties by first looking at UiO-66 that was synthesized with acetic acid as the modulator. Herein, we will refer to this MOF as UiO-66-AA to distinguish it from other procedures. As it is generally considered to contain little to no defects, it makes for an ideal starting point. UiO-66-AA was synthesized by reacting zirconium chloride and terephthalic acid in *N,N*-dimethylformamide (DMF) using acetic acid as the modulator in a ratio of 40:11 (v:v), or a concentration of 3.8 M. It has been well documented that this synthetic procedure produces octahedral shaped crystals with little to no missing ligands.[206] Thus, UiO-66-AA is considered to be "pristine". While defects are always present, in UiO-66-AA, it is well documented that the missing ligands are minimized; Audu *et al*. have shown that the MOF shows 5.5 of 6 ligands.[206] To explore the impact of the acetic acid synthesis on the gas adsorption properties of UiO-66 we first looked at the nitrogen gas adsorption isotherms of UiO-66-AA (Figure 3.3). We see a typical Type I (Section 1.4.1) isotherm for UiO-66-AA with a nitrogen gas accessible BET surface area of 1725 m^2/g (Table 3.1).

Table 3.1:Nitrogen accessable BET surface area of investigated UiO MOFs.

MOF	Surface area (m^2/g)
UiO-66-AA	1725
UiO-66-HCl	1600
UiO-67-AA	1500
UiO-67-HCl	2400
ΔUiO-66-AA	1460
ΔUiO-66-HCl	1560
ΔUiO-67-AA	1530
ΔUiO-67-HCl	2130
MeOH UiO-66-AA	1450
MeOH UiO-66-HCl	1400
MeOH UiO-67-AA	2430
MeOH UiO-67-HCl	2100

The pore size distribution was calculated (Figure 3.3) using the DFT model for cylindrical pores on an oxide surface. This revealed that we see one dominant pore around 11 Å consistent with the literature and the octahedral shaped pore of UiO-66.[56,82,184] The pore size distribution shows a small number of defect-based pores at 19 Å; this is far less than was observed in Chapter 2 (and below) for UiO-66 made with hydrochloric acid (UiO-66-HCl). While we cannot see the tetrahedral pore (computationally determined to be 3.8 Å)[82] due to the limitations of the pore size distribution models available to us, the

presence of an octahedral pore size and the lack of a considerable amount of defect-based pores suggests that the tetrahedral pore of UiO-66 is intact.

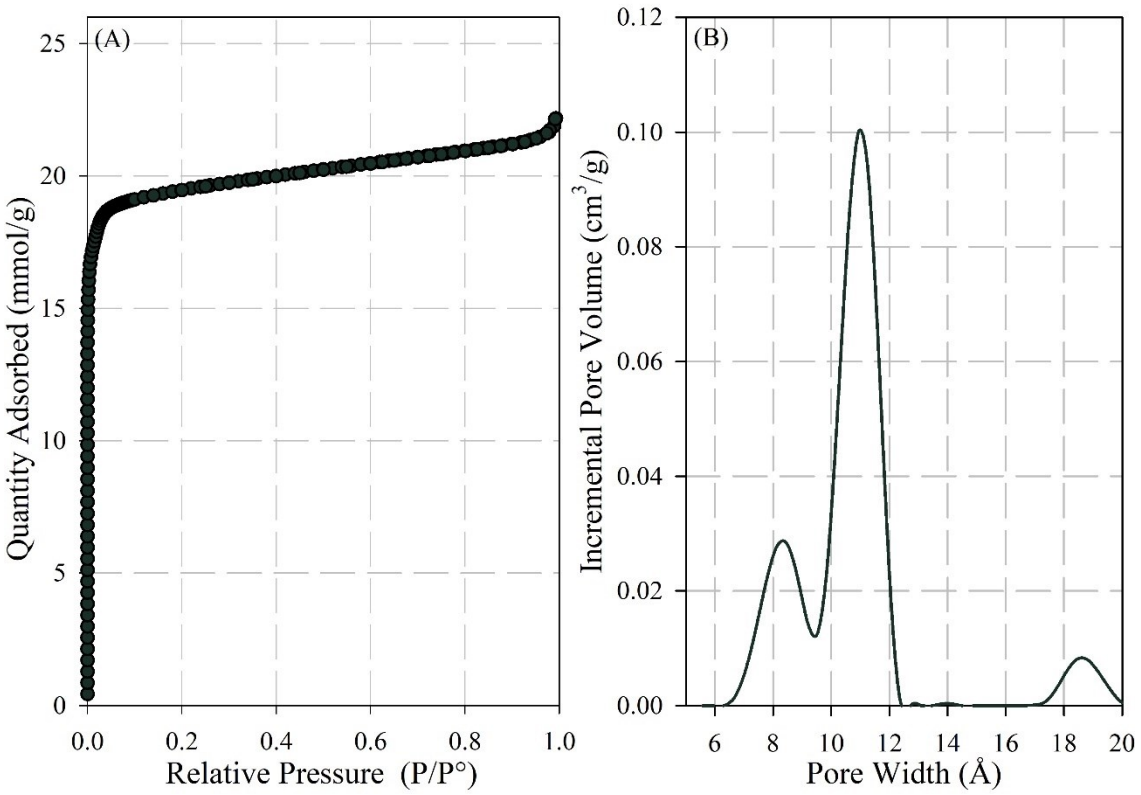

Figure 3.3: Nitrogen gas adsorption isotherm (A) measured at 77 K and the pore size distribution of UiO-66-AA (B).

With the pristine nature of UiO-66-AA confirmed, it would be used as the baseline for comparison for all the other UiO-66 derivatives explored in this study. We explored the carbon dioxide gas adsorption properties as a function of temperature (278, 283 and 288 K) shown in Figure 3.4. In order to gain further insights into the thermodynamics of gas adsorption, we fit the three isotherms to single-site Langmuir equation (Equation 3.2). From the equilibrium constants obtained in the fit (K in Equation 3.2), we were able to extract the enthalpy of gas adsorption using a Van 't Hoff plot as shown in Section 1.4.2. As shown in Table 3.2, the estimated maximum adsorption capacity for UiO-66-AA is

6.84 mmol/g with an exothermic enthalpy of adsorption of −24.3 ± 1.5 kJ/mol. This is close to the computationally calculated value of −26.2 kJ/mol by Maurin and co-workers and within the experimentally determined value of −26 to −24 kJ/mol by Walton and coworkers.[207,208] The differences may be due to varying synthetic procedures. Walton and co-workers used a modulator free synthesis that may produce a different number of defects than the procedure we followed using acetic acid. The activation of the materials was also different, Walton activated their MOFs at 378 K under vacuum, while the MOFs that were used in this study were activated at 423 K.

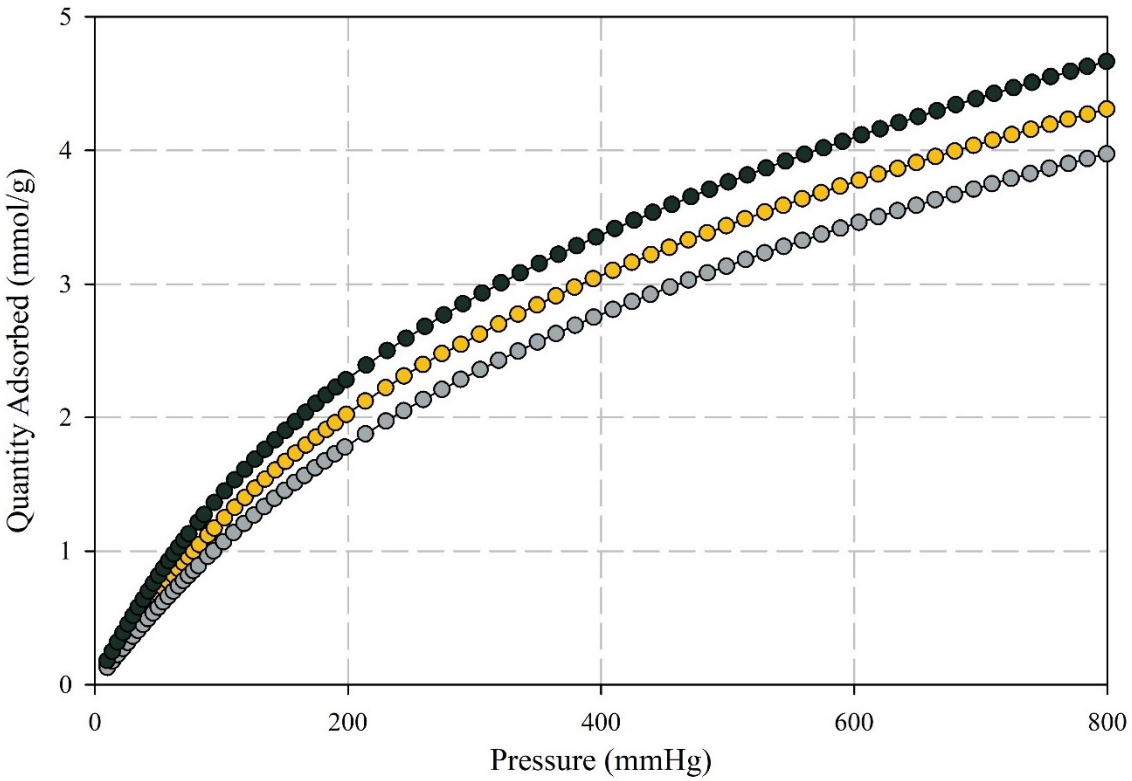

Figure 3.4: Carbon dioxide gas adsorption isotherms of UiO-66-AA measured at 278 K (green trace), 283 K (yellow trace), and 288 K (grey trace).

With our pristine UiO-66 examined, we turn our attention to a different synthetic procedure to form UiO-66. UiO-66 was synthesized using the same starting materials and

solvent but using hydrochloric acid as the modulator (UiO-66-HCl) in a much lower ratio than acetic acid (DMF:HCl 15:1, v:v). This procedure has been shown to readily produce large quantities of UiO-66, derivatives of UiO-66, UiO-67, and derivatives of UiO-67.[56] Aside from the versatility of the hydrochloric acid procedure, it has been determined that this procedure produces UiOs with missing ligands (see Section 1.2.1). For UiO-66, it has been estimated that approximately one to two of the six ligands are missing.[56] For every missing ligand, four zirconium-ligand bonds are replaced (two neutral and two anionic) with two water and two hydroxide groups (one pair per node); this retains the original geometry around each zirconium and the charge neutrality of the MOF. Given this, UiO-66-HCl would contain larger pores, more hydrogen bonding sites, and potentially metal sites that a guest can bond with (e.g., via a ligand substitution reaction).

The obtained BET surface area of UiO-66-HCl is 1600 m^2/g. This is slightly lower than that of UiO-66-AA, but not drastically different making these two MOFs easy to compare to one another. In looking at the two nitrogen gas adsorption isotherms (Figure 3.5), we also note that UiO-66-AA has a sharper bend (i.e., the "knee" of the isotherm) in the low-pressure region compared to UiO-66-HCl. The knee of the isotherm relates to the C constant is obtained when fitting data to the BET criteria (Section 1.4.4.1). The sharper the knee, the higher the C constant, indicating stronger interactions between the gas and the material. UiO-66-HCl is also suggested to have more defect pores, these pores occur at a larger pore size and can potentially account for the some of the observed difference in the curvature of the nitrogen isotherm.

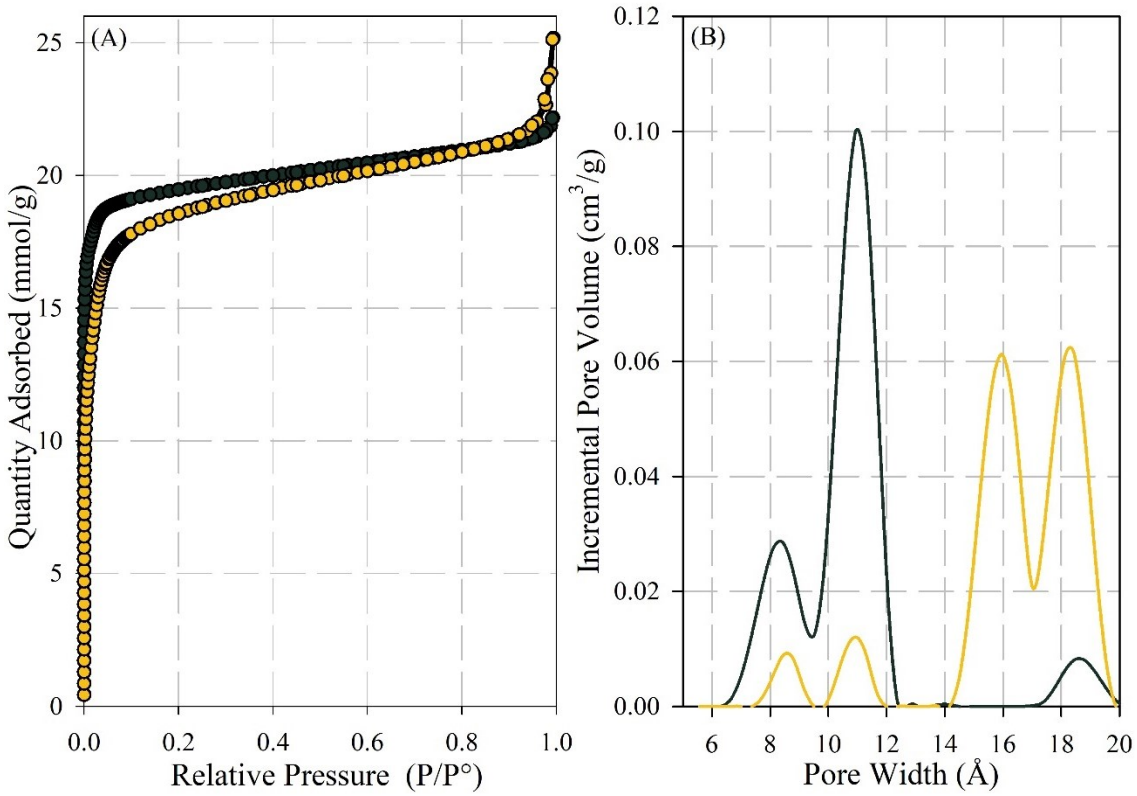

Figure 3.5: Nitrogen gas adsorption isotherms (A) measured at 77 K and pore size distribution plots (B) of UiO-66-AA (green trace) and UiO-66-HCl (yellow trace).

To further explore the differences between these two MOFs, we also looked at the pore size distribution of UiO-66-HCl (Figure 3.5B). Unlike UiO-66-AA, we see a large decrease in the 8 Å and 11 Å pore with a concomitant increase in the defect-based pores (ca. 17 Å). As shown by Liang and coworkers as defect-based pores increase, the number of tetrahedral and octahedral pores decrease.[184]

With these structural differences in mind, we were able to explore the relationship between the missing ligand defects and the carbon dioxide adsorption properties. As with UiO-66-AA, the carbon dioxide gas adsorption properties of UiO-66-HCl were measured at 278, 283, and 288 K.

In looking at the difference between the carbon dioxide adsorption isotherms for UiO-66-HCl and UiO-66-AA (Figure 3.6), there is one main difference. In UiO-66-HCl, the curvature of the isotherms are less curved than that of UiO-66-AA. This indicates that UiO-66-HCl has a smaller equilibrium constant. To take a closer look at the thermodynamic parameters, we fit the isotherms to a single-site Langmuir equation and extracted the enthalpy parameters from a Van't Hoff plot (Table 3.2). Calculating the enthalpy of adsorption for UiO-66-HCl, it was found to be −20.9 ± 0.7 kJ/mol which is 3.4 kJ/mol higher (less exothermic) than UiO-66-AA. The maximum adsorption quantity (Q_{max}) between UiO-66-AA and UiO-66-HCl is very similar (6.84 versus 7.15 mmol/g, respectively); correcting for the molecular mass differences of the two, we get a near identical maximum adsorbed quantity of 11.2 mole CO_2/mole UiO-66-AA versus 11.3 mole CO_2/mole UiO-66-HCl. The biggest difference between the two MOFs is that UiO-66-HCl has a 14% higher (less exothermic) enthalpy of adsorption (−20.9 kJ/mol vs. −24.3 kJ/mol) than the pristine UiO-66-AA.

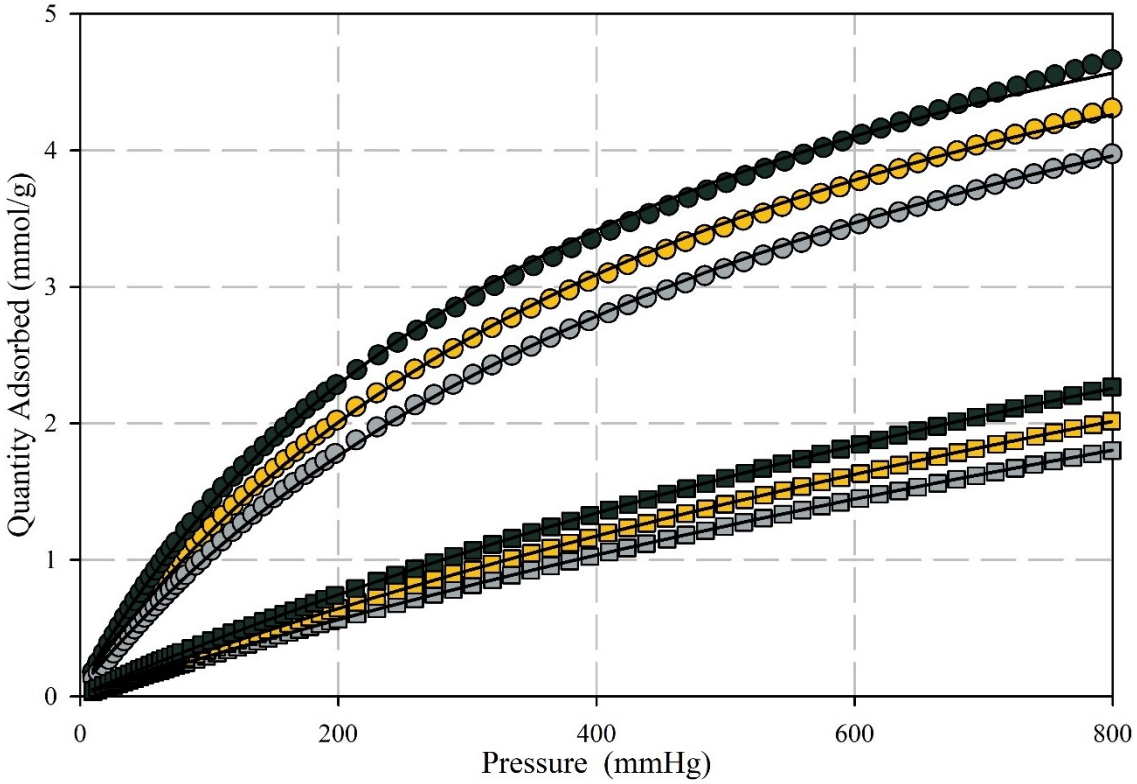

Figure 3.6 Carbon dioxide gas adsorption isotherms of UiO-66-AA (circles) and UiO-66-HCl measured at 278 K (green trace), 283 K (yellow trace), and 288 K (grey trace). Solid line repersents the isotherm after fitting to the single-site Langmuir equation.

Table 3.2: Calculated enthalpies of adsorption and maximum loadings.

MOF	***ΔH* (kJ/mol) (error)**	***Q*$_{max}$ (mmol/g) (error)**
UiO-66-AA	−24.3 (1.5)	6.84 (0.03)
UiO-66-HCl	−20.9 (0.7)	7.15 (0.03)
UiO-67-AA	−16.9 (1.8)	5.87 (0.06)
UiO-67-HCl	−21.2 (2.2)	8.93 (0.12)
ΔUiO-66-AA	−21.4 (1.4)	8.01 (0.06)
ΔUiO-66-HCl	−21.1 (1.0)	8.02 (0.04)

Table 3.2 (Continued)

MOF	***ΔH* (kJ/mol) (error)**	**Q_{max} (mmol/g) (error)**
ΔUiO-67-AA	−13.4 (2.4)	9.53 (0.15)
ΔUiO-67-HCl	−13.6 (2.7)	10.64 (0.18)
MeOH UiO-66-AA	−23.5 (1.7)	5.22 (0.03)
MeOH UiO-66-HCl	−28.4 (2.1)	7.91 (0.05)
MeOH UiO-67-AA	−19.4 (1.7)	7.70 (0.09)
MeOH UiO-67-HCl	−19.7 (2.5)	7.18 (0.07)

The approximately 4 kJ/mol difference between UiO-66-AA and UiO-66-HCl suggests that there is a clear difference between the pristine material and the missing ligand-containing material. One possibility is that the structure of the pristine material contains surface binding sites (e.g., edges/corners) that are ideal for carbon dioxide adsorption. Alternatively, it is possible that one of the two pore sizes (tetrahedral or octahedral) is perfectly sized to tightly bind carbon dioxide. Morris and co-workers suggested that bridging in the tetrahedral site was important.[202] To differentiate between these two hypotheses, we looked at UiO-67 made via the acetic acid and the hydrochloric acid route.

UiO-67 contains the same zirconium-based node as UiO-66 but incorporates the longer biphenyl-4,4'-dicarboxylate ligand.[56] For UiO-67, the pore size is much larger (3.8 versus 5.5 Å for the tetrahedral and 8.0 versus 13.1 Å for the octahedral). Thus, if the shape of the pores or a portion of the pores is important, then we should expect to see a

difference in the enthalpy of adsorption between UiO-67-AA and UiO-67-HCl, consistent with what was observed for UiO-66-AA and UiO-66-HCl. If it is the volume or size of the pores, then we expect a weaker interaction between carbon dioxide and either of these MOFs, as the pores are larger relative to UiO-66-AA or UiO66-HCl.

Before we could explore the carbon dioxide adsorption of UiO-67-AA and UiO-67-HCl, we first examined the nitrogen gas adsorption isotherms and associated pore size distributions (Figure 3.7, Table 3.1). UiO-67-HCl has a 900 m^2/g higher surface area than the pristine UiO-67-AA. Furthermore, UiO-67-HCl shows a clear step in the isotherm around a relative pressure of 0.15 P/P^o. This step in the isotherm indicates the presence of defect-based pores. As shown in the pore size distribution, UiO-67-AA contains two pores at 12.7 and 15.5 Å. Meanwhile, UiO-67-HCl shows four different pore sizes, with one large broad pore centred around 25 Å. Just as in UiO-66-HCl, UiO-67-HCl has more ligand defect-based pores than the acetic acid made UiO-67-AA. This illustrates that UiO-67-AA and UiO-67-HCl are a good comparison for UiO-66-AA and UiO-66-HCl.

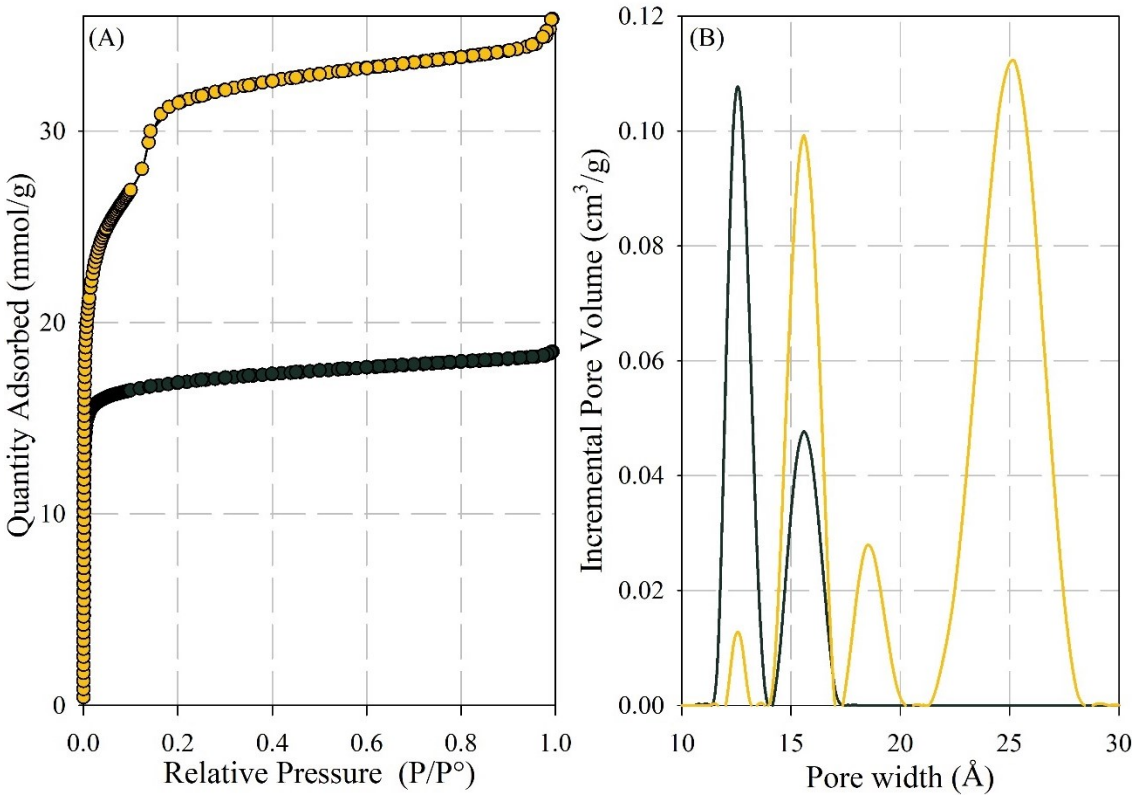

Figure 3.7: Nitrogen gas adsorption isotherms (A) measured at 77 K, and pore size distribution plots (B) of UiO-67-AA (green trace) and UiO-67-HCl (yellow trace).

The carbon dioxide isotherms for UiO-67-AA and UiO-67-HCl are shown in Figure 3.8. Unlike the two UiO-66 MOFs explored, these isotherms look very similar to each other. The isotherms were fit to a single-site Langmuir model (Table 3.2). Comparing the two UiO-67s, it is important to note that UiO-67-HCl contains more adsorption sites (Q_{max}) than UiO-67-AA (8.93 mmol/g vs. 5.87 mmol/g); the difference is even larger if we consider the molecular weight differences between the two samples (18.9 versus 11.6 mole CO_2/mole MOF, UiO-67-HCl and UiO-67-AA respectively). This suggests that the added defects in UiO-67-HCl allow for more carbon dioxide binding sites to exist; this is consistent with the much larger gravimetric surface area of UiO-67-HCl.

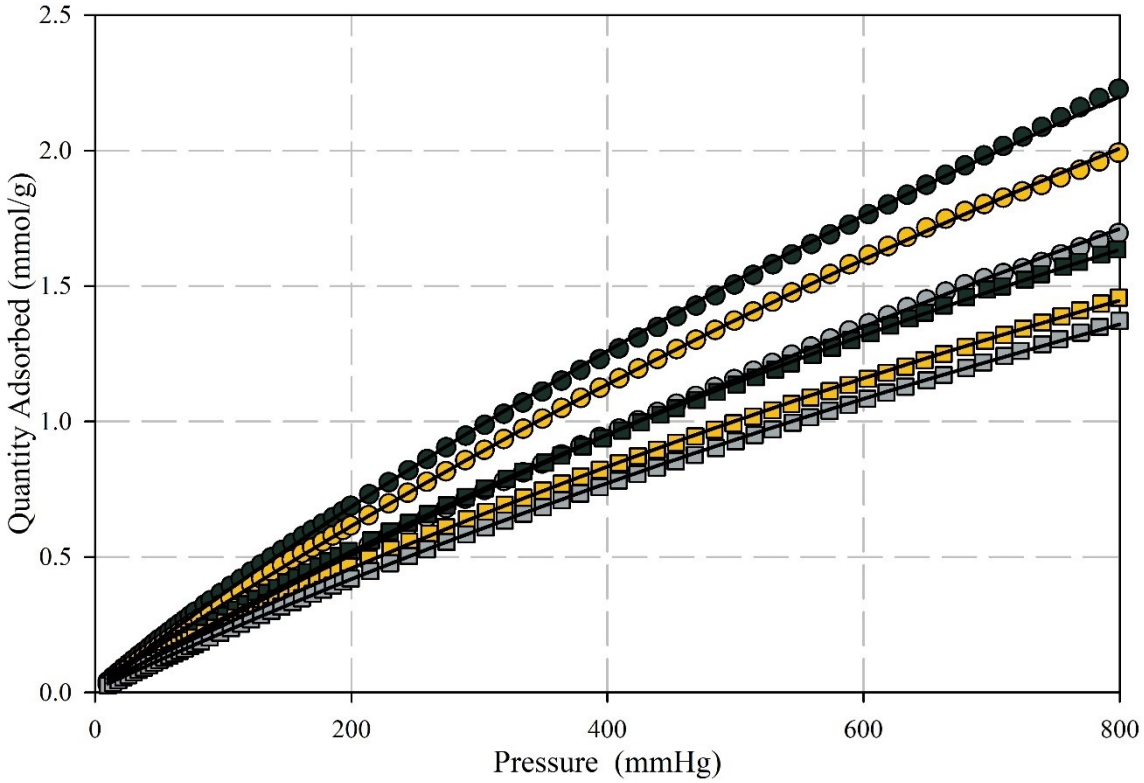

Figure 3.8: Carbon dioxide gas adsorption of UiO-67-AA (circles) and UiO-67-HCl (squares) at 278 K (green) 283 K (yellow) and 288 K (grey). Solid line repersents the isotherm after fitting to the single-site Langmuir equation.

The carbon dioxide adsorption data suggests a few key points. Comparing UiO-67-HCl and UiO-66-HCl, we notice relatively similar enthalpies (−21.2 ± 2.2 kJ/mol vs. −20.9 ± 0.7 kJ/mol). However, for UiO-67-AA and UiO-66-AA, the enthalpies of adsorption are considerably different (−16.9 ± 1.8 kJ/mol vs. −24.3 ± 1.5 kJ/mol). The observation that UiO-66-AA has a notably lower (more exothermic) enthalpy of adsorption versus UiO-67-AA suggests that UiO-66-AA likely has an ideal pore size and architecture for carbon dioxide adsorption. This is likely due to confinement effects in one of the pores; if it was a structural effect (e.g., shape of the pore wall rather than the size of the pore),

then we would expect these MOFs to have similar enthalpies. With the larger pores in UiO-67, the confinement effects are greatly reduced.

Given these results, UiO-67 allows us to explore the role of other structural effects in the absence of the confinement effects. For UiO-67-HCl, the presence of more defects seems to enhance carbon dioxide adsorption enthalpies and provide more adsorption sites. We hypothesis that the change in enthalpies is due to the presence of the OH^-/H_2O defects on the node that provide a hydrogen bonding site for the carbon dioxide molecule. As such, hydrogen bonding is important for carbon dioxide adsorption, but maybe not as important as confinement effects. It is possible the effects work in tandem or even that the presence of the hydrogen bonding groups are enough to constrict the pore to the "perfect" confined pore for carbon dioxide adsorption.

3.2.2 Dehydration of the Zirconium Cluster

To further explore the impact of hydrogen bonding, we heated the four MOFs at 573 K overnight to dehydrate the MOF (Figure 3.9).[38] In this scenario, the μ_3-OH present on the cluster are removed in the form of a water molecule, an open metal site is created, and the OH^-/H_2O present on the node from defects are at least partially removed.

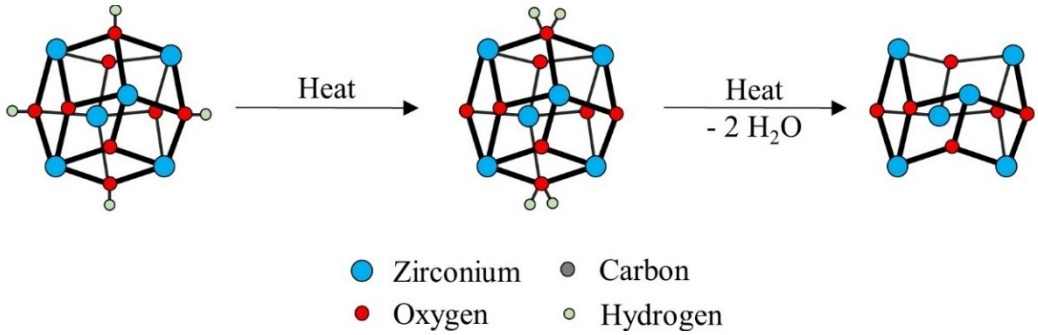

Figure 3.9: Dehydration of the cluster in the UiO family of MOFs.

Examining the nitrogen isotherms (Figure 3.10A) of the heated UiO-66 samples, (ΔUiO-66) we notice that there is no significant change in the shape of the nitrogen isotherm or the nitrogen accessible BET surface area (Table 3.1). ΔUiO-66-AA had a surface area of 1460 m^2/g compared to 1725 m^2/g in the parent material. ΔUiO-66-HCl had a surface area of 1560 m^2/g compared to the surface area of 1600 m^2/g in the parent material. This indicates that there are little-to-no structural changes in the materials. To further explore this, we measured the powder X-ray diffractograms of these MOFs after heating (Figure 3.11). As shown in Figure 3.11, very little change was observed confirming that dehydration of the MOF did not result in structural collapse or other considerable changes to the porous structure.

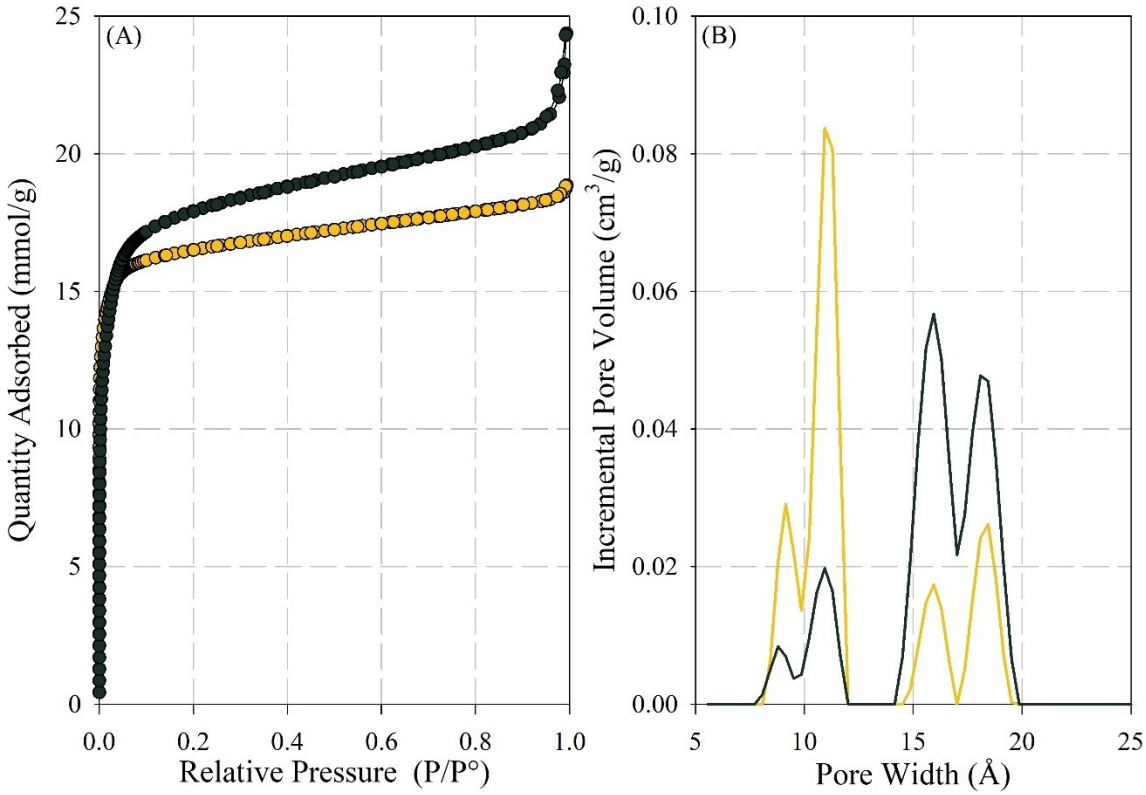

Figure 3.10: Nitrogen gas adsorption isotherms (A) measured at 77 K and the pore size distrubuition plots (B) of ΔUiO-66-AA (yellow trace) and ΔUiO-66-HCl (green trace).

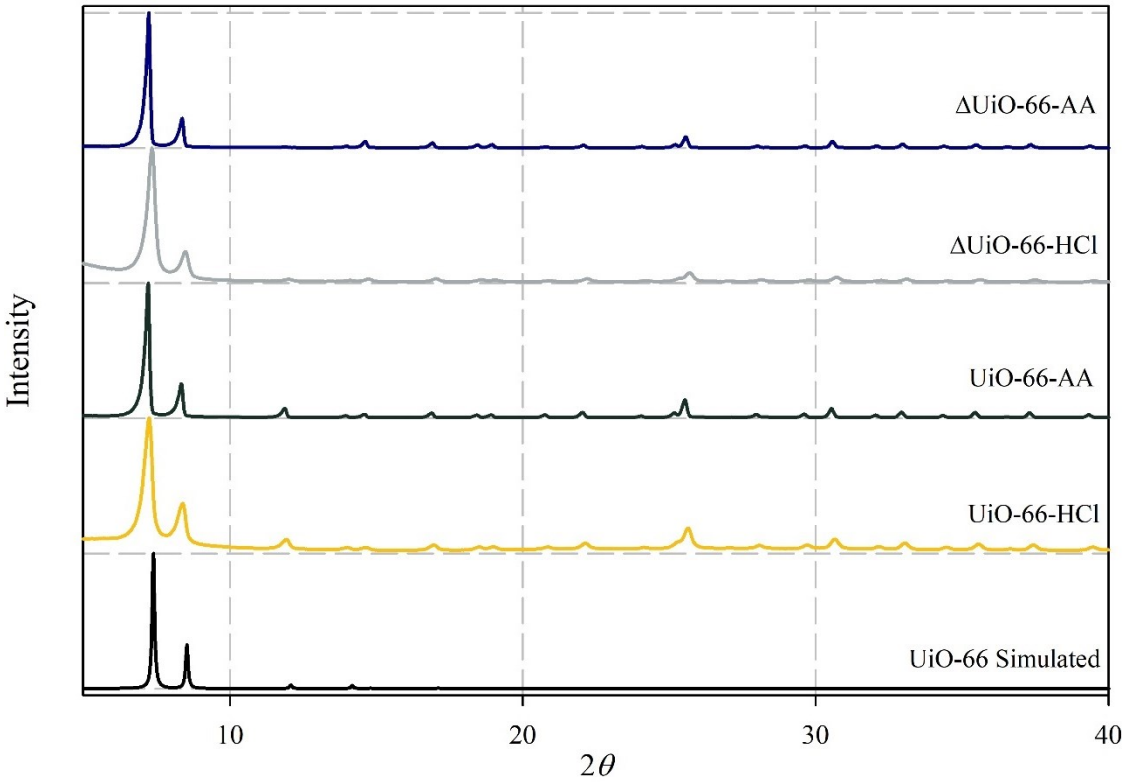

Figure 3.11: Powder X-ray diffractograms of simulated UiO-66, UiO-66-HCl, UiO-66-AA, ΔUiO-66-HCl, and ΔUiO-66-AA.

Examining the pore size distributions that are calculated from the nitrogen gas adsorption isotherms of the ΔUiO-66 samples (Figure 3.10B), we notice that the original trend that the acetic acid synthesis provides more of the octahedral pores and less of the defect-based pores remain even after heating; this further confirms that heating the material did not produce large changes in the number of defects or other structural changes (i.e., UiO-66 and ΔUiO-66 defer only in the presence/absence of H_2O/OH^- groups that can be thermally removed). Additionally, as shown in Figure 3.12, the pore size distribution did not drastically change from the original distribution. The comparison of UiO-66-AA pre- and post-heating show that there is slightly more of the defect-based pores present. In

UiO-66-HCl after heating the materials look very similar with almost no change in the pore size distribution.

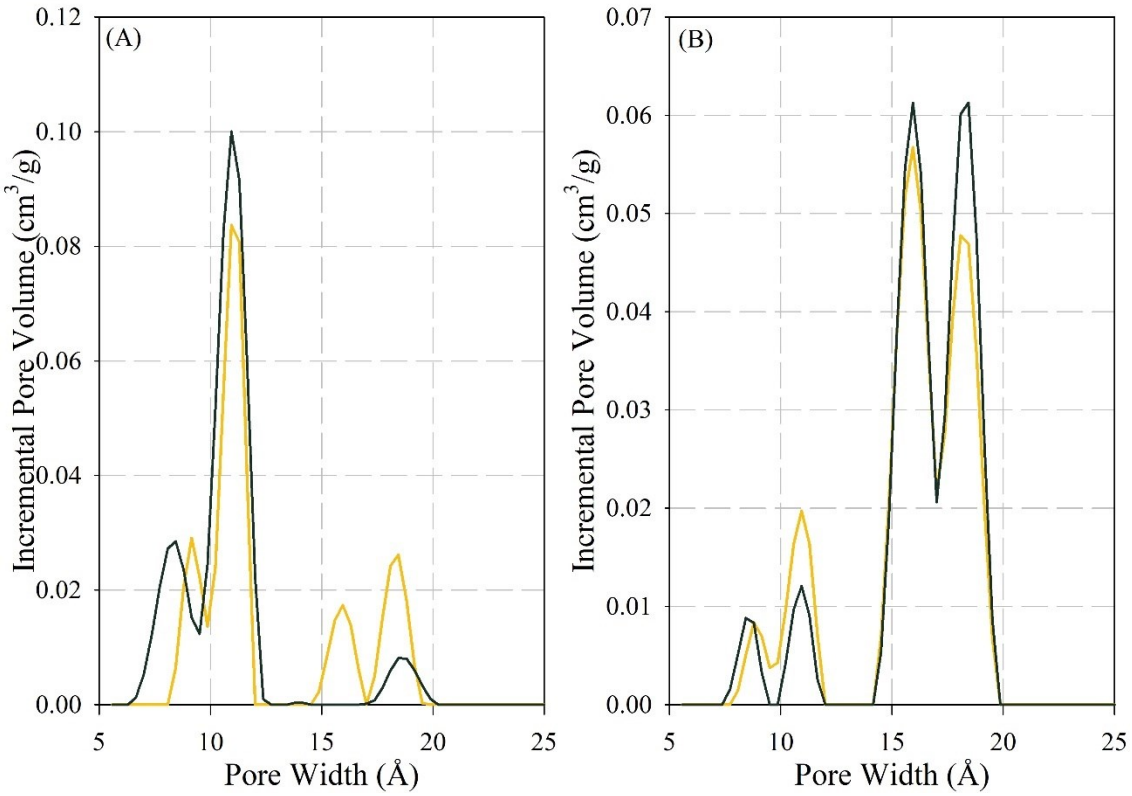

Figure 3.12: Pore size distributions of UiO-66-AA (A) and UiO-66-HCl (B) before (green trace) and after (yellow trace) heating at 573 K overnight.

Looking at the carbon dioxide gas adsorption isotherms (Figure 3.13), we notice that the maximum uptakes (8.02 mmol/g, or 13.0 mole CO_2/mole ΔUiO-66-AA, and 8.01 mmol/g 11.7 mole CO_2/mole ΔUiO-66-HCl) are relatively similar to one another as was observed in the hydrated UiO-66-AA and UiO-66-HCl. However, in the dehydrated samples, there is a roughly 4 kJ/mol increase (less exothermic) in the heats of adsorption for ΔUiO-66-AA (−24.3 ± 1.5 and −21.4 ± 1.0 kJ/mol respectively) and no change in the heats of adsorption for ΔUiO-66-HCl. For UiO-66-AA, this presents two options. Firstly, it is possible that the confinement effects in UiO-66-AA work in concert with hydrogen

bonding to generate the observed enthalpy of adsorption for UiO-66-AA. Alternatively, the hydrogen bonding due to the presence of the μ_3-OH may be negligible, and the increased enthalpy of adsorption may be due to the steric profile of the μ_3-OH present in the node leading to the overall confinement effects. When the hydrogen bonding between the μ_3-OH on the cluster and the carbon dioxide gas is lost, then the confinement effect is not as strong or completely absent leading to enthalpies similar to UiO-66-HCl, which do not have the confinement effects. For ΔUiO-66-HCl, the enthalpies of adsorption either suggest that hydrogen bonding is unimportant for carbon dioxide adsorption or that the dispersion interactions are similar in energy to the hydrogen bonding interactions. Once the MOF has been dehydrated, there are several open metal sites present (Figure 3.9), this is a common strategy used in the literature as previously discussed (Section 1.3.2.2). However, we see no significant increase in the adsorption of carbon dioxide when the cluster is dehydrated, indicating that while it may be effective for other MOFs, it is not effective in the UiO family.

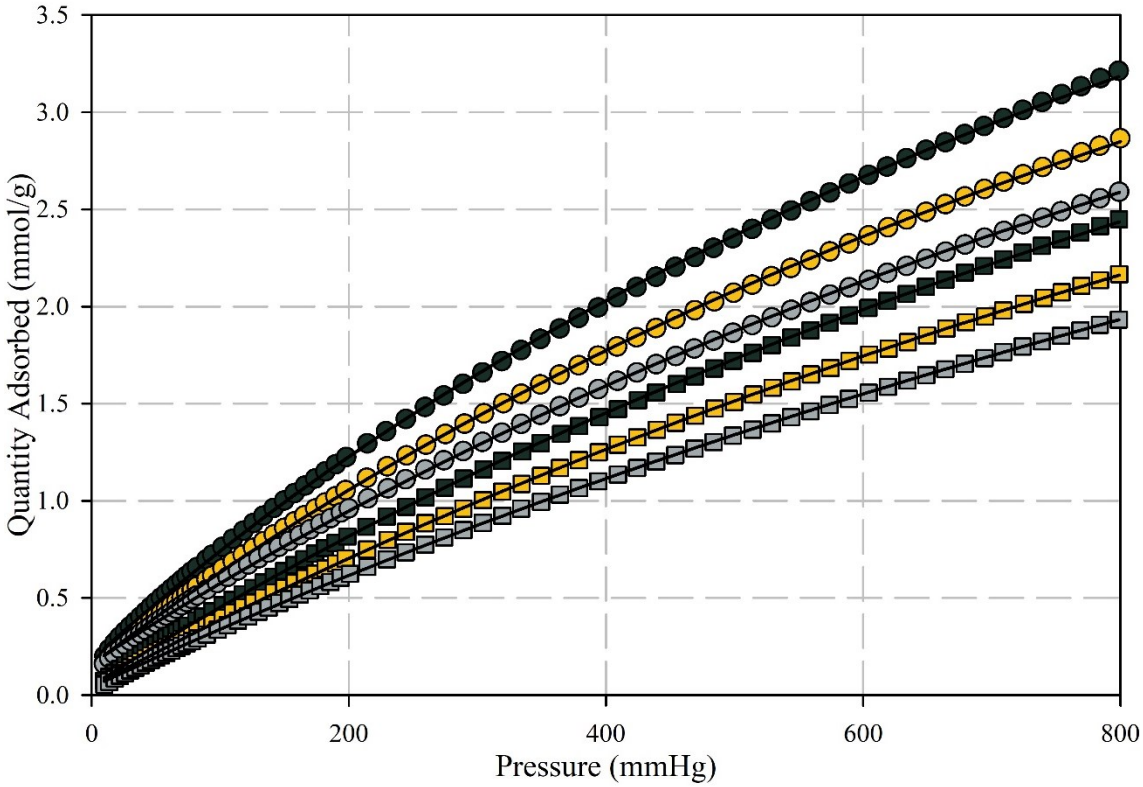

Figure 3.13: Carbon dioxide gas adsorption of ΔUiO-66-AA (circles) and ΔUiO-66-HCl (squares) at 278 K (green) 283 K (yellow) and 288 K (grey). Solid line repersents the isotherm after fitting to the single-site Langmuir equation.

To further understand why once the cluster has been dehydrated the enthalpies of adsorption for the UiO-66 samples were the same we examined the amount of carbon dioxide that was adsorbed at 800 mmHg. ΔUiO-66-HCl had an uptake of 2.16 mmol/g MOF. If we convert this to volume of carbon dioxide by using Equation 3.1, which is also known as the Gurvich rule.[159] We see that the volume is 0.091 cm^3 of carbon dioxide per gram of MOF.

$$V_{pore} = \frac{n_{gas\ ads}}{\rho_{liquid}} \qquad 3.1$$

In Equation 3.1 V_{pore} represents the volume of the pore, while $n_{gas\ ads}$ represents the moles of gas adsorbed, and ρ_{liquid} represent the density of the prob gas in liquid form.

Using Equation 3.1, the total pore volume required to hold the carbon dioxide at the point where the isotherm ends (800 mmHg) can be determined. This pore volume can then be compared to the pore volume calculated in the pore size distributions to determine what sized pores contain carbon dioxide. First, examining ΔUiO-66-HCl it is found that pores up to and including 14.5 Å contain carbon dioxide. If we compare that to ΔUiO-66-AA we see that the pores required to hold the quantity of carbon dioxide at 800 mmHg end at approximately 10.2 Å. If we relate the pore enthalpy of adsorption to the size of the filled pores, we observe that UiO-66-AA has a stronger interaction with carbon dioxide compared to ΔUiO-66-AA. With the hydrogen bonding of the μ_3-OH removed, we can see how important the confinement effects are as previously suggested.

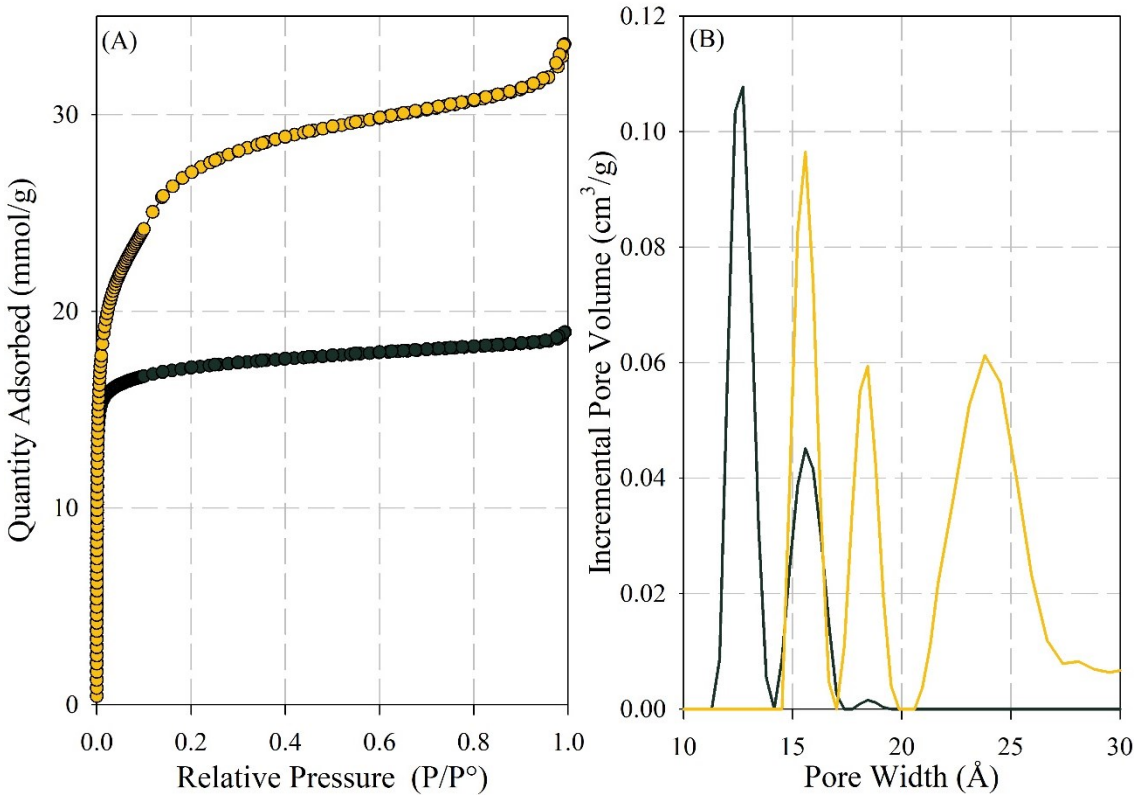

Figure 3.14: Nitrogen gas adsorption isotherms (A) measured at 77 K, and the pore size distribution plots (B) of ΔUiO-67 AA (green trace) and ΔUiO-67-HCl (yellow trace).

To further explore the role of hydrogen bonding, we examined the enthalpies of adsorption for ΔUiO-67-AA and ΔUiO-67-HCl. Using UiO-67 we are able to probe the importantance of hydrogen bonding as the larger pores that are present in UiO-67 to not have the confinement effects that we see in UiO-66. As with ΔUiO-66-HCl and ΔUiO-66-AA we examined the nitrogen gas adsorption isotherms and powder X-ray diffractograms to ensure that there was no notable change of the material caused by the dehydration of the MOF at 573 K. As illustrated in Figure 3.15 we see that there was no significant change in the nitrogen gas adsorption isotherms and both samples remained porous, while the powder X-ray diffractograms show that there was no change in the crystallinity of the material (Figure 3.15).

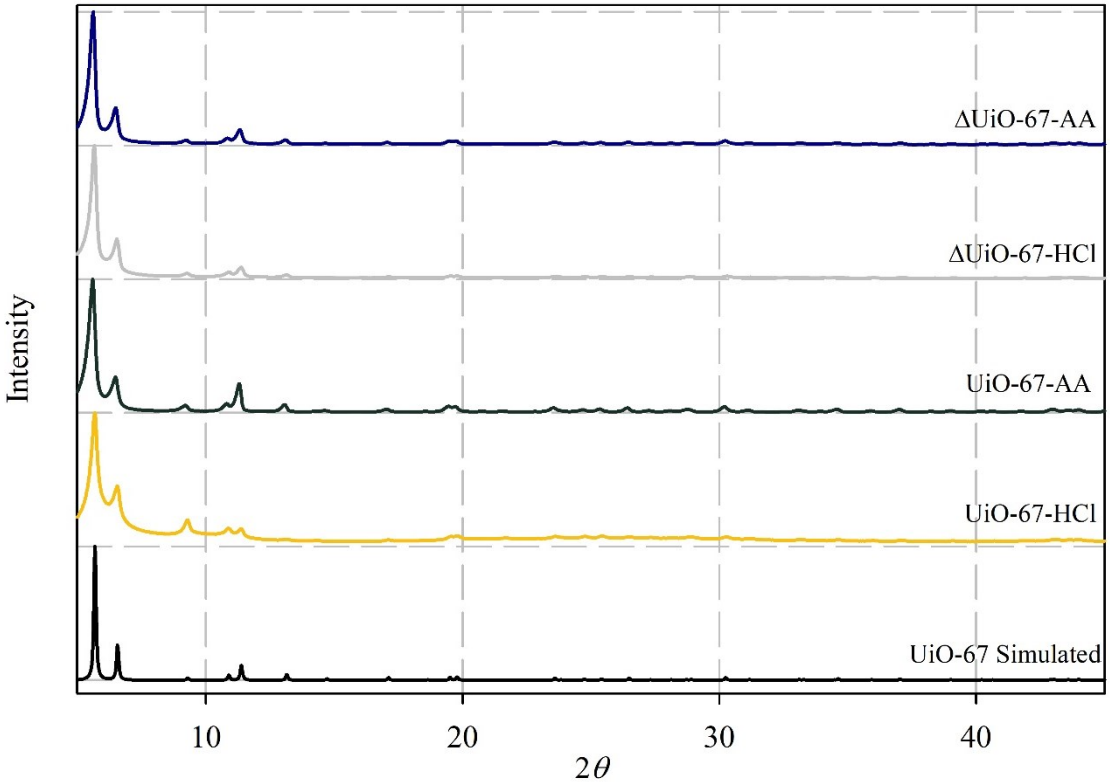

Figure 3.15: Powder X-ray diffractograms of simulated UiO-67, UiO-67-HCl, UiO-67-AA, ΔUiO-67-HCl and ΔUiO-67-AA.

Comparing the pore size distributions of the heated samples to the parent material, as illustrated in Figure 3.16, we see that there has been no detrimental change in the pore sizes and the MOFs synthesized via the acetic acid procedure looks identical to the parent material Figure 3.16.

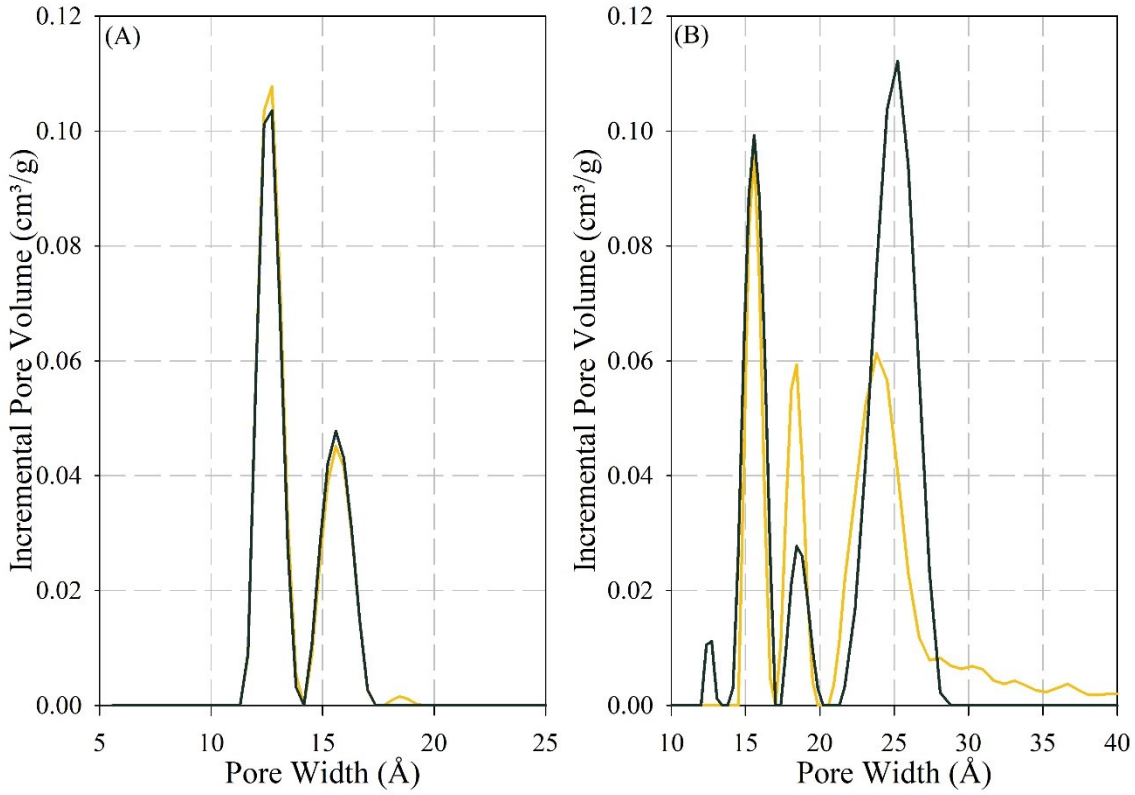

Figure 3.16: Pore size distributions of ΔUiO-67-AA (A) and ΔUiO-67-HCl (B) before (green trace) and after (yellow trace) heating at 573 K overnight.

Turning our attention to the carbon dioxide gas adsorption isotherms of the ΔUiO-67 samples, we notice something quite interesting. The isotherms for both the UiO-67-AA and UiO-67-HCl synthesis both lose much of their curvature and look very linear (Figure 3.17). This indicates a much lower equilibrium constant, which most likely reflects a much less exothermic enthalpy of adsorption.

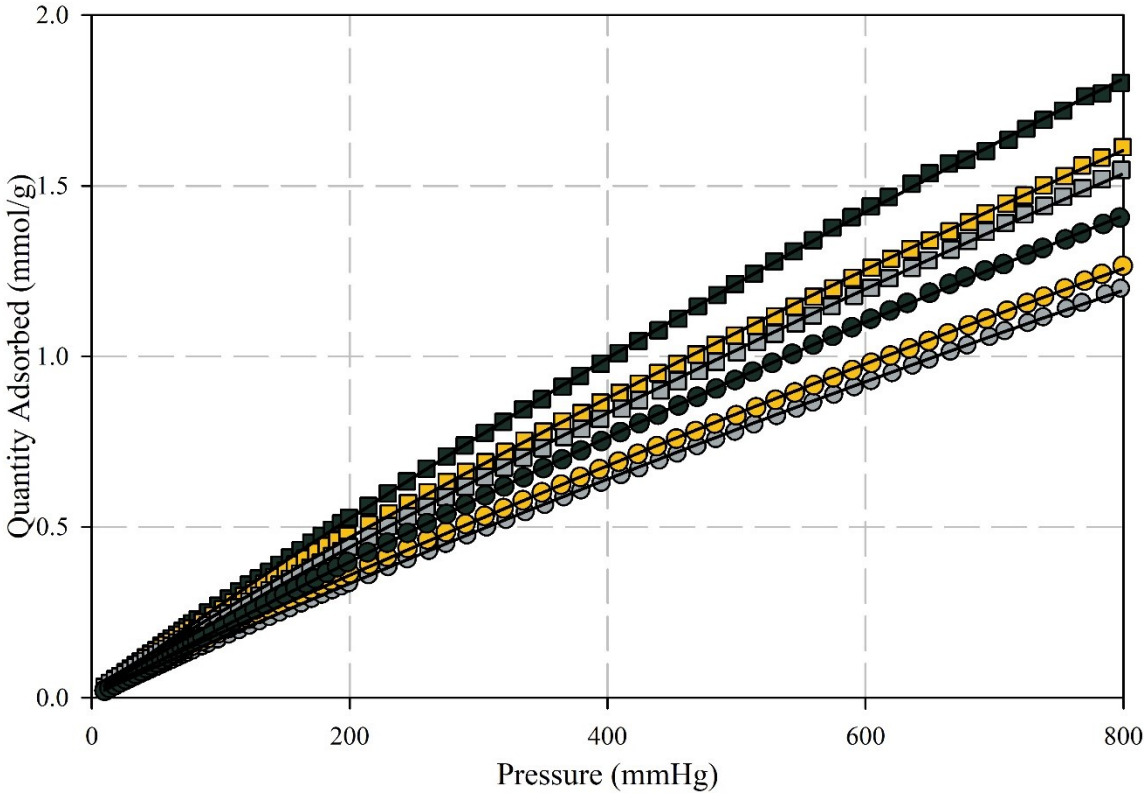

Figure 3.17: Carbon dioxide gas adsorption of ΔUiO-67-AA (circles) and ΔUiO-67-HCl (squares) at 278 K (green), 283 K (yellow), and 288 K (grey). Solid line repersents the isotherm after fitting to the single-site Langmuir equation.

Fitting the variable temperature carbon dioxide gas adsorption isotherms of ΔUiO-67-AA and ΔUiO-67-HCl to a single-site Langmuir isotherm model resulted in the enthalpies of adsorption becoming less exothermic for both MOFs, along with an increase in the Q_{max} values. The Q_{max} increased from 5.87 and 8.93 mmol/g to 9.53 and 10.64 mmol/g. While the obtained curves of UiO-67-AA and UiO-67-HCl are able to be fit to a single-site Langmuir isotherm to determine the Q_{max} value with low errors associated, the plots lack the obvious curvature that is observed in UiO-66-AA and UiO-66-HCl. For this reason, I am hesitant to overinterpret the calculated Q_{max} values for these samples. If we turn our attention to the heats of adsorption, for ΔUiO-67-AA we

observe a change from −16.9 to −13.4 kJ/mol, and for ΔUiO-67-HCl the enthalpies increase (became less exothermic) from −21.2 to −13.6 kJ/mol. Clearly, the presence of hydrogen bonding groups is important for higher enthalpies of adsorption. With the hydrogen bonding sites present, there are favorable interactions leading to a higher enthalpy of adsorption. When these hydrogen boding sites are removed in the heated samples, both procedures yield identical (within error) enthalpy of adsorption. This suggests that the enthalpies of adsorption associated with hydrogen bonding between carbon dioxide and either UiO-66 or UiO-67 are similar.

The enthalpy of adsorption for ΔUiO-66-HCl showed almost no change, and ΔUiO-66-AA showed approximately 3 kJ/mol increase as previously mentioned. If removing the μ_3-OH only changed the hydrogen bonding environment, then the change in the ΔUiO-67 samples should be similar to what was observed in the ΔUiO-66 samples. Since the same increase is not observed in ΔUiO-67 (3.5 kJ/mol in ΔUiO-67-AA and 7.6 kJ/mol in ΔUiO-67-HCl), there must be another difference in these samples. This difference can be accounted for through the dispersion interactions between carbon dioxide and the ligand, and they are lower in UiO-67. This can be explained by the electron withdrawing nature of the zirconium(IV) centres. The strongly withdrawing nature of four zirconium(IV) molecules on one aryl group (UiO-66) is greater than the two zirconium(IV) molecules (UiO-67) onto a singular aryl group; this puts a larger δ+ charge on the aryl ring in UiO-66 vs. UiO-67. This δ+ charge will attract a δ- charge, that can be found on the oxygen of the carbon dioxide. The stronger the δ+ charge the stronger the interaction with the carbon dioxide, and therefore the more exothermic the enthalpy of adsorption, as

observed in the ΔUiO-66. Returning to UiO-66-HCl, we hypothesize that the energy of the dispersion interaction are similar to that of the hydrogen bonding and thus the lack of hydrogen bonding does not amount to a large change in the observed enthalpies.

Comparing the volume of carbon dioxide adsorbed in relationship to the pore volumes, as was performed for the ΔUiO-66 samples, it is observed that ΔUiO-67-AA has all its adsorption in pores that are 12 Å or smaller, while ΔUiO-67-HCl has carbon dioxide adsorbed in its 15 Å and smaller pores (Figure 3.14). Since the data are being fit to a single-site isotherm, the calculated enthalpy of adsorption that is observed comes from each pore that carbon dioxide is adsorbed in. We have previously seen how a smaller pore has a stronger interaction with carbon dioxide leading to a lower enthalpy of adsorption. As larger pores begin to adsorb carbon dioxide, the interaction would be weaker, and an increase in the enthalpy of adsorption would be observed. This trend is reported above for both ΔUiO-66 and ΔUiO-67.

3.2.3 Functionalization of the Zirconium Cluster

With this new insight into how defects on the cluster affect the adsorption of carbon dioxide, we decided to examine how modifying the hydrogen bonding environment around the cluster can further improve the enthalpy of adsorption. Ameloot and co-workers have demonstrated that soaking UiO-66 in methanol can produce three different types of defects.[86] In pristine UiO-66, the first type of defect occurs when the methanol cleaves one of the two carboxylic acids. In this scenario, the ligand is still connected to one cluster and is now dangling in the pore. The node is now charge and compensated and coordinatively

saturated with a methoxy and methanol groups, respectively. If the solvolysis continues to break the remaining ligand-metal bonds, then the MOF is in the second scenario where there has been complete solvolysis of a ligand and both clusters are now capped with methanol/methoxy groups. The final scenario involves just the exchange of the water and hydroxide that we hypothesize is present in the defective MOFs, in this case UiO-66-HCl and UiO-67-HCl (Figure 3.18).

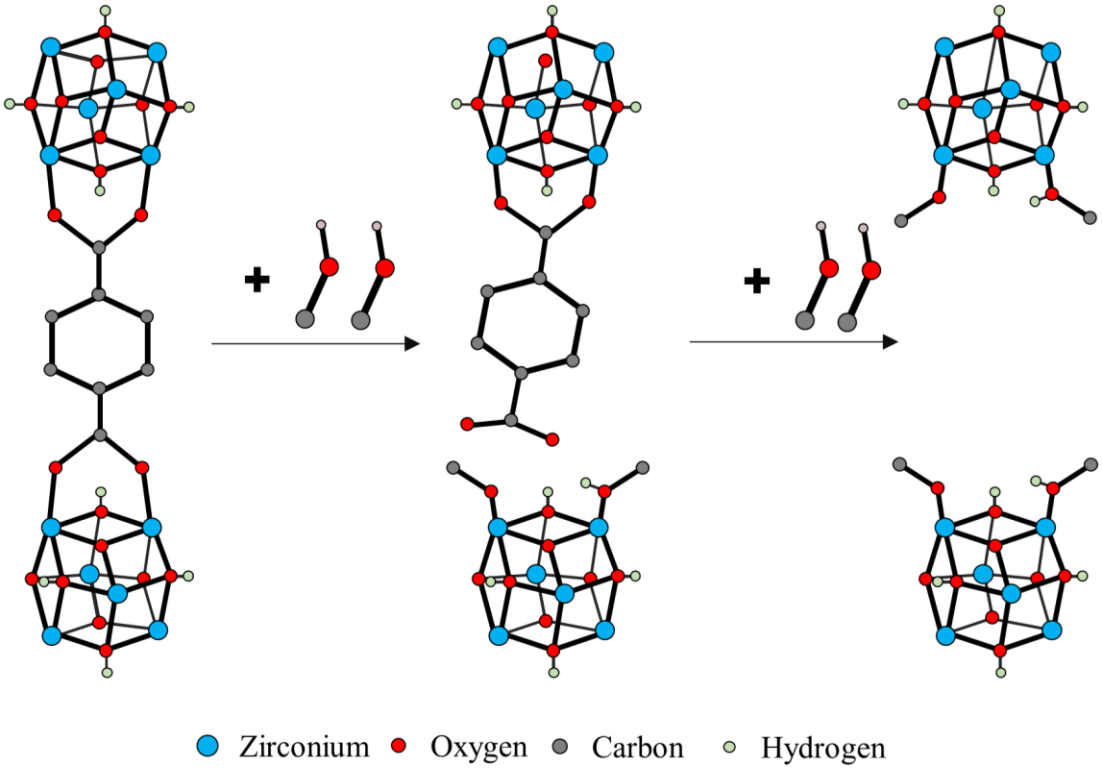

Figure 3.18: Displacement of benzene dicarboxylate via methanol solvolysis. Pristine MOF (left), partial benzene dicarboxylate removal resulting in dangling ligand and cluster capped with methanol and methoxy (middle), and complete removal of the benzene dicarboxylate ligand with methanol and methoxy capped defects. Blue spheres represent zirconium, red spheres represent oxygen, grey spheres represent carbon and light green spheres represent hydrogen.

Ameloot *et al.* have shown that the degree to which each type of defect is formed depends on the total number of missing ligands in the parent MOF.[86] With the goal of studying the effects of modifying the defects/surface of UiO-66 and UiO-67, we followed the procedure published by Ameloot *et al.* and soaked the MOFs in methanol for three days at room temperature to ensure the water/hydroxide constituents were replaced with the methanol and methoxy groups.[86] The powder X-ray diffractograms of the methanol-soaked MOFs were also measured to ensure there was no loss of crystallinity during the methanol soaking process (Figure 3.19). As illustrated in Figure 3.19, there is no loss of crystallinity or other notable changes to the diffractograms upon methanol soaking. This indicates that the structures remain intact and have not begun to collapse.

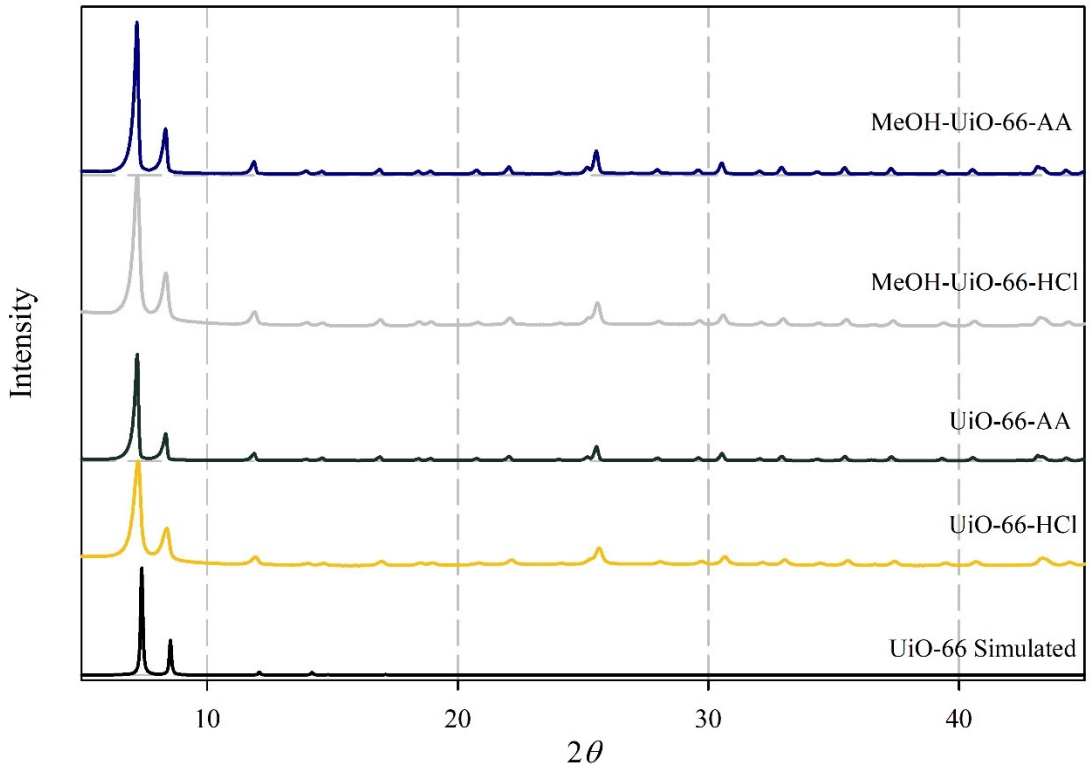

Figure 3.19: Powder X-ray diffractograms of simulated UiO-66 (black), UiO-66-HCl (yellow), UiO-66-AA (green), MeOH-UiO-66-HCl (grey) and MeOH-UiO-66-AA (blue).

Measuring the nitrogen gas adsorption isotherms of MeOH-UiO-66-AA and MeOH-UiO-66-HCl showed that after methanol soaking and activation the materials remained porous and retained most of their surface areas (Table 3.1), UiO-66-AA showed a slight loss of surface area when soaked in methanol as it fell from 1725 to 1450 m^2/g and UiO-66-HCl showed a decrease from 1600 to 1400 m^2/g. In combination with the PXRD results, this data cannot be explained by partial collapse of the structure. As discussed in Chapter 1 and Chapter 2, a change in surface area becomes difficult to assess as there is both a loss of surface due to the missing ligands, and decrease in molar mass that have opposing effects.

The decrease in surface area after methanol soaking can be explained in one of two ways. The first explanation is that there is complete solvolysis and removal of the ligand. This would remove a BDC from the structure of the MOF (Figure 3.18 left). Once the BDC is removed, two methanol and two methoxy ligands would fill in the vacant coordination site on the clusters. As previously discussed in Section 1.2.1, adding defects will change the molar mass of our material. Replacing one BDC with two methoxy and two methanol groups would cause a slight decrease in the molecular weight, approximately 38 g/mol. This decrease in molecular weight would lead to more moles of MOF in one gram of MOF, which would lead to an increase in the gravimetric surface area. Additionally, the BDC provides more surface for the gas to bind to relative to the methanol and methoxy groups. This leads to less overall surface for gas to bind to, which causes an overall decrease in the surface area. Thus, if a ligand is removed via solvolysis, then we would predict a decrease in the surface area.

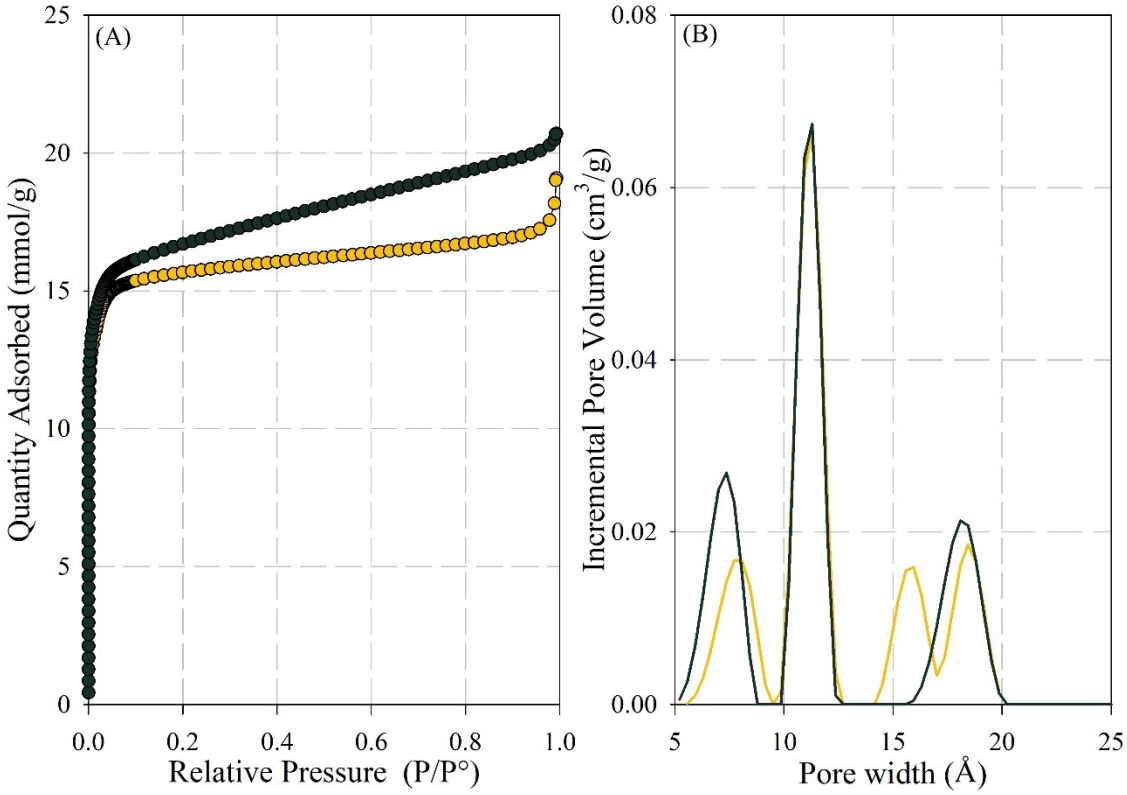

Figure 3.20: Nitrogen gas adsorption isotherms (A) measured at 77 K and the pore size distrubuition plots (B) of MeOH-UiO-66-AA (yellow trace) and MeOH-UiO-66-HCl (green trace).

The second scenario is that there is not complete displacement of the ligand, but the BDC becomes partially displaced from one cluster and stays attached to another. The vacant site on the cluster becomes filled with one methanol and one methoxy group (Figure 3.18 middle). In this scenario the BDC is still incorporated into the MOF, which still provides surface for the gas to bind, but there is an additional 63 g/mol added to the molecular weight of the MOF, which would cause there to be less moles of MOF in one gram of material. This change would decrease the overall surface area of the material. From the data we have obtained, we can not be certain which scenario is occurring but both

scenarios would lead to an overall decrease in the surface area of the MOFs, which is what we observe.

We turned our attention to the pore size distributions of the methanol-soaked MOFs. Examining MeOH-UiO-66-AA first (Figure 3.21A), we notice that the pore size distributions remain very similar to the parent material, UiO-66-AA. If anything, we notice a small increase in the defect pore (17 Å), which can indicate a very small amount of solvolysis occurring. If the BDC ligand is only partially displaced (i.e., only one of the two carboxylic acids is replaced with methanol/methoxy defects), then it is possible that very little change in the pore sizes would be observed, or that thermal solvent activation is sufficient to remove the methanol/methoxy groups and re-coordinate the ligand. If complete solvolysis of the ligand occurred, then one potential explanation for this is that once a BDC is removed and the two methanol and methoxy groups are coordinated to the cluster, the gap between these two defects/clusters is too small for the probe gas to occupy To the isotherm, this would effectively make the MOF look unchanged with respect to the pore filling process and thus no significant change would be observed in the isotherm.

Turning our attention to the pore size distributions for MeOH-UiO-66-HCl, we see a significant change. While the observed pore sizes of MeOH-UiO-66-HCl remain in the same location relative to the parent material, there is a large decrease in the defect pores observed in the 15-20 Å region and a large increase in the octahedral region. This indicates that there are more of the octahedral based pores, and by extension this would lead to an

increase in the amount of tetrahedral based pores. There are two possible explanations for this data.

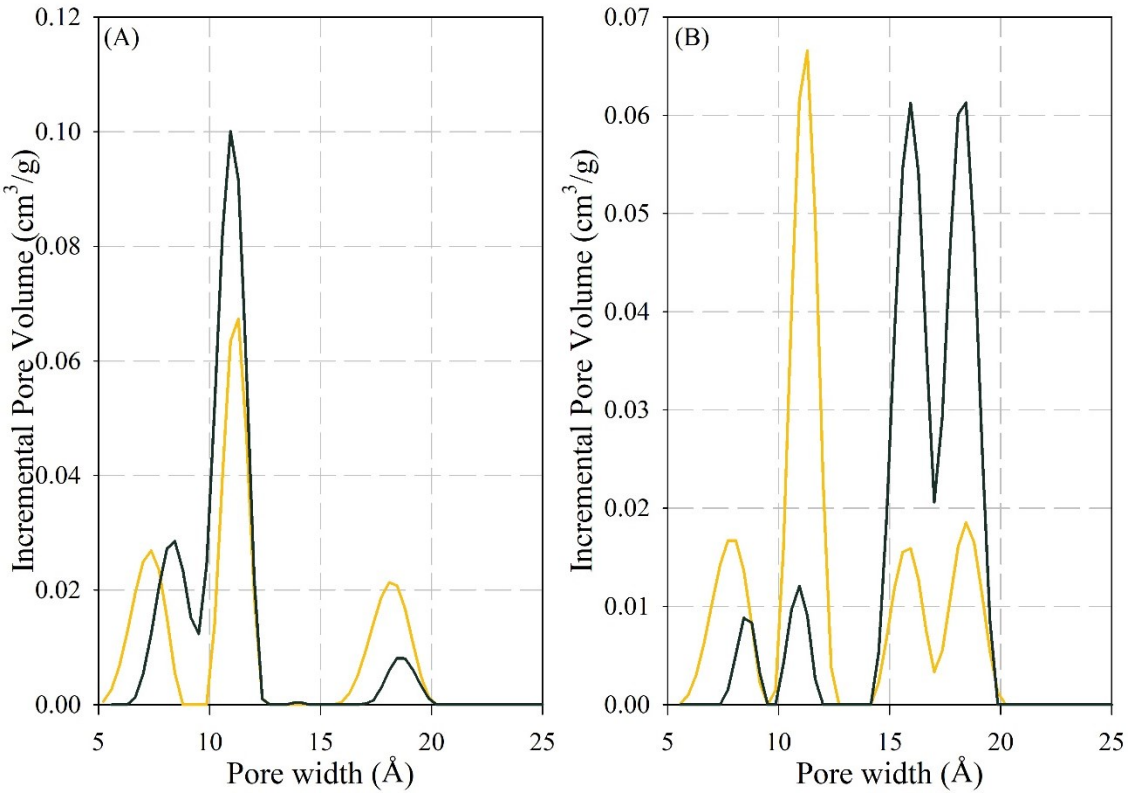

Figure 3.21: Pore size distributions of MeOH-UiO-66-AA (A), and MeOH-UiO-66-HCl (B) before (green trace) and after (yellow trace) soaking in methanol for three days.

Ameloot *et al*. suggest that the exchange is an equilibrium process.[86] One scenario that may be occurring is there is solvolysis of some of the BDC ligands found on the surface of the MOF. Once those ligands are now in solution, they can diffuse into the MOF and potentially re-incorporate back into the structure of the MOF. This would cause the internal defects to be "healed", producing a more perfect pore structure.

The second option is that the terminal methoxy/methanol defects close the gap between the two nodes sufficiently such that the probe gas can't occupy the space and thus

the isotherm would appear as if the material is "healed". This is similar to what we propose is occurring in MeOH-UiO-66-AA.

With the current data, we cannot conclude which of these options, or if another option that we haven't considered, is occurring. However, additional experiments can be preformed (TGA or quantitative NMR) to determine the number of ligands that are incorporated into the MOF. Regardless, what we observe is that the pore structure of MeOH-UiO-66-HCl appears to look very similar to that of pristine UiO-66.

Turning our attention to the carbon dioxide gas adsorption isotherms of the methanol soaked UiO-66 MOFs (Figure 3.22) we had observed some interesting results. In the parent UiO-66-HCl and UiO-66-AA MOFs we observed a higher curvature, and thus equilibrium constant, for UiO-66-AA. We see the opposite trend with the methanol-soaked MOFs; MeOH-UiO-66-HCl has a higher gas uptake and higher curvature compared to MeOH-UiO-66-AA. Fitting the isotherms to the single-site Langmuir equation to obtain the enthalpies of adsorption, we see MeOH-UiO-66-HCl has a much more exothermic enthalpy of adsorption compared to the parent material. The enthalpy of adsorption decreases from -20.9 ± 0.7 to -28.5 ± 2.1 kJ/mol after soaking in methanol. There are two main reasons for this change that we have hypothesized. The first hypothesis is the stark change in the pore sizes. We have seen from previous results that the presence of more of the smaller pores in UiO-66-AA leads to a large increase in the enthalpy of adsorption compared to UiO-66-HCl. Given that MeOH-UiO-66-HCl shows pore sizes similar to

UiO-66-AA, it is reasonable to expect the enthalpies to become more exothermic due to the creation of these confinement effects.

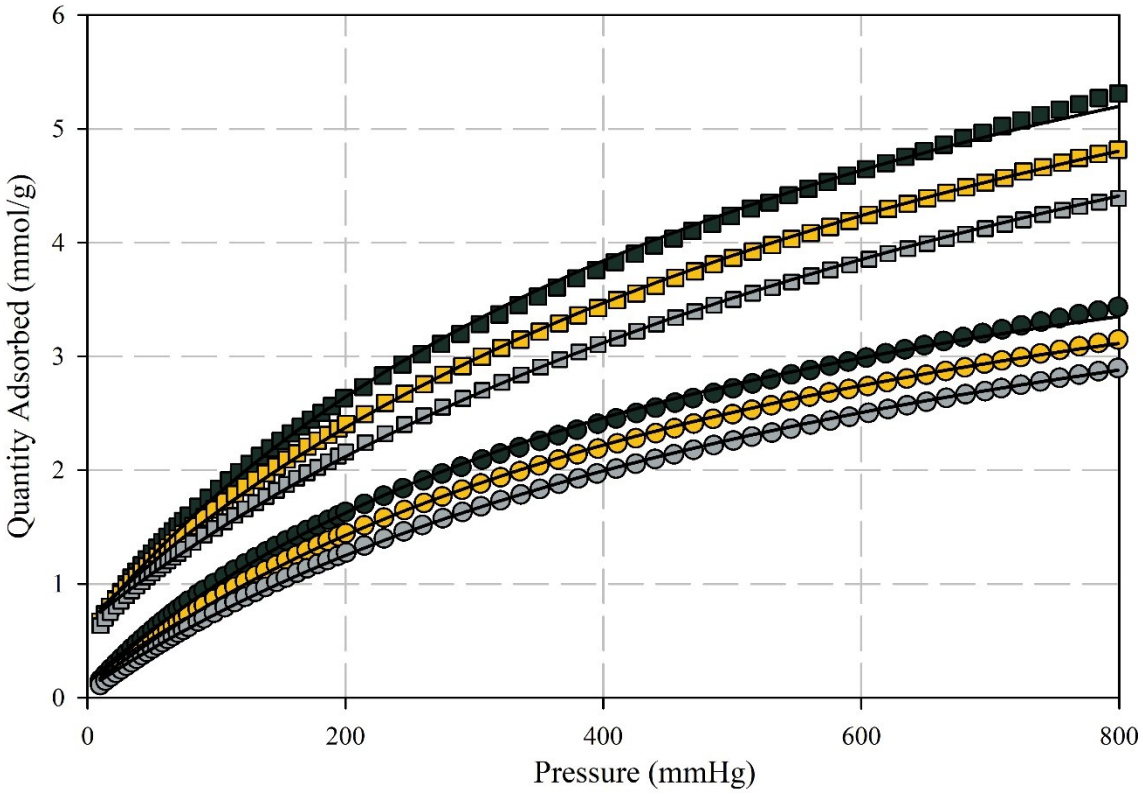

Figure 3.22: Carbon dioxide adsorption of MeOH-UiO-66-AA (circles) and MeOH-UiO-66-HCl (squares) at 278 K (green), 283 K (yellow), and 288 K (grey). Solid line repersents the isotherm after fitting to the single-site Langmuir equation.

Computational studies by Calero *et al.* have shown that the incorporation of a small amount of methanol inside the pores of UiO-66 causes an enhancement of adsorption of carbon dioxide in UiO-66. They suggest that methanol can adsorb in the octahedral pore first, and this causes a reduction in the pore size causing an increase in the confinement effect which is favorable for the carbon dioxide adsorption.[209] With this in mind we hypothesize that the coordinated methanol and methoxy groups could have the same impact on the enthalpy of adsorption in UiO-66 and UiO-67 as observed by Calero *et al.*

Turning our attention to UiO-66-AA, the enthalpies are relatively unchanged (−23.5 ± 1.7 vs. −24.3 ± 1.5 kJ/mol) for MeOH-UiO-66-AA and UiO-66-AA. This suggests that either the partial ligand solvolysis is ineffective, or that the thermal activation resulted in loss of methanol groups and the formation of UiO-66-AA from MeOH-UiO-66-AA; the pore size distribution would be consistent with both interpretations. This is not the case for MeOH-UiO-66-HCl, which looked very different upon thermal activation prior to gas adsorption.

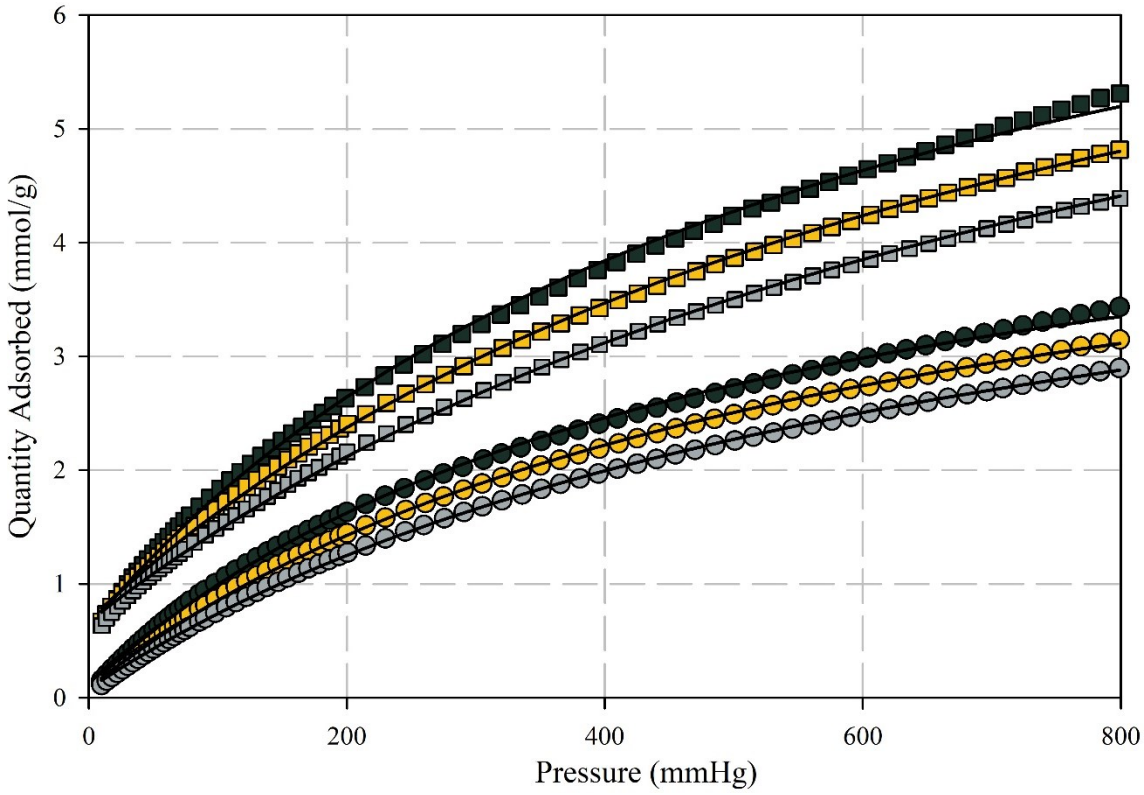

Figure 3.23: Carbon dioxide gas adsorption isotherm of UiO-66-AA (circles) and MeOH-UiO-66-HCl (squares) measured at 278 K (green), 283 K (yellow), and 288 K (grey).

Interestingly, however, is that the enthalpies for MeOH-UiO-66-HCl are more exothermic than UiO-66-AA (Figure 3.23). This may be due to the difference between a tetrahedral pore with six BDC ligands is not as ideal as a tetrahedral pore with 6-*x* ligands and 2*x* flexible methoxy/methanol defect groups nearly closing the tetrahedral pore. Alternatively, it is possible that the μ_3-OH is substituted by a μ_3-MeO groups. In combination with the pore healing effect, the μ_3-MeO has a higher steric profile on the pore which may lead to better confinement effects. This would suggest that the role of the μ_3-OH in UiO-66-AA may be more of a steric role than an electronic role on the confinement effects and the associated enthalpies of adsorption.

It is interesting to note that methanol soaking did not affect the enthalpies in UiO-66-AA despite the positive effects in MeOH-UiO-66-HCl. This would suggest that the role of the methanol is different in these two materials beyond the healing effect on the pore. Assuming the μ_3-MeO are being produced in MeOH-UiO-66-HCl, it is possible that these groups cannot be formed in UiO-66-AA because the mechanism for μ_3-MeO inclusion requires defects to be present at the onset of methanol soaking.

With these results in mind, we wanted to determine how soaking UiO-67 in methanol would change the uptake carbon dioxide adsorption properties of these materials. We hypothesized that the introduction of the larger MeO^-/MeOH may potentially enhance the gas uptake properties, along with the addition of a more favorable interaction site as seen in the methanol soaked UiO-66 MOFs. To ensure that there was no destruction to UiO-67 after soaking in methanol the nitrogen gas adsorption and powder X-ray

diffractograms were measured. The BET accessible surface area in MeOH-UiO-67-AA increased from 1500 to 2430 m^2/g, while the surface area for MeOH-UiO-67-HCl decreased from 2400 to 2100 m^2/g.

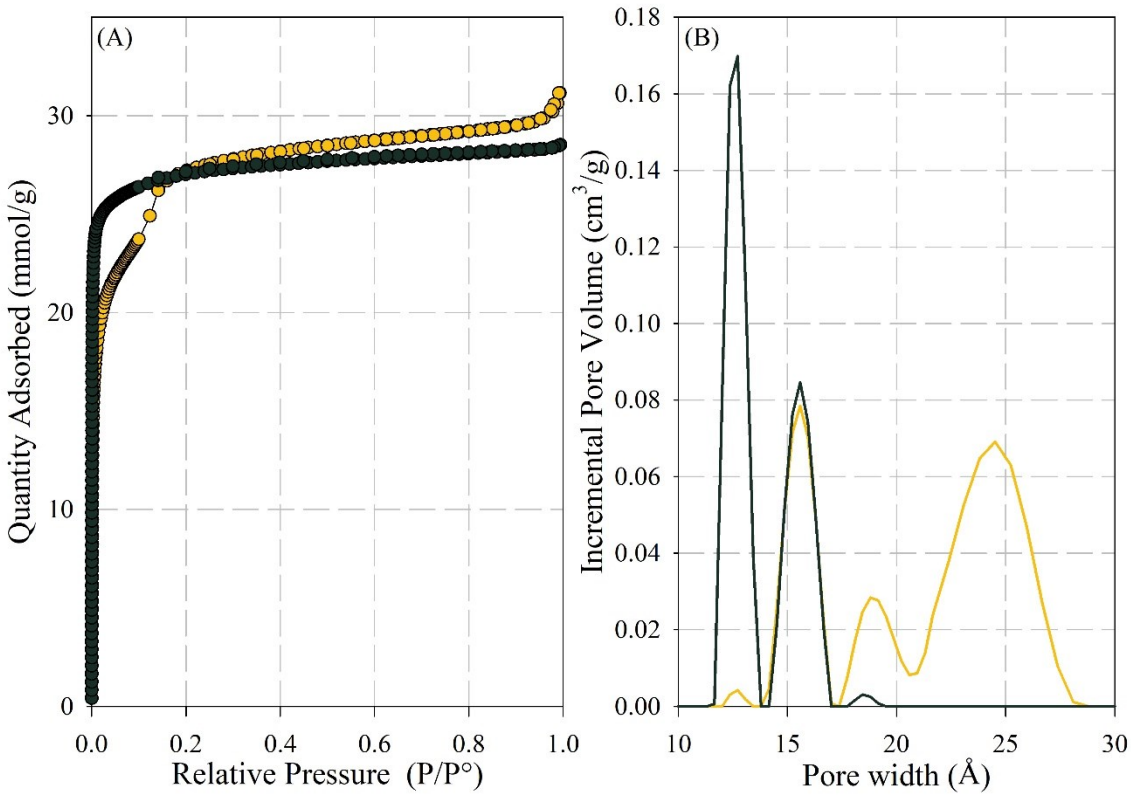

Figure 3.24: Nitrogen isotherms (A) measured at 77 K and the pore size distrubuition plots (B) of MeOH-UiO-67-AA (green trace), and MeOH-UiO-67-HCl (yellow trace).

From the pore size distributions, it is evident that the MeOH-UiO-67-AA still possess a smaller pore at approximately 12 Å, and neither of the MOFs show much deviation in the pore size distribution when compared to the parent materials (Figure 3.25). From Figure 3.25 it is evident that soaking the UiO-67s did not provide a large difference in the pore size distribution as was observed in UiO-66-HCl. The powder X-ray diffractograms collected show no loss of crystallinity as shown in Figure 3.26.

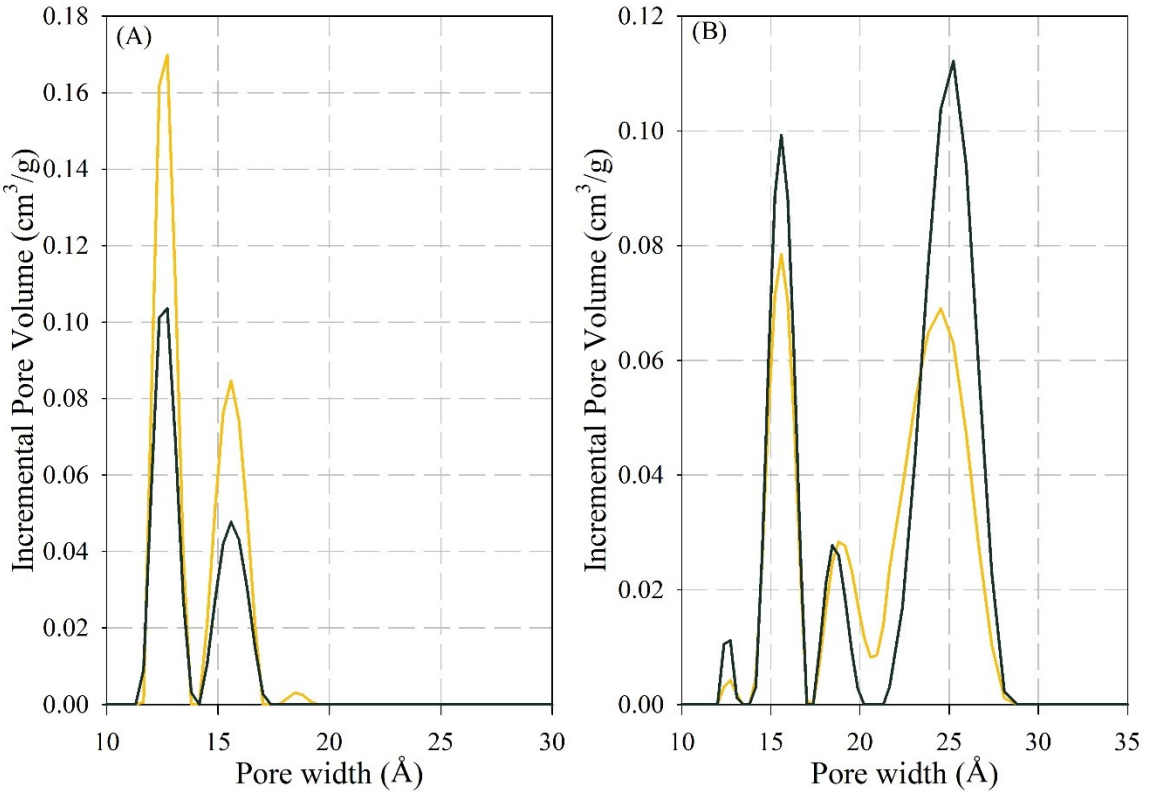

Figure 3.25: Pore size distributions of MeOH-UiO-67-AA (A) and MeOH-UiO-67-HCl (B) before (green trace) and after (yellow trace) soaking in methanol for three days.

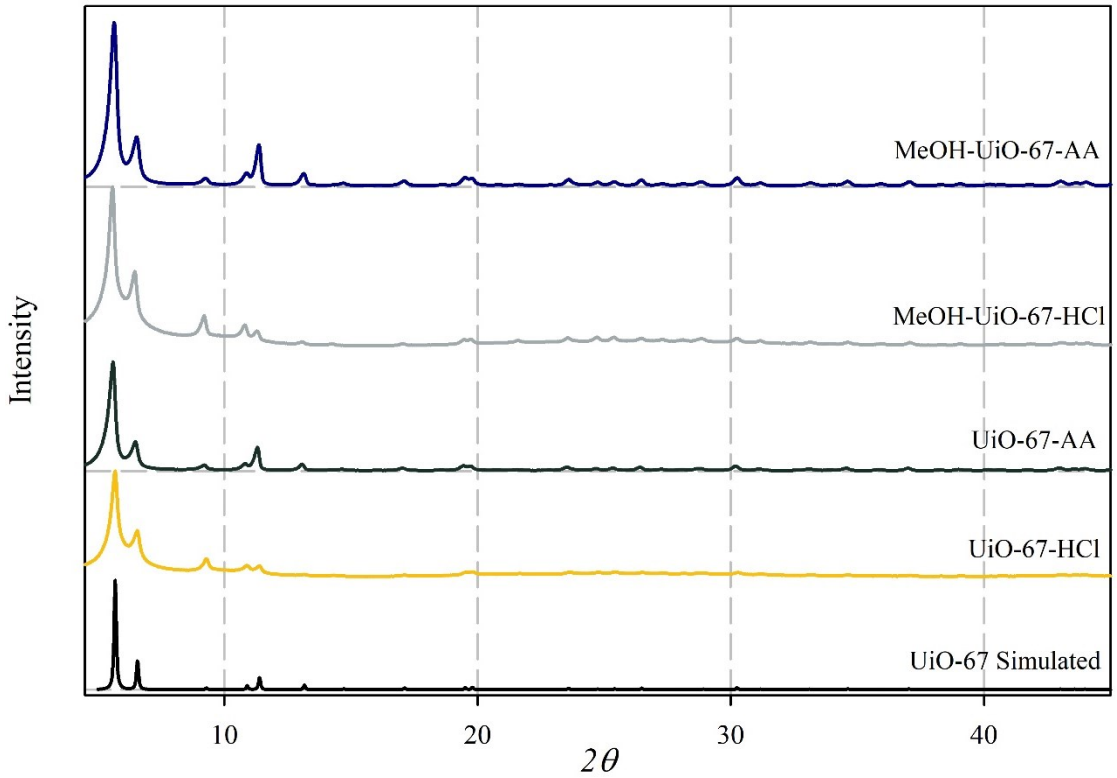

Figure 3.26: Powder X-ray diffractograms of simulated UiO-67 (black), UiO-67-HCl (yellow), UiO-67-AA (green), MeOH-UiO-67-HCl (grey), and MeOH-UiO-67-AA (blue).

The carbon dioxide gas adsorption isotherms of the methanol-soaked UiO-67 looked very similar to all the previous UiO-67 samples, where there was very little difference between the hydrochloric acid synthesis and the glacial acetic acid synthesis. First, examining the Q_{max} values from a single-site Langmuir isotherm we see an increase in the UiO-67-AA after soaking in methanol, it increased from 5.86 to 7.70 mmol/g, while there was a small decrease in the UiO-67-HCl sample from 8.93 to 7.18 mmol/g. These samples do show slightly more curvature than the ΔUiO-67 samples.

The calculated enthalpies of adsorption were found to be very similar in these samples, MeOH-UiO-67-AA had an enthalpy of adsorption of −19.4 ± 1.7 kJ/mol, a slight

decrease from the −16.9 ± 1.8 kJ/mol of the parent material. MeOH-UiO-67-HCl had a calculated value of −19.7 ± 2.5 kJ/mol, a slight increase from the parent material that had a value of −21.2 ± 2.2 kJ/mol. The calculated enthalpies of adsorption for both MeOH-UiO-67 samples are within error, suggesting that there may not be a large difference in the parent and modified materials.

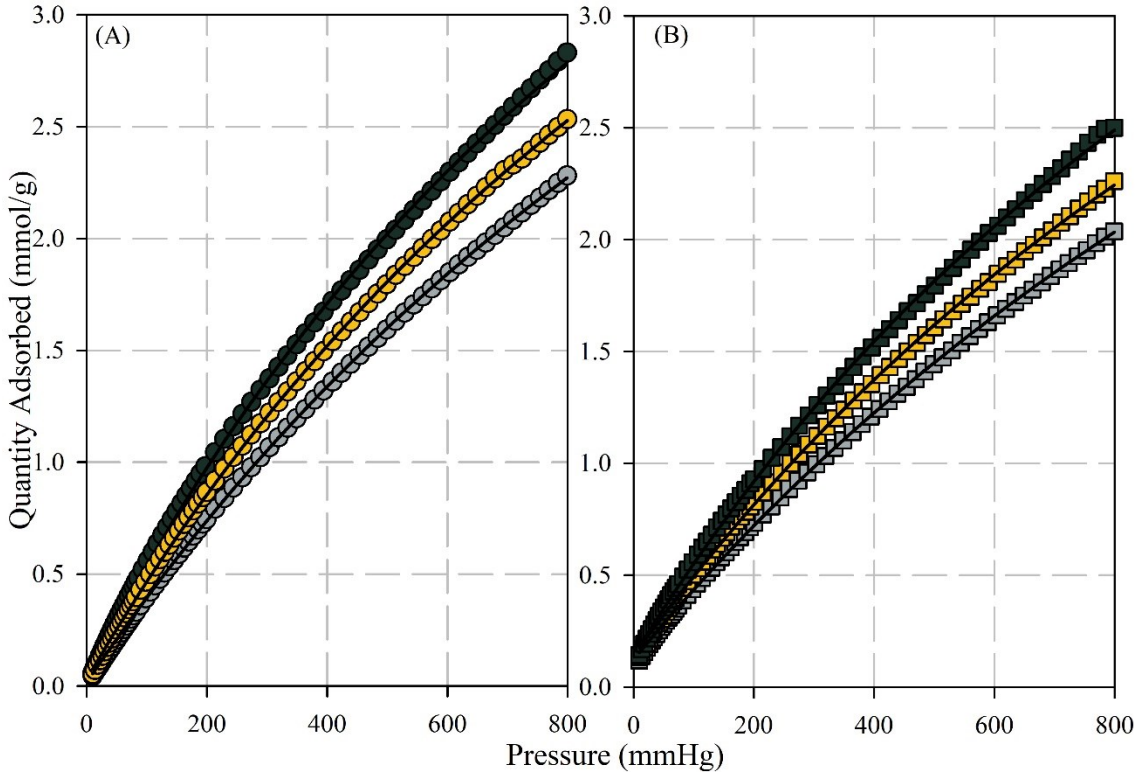

Figure 3.27: Carbon dioxide gas adsorption isotherm of MeOH-UiO-67-AA (A) and MeOH-UiO-67-HCl (B) at 278 K (green), 283 K (yellow), and 288 K (grey). Solid line repersents the isotherm after fitting to the single-site Langmuir equation.

Interestingly, from the methanol-soaked materials, the calculated enthalpies of adsorption are quite similar, regardless of the acid modulator that was used during synthesis. Similar to the heated samples of UiO-67, this provides insight into the adsorption interactions between the functional groups on the cluster and the carbon dioxide gas. From

our previous experiments we know that UiO-67 does not contain a pore size that is ideal for adsorption of carbon dioxide, and there is no drastic change in pore size observed. This indicates that the small decrease in the heats of adsorption observed in the methanol-soaked samples is from the addition of the more favorable interactions provided from the methanol/methoxy groups that are now present on the cluster.

3.3 Conclusions

In examining the carbon dioxide adsorption of modified and functionalized UiO-66 and UiO-67, synthesized through two different methods, we were able to determine the structure property relationship between pore size, presence/absence of defects, dehydration and functionalization of the cluster. It has been demonstrated that the pore size, leading to confinement effects played the biggest role in an increased enthalpy of adsorption of UiO-66. UiO-66-AA and MeOH-UiO-66 had the smallest pore sizes as found in the pore size distribution, and the highest heats of adsorption. Derivatives of UiO-67 had the largest pore size and contained the lowest heats of adsorption. Furthermore, we were able to show that the presence of the μ_3-OH present in the cluster also plays a crucial role in carbon dioxide adsorption, when all samples of UiO-66 and UiO-67 were heated past 573 K there was a decrease in the enthalpy of adsorption. Using these findings, the development of more efficient carbon dioxide adsorbing MOFs is possible due to the better understanding of the structure property relationship of the UiO family of MOFs and the interactions of carbon dioxide.

3.4 Experimental

3.4.1 General Methods

All reagents were purchased from chemical suppliers and used without further purification.

3.4.2 Synthesis

UiO-66-HCl

Following a literature procedure,[56] 0.1255 g (0.5385 mmol) of $ZrCl_4$ and 0.1247 g (0.7506 mmol) of terephthalic acid were added to a 25 mL Duran vial. To the vial 15 mL of *N,N*-dimethylformamide (DMF) and 1 mL of concentrated hydrochloric acid was added and the vial capped. The solution was sonicated until all solids were dissolved resulting in a clear colourless solution, this took approximately five minutes. Once all solids were dissolved the vials were placed in a 353 K oven overnight. The jar was removed from the oven cooled to room temperature and the resulting solid and solution was transferred to a 50 mL centrifuge tube and centrifuged at 7800 RPM for 3 mins, the solution was decanted and 15 mL of fresh DMF was added, and the process was repeated three times. After three washes with DMF the same process was repeated with methanol three times. After the final washing the centrifuge tube with the white powder was placed in an oven at 353 K overnight to remove any residual methanol.

UiO-67-HCl

Following a literature procedure,[56] 0.0673 g (0.2888 mmol) of $ZrCl_4$ and 0.0922 g (0.3806 mmol) of 4,4-biphenyldicarboxylic acid were added to a 25 mL Duran vial. To the vial 15 mL of DMF and 0.5 mL of concentrated hydrochloric acid was added and the vial capped. The solution was sonicated for approximately ten minutes, not all the solids dissolved. Once sonication was completed vials were placed in a 353 K oven overnight. The jar was removed from the oven cooled to room temperature and the resulting solid and solution was transferred to a 50 mL centrifuge tube and centrifuged at 7800 RPM for three minutes, the solution was decanted and 15 mL of fresh DMF was added, and the process was repeated three times. After three washes with DMF the same process was repeated with methanol three times. After the final washing the centrifuge tube with the white powder was placed in an oven at 353 K overnight to remove any residual methanol.

UiO-66-AA

Following a modified literature procedure,[206] in a 50 mL Duran vial 0.1488 mg (0.6385 mmol) of $ZrCl_4$ and 0.1064 mg (0.6405 mmol) of terephthalic acid was combined, and 40 mL of DMF was added along with 11 mL of glacial acetic acid. The mixture was then sonicated until all the precipitate had dissolved, approximately ten minutes. Once a clear colourless solution remained this was placed in a 393 K oven overnight. The jar was removed from the oven cooled to room temperature and the resulting solid and solution was transferred to a 50 mL centrifuge tube and centrifuged at 7800 RPM for three minutes, the solution was decanted and 30 mL of fresh DMF was added, and the process was

repeated three times. After three washes with DMF the same process was repeated with methanol three times. After the final washing the centrifuge tube with the white powder was placed in an oven at 353 K overnight to remove any residual methanol.

UiO-67-AA

Following a modified literature procedure,[206] in a 50 mL Duran vial 0.1488 mg (0.6385 mmol) of $ZrCl_4$ and 0.1551 mg (0.6403 mmol) of 4,4-biphenyldicarboxylic acid was combined, and 40 mL of DMF was added along with 11 mL of glacial acetic acid. The mixture was then sonicated for approximately ten minutes, not all the precipitate dissolved. Once a clear solution remained this was placed in a 393 K oven overnight. The jar was removed from the oven cooled to room temperature and the resulting solid and solution was transferred to a 50 mL centrifuge tube and centrifuged at 7800 RPM for three minutes, the solution was decanted and 30 mL of fresh DMF was added, and the process was repeated three times. After three washes with DMF the same process was repeated with methanol three times. After the final washing the centrifuge tube with the white powder was place in an oven at 353 K overnight to remove any residual methanol.

Dehydration of the MOFs

Dehydrated node UiO-66 and UiO-67 (ΔUiO-66-AA, ΔUiO-66-HCl, ΔUiO-67-AA, and ΔUiO-67-HCl) were synthesized by a stepwise heating profile. Initially the samples were heated on a Micrometrics SmartVac Prep under vacuum to 363 K at a rate of 5 deg/min and held for thirty minutes, followed by heating to 423 K at 5 deg/min and held for sixty minutes and finally heated to 573 K with a heating rate of 5 deg/min and

held for five hundred and forty minutes. Heating to 573 K allowed for the dehydration of the node.

Solvolysis of the MOFs

Solvolysis of the node/ligand of both UiO-66 and UiO-67 (MeOH-UiO-66-AA, MeOH-UiO-66-HCl, MeOH-UiO-67-AA, and MeOH-UiO-67-HCl) were formed according to a literature procedure. Briefly, a sample of the parent MOF (0.0400 - 0.0600 g) was placed in a vial with 10 mL of methanol and allowed to soak for three days.[86] The samples were then centrifuged at 7800 RPM for five minutes and the methanol decanted off. The MOFs were then dried in a 323 K oven overnight.

3.4.3 Gas Adsorption Studies

Prior to gas adsorption measurements samples were activated on a Micrometrics Smart VacPrep or a Micrometrics VacFlow prep. Caution must be taken with the dehydrated samples (ΔUiO-66-AA, ΔUiO-66 HCl, ΔUiO-67-AA, and ΔUiO-67-HCl), overheating can lead to degradation of the material. For this reason, all dehydrated samples were activated on a Micromeritics Smart VacPrep as it allowed for more precise control of the heating rate. For the remaining samples, the gas adsorption results were consistent between samples activated on both a Smart VacPrep and a VacFlow Prep. On the SmartVac Prep samples were heated to 363 K at a rate of 5 deg/min and held for thirty minutes, followed by heating to 423 K at a rate of 5 deg/min and held for six hundred minutes. On the VacFlow prep, samples were evacuated by slowly opening the vacuum valve for the sample compartment and leaving the sample exposed for three minutes. Afterwards, the

valve was closed for three minutes. This process was repeated three times. Afterward, the sample was placed under vacuum and the temperature was set to 363 K and left for forty-five minutes. This was followed by overnight heating at 423 K under vacuum.

Nitrogen and carbon dioxide gas adsorption isotherms were measured on a Micrometrics 3Flex. Nitrogen gas adsorption isotherms were measured at 77 K. Carbon dioxide gas adsorption isotherms were measured using a water circulating bath to maintain a temperature of 278 K, 283 K or 288 K; this enabled us to extract thermodynamic adsorption parameters.

3.4.4 Powder X-ray Diffraction

Powder X-ray diffraction patterns were measured on a Rigaku Miniflex 600 with a copper radiation source. Patterns were measured from 3º to 60º in 2θ with a step size of 0.02º 2θ at a rate of 5º/minute.

3.4.5 Data Fitting

Section 1.4.2 discusses how thermodynamic properties can be extracted from gas isotherms, however, it does not cover how the equilibrium constant can be determined from the isotherm. For this discussion three isotherms of UiO-66-AA (Figure 3.28) will be used, and the results have been previously discussed in Section 3.2. Fitting was done using SigmaPlot 13 graphing software. The errors provided from the software only represent the error of how the data fits, we did not think that this was the most accurate representation of the errors.

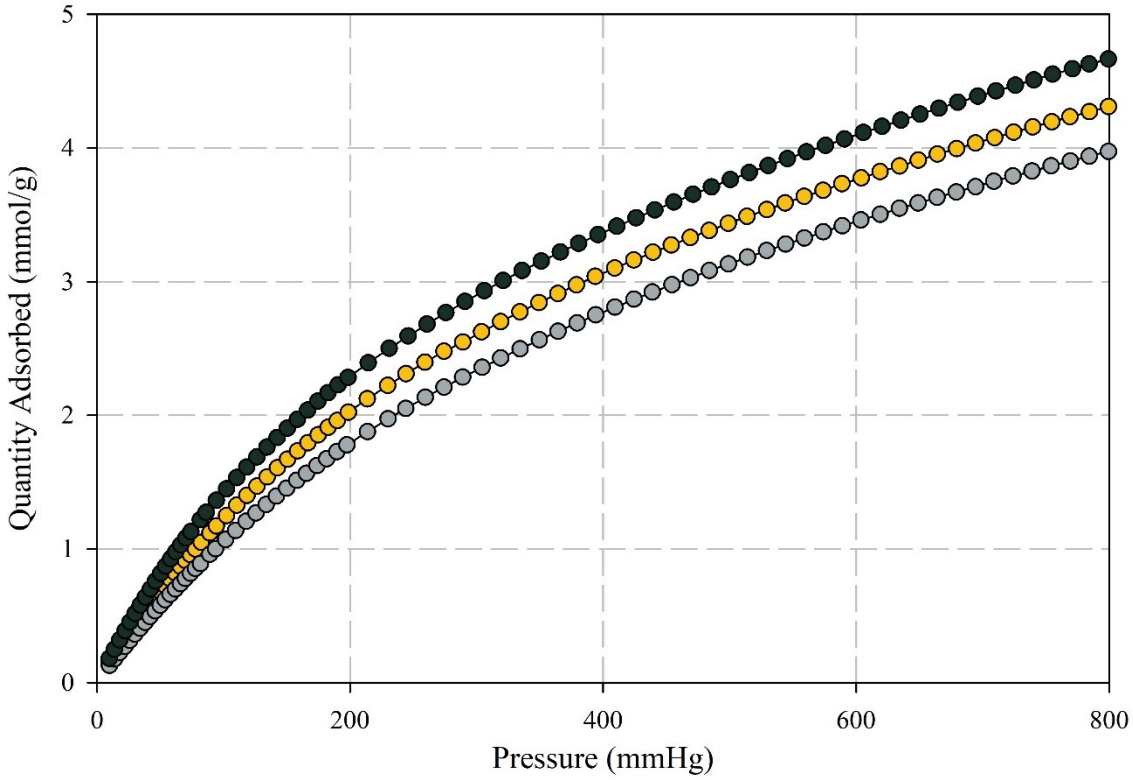

Figure 3.28: Carbon dioxide isotherms of UiO-66-AA measured at 278 K (green) 283 K (yellow) and 288 K (grey).

When fitting this isotherm to the single-site Langmuir equation (Equation 1.8), there are a few assumptions that are made to obtain the most accurate enthalpy of adsorption. Since the three temperature runs are performed on the same material, a safe assumption is that the value for Q_{max} should be constant between the three runs. In other words, the maximum amount a gas that the MOF can hold is not temperature dependent but is a physical attribute. Using only one parameter of Q_{max} for the three isotherms would reduce the number of variables that need to be extracted from the fit thereby reducing the errors on the fits. For example, in the absence of this assumption, each isotherm would produce a value of Q_{max} and a value of K (6 parameters overall) but fixing the fit to one value of Q_{max} would reduce the number of parameters to 4. The other assumption that was

made was that there is some background adsorption, from the tube or small leaks in the instrument that are completely unavoidable and must be accounted for. To account for this, we introduce a correction factor (Equation 3.2; c) to the equation. This simply introduces an offset in the y-axis to account for a constant background adsorption. This results in the single-site Langmuir equation that was used to fit our collected data.

$$Q_{ads} = Q_{max}\frac{KP}{(1+KP)} + c \qquad 3.2$$

Fitting the isotherms shown in Figure 3.28 to the single-site Langmuir equation without the c constant and not fixing Q_{max} to a single value gave an enthalpy of adsorption to be −19.7 kJ/mol, while demonstrating an error of 0.3 kJ/mol. While this value may be considered a good measurement because of the low error, it may not be an accurate representation of the enthalpy of adsorption. The Q_{max} values that were calculated varied from 6.8 to 6.7 and 6.5 mmol/g as the temperature was increased from 278 to 283 to 288 K. The decrease in the Q_{max} is not chemically reasonable as stated above, with a Q_{max} that is not chemically reasonable the obtained equilibrium constant is likely not chemically reasonable. Knowing that Q_{max} should remain unchanged we can now look into how the equilbirum constant, and calculated enthalpy of adsorption will change under these assumptions. The new enthalpy of adsorption is calculated to be −24.3 +/- 0.1 kJ/mol, with an error associated with this just as low as the value not using the outlined assumptions. Given that our constraints and assumptions are chemically reasonable, and the errors are approximately the same, we opted for a fitting model with a global Q_{max} and a background correction term.

To gauge the error in our measurements we propagated the error from the calculation of the equilibrium constant to the Van 't Hoff plot (Figure 3.29). We fit the data to the line of best fit. While it is possible to get the error of the slope and intercept, and thus the error of the enthalpy and entropy from the fit of the line, this represents the error of the fit of the line and does not factor in the error of the equilibrium constants (i.e., the errors from the original fit). To address this, we also fit the data to the max and min lines from the error bars to obtain a high and low estimate for the enthalpy of adsorption (Table 3.3). This allowed us to estimate the error from the data. To illustrate the difference here, when we used the error from the line, we get a heat of −24.3 ± 0.1 kJ/mol, but when we use the errors from the equilibrium constant, we get −24.3 ± 1.5 kJ/mol. The latter seems more reasonable as it reflects the errors of the original fit.

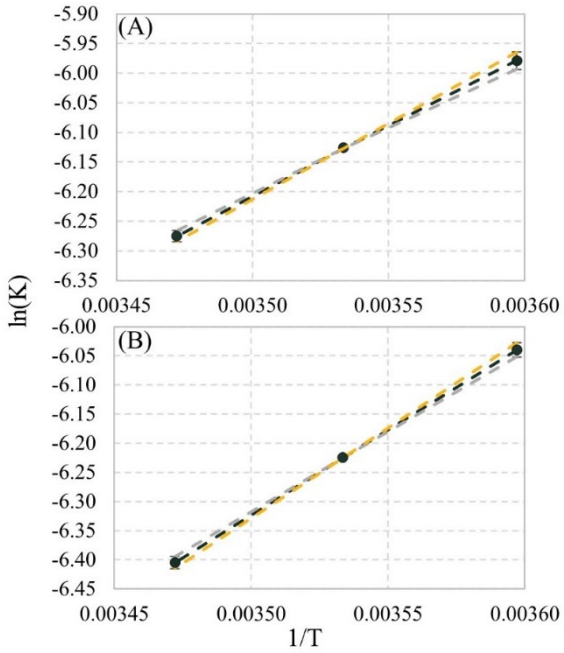

Figure 3.29: Errors in the equilibrium constant when fitting the carbon dioxide data for UiO-66-AA with no constraints and no c constatn (A) and with constraints and a c constant (B) The green trace repersents the original equlibrium data, yellow repersents the high end estimation while grey repersents the low end estimation.

Table 3.3: Calculated enthalpies of adsorption for UiO-66-AA using a single-site Langmuir equation with and without constraints and a C constant.

	Low Estimate (kJ/mol)	**High Estimate (kJ/mol)**	**Fit Data (kJ/mol)**	**Standard Deviation (kJ/mol)**
Unconstrained with no c	−18.1	−21.3	−19.7	1.6
Constrained with c	−22.8	−25.8	−24.3	1.5

We also attempted to fit the data to a dual site Langmuir isotherm, using the same constraints listed above to determine if this model was better at fitting our experimental data. For some of the fitting parameters, the obtained values provided errors so large the results were rendered meaningless. For UiO-66-AA one of the Q_{max} values were found to have an error three orders of magnitude higher than the calculated Q_{max} value.

Chapter 4: Future Work

A good project is never truly complete and there are always other avenues to explore. With that in mind, this chapter builds on the work in Chapter 2 and 3. Several of these projects were started during my PhD but could not be completed due to time constraints. Some of these research directions are in their infancy with only a few data points, while others have some initial results that can help guide future students. Finally, a few projects are presented that have been imagined while in the lab and writing this thesis will be outlined.

4.1 Mixed Gas Measurements

4.1.1 Scope and Early Results

One of the most interesting results found when exploring the water uptake capabilities of UiO-66, UiO-67, and UiO-68 was the larger MOFs (UiO-67 and UiO-68) do not completely saturate with water. From the work in Chapter 2, I believe that there should be additional space in the pore for other gases to adsorb around the ligand while water is present around the node. At the time of conducting the experiments, we did not have a good method to explore this hypothesis. Specifically, I wonder if there is competitive binding with gases in the MOF, or if it possible to spatially separate gases in the MOF to the node and the ligand. The Katz research group now has two unique ways of exploring this. The research team recently installed a Hiden Automated Breakthrough Analyzer. A breakthrough reactor takes a packed column of material and flows a pure gas, gas mixture, or gas-vapour mixture through the column while monitoring the downstream gas composition via mass spectrometry. This can be done as a function of temperature and pressure as well. Thus, with this new instrument, the competitive binding of water and other gases such as nitrogen, carbon dioxide, and methane can be measured, and insight can be provided in the quantity of gases that can be stored simultaneously inside the MOF. Additionally, the research team has an IR system with a praying mantis cell capable of measuring the IR of a material as a function of time and gas exposure. These offer a unique opportunity to study competitive binding, cooperative binding, and spatially separated gas storage.

In our early results we have measured the breakthrough times (the amount of time required for gas to pass through a material) of both UiO-66-HCl and UiO-66-AA with a stream of gas comprised of 85% nitrogen and 15% carbon dioxide (8.5 mL/min nitrogen, 1.5 mL/min carbon dioxide). This is approximately the composition of post-combustion gas. I ran these experiments at a range of different pressures at 293 K. The breakthrough times were normalized per gram of material and reported in Table 4.1 below.

Table 4.1: Breakthrough times (reported in seconds/g) for nitrogen and carbon dioxide for UiO-66-AA and UiO-66-HCl.

		Breakthrough time (s/gram) at different pressures			
UiO-66	**Gas**	**1 bar**	**2 bar**	**3 bar**	**3.5 bar**
Acetic Acid	Carbon Dioxide	213.2	491.3	729.2	137.8
	Nitrogen	74.0	136.1	162.9	101.2
Hydrochloric Acid	Carbon Dioxide	375.3	553.7	701.0	747.4
	Nitrogen	46.6	70.5	55.1	108.6

From this preliminary data, we can see that as there is an increase in the pressure of the gas, there is an increase in the breakthrough time. Assuming approximately similar kinetics, this indicates that as pressure increases the material can store more of each gas. This is what would be expected if the carbon dioxide isotherm continued to absorb more gas at higher pressures (Chapter 3). Furthermore, we note that the breakthrough time of carbon dioxide is much higher than the breakthrough time of nitrogen, indicating that the interaction between carbon dioxide and the MOF is stronger than the interaction between

nitrogen and the MOF (at 293 K). Under ambient conditions, this means that both UiO-66-HCl and UiO-66-AA are more selective to carbon dioxide over nitrogen. Again, this is unsurprising. Of particular note, however, is that the 3.5 bar data for UiO-66-AA shows different behaviour than UiO-66-HCl. UiO-66-AA has a shorter breakthrough time than UiO-66-HCl. This suggests that there is a change in the adsorption capacity at higher pressures due to the presence of defects. This, and other breakthrough and IR data are worth further exploration.

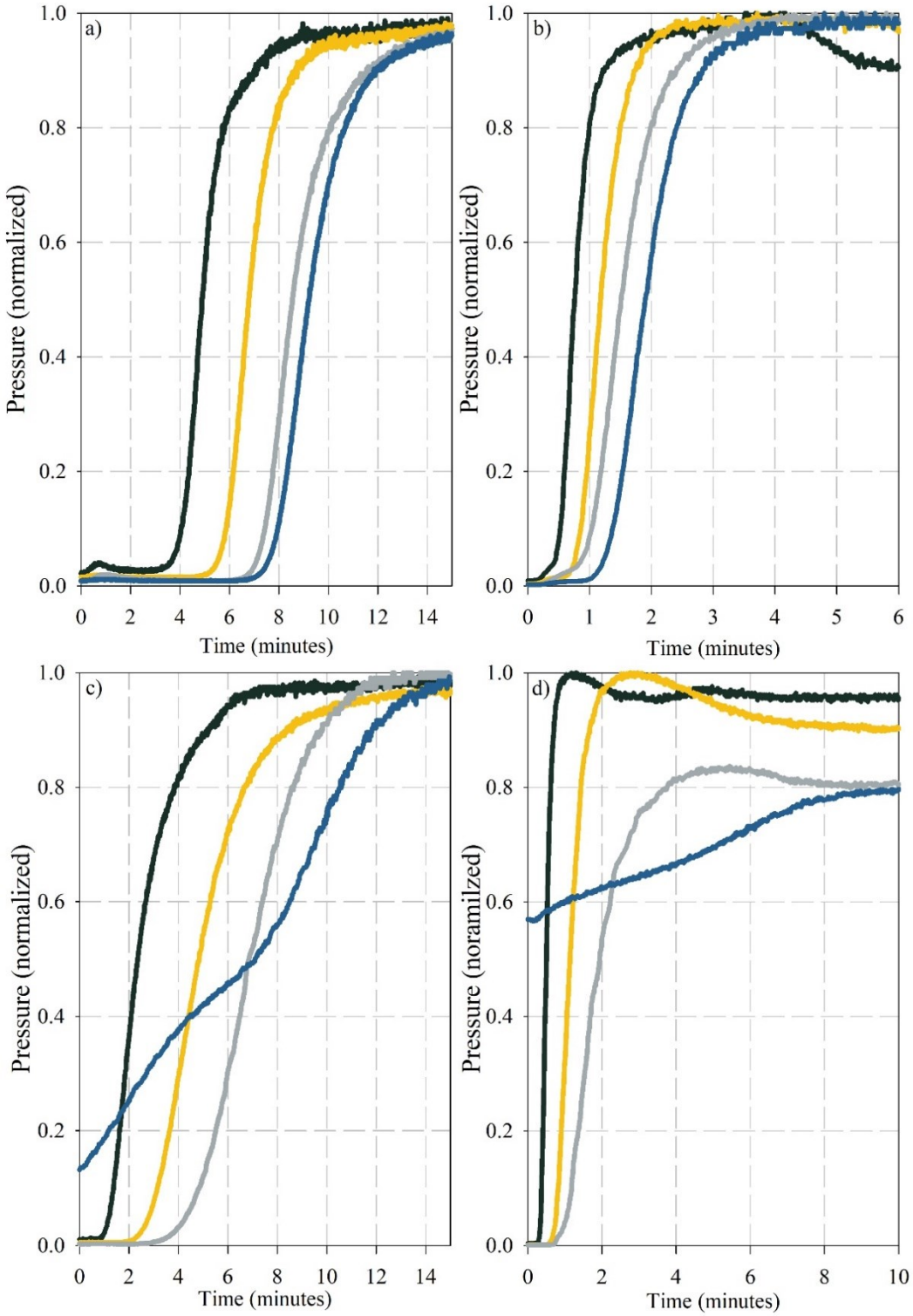

Figure 4.1: Breakthrough curves of carbon dioxide (A) and nitrogen (B) for UiO-66-HCl UiO-66-AA (C - carbon dioxide and D - nitrogen). Measured at 1 bar (green trace) 2 bar (yellow trace) 3 bar (grey trace) 3.5 (blue trace).

Examining the difference in the breakthrough times of the two synthetic procedures, we do notice a difference between the two materials. This is expected as they both show different pore sizes, and different uptake capacities. These breakthrough experiments can be very beneficial to further understand the kinetics of how these gases move through the materials, and how having different gas mixtures may impact the adsorption capacity of the MOFs.

Upon first inspection, UiO-66-HCl has a longer breakthrough time at both 1 bar and 2 bar. In Chapter 3 the pore sizes of both materials were extensively characterized, and it was discovered that UiO-66-HCl had the larger pore size. The larger pore could allow for the gas to flow much faster through the material resulting in faster kinetics and breakthrough times. This rationalization can be applied to both nitrogen and carbon dioxide breakthrough times. However, we see the reverse trend with UiO-66-HCl having longer breakthrough times up until nearly 3 bar vs. UiO-66-AA. This may suggest that the adsorption capacity of these gases is higher for UiO-66-HCl at these pressures. I believe future work should explore how temperature, pressure, and gas composition (CO_2:N_2, and CO_2:N_2:H_2O) affect the breakthrough time, shape of the curve, and adsorption capacity. This should be compared to the thermodynamic gas adsorption data for the pure gases/vapours in order to determine if cooperative effects or detrimental effects occur when mixtures are studied.

From the data above, a plot comparing pressure and breakthrough time (Figure 4.2) can be assembled. Leaving out the 3.5 bar data, I observed that UiO-66-AA has a much

larger slope (258 versus 163 seconds/g/bar), which indicates as the pressure increases, there is a stronger affinity for carbon dioxide in the MOF. This trend may be due to competitive binding of nitrogen and carbon dioxide. This plot may be a good way to illustrate if competitive binding or cooperative effects are possible. By repeating the data above and comparing the slopes, it should be possible to assess how much of a role mixed gases have on the overall material performance.

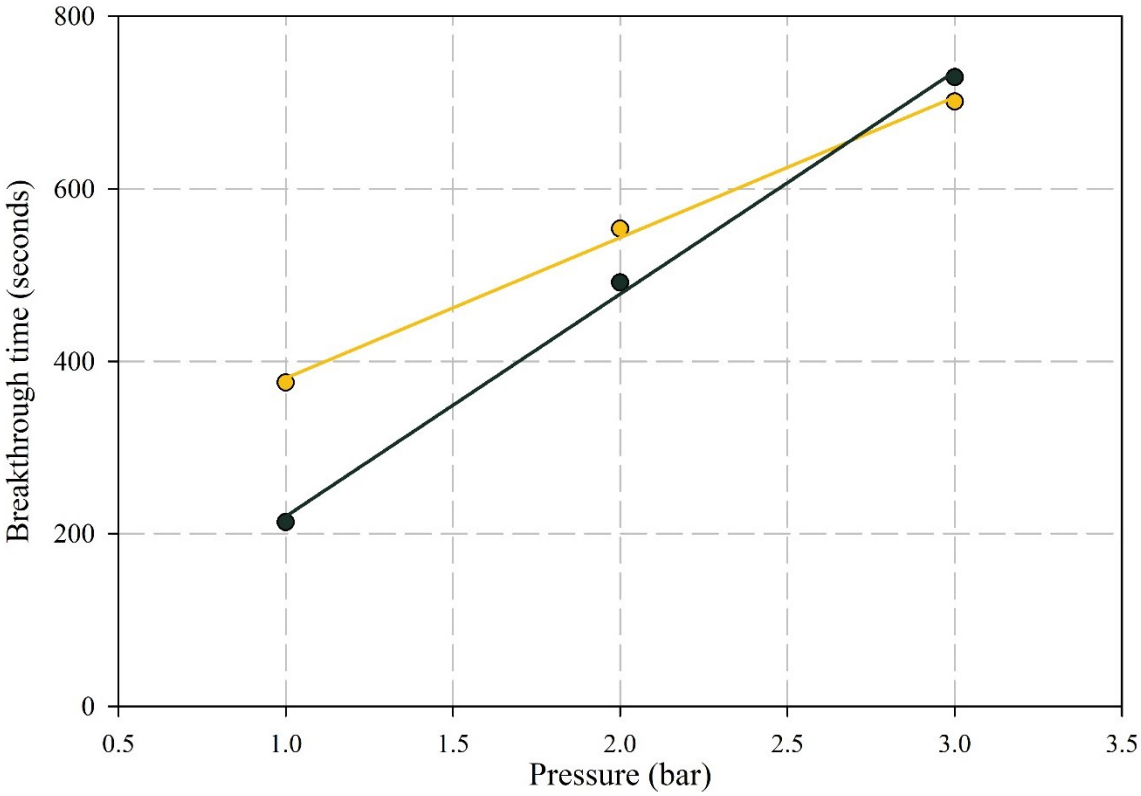

Figure 4.2: Breakthrough time versus pressure for carbon dioxide in UiO-66-HCl (yellow) and UiO-66-AA (green).

4.1.2 Future Experiments

Further investigation into how the change in temperature and pressure would change the breakthrough times of nitrogen and carbon dioxide to see if there is a

relationship between pressure, temperature, and breakthrough time. The data indicates that there are differences between these materials, but further exploration is needed. In addition to the breakthrough data, nitrogen gas adsorption isotherms at these temperatures may shed some light into the competitive binding. At the very least, with nitrogen isotherms at these temperatuers, we should be able to determine the theoretical separation selectivity vs. the observed selectivity from the breakthrough data.

In all the early experiments illustrated above, we have not explored how the addition of water vapour has impacted the breakthrough times or adsorption capacity of UiO-66. Future work would include measuring the breakthrough times of the MOF under two situations. The first scenario would be with water vapour present in the carrier gas, this would provide insight into how competitive binding would occur when the MOF was freshly synthesized and did not have any gases inside the pore. Based on the breakthrough times, we could determine how water vapour affects a dry MOF during its first moisture exposure.

The second scenario involved performing these measurements on a MOF that has already been pre-saturated with water. In the case of UiO-66 we have determined that storing the MOF at a relative humidity much above its saturation point does not have any detrimental effects. UiO-66 could be stored in a relative humidity environment above the point of saturation until it has equilibrated, then the breakthrough times measured without prior sample activation. Alternatively, the breakthrough instrument could be used to do a humid breakthrough of nitrogen gas and then the gas composition changed to determine the effect of pre-humidified MOF on the sample. Comparing the breakthrough times and

the shapes of the curves from the unsaturated materials and the saturated materials would provide information to how much space is available once the MOF is saturated.

The ratio of nitrogen to carbon dioxide should also be explored, the initial experiments were performed at 85% nitrogen and 15% carbon dioxide mixture. By varying the concentration of these gases it may provide some insight into the competitive binding between nitrogen and carbon dioxide that may be happening in the MOF.

These experiments can then be further carried out on UiO-67 and UiO-68. We know that the desorption of water in these MOFs can be problematic, therefore the second scenario outlined above would not be appropriate for these materials. The second scenario could be modified, we had discovered that adsorption and desorption below the large uptake of water vapour does not lead to decomposition of UiO-67 and UiO-68. These two MOFs could be stored in an environment where some water vapour is adsorbed, but not enough to cause detrimental effects to the material. Once they have equilibrated, the breakthrough times could then be measured and compared to the freshly synthesized materials.

4.1.3 Experimental

4.1.3.1 General Methods

All reagents were purchased from chemical suppliers and used without further purification.

4.1.3.2 Synthesis

UiO-66-HCl

A similar procedure outlined in Section 3.4.2 was followed, however the synthesis was scaled up. In a 50 mL Duran container 0.2500 g (1.073 mmol) of zirconium chloride and 0.2460 g (1.481 mmol) of terephthalic acid were combined and dissolved in 30 mL of DMF and 2 mL of hydrochloric acid with the aid of sonication. Once a clear colourless solution remained it was placed in an oven at 353 K. The jar was removed from the oven cooled to room temperature and the resulting solid and solution was transferred to a 50 mL centrifuge tube and centrifuged at 7800 RPM for three minutes, the solution was decanted and 30 mL of fresh DMF was added, and the process was repeated three times. After three washes with DMF the same process was repeated with methanol three times. After the final washing the centrifuge tube with the white powder was placed in an oven at 353 K overnight to remove any residual methanol.

To obtain enough material for the sample holder of the Hiden Automated Breakthrough analyzer, two batches of UiO-66-HCl were synthesized and combined.

UiO-66-AA

The procedure for UiO-66-AA, does not scale up well therefore several batches were synthesized and combined for breakthrough measurements. The procedure for the synthesis of UiO-66-AA was as follows. In a 50 mL Duran Vial 0.1488 g (0.6385 mmol) of zirconium chloride and 0.1064 mg (0.6405 mmol) of terephthalic acid was combined, and 40 mL of DMF was added along with 11 mL of glacial acetic acid. The mixture was

then sonicated until all the precipitate had dissolved, approximately ten minutes. Once a clear solution remained this was placed in a 393 K oven overnight. The jar was removed from the oven cooled to room temperature and the resulting solid and solution was transferred to a 50 mL centrifuge tube and centrifuged at 7800 RPM for three minutes, the solution was decanted and 30 mL of fresh DMF was added, and the process was repeated three times. After three washes with DMF the same process was repeated with methanol three times. After the final washing, the centrifuge tube with the white powder was placed in an oven at 353 K overnight to remove any residual methanol.

Breakthrough Experiments

Breakthrough experiments were performed on a Hiden Automated Breakthrough analyzer. The sample was activated under a 1 bar of helium with a flow rate of 20 mL/min at 393 K. Once activation was complete, the temperature was lowered to 293 K and the gas composition was switched to a flow rate of 8.5 mL/min of nitrogen and 1.5 mL/min of carbon dioxide that was flown at a pressure of 1, 2, 3 or 3.5 bar depending on the experiment being performed.

4.2 Further Enhancement of the Zirconium Cluster in UiO-66-HCl for Carbon Dioxide Adsorption

4.2.1 Early Results

It had become apparent to us that the addition of methanol groups on the cluster of hydrochloric acid synthesized UiO-66 had enhanced the carbon dioxide adsorption of the

gas tremendously (Section 3.2.3). With this discovery we briefly examined the effect of other node-modifying groups using the same procedure as soaking the MOFs in methanol. The difference was that rather than soaking the MOF in pure methanol, we included an additional carboxylic acid containing molecule. Ameloot and coworkers had shown that soaking the MOF in methanol, with a small amount of heat and an additional carboxylic acid would lead to ligand exchange, for this reason we decided to explore a variety of small carboxylic acids.[86] We had chosen to explore crotonic acid, 2-butynoic acid, acetic acid, formic acid, benzoic acid, and trifluoracetic acid.

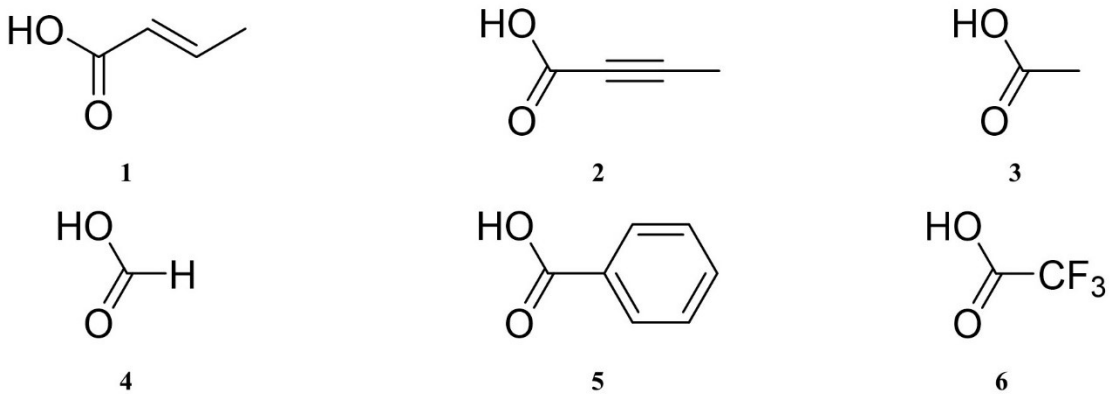

Figure 4.3: Organic acids used in attempts to functionalize the cluster of UiO-66-HCl. 1) crotonic acid 2) 2-buytonic acid 3) acetic acid 4) formic acid 5) benzoic acid 6) trifluoro acetic acid.

Similar to all other experiments, before the carbon dioxide isotherms could be measured the nitrogen isotherms were collected to ensure the sample remained porous. The BET nitrogen accessible surface area for these samples is shown in the table below.

Table 4.2: BET surface area of UiO-66-HCl methanol soaking with the presence of additional acids.

Additional Acid	**BET Surface Area (m^2/g)**
Crotonic acid	1500
2-Butynoic acid	1600
Acetic acid	1520
Formic acid	1900
Benzoic acid	1480
Trifluoro acetic acid	1970

From the results obtained in Table 4.2, it is clear that there was no structural change in the material as its surface area had not significantly decreased. With these materials in hand, we measured the carbon dioxide isotherms at three temperatures (278, 283, 288 K) and extracted the thermodynamic parameters as outlined in Section 3.4.5. The obtained values for the enthalpy of adsorption are listed in Table 4.3.

Table 4.3: Enthalpy of adsorption of acid modified UiO-66-HCl.

Acid Functionalization	**ΔH (kJ/mol)**	**Q_{max} (mmol/g)**
Crotonic acid	−11.4	10.2
2-Butynoic acid	25.4	6.9
Acetic acid	−27.3	5.9
Formic acid	−25.8	7.1
Benzoic acid	−23.8	5.9
Trifluoro acetic acid	−17.3	6.1

The obtained enthalpies of adsorption look promising. Acetic acid, formic acid, and benzoic acid enhance the adsorption enthalpy over the unfunctionalized UiO-66-HCl. The data from these three samples, when fit to a single-site Langmuir isotherm, do fit rather well and have low associated errors. However, additional measurements should be made to verify these calculated values. Trifluoro acetic acid had a calculated enthalpy of adsorption value of −17.3 kJ/mol, the low end for what we have observed for UiO-66. Additionally, the errors associated with these fits were found to be higher than for other samples, indicating that the data does not fit a single-site Langmuir isotherm. We hypothesize that the values for the trifluoracetic acid functionalized MOF was so different from the other functionalized MOFs was due to the presence of the fluorine group. We see that using acetic acid enhanced the enthalpy of adsorption, the trifluoracetic acid is a similar shape and size as the acetic acid but had a much lower enthalpy of adsorption with the only difference being the hydrogen atoms on the methyl groups were replace with fluorine atoms.

2-Butyonic acid yielded an endothermic enthalpy of adsorption, indicating that heat was required for carbon dioxide to adsorb to the material. This does not make any chemical sense as physisorption is an exothermic process. This value should not be taken as a true measurement and should be revisited. Crotonic acid did provide a negative enthalpy of adsorption, and while the data did have a low associated error, this value still should not be taken to be accurate. The obtained enthalpy of adsorption is not as exothermic as the other samples. This is the least exothermic sample that we have observed and less exothermic than the associated energy of the enthalpy of condensation of carbon dioxide.

For this reason, the calculated value of −11.4 kJ/mol should not be over interpreted and should be remeasured as it does not make chemical sense. The data may suggest that a Langmuir isotherm may not reflect the true chemistry inside the pore and would need to be revisited.

4.2.2 Future Directions

The functionalization of the cluster with these six organic acids has proven to provide interesting results, and there is potential for further understanding of how the functionalization of the cluster can modify the carbon dioxide capabilities of these materials. It was alluded too in the previous section that the future work in this project would entail performing these measurements again to verify the calculated values. The project also requires further characterization of these materials. It is known that soaking the MOF in methanol will cause replacement of ligands or defects on the cluster, but we need to determine if the acids used have been incorporated, and how much of these acids vs. methanol vs. leached ligand have also been incorporated or removed. To explore the ratio of methanol to organic acid incorporated into the MOF, simple ^{1}H-NMR or thermogravimetric analysis can be used to determine the ratio of the organic acid, ligand, and methanol, along with the number of ligands that remain in the material.

Previous literature has used gas phase NMR experiments to determine the interaction site between carbon dioxide gas and the solid MOF.[202] We have briefly tried to study the ^{13}C-NMR of $^{13}CO_2$ adsorbed onto UiO-66. However, due to the move to the new Core Science Facility and instrument breakdowns, we have not been able to investigate

these as in depth as we would have liked. Using NMR experiments can provide insight to how the carbon dioxide binds with different functional groups attached to the cluster.

Exploring even further, the enthalpy of adsorption of many different gases can be explored with these functionalized MOFs. It would be interesting to see how the functionalization of the cluster would impact the adsorption of gases like carbon monoxide, hydrogen, and methane to name a few. Finally, exploring more of the organic acids or different Lewis-basic molecules that could functionalize the cluster and their gas adsorption capabilities would be interesting.

4.2.3 Experimental

4.2.3.1 General Methods

All reagents were purchased from chemical suppliers and used without further purification.

4.2.3.2 Synthesis

In a 20 mL glass vial between 0.0417 g and 0.0530 g of UiO-66 (0.0238 mmol to 0.0318 mmol; Table 4.4) and 10 mL of methanol were combined. To each vial between 0.0061 mg and 0.2360 mg (0.334 to 1.04 mmol) of the acid to functionalize the cluster was added. These vials were then placed in a 313 K oven for three days. The vials were then removed from the oven and transferred to a 50 mL centrifuge tube and centrifuged at 7800 RPM for three minutes. The methanol was then decanted off and 10 mL of fresh methanol was added. This process was repeated a total of three times. After the final

washing, the sample was placed in an oven at 353 K overnight to completely remove any residual solvent.

Table 4.4: Masses of UiO-66 and functionalizing acids.

Functionalizing acid	**Mass of UiO-66 (g)**	**Moles of UiO-66 (mmol)**	**Mass of functionalizing acid (g)**	**Moles of functionalizing acid (mmol)**
Crotonic acid	0.0530	3.18×10^{-2}	0.0067	6.16×10^{-1}
2-Butynoic acid	0.0495	2.97×10^{-2}	0.0061	5.89×10^{-1}
Acetic acid	0.0417	2.51×10^{-2}	0.2363	6.94×10^{-1}
Formic acid	0.0477	2.87×10^{-2}	0.4148	1.04
Benzoic acid	0.0396	2.38×10^{-2}	0.0064	3.24×10^{-1}
Trifluoro acetic acid	0.0481	2.89×10^{-2}	0.4470	3.34×10^{-1}

4.3 Turning off Cluster-Gas Interactions

4.3.1 Introduction

In both Chapter 2 and Chapter 3 it was observed how important the cluster is for the adsorption of incoming gases. In Chapter 2 we had shown that the zirconium cluster is a viable place for water vapour to begin adsorbing. In Chapter 3 we reported how important the μ_3-hydroxo inside the cluster was for the adsorption of carbon dioxide in UiO-67. An interesting exploration would be how these gases interact with both UiO-66 and UiO-67 if the cluster was blocked. One potential route that this could be explored would be through

the addition of functional groups on to the biphenyl dicarboxylate ligand, pointing towards the cluster (Figure 4.4).

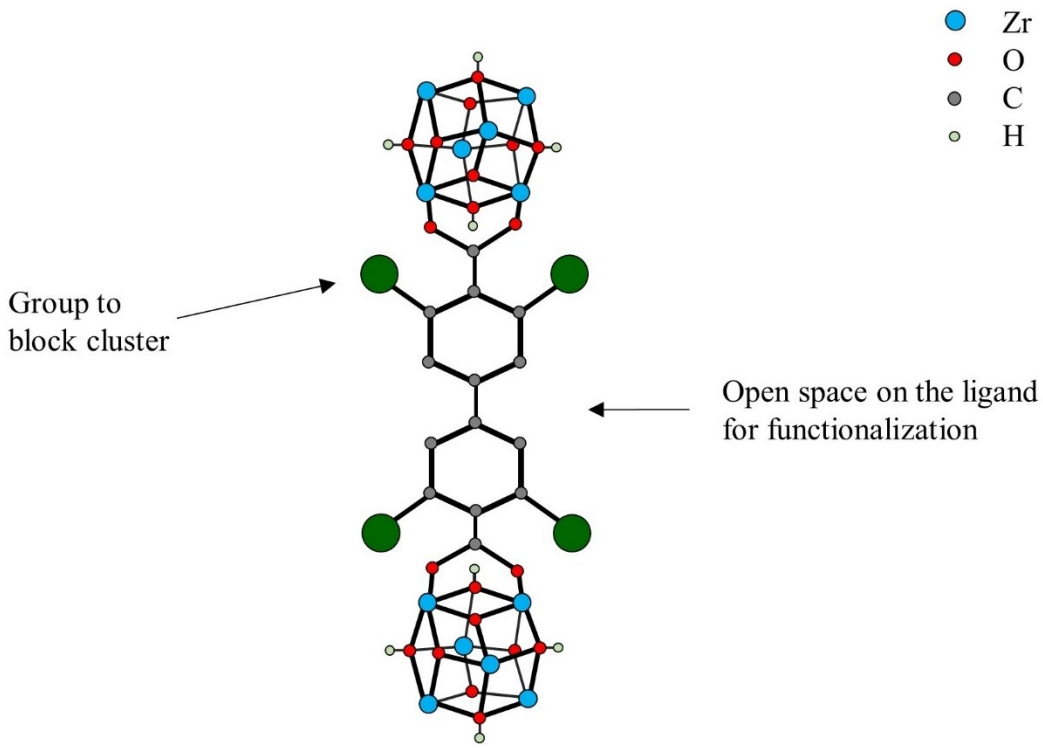

Figure 4.4: Proposed modifications to the ligand to help block gases from interacting with the cluster.

When choosing an appropriate functional group to introduce around the cluster, we initially wanted a heteroatom as we figured a larger group (e.g., methyl) would be too bulky and could inhibit the synthesis of the MOF or produce a MOF with a large number of missing ligands. For this reason, we had decided to explore the halogens as potential functional groups. Fluorine was an ideal functional group for a magnitude of reasons. First of all, it was a synthetically obtainable target in very few steps; given that we began working on this at the tail end of my PhD, this was a reasonable consideration. Second of all, fluorine-containing molecules are often very hydrophobic. We had hypothesized that

this could reduce the amount of water adsorbed in UiO-67. We believe that this could completely transition the mechanism away from node cluster growth and force it into the water clustering inside of the pore. We had also chosen fluorine as it is smaller than the other halogens, we believed that this would allow for a relatively pristine material to be formed, and increasing the size to chlorine or bromine be too large and could hinder the formation of the MOF.

We had proposed two ligands to incorporate into UiO-67 that would be interesting for this project. We had proposed a di-substituted biphenyl dicarboxylate along with a tetra-substituted biphenyl dicarboxylate as shown in Figure 4.5.[210]

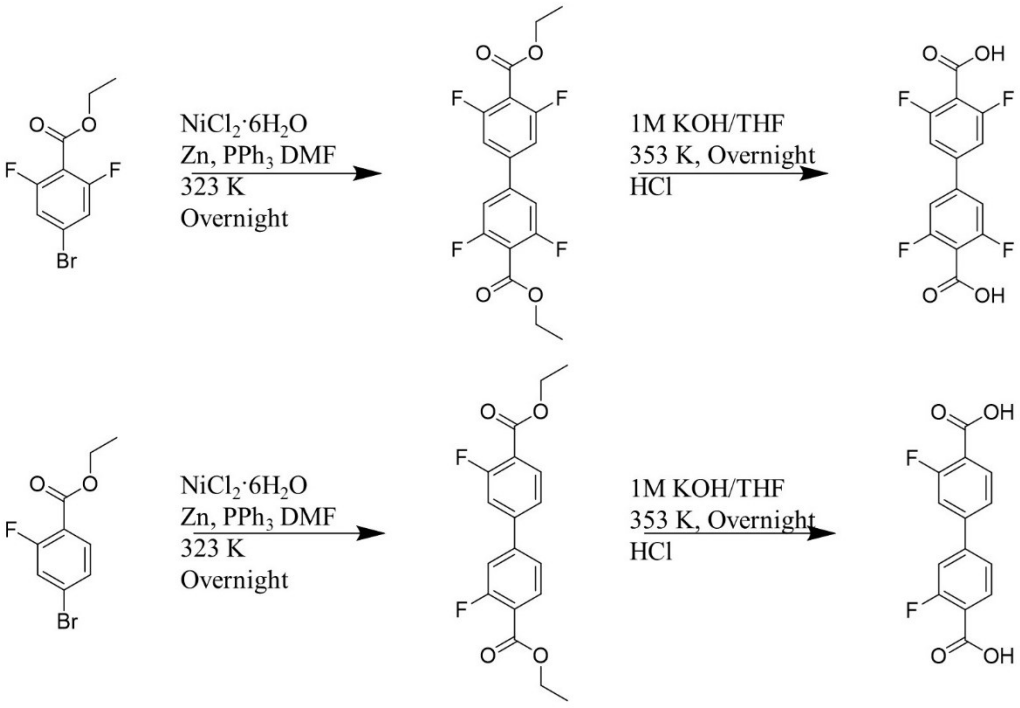

Figure 4.5: Synthesis to obtain proposed fluorinated biphenyl dicarboxylate ligands.

4.3.2 Preliminary Results

Following the synthetic route outlined in Figure 4.5 we were able to obtain the pure tetra- and di-substituted ligands and were able to begin attempting to synthesize UiO-67 containing these ligands. Using the tetra-substituted ligand we were able to obtain a small amount of UiO-67-2,2-F. The synthesis of this MOF required a large amount of ligand, but early attempts only yielded a very small amount of MOF. We were able to obtain a nitrogen isotherm for this MOF, and it had a nitrogen accessible BET surface area of 1150 m^2/g. We were also able to synthesize a small amount of UiO-67 with the di-substituted ligand (UiO-67-1,1-F) and it had a nitrogen accessible BET surface area of 1780 m^2/g. We propose that the difference in surface areas between these two MOFs and the unfunctionalized UiO-67 is due to the addition of the fluorine groups and the additional mass associated with these ligands. The procedure for the synthesis of these MOFs (Section 4.3.4.3) is very similar to the glacial acetic acid prep used in this thesis.[206] The primary difference is that a larger amount of acetic acid was necessary in comparison with the parent UiO-67 procedure. The obtained surface area also closely resembles that of the acetic acid synthesis discussed in Chapter 3, where we see the modification of the acid result in a lower surface area. Due to the small amount of material present, we were unable to perform any further experiments on these MOFs.

4.3.3 Future Work

There are many promising directions that these experiments can be taken but before any of these avenues can be explored the scale up synthesis of these MOFs must be

completed. Once a viable synthetic route is established, the MOFs will need to be further characterized via thermogravimetric analysis to determine the number of ligands that were incorporated. Assuming little-to-no missing ligands and with plenty of material in hand, other experiments can be performed including water vapour adsorption isotherms to determine if there has been any change to the uptake capacity or a potential switch in the adsorption mechanism of the material, and carbon dioxide isotherms to determine if the enthalpies of adsorption have changed due to the addition of the fluorene groups. Furthermore, the fluorine functionalization can be moved into the meta position on the aromatic ring to help determine if the change in adsorption properties is due to the addition of the fluorine group or if the cluster has been successfully blocked.[198]

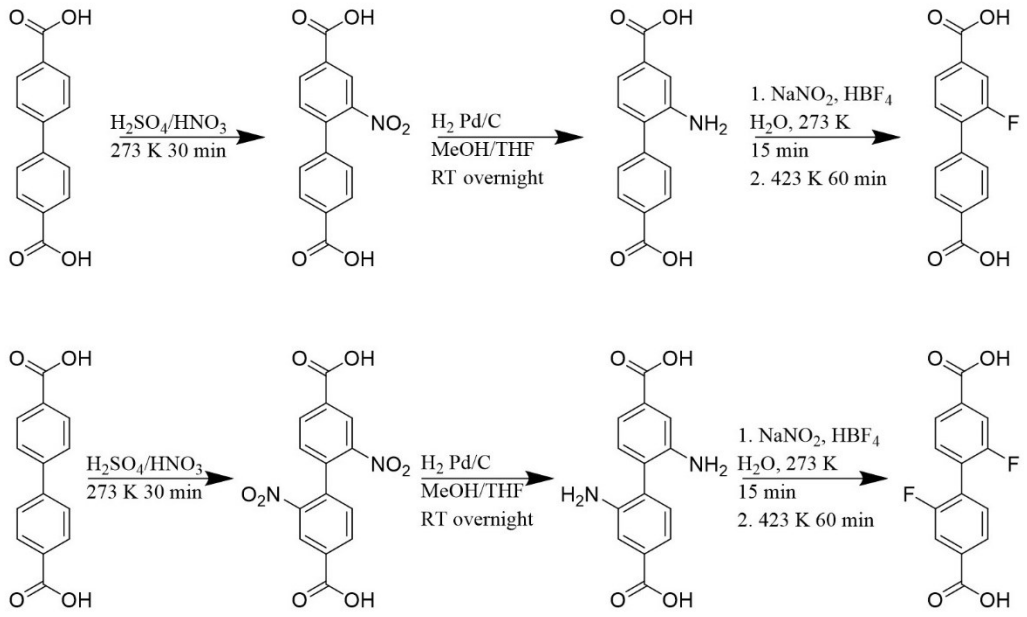

Figure 4.6: One potential synthetic route to mono- and di-fluorinated 4,4'-biphenyldicarboxylic acid ligands.

It is also quite possible that the addition of the fluorine groups are not quite large enough to block gas molecules from entering the cluster. Instead of installing a larger

halogen, there is an alternative route to follow; we could remove the cluster entirely. In the literature, click chemistry has been used to install cross ligands between the ligands in porous materials. What I propose is similar to the installation of cross ligands, where one end of the ligand will contain an azide, while another ligand will contain an alkyne.[211] Once these ligands are incorporated into the MOF, a small amount of copper catalyst can be added and the two ligands should become tethered to one another (Figure 4.7). It is possible that the tethering of the ligands will result in an effective blocking group, however, the entire cluster may be removable by soaking the MOF in acid. If the cluster is completely removed, then we can explore how the gas molecules interact with just the ligands of the porous material.

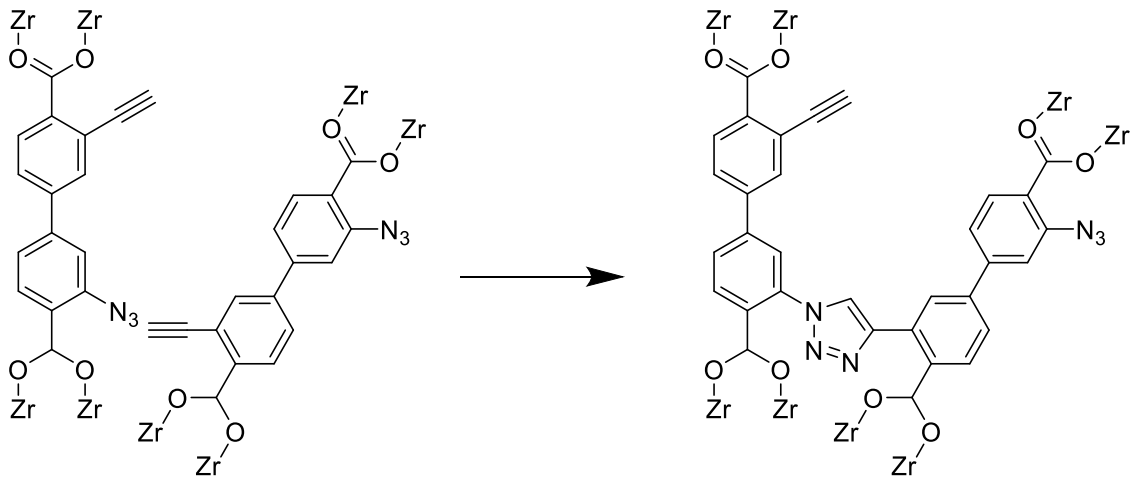

Figure 4.7: Potential click coupling reaction between an azide and alkene on the functionalized biphenyl dicarboxylate.

4.3.4 Experimental

4.3.4.1 General Methods

All reagents were purchased from chemical suppliers and used without further purification. ^{1}H-NMR was collected on a Bruker 300 or 500 Avance spectrometer, with the instrument used specified in the description for each synthesis procedure.

4.3.4.2 Ligand Synthesis

To synthesize 3,3′,5,5′-tetrakis(fluro)biphenyl-4,4′-dicarboxylate and 3,3′-difluoro[1,1′-biphenyl]-4,4′-dicarboxylate a slightly modified literature procedure was used.[210]

Dimethyl 3,3′,5,5′-tetrakis(fluro)biphenyl-4,4′-dicarboxylate

In a 50 mL 3-neck round bottom flask 0.2360 g of nickel(II) chloride hexahydrate (0.9928 mmol) and 1.04 g of triphenylphosphine (3.67 mmol) and the flask was placed under dynamic nitrogen. In a second 50 mL round bottom flask, 15 mL of DMF was sparged with nitrogen for thirty minutes. After the sparging was complete the DMF was canula transferred into the 50 mL 3 neck round bottom flask. Once the nickel(II) chloride hexahydrate and the triphenylphosphine had completely dissolved, 0.0648 g of zinc powder (0.991 mmol) was added, and the reaction was stirred for one hour. After stirring was completed 0.2490 g of methyl 4-bromo-2,6-difluorobenzoate (0.9920 mmol) was added under nitrogen gas. The reaction was then stirred overnight under dynamic nitrogen. The reaction was removed from heat and cooled to room temperature. Afterwards, 0.250 mL of methyl iodide (4.016 mmol) was added to the reaction and allowed to stir for one hour. The

resulting mixture was then poured into 200 mL of water and a precipitate formed. This precipitate was collected by suction filtration and washed with water (3 × 50 mL). The precipitate was then added to 150 mL of ethyl acetate and stirred at room temperature for thirty minutes. The resulting precipitate was isolated by suction filtration and discarded. The filtrate was collected, and the solvent was removed under heat and reduced pressure to yield the desired product. ^{1}H-NMR (300 MHz, DMSO-*d6*): δ 7.84 (d, *J* = 9.7 Hz, 4H), 3.92 (s, 6H). ^{19}F-NMR (300 MHz, DMSO-*d6*) δ -110.13 (d, *J* = 9.7 Hz).

3,3',5,5'-Tetrakis(fluro)biphenyl-4,4′-dicarboxylic acid (2,2-F-BPDC)

To a 250 ml round bottom flask 0.5000 g of Dimethyl 3,3′,5,5′-tetrakis(fluro)biphenyl-4,4′-dicarboxylate (1.461 mmol) was added and dissolved in 100 mL of a 50/50 mixture of THF and 1 M KOH. Once the solid had completely dissolved it was heated to 357 K and allowed to reflux overnight. The THF was removed under heat and reduced pressure. Once all the THF was removed the solution was acidified to a pH of 1 with 1 M hydrochloric acid. At this point a white precipitate had formed. The precipitate was isolated by suction filtration and washed with methanol (3 × 25 mL). ^{1}H-NMR (300 MHz, DMSO-*d6*): δ 7.76 (d, *J* = 9.3 Hz, 4H). ^{19}F-NMR (300 MHz, DMSO-*d6*): δ -111.07 (d, *J* = 9.6 Hz).

Dimethyl 3,3′-difluoro[1,1′-biphenyl]-4,4′-dicarboxylate

The synthesis of this compound was the same as dimethyl 3,3′,5,5′tetrakis(fluro)biphenyl-4,4′-dicarboxylate. In a scaled-up reaction, 1.07 g of nickel(II) chloride hexahydrate (4.50 mmol) and 4.47 g of triphenylphosphine

(17.0 mmol) was placed in a 250 mL 3 neck round bottom flask and placed under dynamic nitrogen. In a separate 250 mL round bottom flask 100 mL of DMF was sparged with nitrogen for approximately thirty minutes. The DMF was then canula transferred into the flask containing the nickel(II) chloride hexahydrate and the triphenylphosphine and allowed to stir until all solids were dissolved. Once all solids had dissolved, 0.2711 g of zinc powder (0.4146 mmol) was added under nitrogen protection and the solution was allowed to stir for one hour. Then 1.0192 g of methyl 4-bromo-2-fluorobenzoate (0.4373 mmol) was added to the reaction under nitrogen protection and stirred overnight. The reaction was removed from heat and cooled to room temperature before 1 mL of methyl iodide was added to the reaction and allowed to stir for one hour. The resulting mixture was then poured into 400 mL of water and a precipitate formed. This precipitate was collected by suction filtration and washed (3 × 100 mL). The precipitate was then added to 300 mL of ethyl acetate and stirred at room temperature for thirty minutes. The resulting precipitate was isolated by suction filtration and discarded. The filtrate was collected, and the solvent was removed under heat and reduced pressure to yield the desired product. ^{1}H-NMR (300 MHz, DMSO-*d6*): δ 8.00 (dd, *J* = 8.0 Hz, 12.3 Hz 2H), 7.86 (d, *J* = 12.4 Hz, 2H), 7.79 (d, *J* = 8.1 Hz, 2H) 3.89 (s, 6H). ^{19}F-NMR -109.42 (dd, *J* = 12.3, 7.7 Hz).

3,3'-Difluoro-[1,1'-biphenyl]-4,4'-dicarboxylic acid (1,1-F-BPDC)

Similar to the synthesis of 3,3’,5,5’-tetrakis(fluro)biphenyl-p,p’-dicarboxylate, 0.5000 g of dimethyl-3,3′-difluoro[1,1′biphenyl]-4,4′-dicarboxylate (0.1633 mmol) was placed in a 250 mL round bottom flask and 100 mL of a 50/50 mixture of THF and 1 M

KOH was added. The reaction was refluxed overnight, cooled to room temperature and the THF was removed under heat and reduced pressure, and the resulting solution was acidified with 1 M hydrochloric acid to give a white solid precipitate that was further isolated by suction filtration. ^{1}H NMR (300 MHz, DMSO-*d6*) δ 7.97 (dd, *J* = 8.0 Hz, 12.3 Hz, 2H), 7.80 (dd, *J* = 12.2, 1.7 Hz, 2H), 7.74 (dd, *J* = 8.2, 1.8 Hz, 2H). ^{19}F NMR δ -109.62 (dd, *J* = 12.3, 7.8 Hz).

4.3.4.3 Fluorinated MOF Synthesis

The glacial acetic acid procedure that was used to synthesize UiO-66-AA and UiO-67-AA was slightly modified for the synthesis of the fluorinated UiO-67s.[206] In a 25 mL bomb flask (thick glass walled pressure flask with a polytetrafluoroethylene screw cap), 0.0060 g (0.26 mmol) of zirconium chloride was dissolved in 5 mL of DMF. Once dissolved, 0.2350 g or 0.2090 g (0.7512 mmol) of 2,2-F-BPDC-H_2 or 1,1-F-BPDC-H_2 were added along with 1.57 mL of acetic acid and the solution was sonicated for five minutes. Once sonication was complete the solution was placed in an oven at 393 K for two days. Once removed from the oven the solution was allowed to cool to room temperature. As the solution cooled solid began to form on the walls of the vessel. Once cooled to room temperature the solution was carefully decanted. Once most of the solution was decanted 10 mL of fresh DMF was added and the powder was scraped from the side of the vessel and transferred to a 50 mL centrifuge tube and centrifuged at 7800 RPM for five minutes. Once this was complete, the DMF was carefully decanted off and another 10 mL of fresh DMF was added and the sample was centrifuged at 7800 RPM again for five minutes. This process was repeated a total of three times. Once this was complete the same procedure

was followed but with methanol as the solvent. Once the washings with methanol were complete the sample was transferred to a 353 K oven to dry.

4.4 UiO-67 Water Stability

4.4.1 Introduction

Throughout this thesis the stability of UiO-67 with respect to water has been brought up. Throughout the preparation of this thesis a question has remained in my mind. With Mondloch and co-workers showing that UiO-67 decomposes when activated from liquid water, but not when UiO-67 is washed with an organic solvent after water exposure.[88] Interestingly, in our hands exposing the MOF to a relative humidity of 54% or 75% leads to the complete decomposition of the MOF after several days. In Chapter 2 we discuss how we believe that the water is causing the decomposition, not necessarily the activation.

This poses the question of what causes UiO-67 to decompose in atmospheric conditions, with elevated relative humidity compared to being stored in liquid water. To ensure that the activation from water was not the cause of decomposition of UiO-67, we stored a sample of the MOF at 75% relative humidity for much longer than it would take to decompose, and exchanged it with methanol three times prior to activation. The surface area of this sample was not retained, and it was completely decomposed indicating that the activation procedure was not destroying the MOF.

The air in the atmosphere is comprised of many gases besides water and nitrogen, it also contains argon, helium, oxygen, and carbon dioxide. Most of these gases are not present in liquid water, or present in negligible concentrations. The gas that is present in the atmosphere that sticks out is carbon dioxide. It may be possible that carbon dioxide can interact with water vapour inside the MOF to create carbonic acid, and further lose a proton to form bicarbonate. This becomes important as Cao *et al*. have shown that UiO-66 can react with the bicarbonate ion in solution causing the MOF to decompose via Equation 4.1.[87] Since UiO-67 contains the same zirconium building block and a similar ditopic ligand, the same or similar reaction may also occur in UiO-67.

$$Zr_6O_4(OH)_4(BDC)_6 + 18HCO_3^- \rightarrow 3[Zr_2(OH)_2(CO_3)_4]^{2-} + 8H_2O + 6CO_2 + 6BDC^{2-} \quad 4.1$$

While Cao *et al.* have shown that the reaction occurs in the liquid phase, it is not a stretch to think that this reaction could also occur in the gas phase.[87] It is quite possible that at 54% and 75% relative humidity there is enough bicarbonate formed to cause the MOF to completely decompose. To prove that carbon dioxide is playing a role in the decomposition of UiO-67 in atmospheric conditions there are a series of experiments to perform.

4.4.2 Proposed Experiments

It has been shown that the desorption curve of a water isotherm can cause UiO-67 to decompose, and it would be very difficult to create an environment with minimal carbon dioxide while still exposing the MOF a high relative humidity. Making these experiments

quite tricky. I propose making a single sample of UiO-67 and characterizing it with PXRD and nitrogen gas isotherms as described throughout this thesis. Once the material has been fully characterized it should be split into two samples and placed into a 3Flex tube containing a sealed frit to eliminate the possibility of any exchange between the sample and gas inside the tube and the atmosphere. Initially both batches would be exposed to a full water isotherm, without a desorption curve. The first sample would be backfilled with nitrogen and allowed to age for several days. The second sample would be backfilled with nitrogen and carbon dioxide to mimic atmospheric concentrations and aged for several days. Both samples would then be activated under heat and vacuum followed by nitrogen isotherms and PXRD measurements to characterize the materials.

Based on the results of other first experiments there are follow up experiments to perform. First, if the sample stored under nitrogen shows gas adsorption or crystallinity consistent with UiO-67, then we cannot eliminate the possibility that the activation of the material had led to the decomposition, as suggested by Mondloch. To confirm that the activation from the water is the issue, we would repeat the experiment, however, prior to activation after the water isotherm, the sample should be washed with an organic solvent such as acetone or methanol to exchange any water remaining in the pores.

Based on the hypothesis above, the sample that was stored under a mixture of carbon dioxide and nitrogen the MOF should decompose due to the formation of the bicarbonate. If the gas adsorption and PXRD has changed after the aging period, it could be due to the activation from water, which we know is an issue, or the MOF would be destroyed due to the bicarbonate. To determine which caused the decomposition another

series of experiments where the MOF is washed with an organic solvent prior to activation would be performed.

There also runs the possibility that there is not enough water vapour present after a single water isotherm for an adequate amount of bicarbonate to form when the tube is backfilled with nitrogen and carbon dioxide, if only a small amount of bicarbonate is formed the MOF may not decompose. This would be evident if after washing with an organic solvent the porosity and crystallinity is retained.

From the results in Chapter 2, I demonstrated that storing the MOF in a sealed container with a saturated salt solution causes the MOF to decompose. There also can be an experiment performed where a saturated salt solution and the MOF are stored in a sealed container that has been flushed with nitrogen prior to the aging period. It would be important to do this experiment under static conditions as dynamic nitrogen may change the relative humidity of the atmosphere.

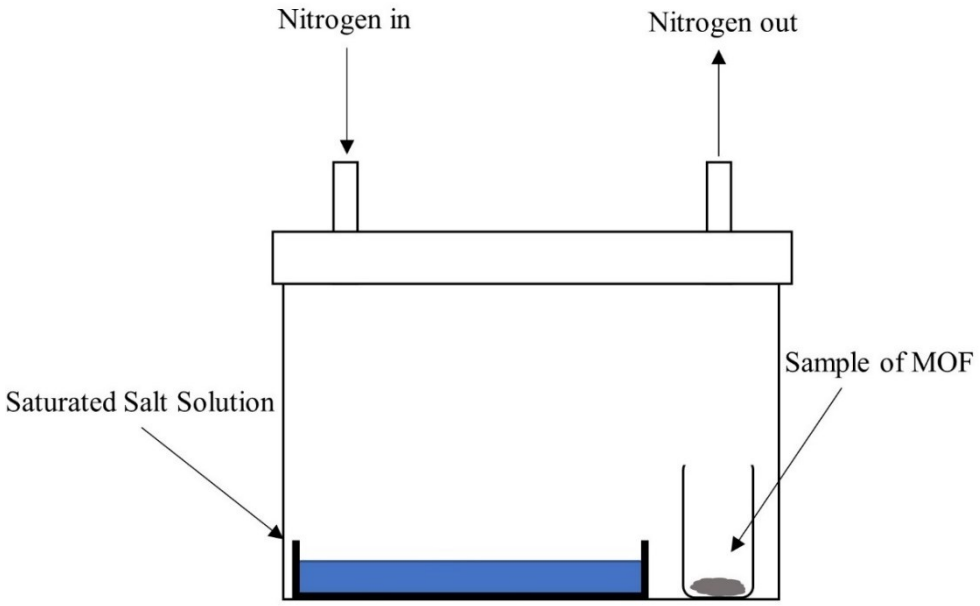

Figure 4.8: Sealed container that can be purged with nitrogen to create an atmosphere with minimal carbon dioxide.

If after aging in the nitrogen sealed container the surface area and crystallinity of the MOF remains intact, then it suggests that the carbon dioxide is responsible for the decomposition of the material.

A crucial component of this project would be to monitor the formation of bicarbonate. To do this we could use a couple of different methods. The first method is Solid-State NMR. With solid state NMR, the ^{13}C nuclei could be monitored, and a change in chemical shift should be observed as it changes from gaseous carbon dioxide to bicarbonate and finally bound to the zirconium cluster as suggested in Equation 4.1. This would confirm the formation of bicarbonate and a potential binding location.

The second method that could be used is a breakthrough measurement. The mass spectrometer would be set to monitor carbon dioxide, water, and carbonic acid. The MOF

would be loaded into the breakthrough instrument and a flow of nitrogen and carbon dioxide gas would initially be used until breakthrough is accomplished. After this the gas flow would be switched to contain carbon dioxide and humidified nitrogen. If bicarbonate is forming, it would be detected by the mass spectrometer. This experiment would confirm the formation of bicarbonate along with insight to how much is forming.

Chapter 5: Conclusions

The introduction stated that MOFs could be made from a variety of metal centres and ligands. With this freedom, the potential of these porous materials is near endless. In the literature we commonly see MOFs that are designed for specific gas phase applications, where one structural feature is said to be responsible for the capability of the material. While this is an effective approach, sometimes the reason why certain results are obtained can be overlooked. If we can understand why and how materials interact with gases, then we can lead to further enhancement in a variety of different MOFs.

In Chapter 2 we examined how the structural properties of six different UiO MOFs played an important role in the adsorption of water vapour. We were able to draw three main conclusions from this work. The first was that under low relative humidity we see water vapour adsorb at a ratio of one water molecule per zirconium molecule, and this is reversable, which indicates that there should still be space inside of the material for other gases to adsorb. The presence of the hydrogen bonding site from the water may even enhance the adsorption of other target gases or assist in other applications such as catalysis. The second conclusion that we were able to take away from this project was pore size plays a big role in the relative pressure that causes the onset of humidity. UiO-66, the MOF that contained the smallest of the pores, had the water vapour adsorption step occur at the lowest relative humidity. Moving to larger pore size MOF, we noticed that the relative humidity required to create a water adsorption step was increased. With MOFs larger than UiO-68, the isotherm step would not occur until 90 % relative humidity or higher. This would result

in minimal water adsorption and there would be no competitive binding between water vapour and other gases in these MOF. The third conclusion was UiO-66 had an operational range, and the recyclability to be used in HVAC systems to maintain comfortable temperature for human health and showed potential for this application. To make these conclusions we had to look at multiple features of the MOFs, not just the pore size but also the number of defects that were present to determine how they played a role in the mechanism at which water vapour adsorption occurred.

Chapter 3 showed a great example of how different topological features played an important role in carbon dioxide gas adsorption in UiO-66 and UiO-67. We have seen in these materials that having a smaller pore can lead to confinement effects with enhanced gas adsorption. However, how that smaller pore is achieved can very. Having a near pristine material, leading to a larger presence of the smaller tetrahedral pore, results in a larger enthalpy of adsorption. As the pore sizes were increased in UiO-67 the interactions between the carbon dioxide and the MOF were much lower due to the lack of confinement effects. The investigation continued to examine how the open metal sites on the zirconium cluster can play a role in the adsorption of carbon dioxide. We established that heating to a point of dehydration hindered the gas adsorption capabilities of the MOF. We had also determined that functionalization of the cluster with methanol/methoxy coordinating groups allowed for the enhancement of carbon dioxide adsorption but only if defects were already present in the MOF. We have attributed this to the new interaction site provided by the methanol/methoxy caps, along with these molecules taking up more room in the pores causing more confinement effects.

While this thesis provides an in-depth investigation into the adsorption capacities, and mechanism of adsorption for water vapour and carbon dioxide gas independently, the investigation into the binding of water vapour and carbon dioxide mixed gas systems can provide much more insight into how these gases may competitively or cooperatively bind. Some potential future experiments to investigate this has been outlined in Chapter 4. While functionalizing materials and examining the gas adsorption capabilities is a method that we see in the literature and will continue to see it is important to fully understand how all properties in a given structure contributes to the observed results. Once we fully understand how materials work, we can further enhance their capabilities and see them in operation in real world conditions.

Chapter 6: References

(1) Lahiri, N.; Lotfizadeh, N.; Tsuchikawa, R.; Deshpande, V. V.; Louie, J. Hexaaminobenzene as a Building Block for a Family of 2D Coordination Polymers. *J. Am. Chem. Soc.* **2017**, *139* (1), 19–22. https://doi.org/10.1021/jacs.6b09889.

(2) Keggin, J.; Miles, F. Structure and Formulae of the Prussian Blues and Related Compounds. *Nature* **1936**, *137*, 586–587. https://doi.org/doi.org/10.1038/137577a0.

(3) Johansson, A.; Widenkvist, E.; Lu, J.; Boman, M.; Jansson, U. Fabrication of High-Aspect-Ratio Prussian Blue Nanotubes Using a Porous Alumina Template. *Nano Lett.* **2005**, *5* (8), 1603–1606. https://doi.org/10.1021/nl050964u.

(4) Ariga, K.; Malgras, V.; Ji, Q.; Zakaria, M. B.; Yamauchi, Y. Coordination Nanoarchitectonics at Interfaces between Supramolecular and Materials Chemistry. *Coord. Chem. Rev.* **2016**, *320–321*, 139–152. https://doi.org/10.1016/j.ccr.2016.01.015.

(5) Buser, H. J.; Schwarzenbach, D.; Petter, W.; Ludi, A. The Crystal Structure of Prussian Blue: $Fe_4[Fe(CN)_6]_3.XH_2O$. *Inorg. Chem.* **1977**, *16* (11), 2704–2710. https://doi.org/10.1021/ic50177a008.

(6) Kitagawa, S.; Kitaura, R.; Noro, S. Functional Porous Coordination Polymers. *Angew. Chem., Int. Ed.* **2004**, *43* (18), 2334–2375. https://doi.org/10.1002/anie.200300610.

(7) Samain, L.; Grandjean, F.; Long, G. J.; Martinetto, P.; Bordet, P.; Strivay, D. Relationship between the Synthesis of Prussian Blue Pigments, Their Color, Physical Properties, and Their Behavior in Paint Layers. *J. Phys. Chem. C* **2013**, *117* (19), 9693–9712. https://doi.org/10.1021/jp3111327.

(8) Guichard, C.; Le Hô, A.-S.; Williams, H. Prussian Blue: Chemistry, Commerce, and Colour in Eighteenth-Century Paris. *Art Hist.* **2022**. https://doi.org/10.1111/1467-8365.12695.

(9) Thompson, D. F.; Church, C. O. Prussian Blue for Treatment of Radiocesium Poisoning. *Pharmacotherapy* **2001**, *21* (11), 1364–1367. https://doi.org/10.1592/phco.21.17.1364.34426.

(10) Hoffman, R. S. Thallium Toxicity and the Role of Prussian Blue in Therapy. *Toxicol. Rev.* **2003**, *22* (1), 29–40. https://doi.org/10.2165/00139709-200322010-00004.

(11) Peng, J.; Zhang, W.; Liu, Q.; Wang, J.; Chou, S.; Liu, H.; Dou, S. Prussian Blue Analogues for Sodium-Ion Batteries: Past, Present, and Future. *Adv Mater* **2022**, *34* (15), 2108384. https://doi.org/10.1002/adma.202108384.

(12) Kitagawa, S.; Matsuda, R. Chemistry of Coordination Space of Porous Coordination Polymers. *Coord. Chem. Rev.* **2007**, *251* (21–24), 2490–2509. https://doi.org/10.1016/j.ccr.2007.07.009.

(13) Leong, W. L.; Vittal, J. J. One-Dimensional Coordination Polymers: Complexity and Diversity in Structures, Properties, and Applications. *Chem. Rev.* **2011**, *111* (2), 688–764. https://doi.org/10.1021/cr100160e.

(14) Nishikiori, S.; Yoshikawa, H.; Sano, Y.; Iwamoto, T. Inorganic−Organic Hybrid Molecular Architectures of Cyanometalate Host and Organic Guest Systems: Specific Behavior of the Guests. *Acc. Chem. Res.* **2005**, *38* (4), 227–234. https://doi.org/10.1021/ar0401707.

(15) Schaeffer, W. D.; Dorsey, W. S.; Skinner, D. A.; Christian, C. G. Separation of Xylenes, Cymenes, Methylnaphthalenes and Other Isomers by Clathration with Inorganic Complexes. *J. Am. Chem. Soc.* **1957**, *79* (22), 5870–5876. https://doi.org/10.1021/ja01579a008.

(16) Culp, J. T.; Natesakhawat, S.; Smith, M. R.; Bittner, E.; Matranga, C.; Bockrath, B. Hydrogen Storage Properties of Rigid Three-Dimensional Hofmann Clathrate Derivatives: The Effects of Pore Size. *J. Phys. Chem. C* **2008**, *112* (17), 7079–7083. https://doi.org/10.1021/jp710996y.

(17) Wen, T.; Zhang, D.-X.; Zhang, J. Two-Dimensional Copper(I) Coordination Polymer Materials as Photocatalysts for the Degradation of Organic Dyes. *Inorg. Chem.* **2013**, *52* (1), 12–14. https://doi.org/10.1021/ic302273h.

(18) Wang, F.; Li, F.-L.; Xu, M.-M.; Yu, H.; Zhang, J.-G.; Xia, H.-T.; Lang, J.-P. Facile Synthesis of a Ag(I)-Doped Coordination Polymer with Enhanced Catalytic Performance in the Photodegradation of Azo Dyes in Water. *J. Mater. Chem. A* **2015**, *3* (11), 5908–5916. https://doi.org/10.1039/C5TA00302D.

(19) Fuku, K.; Miyata, M.; Takaishi, S.; Yoshida, T.; Yamashita, M.; Hoshino, N.; Akutagawa, T.; Ohtsu, H.; Kawano, M.; Iguchi, H. Emergence of Electrical Conductivity in a Flexible Coordination Polymer by Using Chemical Reduction. *Chem. Comm.* **2020**, *56* (61), 8619–8622. https://doi.org/10.1039/D0CC03062G.

(20) Liu, Y.; Ma, J.; Xu, C.; Yang, Y.; Xia, M.; Jiang, H.; Liu, W. A Water-Stable Lanthanide Coordination Polymer as a Multiresponsive Luminescent Sensor for Fe^{3+}, Cr(VI) and 4-Nitrophenol. *Dalton Trans.* **2018**, *47* (38), 13543–13549. https://doi.org/10.1039/C8DT02202J.

(21) Wang, S.; Liu, J.; Zhao, H.; Guo, Z.; Xing, H.; Gao, Y. Electrically Conductive Coordination Polymer for Highly Selective Chemiresistive Sensing of Volatile Amines. *Inorg. Chem.* **2018**, *57* (2), 541–544. https://doi.org/10.1021/acs.inorgchem.7b02464.

(22) Li, H.; Eddaoudi, M.; O'Keeffe, M.; Yaghi, O. M. Design and Synthesis of an Exceptionally Stable and Highly Porous Metal-Organic Framework. *Nature* **1999**, *402* (6759), 276–279. https://doi.org/10.1038/46248.

(23) Cavka, J. H.; Jakobsen, S.; Olsbye, U.; Guillou, N.; Lamberti, C.; Bordiga, S.; Lillerud, K. P. A New Zirconium Inorganic Building Brick Forming Metal Organic Frameworks with Exceptional Stability. *J. Am. Chem. Soc.* **2008**, *130* (42), 13850–13851. https://doi.org/10.1021/ja8057953.

(24) Millange, F.; Serre, C.; Férey, G. Synthesis, Structure Determination and Properties of MIL-53as and MIL-53ht: The First Cr(III) Hybrid Inorganic–Organic Microporous Solids: $Cr^{III}(OH)\cdot\{O_2C–C_6H_4–CO_2\}\cdot\{HO_2C–C_6H_4–CO_2H\}x$. *Chem. Commun.* **2002**, No. 8, 822–823. https://doi.org/10.1039/b201381a.

(25) Chui, S. S.-Y.; Lo, S. M.-F.; Charmant, J. P. H.; Orpen, A. G.; Williams, I. D. A Chemically Functionalizable Nanoporous Material $[Cu_3(TMA)_2(H_2O)_3]_n$. *Science* **1999**, *283* (5405), 1148–1150. https://doi.org/10.1126/science.283.5405.1148.

(26) Senkovska, I.; Hoffmann, F.; Fröba, M.; Getzschmann, J.; Böhlmann, W.; Kaskel, S. New Highly Porous Aluminium Based Metal-Organic Frameworks: Al(OH)(Ndc) (Ndc=2,6-Naphthalene Dicarboxylate) and Al(OH)(Bpdc) (Bpdc=4,4′-Biphenyl Dicarboxylate). *Microporous Mesoporous Mater.* **2009**, *122* (1), 93–98. https://doi.org/10.1016/j.micromeso.2009.02.020.

(27) Lin, J.-B.; Nguyen, T. T. T.; Vaidhyanathan, R.; Burner, J.; Taylor, J. M.; Durekova, H.; Akhtar, F.; Mah, R. K.; Ghaffari-Nik, O.; Marx, S.; Fylstra, N.; Iremonger, S. S.; Dawson, K. W.; Sarkar, P.; Hovington, P.; Rajendran, A.; Woo, T. K.; Shimizu, G. K. H. A Scalable Metal-Organic Framework as a Durable Physisorbent for Carbon Dioxide Capture. *Science* **2021**, *374* (6574), 1464–1469. https://doi.org/10.1126/science.abi7281.

(28) Farha, O. K.; Özgür Yazaydın, A.; Eryazici, I.; Malliakas, C. D.; Hauser, B. G.; Kanatzidis, M. G.; Nguyen, S. T.; Snurr, R. Q.; Hupp, J. T. De Novo Synthesis of a Metal–Organic Framework Material Featuring Ultrahigh Surface Area and Gas Storage Capacities. *Nature Chem* **2010**, *2* (11), 944–948. https://doi.org/10.1038/nchem.834.

(29) Saha, D.; Bao, Z.; Jia, F.; Deng, S. Adsorption of CO_2, CH_4, N_2O, and N_2 on MOF-5, MOF-177, and Zeolite 5A. *Environ. Sci. Technol.* **2010**, *44* (5), 1820–1826. https://doi.org/10.1021/es9032309.

(30) Deng, H.; Grunder, S.; Cordova, K. E.; Valente, C.; Furukawa, H.; Hmadeh, M.; Gándara, F.; Whalley, A. C.; Liu, Z.; Asahina, S.; Kazumori, H.; O'Keeffe, M.; Terasaki, O.; Stoddart, J. F.; Yaghi, O. M. Large-Pore Apertures in a Series of Metal-Organic Frameworks. *Science* **2012**, *336* (6084), 1018–1023. https://doi.org/10.1126/science.1220131.

(31) Sung Cho, H.; Deng, H.; Miyasaka, K.; Dong, Z.; Cho, M.; Neimark, A. V.; Ku Kang, J.; Yaghi, O. M.; Terasaki, O. Extra Adsorption and Adsorbate Superlattice Formation in Metal-Organic Frameworks. *Nature* **2015**, *527* (7579), 503–507. https://doi.org/10.1038/nature15734.

(32) Feng, D.; Gu, Z.-Y.; Li, J.-R.; Jiang, H.-L.; Wei, Z.; Zhou, H.-C. Zirconium-Metalloporphyrin PCN-222: Mesoporous Metal–Organic Frameworks with Ultrahigh Stability as Biomimetic Catalysts. *Angew. Chem., Int. Ed.* **2012**, *51* (41), 10307–10310. https://doi.org/10.1002/anie.201204475.

(33) Hayashi, H.; Côté, A. P.; Furukawa, H.; O'Keeffe, M.; Yaghi, O. M. Zeolite A Imidazolate Frameworks. *Nat. Mat.* **2007**, *6* (7), 501–506. https://doi.org/10.1038/nmat1927.

(34) Pan, Y.; Liu, Y.; Zeng, G.; Zhao, L.; Lai, Z. Rapid Synthesis of Zeolitic Imidazolate Framework-8 (ZIF-8) Nanocrystals in an Aqueous System. *Chem. Commun.* **2011**, *47* (7), 2071–2073. https://doi.org/10.1039/C0CC05002D.

(35) Goswami, S.; Miller, C. E.; Logsdon, J. L.; Buru, C. T.; Wu, Y.-L.; Bowman, D. N.; Islamoglu, T.; Asiri, A. M.; Cramer, C. J.; Wasielewski, M. R.; Hupp, J. T.; Farha, O. K. Atomistic Approach toward Selective Photocatalytic Oxidation of a Mustard-

Gas Simulant: A Case Study with Heavy-Chalcogen-Containing PCN-57 Analogues. *ACS Appl. Mater. Interfaces* **2017**, *9* (23), 19535–19540. https://doi.org/10.1021/acsami.7b07055.

(36) Lawrence, M. C.; Katz, M. J. Analysis of the Water Adsorption Isotherms in UiO-Based Metal–Organic Frameworks. *J. Phys. Chem. C* **2022**, *126* (2), 1107–1114. https://doi.org/10.1021/acs.jpcc.1c05190.

(37) Trousselet, F.; Archereau, A.; Boutin, A.; Coudert, F.-X. Heterometallic Metal–Organic Frameworks of MOF-5 and UiO-66 Families: Insight from Computational Chemistry. *J. Phys. Chem. C* **2016**, *120* (43), 24885–24894. https://doi.org/10.1021/acs.jpcc.6b08594.

(38) Shearer, G. C.; Chavan, S.; Bordiga, S.; Svelle, S.; Olsbye, U.; Lillerud, K. P. Defect Engineering: Tuning the Porosity and Composition of the Metal–Organic Framework UiO-66 via Modulated Synthesis. *Chem. Mater.* **2016**, *28* (11), 3749–3761. https://doi.org/10.1021/acs.chemmater.6b00602.

(39) Bordiga, S.; Vitillo, J. G.; Ricchiardi, G.; Regli, L.; Cocina, D.; Zecchina, A.; Arstad, B.; Bjørgen, M.; Hafizovic, J.; Lillerud, K. P. Interaction of Hydrogen with MOF-5. *J. Phys. Chem. B* **2005**, *109* (39), 18237–18242. https://doi.org/10.1021/jp052611p.

(40) Maiti, S.; Pramanik, A.; Manju, U.; Mahanty, S. Reversible Lithium Storage in Manganese 1,3,5-Benzenetricarboxylate Metal–Organic Framework with High Capacity and Rate Performance. *ACS Appl. Mater. Interfaces* **2015**, *7* (30), 16357–16363. https://doi.org/10.1021/acsami.5b03414.

(41) Serre, C.; Millange, F.; Thouvenot, C.; Noguès, M.; Marsolier, G.; Louër, D.; Férey, G. Very Large Breathing Effect in the First Nanoporous Chromium(III)-Based Solids: MIL-53 or CrIII(OH)·{$O_2C{-}C_6H_4{-}CO_2$}·{$HO_2C{-}C_6H_4{-}CO_2H$}x·H_2Oy. *J. Am. Chem. Soc.* **2002**, *124* (45), 13519–13526. https://doi.org/10.1021/ja0276974.

(42) Jeremias, F.; K. Henninger, S.; Janiak, C. Ambient Pressure Synthesis of MIL-100(Fe) MOF from Homogeneous Solution Using a Redox Pathway. *Dalton Trans.* **2016**, *45* (20), 8637–8644. https://doi.org/10.1039/C6DT01179A.

(43) Xie, S.; Qin, Q.; Liu, H.; Jin, L.; Wei, X.; Liu, J.; Liu, X.; Yao, Y.; Dong, L.; Li, B. MOF-74-M (M = Mn, Co, Ni, Zn, MnCo, MnNi, and MnZn) for Low-Temperature NH_3-SCR and In Situ DRIFTS Study Reaction Mechanism. *ACS Appl. Mater. Interfaces* **2020**, *12* (43), 48476–48485. https://doi.org/10.1021/acsami.0c11035.

(44) Wu, P.; Liu, Y.; Liu, Y.; Wang, J.; Li, Y.; Liu, W.; Wang, J. Cadmium-Based Metal–Organic Framework as a Highly Selective and Sensitive Ratiometric Luminescent Sensor for Mercury(II). *Inorg. Chem.* **2015**, *54* (23), 11046–11048. https://doi.org/10.1021/acs.inorgchem.5b01758.

(45) Berdichevsky, E. K.; Downing, V. A.; Hooper, R. W.; Butt, N. W.; McGrath, D. T.; Donnelly, L. J.; Michaelis, V. K.; Katz, M. J. Ultrahigh Size Exclusion Selectivity for Carbon Dioxide from Nitrogen/Methane in an Ultramicroporous Metal–Organic Framework. *Inorg. Chem.* **2022**, *61* (20), 7970–7979. https://doi.org/10.1021/acs.inorgchem.2c00608.

(46) Yılmaz, E.; Sert, E.; Atalay, F. S. Synthesis, Characterization of a Metal Organic Framework: MIL-53 (Fe) and Adsorption Mechanisms of Methyl Red onto MIL-53

(Fe). *J. Taiwan. Inst. Chem. Eng.* **2016**, *65*, 323–330. https://doi.org/10.1016/j.jtice.2016.05.028.

(47) Tian, Y.-Q.; Yao, S.-Y.; Gu, D.; Cui, K.-H.; Guo, D.-W.; Zhang, G.; Chen, Z.-X.; Zhao, D.-Y. Cadmium Imidazolate Frameworks with Polymorphism, High Thermal Stability, and a Large Surface Area. *Chem. Eur. J.* **2010**, *16* (4), 1137–1141. https://doi.org/10.1002/chem.200902729.

(48) Millange, F.; Walton, R. I. MIL-53 and Its Isoreticular Analogues: A Review of the Chemistry and Structure of a Prototypical Flexible Metal-Organic Framework. *Isr. J. Chem.* **2018**, *58* (9–10), 1019–1035. https://doi.org/10.1002/ijch.201800084.

(49) Natarajan, S.; Mahata, P. Metal–Organic Framework Structures – How Closely Are They Related to Classical Inorganic Structures? *Chem. Soc. Rev.* **2009**, *38* (8), 2304–2318. https://doi.org/10.1039/B815106G.

(50) Farha, O. K.; Hupp, J. T. Rational Design, Synthesis, Purification, and Activation of Metal−Organic Framework Materials. *Acc. Chem. Res.* **2010**, *43* (8), 1166–1175. https://doi.org/10.1021/ar1000617.

(51) Vaidhyanathan, R.; S. Iremonger, S.; W. Dawson, K.; H. Shimizu, G. K. An Amine-Functionalized Metal Organic Framework for Preferential CO_2 Adsorption at Low Pressures. *Chem. Commun.* **2009**, *0* (35), 5230–5232. https://doi.org/10.1039/B911481E.

(52) Dhakshinamoorthy, A.; Li, Z.; Garcia, H. Catalysis and Photocatalysis by Metal Organic Frameworks. *Chem. Soc. Rev.* **2018**, *47* (22), 8134–8172. https://doi.org/10.1039/C8CS00256H.

(53) Bunge, M. A.; Davis, A. B.; West, K. N.; West, C. W.; Glover, T. G. Synthesis and Characterization of UiO-66-NH_2 Metal–Organic Framework Cotton Composite Textiles. *Ind. Eng. Chem. Res.* **2018**, *57* (28), 9151–9161. https://doi.org/10.1021/acs.iecr.8b01010.

(54) Kandiah, M.; Nilsen, M. H.; Usseglio, S.; Jakobsen, S.; Olsbye, U.; Tilset, M.; Larabi, C.; Quadrelli, E. A.; Bonino, F.; Lillerud, K. P. Synthesis and Stability of Tagged UiO-66 Zr-MOFs. *Chem. Mater.* **2010**, *22* (24), 6632–6640. https://doi.org/10.1021/cm102601v.

(55) Rada, Z. H.; Abid, H. R.; Shang, J.; Sun, H.; He, Y.; Webley, P.; Liu, S.; Wang, S. Functionalized UiO-66 by Single and Binary $(OH)_2$ and NO_2 Groups for Uptake of CO_2 and CH_4. *Ind. Eng. Chem. Res.* **2016**, *55* (29), 7924–7932. https://doi.org/10.1021/acs.iecr.5b04061.

(56) Katz, M.; Brown, Z.; Colón, Y.; Siu, P.; Scheidt, K.; Snurr, R.; Hupp, J.; Farha, O. A Facile Synthesis of UiO-66, UiO-67 and Their Derivatives. *Chem. Commun.* **2013**, *49*. https://doi.org/10.1039/c3cc46105j.

(57) Sun, D.; Ma, S.; Ke, Y.; Collins, D. J.; Zhou, H.-C. An Interweaving MOF with High Hydrogen Uptake. *J. Am. Chem. Soc.* **2006**, *128* (12), 3896–3897. https://doi.org/10.1021/ja058777l.

(58) He, B.; Macreadie, L. K.; Gardiner, J.; Telfer, S. G.; Hill, M. R. *In Situ* Investigation of Multicomponent MOF Crystallization during Rapid Continuous Flow Synthesis. *ACS Appl. Mater. Interfaces* **2021**, *13* (45), 54284–54293. https://doi.org/10.1021/acsami.1c04920.

(59) Zeng, Z.; Flyagina, I. S.; Tan, J.-C. Nanomechanical Behavior and Interfacial Deformation beyond the Elastic Limit in 2D Metal–Organic Framework Nanosheets. *Nanoscale Adv.* **2020**, *2* (11), 5181–5191. https://doi.org/10.1039/D0NA00475H.

(60) Wang, S.; Wahiduzzaman, M.; Davis, L.; Tissot, A.; Shepard, W.; Marrot, J.; Martineau-Corcos, C.; Hamdane, D.; Maurin, G.; Devautour-Vinot, S.; Serre, C. A Robust Zirconium Amino Acid Metal-Organic Framework for Proton Conduction. *Nat Commun* **2018**, *9* (1), 4937. https://doi.org/10.1038/s41467-018-07414-4.

(61) Roy, S.; M. Suresh, V.; Kumar Maji, T. Self-Cleaning MOF: Realization of Extreme Water Repellence in Coordination Driven Self-Assembled Nanostructures. *Chem.* **2016**, *7* (3), 2251–2256. https://doi.org/10.1039/C5SC03676C.

(62) Kleist, W.; Maciejewski, M.; Baiker, A. MOF-5 Based Mixed-Linker Metal–Organic Frameworks: Synthesis, Thermal Stability and Catalytic Application. *Thermochimica Acta* **2010**, *499* (1), 71–78. https://doi.org/10.1016/j.tca.2009.11.004.

(63) Wang, T. C.; Vermeulen, N. A.; Kim, I. S.; Martinson, A. B. F.; Stoddart, J. F.; Hupp, J. T.; Farha, O. K. Scalable Synthesis and Post-Modification of a Mesoporous Metal-Organic Framework Called NU-1000. *Nat. Protoc.* **2016**, *11* (1), 149–162. https://doi.org/10.1038/nprot.2016.001.

(64) Zhang, S.; Ma, J.; Zhang, X.; Duan, E.; Cheng, P. Assembly of Metal–Organic Frameworks Based on 3,3′,5,5′-Azobenzene-Tetracarboxylic Acid: Photoluminescences, Magnetic Properties, and Gas Separations. *Inorg. Chem.* **2015**, *54* (2), 586–595. https://doi.org/10.1021/ic502488c.

(65) Schumacher, W. T.; Mathews, M. J.; Larson, S. A.; Lemmon, C. E.; Campbell, K. A.; Crabb, B. T.; Chicoine, B. J.-A.; Beauvais, L. G.; Perry, M. C. Organocatalysis by Site-Isolated N-Heterocyclic Carbenes Doped into the UIO-67 Framework. *Polyhedron* **2016**, *114*, 422–427. https://doi.org/10.1016/j.poly.2016.02.033.

(66) Lu, W.; Yuan, D.; Makal, T. A.; Li, J.-R.; Zhou, H.-C. A Highly Porous and Robust (3,3,4)-Connected Metal–Organic Framework Assembled with a 90° Bridging-Angle Embedded Octacarboxylate Ligand. *Angew. Chem., Int. Ed.* **2012**, *51* (7), 1580–1584. https://doi.org/10.1002/anie.201106615.

(67) Chaemchuen, S.; Zhou, K.; Kabir, N. A.; Chen, Y.; Ke, X.; Van Tendeloo, G.; Verpoort, F. Tuning Metal Sites of DABCO MOF for Gas Purification at Ambient Conditions. *Microporous Mesoporous Mater.* **2015**, *201*, 277–285. https://doi.org/10.1016/j.micromeso.2014.09.038.

(68) Mousavi, B.; Chaemchuen, S.; Moosavi, B.; Zhou, K.; Yusubov, M.; Verpoort, F. CO_2 Cycloaddition to Epoxides by Using M-DABCO Metal–Organic Frameworks and the Influence of the Synthetic Method on Catalytic Reactivity. *ChemistryOpen* **2017**, *6* (5), 674–680. https://doi.org/10.1002/open.201700060.

(69) Kawamura, A.; Greenwood, A. R.; Filatov, A. S.; Gallagher, A. T.; Galli, G.; Anderson, J. S. Incorporation of Pyrazine and Bipyridine Linkers with High-Spin Fe(II) and Co(II) in a Metal–Organic Framework. *Inorg. Chem.* **2017**, *56* (6), 3349–3356. https://doi.org/10.1021/acs.inorgchem.6b02883.

(70) Peters, S.; Varathan, E.; Pillai, R. S. Investigation of Guest-Induced Flexibility in Pyrazine Derivative of ALFFIVE MOF via Molecular Simulation. *Langmuir* **2023**, *39* (4), 1373–1385. https://doi.org/10.1021/acs.langmuir.2c02027.

(71) Dybtsev, D. N.; Chun, H.; Kim, K. Rigid and Flexible: A Highly Porous Metal–Organic Framework with Unusual Guest-Dependent Dynamic Behavior. *Angew. Chem., Int. Ed.* **2004**, *43* (38), 5033–5036. https://doi.org/10.1002/anie.200460712.

(72) Kim, Y.; Haldar, R.; Kim, H.; Koo, J.; Kim, K. The Guest-Dependent Thermal Response of the Flexible MOF $Zn_2(BDC)_2(DABCO)$. *Dalton Trans.* **2016**, *45* (10), 4187–4192. https://doi.org/10.1039/C5DT03710G.

(73) Rubio-Martinez, M.; Avci-Camur, C.; W. Thornton, A.; Imaz, I.; Maspoch, D.; R. Hill, M. New Synthetic Routes towards MOF Production at Scale. *Chem. Soc. Rev.* **2017**, *46* (11), 3453–3480. https://doi.org/10.1039/C7CS00109F.

(74) Cheng, P.; Wang, C.; Kaneti, Y. V.; Eguchi, M.; Lin, J.; Yamauchi, Y.; Na, J. Practical MOF Nanoarchitectonics: New Strategies for Enhancing the Processability of MOFs for Practical Applications. *Langmuir* **2020**, *36* (16), 4231–4249. https://doi.org/10.1021/acs.langmuir.0c00236.

(75) Hönicke, I. M.; Senkovska, I.; Bon, V.; Baburin, I. A.; Bönisch, N.; Raschke, S.; Evans, J. D.; Kaskel, S. Balancing Mechanical Stability and Ultrahigh Porosity in Crystalline Framework Materials. *Angew. Chem., Int. Ed.* **2018**, *57* (42), 13780–13783. https://doi.org/10.1002/anie.201808240.

(76) Farha, O. K.; Eryazici, I.; Jeong, N. C.; Hauser, B. G.; Wilmer, C. E.; Sarjeant, A. A.; Snurr, R. Q.; Nguyen, S. T.; Yazaydın, A. Ö.; Hupp, J. T. Metal–Organic Framework Materials with Ultrahigh Surface Areas: Is the Sky the Limit? *J. Am. Chem. Soc.* **2012**, *134* (36), 15016–15021. https://doi.org/10.1021/ja3055639.

(77) Cuchiaro, J.; DeRoo, J.; Thai, J.; Reynolds, M. M. Evaluation of the Adsorption-Accessible Surface Area of MIL-53(Al) Using Cannabinoids in a Closed System. *ACS Appl. Mater. Interfaces* **2022**, *14* (10), 12836–12844. https://doi.org/10.1021/acsami.1c24391.

(78) Fang, Z.; Bueken, B.; De Vos, D. E.; Fischer, R. A. Defect-Engineered Metal–Organic Frameworks. *Angew. Chem., Int. Ed.* **2015**, *54* (25), 7234–7254. https://doi.org/10.1002/anie.201411540.

(79) K. Cheetham, A.; D. Bennett, T.; Coudert, F.-X.; L. Goodwin, A. Defects and Disorder in Metal Organic Frameworks. *Dalton Trans.* **2016**, *45* (10), 4113–4126. https://doi.org/10.1039/C5DT04392A.

(80) De Vos, A.; Hendrickx, K.; Van Der Voort, P.; Van Speybroeck, V.; Lejaeghere, K. Missing Linkers: An Alternative Pathway to UiO-66 Electronic Structure Engineering. *Chem. Mater.* **2017**, *29* (7), 3006–3019. https://doi.org/10.1021/acs.chemmater.6b05444.

(81) Gutov, O. V.; Hevia, M. G.; Escudero-Adán, E. C.; Shafir, A. Metal–Organic Framework (MOF) Defects under Control: Insights into the Missing Linker Sites and Their Implication in the Reactivity of Zirconium-Based Frameworks. *Inorg. Chem.* **2015**, *54* (17), 8396–8400. https://doi.org/10.1021/acs.inorgchem.5b01053.

(82) Al-Jadir, T. M.; Siperstein, F. R. The Influence of the Pore Size in Metal−Organic Frameworks in Adsorption and Separation of Hydrogen Sulphide: A Molecular Simulation Study. *Microporous Mesoporous Mater.* **2018**, *271*, 160–168. https://doi.org/10.1016/j.micromeso.2018.06.002.

(83) Shearer, G. C.; Chavan, S.; Ethiraj, J.; Vitillo, J. G.; Svelle, S.; Olsbye, U.; Lamberti, C.; Bordiga, S.; Lillerud, K. P. Tuned to Perfection: Ironing Out the Defects in Metal–Organic Framework UiO-66. *Chem. Mater.* **2014**, *26* (14), 4068–4071. https://doi.org/10.1021/cm501859p.

(84) Tan, K.; Pandey, H.; Wang, H.; Velasco, E.; Wang, K.-Y.; Zhou, H.-C.; Li, J.; Thonhauser, T. Defect Termination in the UiO-66 Family of Metal–Organic Frameworks: The Role of Water and Modulator. *J. Am. Chem. Soc.* **2021**, *143* (17), 6328–6332. https://doi.org/10.1021/jacs.1c01408.

(85) Vandichel, M.; Hajek, J.; Ghysels, A.; De Vos, A.; Waroquier, M.; Van Speybroeck, V. Water Coordination and Dehydration Processes in Defective UiO-66 Type Metal Organic Frameworks. *CrystEngComm* **2016**, *18* (37), 7056–7069. https://doi.org/10.1039/C6CE01027J.

(86) Marreiros, J.; Caratelli, C.; Hajek, J.; Krajnc, A.; Fleury, G.; Bueken, B.; De Vos, D. E.; Mali, G.; Roeffaers, M. B. J.; Van Speybroeck, V.; Ameloot, R. Active Role of Methanol in Post-Synthetic Linker Exchange in the Metal–Organic Framework UiO-66. *Chem. Mater.* **2019**, *31* (4), 1359–1369. https://doi.org/10.1021/acs.chemmater.8b04734.

(87) Chu, J.; Ke, F.-S.; Wang, Y.; Feng, X.; Chen, W.; Ai, X.; Yang, H.; Cao, Y. Facile and Reversible Digestion and Regeneration of Zirconium-Based Metal-Organic Frameworks. *Commun Chem* **2020**, *3* (1), 1–7. https://doi.org/10.1038/s42004-019-0248-7.

(88) Mondloch, J. E.; Katz, M. J.; Planas, N.; Semrouni, D.; Gagliardi, L.; Hupp, J. T.; Farha, O. K. Are Zr_6-Based MOFs Water Stable? Linker Hydrolysis vs. Capillary-Force-Driven Channel Collapse. *Chem. Commun.* **2014**, *50* (64), 8944–8946. https://doi.org/10.1039/C4CC02401J.

(89) Lawrence, M. C.; Schneider, C.; Katz, M. J. Determining the Structural Stability of UiO-67 with Respect to Time: A Solid-State NMR Investigation. *Chem. Commun.* **2016**, *52* (28), 4971–4974. https://doi.org/10.1039/C5CC09919F.

(90) Ayoub, G.; Islamoglu, T.; Goswami, S.; Friščić, T.; Farha, O. K. Torsion Angle Effect on the Activation of UiO Metal–Organic Frameworks. *ACS Appl. Mater. Interfaces* **2019**, *11* (17), 15788–15794. https://doi.org/10.1021/acsami.9b02764.

(91) Athar, M.; Rzepka, P.; Thoeny, D.; Ranocchiari, M.; Bokhoven, J. A. van. Thermal Degradation of Defective High-Surface-Area UiO-66 in Different Gaseous Environments. *RSC Adv.* **2021**, *11* (61), 38849–38855. https://doi.org/10.1039/D1RA05411B.

(92) Goodenough, I.; Devulapalli, V. S. D.; Xu, W.; Boyanich, M. C.; Luo, T.-Y.; De Souza, M.; Richard, M.; Rosi, N. L.; Borguet, E. Interplay between Intrinsic Thermal Stability and Expansion Properties of Functionalized UiO-67 Metal–Organic Frameworks. *Chem. Mater.* **2021**, *33* (3), 910–920. https://doi.org/10.1021/acs.chemmater.0c03889.

(93) DeCoste, J. B.; Peterson, G. W.; Jasuja, H.; Glover, T. G.; Huang, Y.; Walton, K. S. Stability and Degradation Mechanisms of Metal–Organic Frameworks Containing the $Zr_6O_4(OH)_4$ Secondary Building Unit. *J. Mater. Chem. A* **2013**, *1* (18), 5642–5650. https://doi.org/10.1039/C3TA10662D.

(94) Lin, S.; Kumar Reddy, D. H.; Bediako, J. K.; Song, M.-H.; Wei, W.; Kim, J.-A.; Yun, Y.-S. Effective Adsorption of Pd(II), Pt(IV) and Au(III) by Zr(IV)-Based Metal–Organic Frameworks from Strongly Acidic Solutions. *J. Mater. Chem. A* **2017**, *5* (26), 13557–13564. https://doi.org/10.1039/C7TA02518A.

(95) Ahmadijokani, F.; Molavi, H.; Rezakazemi, M.; Tajahmadi, S.; Bahi, A.; Ko, F.; Aminabhavi, T. M.; Li, J.-R.; Arjmand, M. UiO-66 Metal–Organic Frameworks in Water Treatment: A Critical Review. *Prog. Mater. Sci.* **2022**, *125*, 100904. https://doi.org/10.1016/j.pmatsci.2021.100904.

(96) Marshall, R. J.; Kalinovskyy, Y.; Griffin, S. L.; Wilson, C.; Blight, B. A.; Forgan, R. S. Functional Versatility of a Series of Zr Metal–Organic Frameworks Probed by Solid-State Photoluminescence Spectroscopy. *J. Am. Chem. Soc.* **2017**, *139* (17), 6253–6260. https://doi.org/10.1021/jacs.7b02184.

(97) Kirchon, A.; Feng, L.; F. Drake, H.; A. Joseph, E.; Zhou, H.-C. From Fundamentals to Applications: A Toolbox for Robust and Multifunctional MOF Materials. *Chem. Soc. Rev.* **2018**, *47* (23), 8611–8638. https://doi.org/10.1039/C8CS00688A.

(98) Cohen, S. M. Postsynthetic Methods for the Functionalization of Metal–Organic Frameworks. *Chem. Rev.* **2012**, *112* (2), 970–1000. https://doi.org/10.1021/cr200179u.

(99) Kutzscher, C.; Nickerl, G.; Senkovska, I.; Bon, V.; Kaskel, S. Proline Functionalized UiO-67 and UiO-68 Type Metal–Organic Frameworks Showing Reversed Diastereoselectivity in Aldol Addition Reactions. *Chem. Mater.* **2016**, *28* (8), 2573–2580. https://doi.org/10.1021/acs.chemmater.5b04575.

(100) Vermoortele, F.; Bueken, B.; Le Bars, G.; Van de Voorde, B.; Vandichel, M.; Houthoofd, K.; Vimont, A.; Daturi, M.; Waroquier, M.; Van Speybroeck, V.; Kirschhock, C.; De Vos, D. E. Synthesis Modulation as a Tool To Increase the Catalytic Activity of Metal–Organic Frameworks: The Unique Case of UiO-66(Zr). *J. Am. Chem. Soc.* **2013**, *135* (31), 11465–11468. https://doi.org/10.1021/ja405078u.

(101) Saleem, H.; Rafique, U.; Davies, R. P. Investigations on Post-Synthetically Modified UiO-66-NH_2 for the Adsorptive Removal of Heavy Metal Ions from Aqueous Solution. *Microporous Mesoporous Mater.* **2016**, *221*, 238–244. https://doi.org/10.1016/j.micromeso.2015.09.043.

(102) Zheng, B.; Oliveira, F. L.; Neumann Barros Ferreira, R.; Steiner, M.; Hamann, H.; Gu, G. X.; Luan, B. Quantum Informed Machine-Learning Potentials for Molecular Dynamics Simulations of CO_2's Chemisorption and Diffusion in Mg-MOF-74. *ACS Nano* **2023**, *17* (6), 5579–5587. https://doi.org/10.1021/acsnano.2c11102.

(103) Liu, J.; Wei, Y.; Li, P.; Zhao, Y.; Zou, R. Selective H_2S/CO_2 Separation by Metal–Organic Frameworks Based on Chemical-Physical Adsorption. *J. Phys. Chem. C* **2017**, *121* (24), 13249–13255. https://doi.org/10.1021/acs.jpcc.7b04465.

(104) Tsivion, E.; Long, J. R.; Head-Gordon, M. Hydrogen Physisorption on Metal–Organic Framework Linkers and Metalated Linkers: A Computational Study of the Factors That Control Binding Strength. *J. Am. Chem. Soc.* **2014**, *136* (51), 17827–17835. https://doi.org/10.1021/ja5101323.

(105) Thirumalai, K.; DiNezio, P. N.; Okumura, Y.; Deser, C. Extreme Temperatures in Southeast Asia Caused by El Niño and Worsened by Global Warming. *Nat Commun* **2017**, *8* (1), 15531. https://doi.org/10.1038/ncomms15531.

(106) Labat, D.; Goddéris, Y.; Probst, J. L.; Guyot, J. L. Evidence for Global Runoff Increase Related to Climate Warming. *Adv Water Resour.global war* **2004**, *27* (6), 631–642. https://doi.org/10.1016/j.advwatres.2004.02.020.

(107) McCulloch, M.; Falter, J.; Trotter, J.; Montagna, P. Coral Resilience to Ocean Acidification and Global Warming through PH Up-Regulation. *Nat. Clim. Change* **2012**, *2* (8), 623–627. https://doi.org/10.1038/nclimate1473.

(108) Obbard, R. W.; Sadri, S.; Wong, Y. Q.; Khitun, A. A.; Baker, I.; Thompson, R. C. Global Warming Releases Microplastic Legacy Frozen in Arctic Sea Ice. *Earth's futur.* **2014**, *2* (6), 315–320. https://doi.org/10.1002/2014EF000240.

(109) Cao, L.; Caldeira, K. Atmospheric CO_2 Stabilization and Ocean Acidification. *Geophys. Res. Lett.* **2008**, *35* (19). https://doi.org/10.1029/2008GL035072.

(110) Dahlke, F. T.; Butzin, M.; Nahrgang, J.; Puvanendran, V.; Mortensen, A.; Pörtner, H.-O.; Storch, D. Northern Cod Species Face Spawning Habitat Losses If Global Warming Exceeds 1.5°C. *Sci. Adv.* **2018**, *4* (11), eaas8821. https://doi.org/10.1126/sciadv.aas8821.

(111) Reddin, C. J.; Aberhan, M.; Raja, N. B.; Kocsis, Á. T. Global Warming Generates Predictable Extinctions of Warm- and Cold-Water Marine Benthic Invertebrates via Thermal Habitat Loss. *Glob. Chang. Biol.* **2022**, *28* (19), 5793–5807. https://doi.org/10.1111/gcb.16333.

(112) Kubisch, E. L.; Corbalán, V.; Ibargüengoytía, N. R.; Sinervo, B. Local Extinction Risk of Three Species of Lizard from Patagonia as a Result of Global Warming. *Can. J. Zool.* **2016**, *94* (1), 49–59. https://doi.org/10.1139/cjz-2015-0024.

(113) Nyong, A.; Adesina, F.; Osman Elasha, B. The Value of Indigenous Knowledge in Climate Change Mitigation and Adaptation Strategies in the African Sahel. *Mitig Adapt Strat Glob Change* **2007**, *12* (5), 787–797. https://doi.org/10.1007/s11027-007-9099-0.

(114) Ross, M. S.; Ruiz, P. L.; Sah, J. P.; Hanan, E. J. Chilling Damage in a Changing Climate in Coastal Landscapes of the Subtropical Zone: A Case Study from South Florida. *Global Change Biology* **2009**, *15* (7), 1817–1832. https://doi.org/10.1111/j.1365-2486.2009.01900.x.

(115) Kellstedt, P. M.; Zahran, S.; Vedlitz, A. Personal Efficacy, the Information Environment, and Attitudes Toward Global Warming and Climate Change in the United States. *Risk Anal.* **2008**, *28* (1), 113–126. https://doi.org/10.1111/j.1539-6924.2008.01010.x.

(116) Norby, R. J.; Luo, Y. Evaluating Ecosystem Responses to Rising Atmospheric CO_2 and Global Warming in a Multi-Factor World. *New Phytol.* **2004**, *162* (2), 281–293. https://doi.org/10.1111/j.1469-8137.2004.01047.x.

(117) Franta, B. Early Oil Industry Knowledge of CO_2 and Global Warming. *Nat. Clim. Change* **2018**, *8* (12), 1024–1025. https://doi.org/10.1038/s41558-018-0349-9.

(118) US Department of Commerce, N. *Global Monitoring Laboratory - Carbon Cycle Greenhouse Gases*. https://gml.noaa.gov/ccgg/trends/graph.html (accessed 2023-04-16).

(119) Wuebbles, D. J.; Jain, A. K. Concerns about Climate Change and the Role of Fossil Fuel Use. *Fuel Process. Technol.* **2001**, *71* (1), 99–119. https://doi.org/10.1016/S0378-3820(01)00139-4.

(120) Paraschiv, S.; Paraschiv, L. S. Trends of Carbon Dioxide (CO_2) Emissions from Fossil Fuels Combustion (Coal, Gas and Oil) in the EU Member States from 1960 to 2018. *Energy Rep.* **2020**, *6*, 237–242. https://doi.org/10.1016/j.egyr.2020.11.116.

(121) Abd, A. A.; Naji, S. Z.; Hashim, A. S.; Othman, M. R. Carbon Dioxide Removal through Physical Adsorption Using Carbonaceous and Non-Carbonaceous Adsorbents: A Review. *J. Environ. Chem. Eng.* **2020**, *8* (5), 104142. https://doi.org/10.1016/j.jece.2020.104142.

(122) Hepburn, C.; Adlen, E.; Beddington, J.; Carter, E. A.; Fuss, S.; Mac Dowell, N.; Minx, J. C.; Smith, P.; Williams, C. K. The Technological and Economic Prospects for CO_2 Utilization and Removal. *Nature* **2019**, *575* (7781), 87–97. https://doi.org/10.1038/s41586-019-1681-6.

(123) Shekhah, O.; Belmabkhout, Y.; Chen, Z.; Guillerm, V.; Cairns, A.; Adil, K.; Eddaoudi, M. Made-to-Order Metal-Organic Frameworks for Trace Carbon Dioxide Removal and Air Capture. *Nat Commun* **2014**, *5* (1), 4228. https://doi.org/10.1038/ncomms5228.

(124) Milner, P. J.; Siegelman, R. L.; Forse, A. C.; Gonzalez, M. I.; Runčevski, T.; Martell, J. D.; Reimer, J. A.; Long, J. R. A Diaminopropane-Appended Metal–Organic Framework Enabling Efficient CO_2 Capture from Coal Flue Gas via a Mixed Adsorption Mechanism. *J. Am. Chem. Soc.* **2017**, *139* (38), 13541–13553. https://doi.org/10.1021/jacs.7b07612.

(125) Mao, V. Y.; Milner, P. J.; Lee, J.-H.; Forse, A. C.; Kim, E. J.; Siegelman, R. L.; McGuirk, C. M.; Zasada, L. B.; Neaton, J. B.; Reimer, J. A.; Long, J. R. Cooperative Carbon Dioxide Adsorption in Alcoholamine- and Alkoxyalkylamine-Functionalized Metal–Organic Frameworks. *Angew. Chem., Int. Ed. Engl.* **2020**, *59* (44), 19468–19477. https://doi.org/10.1002/anie.201915561.

(126) Kong, X.; Scott, E.; Ding, W.; Mason, J. A.; Long, J. R.; Reimer, J. A. CO_2 Dynamics in a Metal–Organic Framework with Open Metal Sites. *J. Am. Chem. Soc.* **2012**, *134* (35), 14341–14344. https://doi.org/10.1021/ja306822p.

(127) Fracaroli, A. M.; Furukawa, H.; Suzuki, M.; Dodd, M.; Okajima, S.; Gándara, F.; Reimer, J. A.; Yaghi, O. M. Metal–Organic Frameworks with Precisely Designed Interior for Carbon Dioxide Capture in the Presence of Water. *J. Am. Chem. Soc.* **2014**, *136* (25), 8863–8866. https://doi.org/10.1021/ja503296c.

(128) Flaig, R. W.; Osborn Popp, T. M.; Fracaroli, A. M.; Kapustin, E. A.; Kalmutzki, M. J.; Altamimi, R. M.; Fathieh, F.; Reimer, J. A.; Yaghi, O. M. The Chemistry of CO_2 Capture in an Amine-Functionalized Metal–Organic Framework under Dry and Humid Conditions. *J. Am. Chem. Soc.* **2017**, *139* (35), 12125–12128. https://doi.org/10.1021/jacs.7b06382.

(129) Couck, S.; Denayer, J. F. M.; Baron, G. V.; Rémy, T.; Gascon, J.; Kapteijn, F. An Amine-Functionalized MIL-53 Metal−Organic Framework with Large Separation Power for CO_2 and CH_4. *J. Am. Chem. Soc.* **2009**, *131* (18), 6326–6327. https://doi.org/10.1021/ja900555r.

(130) Acree, Jr., W. E.; Chickos, J. S. *Phase Transition Enthalpy Measurements of Organic and Organometallic Compounds in NIST Chemistry WebBook, NIST Standard Reference Database Number 69*; Eds. P.J. Linstrom and W.G. Mallard, National Institute of Standards and Technology: Gaithersburg MD, 20899.

(131) Kim, S.-N.; Kim, J.; Kim, H.-Y.; Cho, H.-Y.; Ahn, W.-S. Adsorption/Catalytic Properties of MIL-125 and NH_2-MIL-125. *Catal. Today* **2013**, *204*, 85–93. https://doi.org/10.1016/j.cattod.2012.08.014.

(132) Cabello, C. P.; Berlier, G.; Magnacca, G.; Rumori, P.; Palomino, G. T. Enhanced CO_2 Adsorption Capacity of Amine-Functionalized MIL-100(Cr) Metal–Organic Frameworks. *CrystEngComm* **2015**, *17* (2), 430–437. https://doi.org/10.1039/C4CE01265H.

(133) Britt, D.; Furukawa, H.; Wang, B.; Glover, T. G.; Yaghi, O. M.; Halpern, J. Highly Efficient Separation of Carbon Dioxide by a Metal-Organic Framework Replete with Open Metal Sites. *Proc. Natl. Acad. Sci. U.S.A.* **2009**, *106* (49), 20637–20640.

(134) Dietzel, P. D. C.; Besikiotis, V.; Blom, R. Application of Metal–Organic Frameworks with Coordinatively Unsaturated Metal Sites in Storage and Separation of Methane and Carbon Dioxide. *J. Mater. Chem.* **2009**, *19* (39), 7362. https://doi.org/10.1039/b911242a.

(135) Caskey, S. R.; Wong-Foy, A. G.; Matzger, A. J. Dramatic Tuning of Carbon Dioxide Uptake via Metal Substitution in a Coordination Polymer with Cylindrical Pores. *J. Am. Chem. Soc.* **2008**, *130* (33), 10870–10871. https://doi.org/10.1021/ja8036096.

(136) Li, J.-R.; Yu, J.; Lu, W.; Sun, L.-B.; Sculley, J.; Balbuena, P. B.; Zhou, H.-C. Porous Materials with Pre-Designed Single-Molecule Traps for CO_2 Selective Adsorption. *Nat Commun* **2013**, *4* (1), 1538. https://doi.org/10.1038/ncomms2552.

(137) Wang, H.; Liu, Y.; Li, J. Designer Metal–Organic Frameworks for Size-Exclusion-Based Hydrocarbon Separations: Progress and Challenges. *Advanced Materials* **2020**, *32* (44), 2002603. https://doi.org/10.1002/adma.202002603.

(138) Cui, X.; Chen, K.; Xing, H.; Yang, Q.; Krishna, R.; Bao, Z.; Wu, H.; Zhou, W.; Dong, X.; Han, Y.; Li, B.; Ren, Q.; Zaworotko, M. J.; Chen, B. Pore Chemistry and Size Control in Hybrid Porous Materials for Acetylene Capture from Ethylene. *Science* **2016**, *353* (6295), 141–144. https://doi.org/10.1126/science.aaf2458.

(139) Zhao, X.; Bu, X.; Zhai, Q.-G.; Tran, H.; Feng, P. Pore Space Partition by Symmetry-Matching Regulated Ligand Insertion and Dramatic Tuning on Carbon Dioxide Uptake. *J. Am. Chem. Soc.* **2015**, *137* (4), 1396–1399. https://doi.org/10.1021/ja512137t.

(140) Hanikel, N.; Prévot, M. S.; Yaghi, O. M. MOF Water Harvesters. *Nat. Nanotechnol.* **2020**, *15* (5), 348–355. https://doi.org/10.1038/s41565-020-0673-x.

(141) Canivet, J.; Fateeva, A.; Guo, Y.; Coasne, B.; Farrusseng, D. Water Adsorption in MOFs: Fundamentals and Applications. *Chem. Soc. Rev.* **2014**, *43* (16), 5594–5617. https://doi.org/10.1039/C4CS00078A.

(142) Furukawa, H.; Gándara, F.; Zhang, Y.-B.; Jiang, J.; Queen, W. L.; Hudson, M. R.; Yaghi, O. M. Water Adsorption in Porous Metal–Organic Frameworks and Related

Materials. *J. Am. Chem. Soc.* **2014**, *136* (11), 4369–4381. https://doi.org/10.1021/ja500330a.

(143) Henninger, S. K.; Habib, H. A.; Janiak, C. MOFs as Adsorbents for Low Temperature Heating and Cooling Applications. *J. Am. Chem. Soc.* **2009**, *131* (8), 2776–2777. https://doi.org/10.1021/ja808444z.

(144) Steinert, D. M.; Ernst, S.-J.; Henninger, S. K.; Janiak, C. Metal-Organic Frameworks as Sorption Materials for Heat Transformation Processes. *Eur. J. Inorg. Chem.* **2020**, *2020* (48), 4502–4515. https://doi.org/10.1002/ejic.202000834.

(145) Kim, H.; Yang, S.; Rao, S. R.; Narayanan, S.; Kapustin, E. A.; Furukawa, H.; Umans, A. S.; Yaghi, O. M.; Wang, E. N. Water Harvesting from Air with Metal-Organic Frameworks Powered by Natural Sunlight. *Science* **2017**, *356* (6336), 430–434. https://doi.org/10.1126/science.aam8743.

(146) Kim, H.; Rao, S. R.; Kapustin, E. A.; Zhao, L.; Yang, S.; Yaghi, O. M.; Wang, E. N. Adsorption-Based Atmospheric Water Harvesting Device for Arid Climates. *Nat Commun* **2018**, *9* (1), 1191. https://doi.org/10.1038/s41467-018-03162-7.

(147) Hanikel, N.; Prévot, M. S.; Fathieh, F.; Kapustin, E. A.; Lyu, H.; Wang, H.; Diercks, N. J.; Glover, T. G.; Yaghi, O. M. Rapid Cycling and Exceptional Yield in a Metal-Organic Framework Water Harvester. *ACS Cent. Sci.* **2019**, *5* (10), 1699–1706. https://doi.org/10.1021/acscentsci.9b00745.

(148) Musa, S. G.; Aljunid Merican, Z. M.; Haruna, A. Investigation of Isotherms and Isosteric Heat of Adsorption for PW11@HKUST-1 Composite. *J. Solid State Chem.* **2022**, *314*, 123363. https://doi.org/10.1016/j.jssc.2022.123363.

(149) Mason, J. A.; Sumida, K.; Herm, Z. R.; Krishna, R.; Long, Jeffrey. R. Evaluating Metal–Organic Frameworks for Post-Combustion Carbon Dioxide Capture via Temperature Swing Adsorption. *Energy Environ. Sci.* **2011**, *4* (8), 3030. https://doi.org/10.1039/c1ee01720a.

(150) Ritter, J. A.; Bhadra, S. J.; Ebner, A. D. On the Use of the Dual-Process Langmuir Model for Correlating Unary Equilibria and Predicting Mixed-Gas Adsorption Equilibria. *Langmuir* **2011**, *27* (8), 4700–4712. https://doi.org/10.1021/la104965w.

(151) Bai, R.; Yang, R. T. A Thermodynamically Consistent Langmuir Model for Mixed Gas Adsorption. *J. Colloid Interface Sci.* **2001**, *239* (2), 296–302. https://doi.org/10.1006/jcis.2001.7563.

(152) Pursell, C. J.; Hartshorn, H.; Ward, T.; Chandler, B. D.; Boccuzzi, F. Application of the Temkin Model to the Adsorption of CO on Gold. *J. Phys. Chem. C* **2011**, *115* (48), 23880–23892. https://doi.org/10.1021/jp207103z.

(153) Al-Ghouti, M. A.; Da'ana, D. A. Guidelines for the Use and Interpretation of Adsorption Isotherm Models: A Review. *J. Hazard. Mater.* **2020**, *393*, 122383. https://doi.org/10.1016/j.jhazmat.2020.122383.

(154) Lima, E. C.; Gomes, A. A.; Tran, H. N. Comparison of the Nonlinear and Linear Forms of the van't Hoff Equation for Calculation of Adsorption Thermodynamic Parameters ($\Delta S°$ and $\Delta H°$). *J. of Mol. Liq.* **2020**, *311*, 113315. https://doi.org/10.1016/j.molliq.2020.113315.

(155) Rouquerol, F.; Rouquerol, J.; Sing, K. S. W.; Llewellyn, P.; Maurin, G. *Adsorption by Powders and Porous Solids Principles, Methodology and Applications*, Second edition.; Elsevier, 1998.

(156) Alafnan, S.; Awotunde, A.; Glatz, G.; Adjei, S.; Alrumaih, I.; Gowida, A. Langmuir Adsorption Isotherm in Unconventional Resources: Applicability and Limitations. *J. Pet. Sci. Eng.* **2021**, *207*, 109172. https://doi.org/10.1016/j.petrol.2021.109172.

(157) Mathias, P. M.; Kumar, R.; Moyer, J. D.; Schork, J. M.; Srinivasan, S. R.; Auvil, S. R.; Talu, O. Correlation of Multicomponent Gas Adsorption by the Dual-Site Langmuir Model. Application to Nitrogen/Oxygen Adsorption on 5A-Zeolite. *Ind. Eng. Chem. Res.* **1996**, *35* (7), 2477–2483. https://doi.org/10.1021/ie950291y.

(158) Brunauer, S.; Emmett, P. H.; Teller, E. Adsorption of Gases in Multimolecular Layers. *J. Am. Chem. Soc.* **1938**, *60* (2), 309–319. https://doi.org/10.1021/ja01269a023.

(159) Lowell, S.; Shields, J. E.; Thomas, M. A.; Thommes, M. *Characterization of Porous Solids and Powders: Surface Area, Pore Size and Density*; Spinger Science, 2004.

(160) Gómez-Serrano, V.; González-García, C. M.; González-Martín, M. L. Nitrogen Adsorption Isotherms on Carbonaceous Materials. Comparison of BET and Langmuir Surface Areas. *Powder Technol.* **2001**, *116* (1), 103–108. https://doi.org/10.1016/S0032-5910(00)00367-3.

(161) Ryu, Z.; Zheng, J.; Wang, M.; Zhang, B. Characterization of Pore Size Distributions on Carbonaceous Adsorbents by DFT. *Carbon* **1999**, *37* (8), 1257–1264. https://doi.org/10.1016/S0008-6223(98)00322-4.

(162) Kupgan, G.; Liyana-Arachchi, T. P.; Colina, C. M. NLDFT Pore Size Distribution in Amorphous Microporous Materials. *Langmuir* **2017**, *33* (42), 11138–11145. https://doi.org/10.1021/acs.langmuir.7b01961.

(163) Zeng, M.; Tang, Y.; Mi, J.; Zhong, C. Improved Direct Correlation Function for Density Functional Theory Analysis of Pore Size Distributions. *J. Phys. Chem. C* **2009**, *113* (40), 17428–17436. https://doi.org/10.1021/jp902803t.

(164) Kalmutzki, M. J.; Diercks, C. S.; Yaghi, O. M. Metal–Organic Frameworks for Water Harvesting from Air. *Adv Mater* **2018**, *30* (37), 1704304. https://doi.org/10.1002/adma.201704304.

(165) Rieth, A. J.; Yang, S.; Wang, E. N.; Dincă, M. Record Atmospheric Fresh Water Capture and Heat Transfer with a Material Operating at the Water Uptake Reversibility Limit. *ACS Cent. Sci.* **2017**, *3* (6), 668–672. https://doi.org/10.1021/acscentsci.7b00186.

(166) Rieth, A. J.; Wright, A. M.; Skorupskii, G.; Mancuso, J. L.; Hendon, C. H.; Dincă, M. Record-Setting Sorbents for Reversible Water Uptake by Systematic Anion Exchanges in Metal–Organic Frameworks. *J. Am. Chem. Soc.* **2019**, *141* (35), 13858–13866. https://doi.org/10.1021/jacs.9b06246.

(167) Kim, S.-I.; Yoon, T.-U.; Kim, M.-B.; Lee, S.-J.; Hwang, Y. K.; Chang, J.-S.; Kim, H.-J.; Lee, H.-N.; Lee, U.-H.; Bae, Y.-S. Metal–Organic Frameworks with High Working Capacities and Cyclic Hydrothermal Stabilities for Fresh Water Production. *J. Chem. Eng.* **2016**, *286*, 467–475. https://doi.org/10.1016/j.cej.2015.10.098.

(168) Trapani, F.; Polyzoidis, A.; Loebbecke, S.; Piscopo, C. G. On the General Water Harvesting Capability of Metal-Organic Frameworks under Well-Defined Climatic Conditions. *Microporous Mesoporous Mater.* **2016**, *230*, 20–24. https://doi.org/10.1016/j.micromeso.2016.04.040.

(169) Nguyen, T. N.; Harreschou, I. M.; Lee, J.-H.; Stylianou, K. C.; Stephan, D. W. A Recyclable Metal–Organic Framework for Ammonia Vapour Adsorption. *Chem. Commun.* **2020**, *56* (67), 9600–9603. https://doi.org/10.1039/D0CC00741B.

(170) Huang, W. Z.; Zaheeruddin, M.; Cho, S. H. Dynamic Simulation of Energy Management Control Functions for HVAC Systems in Buildings. *Energy Convers. Manag.* **2006**, *47* (7), 926–943. https://doi.org/10.1016/j.enconman.2005.06.011.

(171) Wei, X.; Kusiak, A.; Li, M.; Tang, F.; Zeng, Y. Multi-Objective Optimization of the HVAC (Heating, Ventilation, and Air Conditioning) System Performance. *Energy* **2015**, *83*, 294–306. https://doi.org/10.1016/j.energy.2015.02.024.

(172) Jeremias, F.; Fröhlich, D.; Janiak, C.; Henninger, S. K. Water and Methanol Adsorption on MOFs for Cycling Heat Transformation Processes. *New J. Chem.* **2014**, *38* (5), 1846–1852. https://doi.org/10.1039/C3NJ01556D.

(173) Henninger, S. K.; Jeremias, F.; Kummer, H.; Janiak, C. MOFs for Use in Adsorption Heat Pump Processes. *European Journal of Inorganic Chemistry* **2012**, *2012* (16), 2625–2634. https://doi.org/10.1002/ejic.201101056.

(174) Jasuja, H.; Walton, K. S. Experimental Study of CO2,CH4, and Water Vapor Adsorption on a Dimethyl-Functionalized UiO-66 Framework. *J. Phys. Chem. C* **2013**, *117* (14), 7062–7068. https://doi.org/10.1021/jp311857e.

(175) McGrath, D. T.; Ryan, M. D.; MacInnis, J. J.; VandenBoer, T. C.; Young, C. J.; Katz, M. J. Selective Decontamination of the Reactive Air Pollutant Nitrous Acid via Node-Linker Cooperativity in a Metal–Organic Framework. *Chem. Sci.* **2019**, *10* (21), 5576–5581. https://doi.org/10.1039/C9SC01357A.

(176) Burtch, N. C.; Jasuja, H.; Walton, K. S. Water Stability and Adsorption in Metal–Organic Frameworks. *Chem. Rev.* **2014**, *114* (20), 10575–10612. https://doi.org/10.1021/cr5002589.

(177) Nijem, N.; Canepa, P.; Kaipa, U.; Tan, K.; Roodenko, K.; Tekarli, S.; Halbert, J.; Oswald, I. W. H.; Arvapally, R. K.; Yang, C.; Thonhauser, T.; Omary, M. A.; Chabal, Y. J. Water Cluster Confinement and Methane Adsorption in the Hydrophobic Cavities of a Fluorinated Metal–Organic Framework. *J. Am. Chem. Soc.* **2013**, *135* (34), 12615–12626. https://doi.org/10.1021/ja400754p.

(178) Peterson, G. W.; Mahle, J. J.; DeCoste, J. B.; Gordon, W. O.; Rossin, J. A. Extraordinary NO_2 Removal by the Metal–Organic Framework UiO-66-NH_2. *Angew. Chem., Int. Ed.* **2016**, *55* (21), 6235–6238. https://doi.org/10.1002/anie.201601782.

(179) Ko, N.; Hong, J.; Sung, S.; Cordova, K. E.; Park, H. J.; Yang, J. K.; Kim, J. A Significant Enhancement of Water Vapour Uptake at Low Pressure by Amine-Functionalization of UiO-67. *Dalton Trans.* **2015**, *44* (5), 2047–2051. https://doi.org/10.1039/C4DT02582B.

(180) Tan, C.; Han, X.; Li, Z.; Liu, Y.; Cui, Y. Controlled Exchange of Achiral Linkers with Chiral Linkers in Zr-Based UiO-68 Metal–Organic Framework. *J. Am. Chem. Soc.* **2018**, *140* (47), 16229–16236. https://doi.org/10.1021/jacs.8b09606.

(181) Schaate, A.; Roy, P.; Godt, A.; Lippke, J.; Waltz, F.; Wiebcke, M.; Behrens, P. Modulated Synthesis of Zr-Based Metal–Organic Frameworks: From Nano to Single Crystals. *Eur. J. Chem.* **2011**, *17* (24), 6643–6651. https://doi.org/10.1002/chem.201003211.

(182) Tortta, F.; Mele, A. *Nanosponges: Synthesis and Applications*; John Wiley & Sons, Ltd, 2019.

(183) Feng, X.; Hajek, J.; Jena, H. S.; Wang, G.; Veerapandian, S. K. P.; Morent, R.; De Geyter, N.; Leyssens, K.; Hoffman, A. E. J.; Meynen, V.; Marquez, C.; De Vos, D. E.; Van Speybroeck, V.; Leus, K.; Van Der Voort, P. Engineering a Highly Defective Stable UiO-66 with Tunable Lewis- Brønsted Acidity: The Role of the Hemilabile Linker. *J. Am. Chem. Soc.* **2020**, *142* (6), 3174–3183. https://doi.org/10.1021/jacs.9b13070.

(184) Liang, W.; Coghlan, C. J.; Ragon, F.; Rubio-Martinez, M.; D'Alessandro, D. M.; Babarao, R. Defect Engineering of UiO-66 for CO_2 and H_2O Uptake – a Combined Experimental and Simulation Study. *Dalton Trans.* **2016**, *45* (11), 4496–4500. https://doi.org/10.1039/C6DT00189K.

(185) Cliffe, M. J.; Wan, W.; Zou, X.; Chater, P. A.; Kleppe, A. K.; Tucker, M. G.; Wilhelm, H.; Funnell, N. P.; Coudert, F.-X.; Goodwin, A. L. Correlated Defect Nanoregions in a Metal–Organic Framework. *Nat Commun* **2014**, *5* (1), 4176. https://doi.org/10.1038/ncomms5176.

(186) Shan, B.; McIntyre, S. M.; Armstrong, M. R.; Shen, Y.; Mu, B. Investigation of Missing-Cluster Defects in UiO-66 and Ferrocene Deposition into Defect-Induced Cavities. *Ind. Eng. Chem. Res.* **2018**, *57* (42), 14233–14241. https://doi.org/10.1021/acs.iecr.8b03516.

(187) Ghosh, P.; Colón, Y. J.; Snurr, R. Q. Water Adsorption in UiO-66: The Importance of Defects. *Chem. Commun.* **2014**, *50* (77), 11329–11331. https://doi.org/10.1039/C4CC04945D.

(188) Schoenecker, P. M.; Carson, C. G.; Jasuja, H.; Flemming, C. J. J.; Walton, K. S. Effect of Water Adsorption on Retention of Structure and Surface Area of Metal–Organic Frameworks. *Ind. Eng. Chem. Res.* **2012**, *51* (18), 6513–6519. https://doi.org/10.1021/ie202325p.

(189) Canivet, J.; Bonnefoy, J.; Daniel, C.; Legrand, A.; Coasne, B.; Farrusseng, D. Structure–Property Relationships of Water Adsorption in Metal–Organic Frameworks. *New J. Chem.* **2014**, *38* (7), 3102–3111. https://doi.org/10.1039/C4NJ00076E.

(190) Ma, Y.; Cao, X.; Feng, X.; Ma, Y.; Zou, H. Fabrication of Super-Hydrophobic Film from PMMA with Intrinsic Water Contact Angle below 90°. *Polymer* **2007**, *48* (26), 7455–7460. https://doi.org/10.1016/j.polymer.2007.10.038.

(191) Zuo, B.; Hu, Y.; Lu, X.; Zhang, S.; Fan, H.; Wang, X. Surface Properties of Poly(Vinyl Alcohol) Films Dominated by Spontaneous Adsorption of Ethanol and Governed by Hydrogen Bonding. *J. Phys. Chem. C* **2013**, *117* (7), 3396–3406. https://doi.org/10.1021/jp3113304.

(192) Alamri, S.; Aguilar-Morales, A. I.; Lasagni, A. F. Controlling the Wettability of Polycarbonate Substrates by Producing Hierarchical Structures Using Direct Laser

Interference Patterning. *Eur. Polym. J.* **2018**, *99*, 27–37. https://doi.org/10.1016/j.eurpolymj.2017.12.001.

(193) Shearer, G. C.; Forselv, S.; Chavan, S.; Bordiga, S.; Mathisen, K.; Bjørgen, M.; Svelle, S.; Lillerud, K. P. In Situ Infrared Spectroscopic and Gravimetric Characterisation of the Solvent Removal and Dehydroxylation of the Metal Organic Frameworks UiO-66 and UiO-67. *Top Catal* **2013**, *56* (9–10), 770–782. https://doi.org/10.1007/s11244-013-0027-0.

(194) DeCoste, J. B.; Peterson, G. W.; Schindler, B. J.; Killops, K. L.; Browe, M. A.; Mahle, J. J. The Effect of Water Adsorption on the Structure of the Carboxylate Containing Metal–Organic Frameworks Cu-BTC, Mg-MOF-74, and UiO-66. *J. Mater. Chem. A* **2013**, *1* (38), 11922–11932. https://doi.org/10.1039/C3TA12497E.

(195) Cao, C.-C.; Chen, C.-X.; Wei, Z.-W.; Qiu, Q.-F.; Zhu, N.-X.; Xiong, Y.-Y.; Jiang, J.-J.; Wang, D.; Su, C.-Y. Catalysis through Dynamic Spacer Installation of Multivariate Functionalities in Metal–Organic Frameworks. *J. Am. Chem. Soc.* **2019**, *141* (6), 2589–2593. https://doi.org/10.1021/jacs.8b12372.

(196) Liu, Y.; Chen, Y.-P.; Liu, T.-F.; Yakovenko, A. A.; Raiff, A. M.; Zhou, H.-C. Selective Gas Adsorption and Unique Phase Transition Properties in a Stable Magnesium Metal-Organic Framework Constructed from Infinite Metal Chains. *CrystEngComm* **2013**, *15* (45), 9688–9693. https://doi.org/10.1039/C3CE41106K.

(197) Jiang, H.-L.; Feng, D.; Liu, T.-F.; Li, J.-R.; Zhou, H.-C. Pore Surface Engineering with Controlled Loadings of Functional Groups via Click Chemistry in Highly Stable Metal–Organic Frameworks. *J. Am. Chem. Soc.* **2012**, *134* (36), 14690–14693. https://doi.org/10.1021/ja3063919.

(198) Ol'khovik, V. K.; Pap, A. A.; Vasilevskii, V. A.; Galinovskii, N. A.; Tereshko, S. N. Synthesis and Properties of Luminophores Derived from Fluorinated Biphenyls. *Russ J Org Chem* **2008**, *44* (8), 1172–1179. https://doi.org/10.1134/S1070428008080113.

(199) Halis, S.; Reimer, N.; Klinkebiel, A.; Lüning, U.; Stock, N. Four New Al-Based Microporous Metal-Organic Framework Compounds with MIL-53-Type Structure Containing Functionalized Extended Linker Molecules. *Microporous Mesoporous Mater.* **2015**, *216*, 13–19. https://doi.org/10.1016/j.micromeso.2015.01.030.

(200) Howarth, A. J.; Peters, A. W.; Vermeulen, N. A.; Wang, T. C.; Hupp, J. T.; Farha, O. K. Best Practices for the Synthesis, Activation, and Characterization of Metal–Organic Frameworks. *Chem. Mater.* **2017**, *29* (1), 26–39. https://doi.org/10.1021/acs.chemmater.6b02626.

(201) Vaidhyanathan, R.; Iremonger, S. S.; Shimizu, G. K. H.; Boyd, P. G.; Alavi, S.; Woo, T. K. Direct Observation and Quantification of CO_2 Binding Within an Amine-Functionalized Nanoporous Solid. *Science* **2010**, *330* (6004), 650–653. https://doi.org/10.1126/science.1194237.

(202) Grissom, T. G.; Driscoll, D. M.; Troya, D.; Sapienza, N. S.; Usov, P. M.; Morris, A. J.; Morris, J. R. Molecular-Level Insight into CO_2 Adsorption on the Zirconium-Based Metal–Organic Framework, UiO-66: A Combined Spectroscopic and Computational Approach. *J. Phys. Chem. C* **2019**, *123* (22), 13731–13738. https://doi.org/10.1021/acs.jpcc.9b02513.

(203) Khutia, A.; Rammelberg, H. U.; Schmidt, T.; Henninger, S.; Janiak, C. Water Sorption Cycle Measurements on Functionalized MIL-101Cr for Heat Transformation Application. *Chem. Mater.* **2013**, *25* (5), 790–798. https://doi.org/10.1021/cm304055k.

(204) An, J.; Rosi, N. L. Tuning MOF CO_2 Adsorption Properties via Cation Exchange. *J. Am. Chem. Soc.* **2010**, *132* (16), 5578–5579. https://doi.org/10.1021/ja1012992.

(205) Wu, H.; Chua, Y. S.; Krungleviciute, V.; Tyagi, M.; Chen, P.; Yildirim, T.; Zhou, W. Unusual and Highly Tunable Missing-Linker Defects in Zirconium Metal–Organic Framework UiO-66 and Their Important Effects on Gas Adsorption. *J. Am. Chem. Soc.* **2013**, *135* (28), 10525–10532. https://doi.org/10.1021/ja404514r.

(206) Audu, C. O.; Nguyen, H. G. T.; Chang, C.-Y.; Katz, M. J.; Mao, L.; Farha, O. K.; Hupp, J. T.; Nguyen, S. T. The Dual Capture of AsV and AsIII by UiO-66 and Analogues. *Chem. Sci.* **2016**, *7* (10), 6492–6498. https://doi.org/10.1039/C6SC00490C.

(207) Yang, Q.; D. Wiersum, A.; L. Llewellyn, P.; Guillerm, V.; Serre, C.; Maurin, G. Functionalizing Porous Zirconium Terephthalate UiO-66(Zr) for Natural Gas Upgrading: A Computational Exploration. *Chem. Comm.* **2011**, *47* (34), 9603–9605. https://doi.org/10.1039/C1CC13543K.

(208) Cmarik, G. E.; Kim, M.; Cohen, S. M.; Walton, K. S. Tuning the Adsorption Properties of UiO-66 via Ligand Functionalization. *Langmuir* **2012**, *28* (44), 15606–15613. https://doi.org/10.1021/la3035352.

(209) Jajko, G.; Kozyra, P.; Gutiérrez-Sevillano, J. J.; Makowski, W.; Calero, S. Carbon Dioxide Capture Enhanced by Pre-Adsorption of Water and Methanol in UiO-66. *Eur. J. Chem.* **2021**, *27* (59), 14653–14659. https://doi.org/10.1002/chem.202102181.

(210) Wong, Y.-L.; Yee, K.-K.; Hou, Y.-L.; Li, J.; Wang, Z.; Zeller, M.; Hunter, A. D.; Xu, Z. Single-Crystalline UiO-67-Type Porous Network Stable to Boiling Water, Solvent Loss, and Oxidation. *Inorg. Chem.* **2018**, *57* (11), 6198–6201. https://doi.org/10.1021/acs.inorgchem.8b00404.

(211) Meldal, M.; Tornøe, C. W. Cu-Catalyzed Azide−Alkyne Cycloaddition. *Chem. Rev.* **2008**, *108* (8), 2952–3015. https://doi.org/10.1021/cr0783479.

Appendix A - Additional information for Chapter 2 - The Mechanism of Water Adsorption in UiO Metal Organic Frameworks

Table A.1: Standard deviation for Pore size Distribution Fits of UiO-68-Me_4 and UiO-68-NH_2

Method A (Post COVID)	**UiO-68-Me_4**	**UiO-68-NH_2**
Tarazona	13.1 cm^3/g	6.1 cm^3/g
Cylindrical Pores on an Oxide Surface	45.3 cm^3/g	69.0 cm^3/g
Pillared Clay	19.8 cm^3/g	20.1 cm^3/g
Method B (Pre COVID)	**UiO-68-Me_4**	**UiO-68-NH_2**
Tarazona	12.0 cm^3/g	7.15 cm^3/g
Cylindrical Pores on an Oxide Surface	35.1 cm^3/g	69.0 cm^3/g
Pillared Clay	16.6 cm^3/g	28.9 cm^3/g

Water Adsorption and Desorption Isotherms

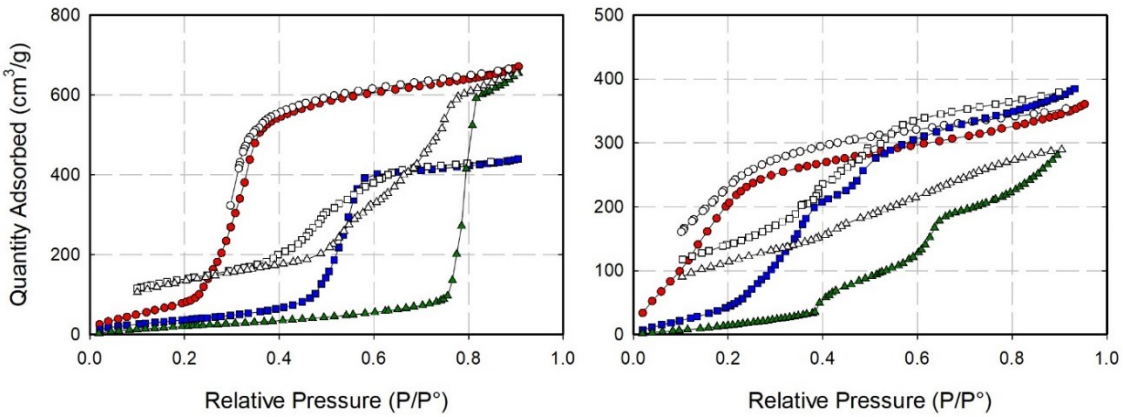

Figure A.1: Water adsorption and desorption isotherms. Left: UiO-66 (Adsorption: red circle trace; Desorption: white circle trace) UiO-67 (Adsorption: blue square trace; Desorption: white square trace), and UiO-68-Me_4 (Adsorption: green triangle trace; Desorption: white tri-angle trace). Right: UiO-66-NH_2 (Adsorption: red circle trace; Desorption: white circle trace) UiO-67-NH_2 (Adsorption: blue square trace; Desorption: white square trace), and UiO-68-NH_2 (Adsorption: green triangle trace; Desorption: white triangle trace)

Pore Size Distributions from Nitrogen Gas and Water Vapour Adsorption Isotherms.

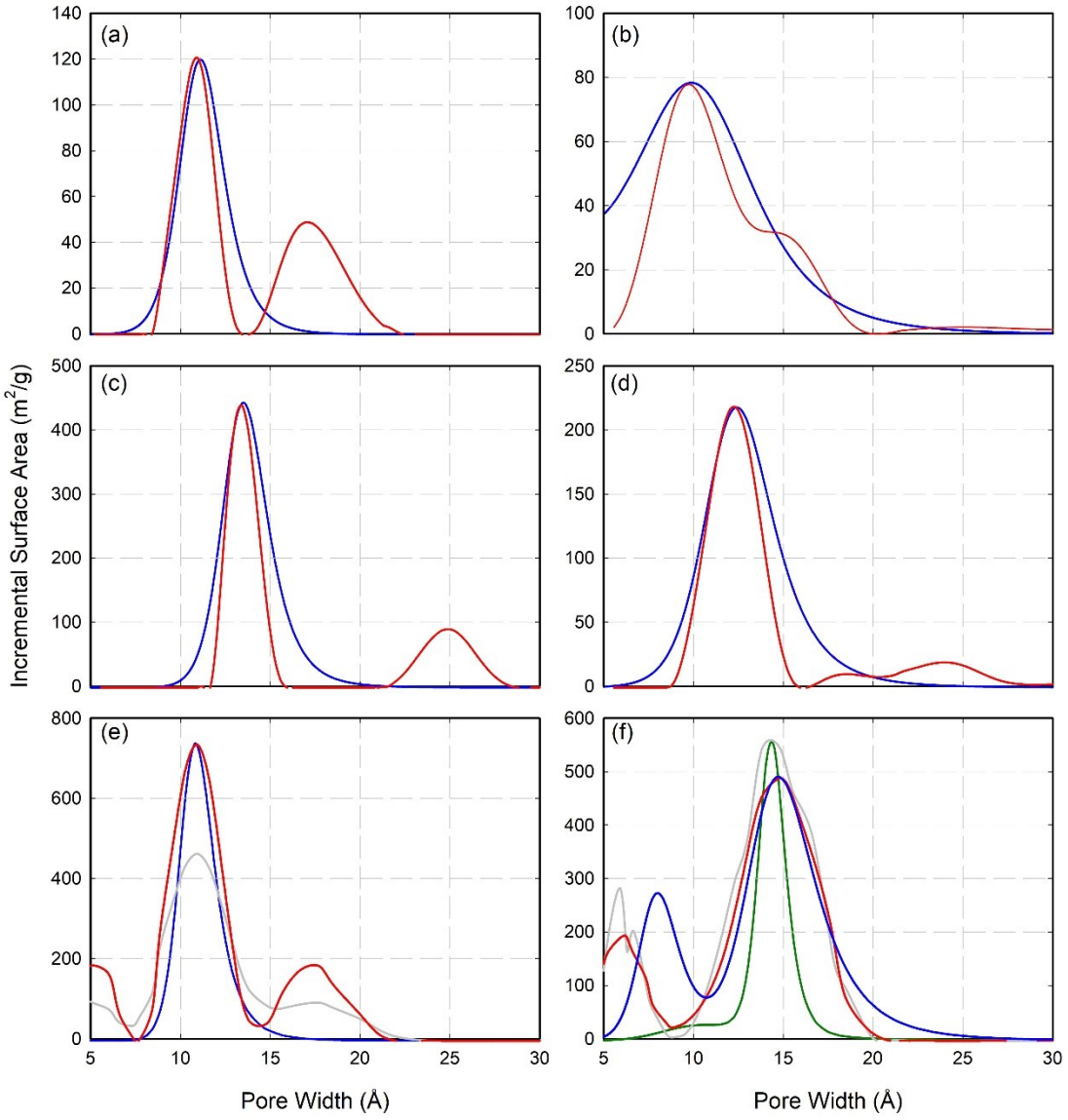

Figure A.2: Comparison of DFT-determined pore size distributions from fits to the nitrogen gas adsorption isotherm (red trace) and the pore size distribution fits from the Kelvin equation-derived water vapour adsorption isotherms. (a) UiO-66, (b) UiO-66-NH_2, (c) UiO-67, (d) UiO-67-NH_2, (e) UiO-68-Me_4 (grey is from synthetic method B), (f) UiO-68-NH_2 (grey and green are from synthetic method B). Note: the pore size fits for UiO-68-Me_4 and UiO-68-NH_2 are not perfect fits, but it does predict the most predominant pore.

Comparison of water isotherms for UiO-68 synthetic procedures.

Over the course of the project, several synthetic procedures for UiO-68-Me_4 and UiO-68-NH_2 were attempted. In our hands, we struggled to get reproducible results. The two synthetic preps (Method A and Method B) were often successful, but occasionally still failed. This suggests that there are additional variables in the synthesis of this MOF that are yet unknown that prevent us from getting reproducible results. Furthermore, the data for these materials were different enough that warrant discussion of these differences. Given that others may also get differing results, we opted to report on the results of two different synthetic procedures to shed light on the MOF itself. Table A.2 shows the differences in the observed BET surface areas. Method B produces materials with notably (~400 m^2/g) lower surface area than Method A. despite this, the pore size distributions for the two MOFs (Figure A.2 e and f red/dark red traces) seem more similar than different. This may suggest that Method A produces fewer impurities. However, given the quality of the pore size distribution fits, we are hesitant to overinterpret this data.

Table A.2: Comparison of BET surface areas between Method A and Method B for the UiO-68 reported in this work.

	BET surface area (m^2/g)		
MOF	**Method A**	**Method B**	**Expected**
UiO-68-Me_4	3475	2950	3300
UiO-68-NH_2	3350	2950	3750

Despite the similarities in the nitrogen adsorption data, the water isotherms looked surprisingly different. For UiO-68-Me_4, the two methods had different condensation step positions. This suggests either a change in the hydrophobicity of the MOF, potentially via conformational changes, or the difference in defect density, which could change the pore size. Based on the pore size distribution data, it seems unlikely that the pore size is changing.

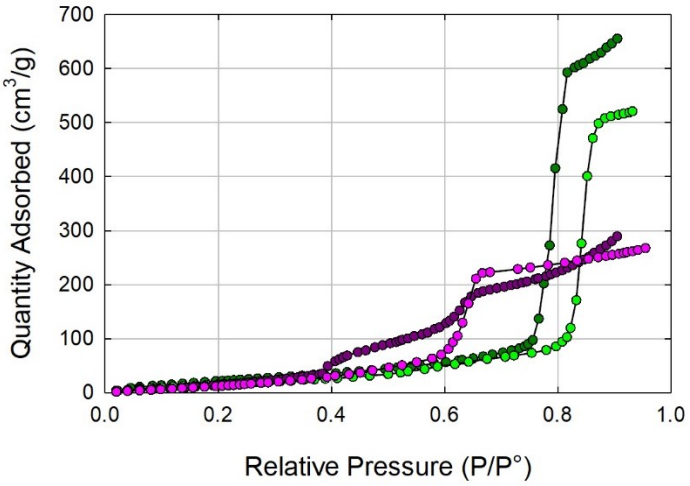

Figure A.3: water adsorption isotherms for UiO-68-Me_4 (Dark green: method A; Light green: method B) and UiO-68-NH2 (Magenta: method A; Pink: method B).

Looking at the water adsorption isotherm for UiO-68-NH_2 there are two steps in the isotherm for Method A, but only one step for Method B. upon closer inspection of the isotherm from method B, the background slope changes around 0.4 P/P_o. This suggests that both MOFs have the same types of pores, but the number of each pore may be different. From the data in this work, we assumed that the condensation step at 0.6 P/P_o is the large octahedral pore and access to the tetrahedral pore may only be possible in the synthesis for Method A. Indeed, if we look at the pore size distribution generated from the water

adsorption isotherms, we see two pores consistent with the tetrahedral and octahedral pore of UiO-68.

Although the interpretation of this data is consistent with the data, given that the synthetic procedures were not as reproducible for the UiO-68 MOFs versus the UiO-66 and UiO-67 MOFs, this is only a hypothesis. Further analysis of the synthetic procedures is necessary to optimize the procedures and analyze the water adsorption/desorption data; this is beyond the scope of this work.